A MID-INFRARED STUDY OF MIRA VARIABLE ATMOSPHERES: PHASE DEPENDENT ANALYSIS OF SPECTRAL LINES OBSERVED WITH THE SPITZER IRS

by

Dana K. Baylis-Aguirre

Submitted in Partial Fulfillment
of the Requirements for the Degree of
Doctor of Philosophy in Physics
with Dissertation in Astrophysics

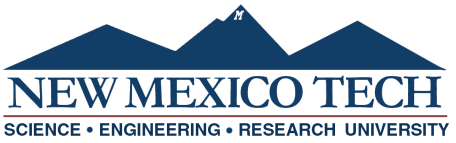

New Mexico Institute of Mining and Technology
Socorro, New Mexico
March 2021

Two roads diverged in a wood, and I—
I took the one less traveled by,
And that has made all the difference.

— Robert Frost

For my Father,
You taught me to love the stars.

For Ben,
You made sure I never quit loving those stars.

And for my Mom,
You taught me to be unstoppable by always
reminding me to be the little engine that could,
"I think I can, I think I can, I think I can".

Dana K. Baylis-Aguirre
New Mexico Institute of Mining and Technology
March 2021

ACKNOWLEDGMENTS

No woman is an island; I have been blessed with incredible people in my life who have supported me on this incredible journey.

I must first thank my wonderful husband and best friend, Ben. Without a doubt, I would not have reached this goal without your support. I uprooted us from our comfortable life near our families, and moved us to a tiny, eccentric town in the middle of the desert in New Mexico, where we did not know a soul. You never once wavered in your support. I have never wanted to quit something so much in my life as I did those first few days out here; I was so homesick that I just wanted to give up and go home. But you would not let me give up. You told me I had come too far to give up without a fight; so fight I did, and now here I am, about to reach the end, and you are still standing beside me. We have shared a truly epic adventure these past few years. Thank you for always seeing something in me, even when I cannot. Thank you for walking beside me on this journey. And thank you for sacrificing so much to help me achieve my lifelong dream.

Next, I would like to thank my amazing parents. This whole journey began when I was no more than five years old, sitting on my Dad's shoulders, looking up at the night sky. I have forgotten his specific words, but I will never forget him placing binoculars in front of my eyes to show me the Orion Nebula, all the while explaining how stars were being born in that "fuzzy blob", and that the light we were seeing had been traveling since long before I was born. I stared at that blob, utterly transfixed; from that moment on I was determined to study the stars. My Dad was there every step of the way. He instilled in me a deep love of physics and mathematics, and a lifelong passion for learning. Not every kid can call home in college and ask for help with their calculus homework, but I always could. My Mom taught me what it means to be fierce woman, capable of thriving in a male-dominated profession. She taught me to never give up, no matter the circumstances. I know I was an incredibly difficult child, but rather than trying to tame my stubborn and wild personality, my Mom and Dad accepted me just as I was, and, with what must have been the biggest reservoir of patience in the entire universe, they managed to guide me into adulthood without squashing my spirit. Now that I have my own son, I hope I can be there for him as much as they were for me. No acknowledgment of my family would be complete without my baby sister, Hanna. I know chasing this dream meant I had to leave; missing so much time with you is one of the biggest sacrifices I had to make. It is not easy being a woman of Faith in my profession, but whenever I struggled, I knew I could turn to you for encouragement. And last, but certainly not least, thank you Mom, for putting your life on hold for most of this past year to help me with

Liam so I could finish this dissertation. I could not have finished in time without your help.

I must also give thanks for the Aguirre family. First, thank you for raising such a wonderful man for me to share my life with. Thank you for supporting me all these years as you watched what must have seemed like such a crazy thing to chase. Thank you Kathleen and Andy for all the amazing trips that often gave me a much needed respite from studying. And Brooke, thank you for being available this past year to come drink wine with me after a hard day (and extra thanks for Kathleen who often supplied AMAZING wine!).

To Tina Güth, my dear, dear friend; a woman with an indomitable spirit, thank you for taking me under your wing. I would have been lost that first year without you. I can still picture sitting in front of your computer in the lab downstairs as you showed me the Spitzer spectra for the first time. I will always treasure all the research discussions, baking sprees, and morning workouts. To my amazing friends Danielle Harck and Joanna Spencer, thank you for your stalwart friendship, even when it could be weeks in between me texting you guys back. I cannot believe we have been friends for over a decade now. I never would have survived those advanced math classes without you Jo. And Danielle, navigating first time motherhood side-by-side with you this past year has been one of the greatest honors of my life. I cannot wait until we can celebrate champagne Thursday together in person again. I have deep appreciation and love for all the rest of the wonderful friends I have made (in no particular order): Dylan Ward, Robert Bentley, Geno Santistevan, Henry Prager, Brandon Gray, and Indy Jones. Graduate school is enormously stressful, and I have Melissa Begay to thank for helping me manage the stress in a healthy way and for making my body as strong as my mind.

I would like to thank Carlos Lopez-Carrillo for being a mentor and a friend. The Prelim exam was one of the biggest hurdles I faced in graduate school; Carlos generously donated his Friday afternoons for over 6 months to help me prepare. His patience and guidance proved invaluable. He always has time to help, and he will patiently answer any physics question, from high-school to graduate level.

There are no words that can properly express my heartfelt gratitude for my advisor Dr. Michelle Creech-Eakman. She has been more than a research advisor; she has been my counsellor, mentor, therapist, life-coach, and confidant. Tina and I used to joke that she was our mother duck, and we were her ducklings. She gave us the greatest gift by providing opportunities to test our wings, until one day we looked up, and suddenly we are strong enough to leave the nest and fly on our own. So thank you Michelle, from the bottom of my heart, for teaching me to fly.

This dissertation was typeset with LaTeX[1] by the author.

[1]The LaTeX document preparation system was developed by Leslie Lamport as a special version of Donald Knuth's TeX program for computer typesetting. TeX is a trademark of the American Mathematical Society. The LaTeX macro package for the New Mexico Institute of Mining and Technology dissertation format was written by John W. Shipman.

ABSTRACT

The dust that formed our planet, and the elements necessary for life to evolve here were created by stars. It is common for supernova to receive credit for our life on Earth, and there is no doubt they played a crucial role, however, theirs is not the only meaningful contribution. Recent observations have shown that Asymptotic Giant Branch (AGB) stars are responsible for returning substantial amounts of enriched material to their surrounding environments. AGB stars are highly-evolved low-to-intermediate mass stars that undergo significant mass loss as they near the end of their lives. The majority of stars that have died in our Universe have done so following the AGB phase (Höfner & Olofsson 2018), indicating these stars have great influence over galactic enrichment and the creation of new solar systems and potential life. Mira variables are AGB stars that undergo regular pulsation every 200-500 days. These pulsations, combined with their cool atmospheres (2000-3000 K), make Mira variables prolific molecule and dust factories. Studying the circumstellar environments surrounding Mira variables provides astrophysicists with the opportunity to observe the processes that created the building blocks of our solar system.

The characteristic pulsations of Mira variables make their circumstellar environments quite dynamic; to study how different atmospheric layers respond to the pulsation we need multiple observations across the entire pulsational period of the star. Observing Mira atmospheres at mid-infrared wavelengths provides access to the molecule and dust forming regions; these observations are best done with space-based instruments to avoid affects of telluric absorption. The Mira variables in this work were all observed at least twice with the Spitzer Space Telescope. High-resolution spectra (R $\sim$600) were taken approximately once a month with the Infrared Spectrograph (IRS) (Houck et al. 2004); the stars in this study are all bright in the infrared, and thus the exposures were kept brief to prevent saturation of the detector. The resulting spectra have high signal-to-noise ratios that display both gaseous and solid-state (dust) features.

The full Spitzer data set contains nearly 100 spectra for 25 stars spanning all three chemical subclasses. This dissertation focuses on analyzing five rovibrational Q-branch bandheads of CO_2 identified in the spectra of the oxygen-rich Miras (M-types,) and a previously un-observed feature at 17.62 μm that was observed across all three chemical subclasses. We have tentatively identified this new feature as Fe I. The CO_2 lines were analyzed using the publicly available code, RADEX (van der Tak et al. 2007), which uses a molecular data file that includes collisions to solve the radiative transfer; RADEX also has the capability of solving the radiative transfer under non-local thermodynamic equilibrium (NLTE) conditions, which is important for Mira atmosphere, because we

do not know how the pulsating atmosphere affects the CO_2 gas. Files for many molecules ready for calculations are included as part of the Leiden Atomic and Molecular Database (LAMDA), however, the majority of these files were built for modeling pure rotational spectra in the radio. We built a custom molecular file of ro-vibrational transitions of CO_2 that includes over 800 radiative transitions, approximately 20,000 collisions with H_2, and spans temperatures from 100-1000 K. We used RADEX to calculate synthetic spectra that match the observed CO_2 Q-branch bandheads. The synthetic spectra allow us to determine atmospheric conditions of the CO_2 gas like column density and kinetic temperature. For the new feature at 17.62 μm we fit every observation with Gaussian line profile to track its behavior with phase; this line has a completely different character than other features, and is extremely narrow, and bright. This behavior may be caused by fluorescence, and we explored several possible pumping mechanisms.

The results of the RADEX calculations show that CO_2 is highly extended throughout the M-type atmospheres. The kinetic temperatures also indicate that the CO_2 gas is much cooler in regions close to the star than radiative equilibrium conditions would predict. This suggests that CO_2 is in a previously theorized "refrigeration zone" that requires a break from radiative equilibrium, and allows dust condensation within a few $R_\star$ (Willson 2000). The behavior of the CO_2 lines shows that the M-types with longer periods are behaving differently than those with shorter periods. This behavior is also seen with the 17.62 μm feature; the line strength are consistently greater across all three chemical subclasses in the Miras with periods over 300 days. These results indicate that Miras with longer periods perturb their surrounding atmospheres differently than Miras with shorter periods.

Keywords: Mira Variables; AGB Star; Stellar Atmospheres; Spitzer; line formation

CONTENTS

LIST OF TABLES

LIST OF FIGURES

Figure **Page**

This dissertation is accepted on behalf of the faculty of the Institute by the following committee:

Michelle J. Creech-Eakman

Academic and Research Advisor

David S. Meier

Sharon L. Sessions

Jolante van Wijk

I release this document to the New Mexico Institute of Mining and Technology.

Dana K. Baylis-Aguirre December 9, 2020

"The nitrogen in our DNA, the calcium in our teeth, the iron in our blood, the carbon in our apple pies were made in the interiors of collapsing stars. We are made of starstuff."

— Carl Sagan

Chapter 1

INTRODUCTION

In five simple words, Carl Sagan summarized perhaps the most profound realization about humans: *"We are made of starstuff."* The human connection to the stars dates back to antiquity. Those who kept track of the positions of the stars and how they related to different seasons were able to adapt and evolve a more sophisticated way of life. Agriculture was only possible after we were able to use this knowledge of the stars to plan a growing season and know when to harvest. The intimate relationship humans have with the stars is unique because even though astronomy is the oldest science, it is the least tangible. All of our knowledge comes from one source: light.

Modern astrophysics was born in 1814 when Joseph von Fraunhofer put a simple prism in front of his telescope and noticed a series of dark bands in the rainbow of light from the Sun. It would not be until the invention of Quantum Mechanics over 100 years later that the true significance of those dark bands was fully grasped. Spectroscopy is the study of patterns in light and the physics behind what creates these patterns tells us what atom or molecule made the pattern, and the conditions they were under. This dissertation focuses on mid-infrared (mid-IR) spectroscopy to study highly evolved stars called Mira variables. These are Sun-like stars that have reached the final stages of their lives and exhibit remarkable variability. Section 1.1 provides context on why it is worthwhile to study Miras. Section 1.2 describes (briefly) stellar evolution concepts. Sections 1.3 & 1.4 provide details of highly evolved stars including Mira variables. This work is focused on mid-IR spectroscopy which allows us to study a very specific region in the Mira atmosphere, and fuller details are provided in Section 1.5.

1.1 A Little Motivation

What exactly is "starstuff", and more importantly how do stars enrich the interstellar medium (ISM) with this material? These two fairly simple questions have driven stellar physics for over 100 years. When the universe was created $\sim$ 14 billion years ago, there was hydrogen, helium, and very trace amounts of lithium. ALL subsequent elements on the periodic table were forged inside the hearts of stars and returned to the ISM when the stars died. This is the heart of "starstuff", but it is not the whole answer. For decades high-mass stars received all the credit for enriching the ISM when they died in a massive explosion called supernovae. However, high mass stars are fairly rare and there is on order only one-to-several supernova every century in a typical spiral galaxy such as the Milky Way (van den Bergh 1991; Li et al. 2011; Rozwadowska et al. 2021). We also must consider material made in Circumstellar Environments (CSE) around highly evolved low-to-intermediate mass stars called Asymptotic Giant Branch (AGB) stars. These stars have cool ($\sim$ 3000 K) atmospheres that allow for highly efficient molecule and dust formation. It is possible that up to 90% of the dust contributed to our galaxy comes from these stars (Sloan et al. 2008; Gehrz 1989). Oxygen-rich AGB stars produce silicate dust species including pyroxene, and olivene (e.g.Waters et al. (1996); Gail & Sedlmayr (1999) while carbon-rich AGB stars create "sooty" species like silicate carbide and polycyclic aromatic hydrocarbons (PAHs) and fullerenes (Buss et al. 1993; Cami et al. 2010; Zhang & Kwok 2013). These are the very building blocks of our Earth and they were created quietly in the atmospheres of garden variety stars. If we truly wish to understand "starstuff" then we must devote attention to the atmospheres of these AGB stars.

1.2 Stellar Evolution

Here we provide a brief introduction to stellar evolution. It is far beyond the scope of this work to include every detail about stellar evolution; in fact this is a highly active area of research and there are many questions waiting to be answered. When a basic search of "stellar evolution" is performed in the SAO/NASA Astrophysics Data System, it returns an astonishing 124,649 publications. This is because stellar evolution describes how stars are born, how they survive for billions of years, and how they die and each stage requires detailed physics to understand.

Stars live their entire lives engaged in a war against gravity. A star is born in clouds of gas and dust created by its predecessors. Gravity gives a star its first breath by collapsing the cloud until it is so hot and dense that nuclear fusion can begin. Radiation from nucleosynthesis keeps the star from collapsing for millions to billions of years. A star reaches the end of its life when it no longer has enough fuel left to "burn" in nucleosynthesis. Gravity gains the upper hand for the final time; as the star dies, it returns material to its surrounding environment that will

form the next generation of stars and planets. Stellar evolution is a beautiful, continuous cycle of life, death, and rebirth on a cosmic scale.

1.2.1 Size Matters

The single driving factor behind a star's evolution is its mass. Once a star is "born" and is fusing hydrogen to helium in its core it is locked in a lifelong duel with gravity. The star remains stable as long as there is enough fuel to support nucleosynthesis and keep the star in a state of *hydrostatic equilibrium*. Consider an idealized "star in a box" which is spherically symmetric, non-rotating, and non-magnetic, with no net forces acting upon it. We assume internal motions average out over time and that internal layers experience isotropic stress. These conditions are not entirely physical, but they let us describe interior layers of the star with simple pressures and balance of forces. When the star is hydrostatic equilibrium the internal pressure from gravity is balanced by radiation pressure from nucleosynthesis. The amount of time a star can maintain hydrostatic equilibrium primarily depends on its initial mass, $M(M_\odot)$[1]. Stellar evolution is driven by conditions that take the star out of hydrostatic equilibrium.

For main sequence stars (see Figure 1.2) the mass-luminosity relationship indicates that the rate of fuel consumption is proportional to $M^{3.37}$ (Kippenhahn et al. 2012) which means high-mass stars use their fuel exponentially faster than their smaller counterparts. A high-mass star will only live a few million years, while a solar-mass star typically lives 10 billion years. The star will undergo mass loss its entire life. For example, the Sun has a mass-loss rate of $\sim 10^{-14} M_\odot/yr$; every time we enjoy aurora from a solar flare the sun has undergone a mass-loss event and released particles into the solar system. Mass loss rates are much higher for high-mass and highly evolved stars. When discussing the mass of a star it is vital to record its estimated evolutionary stage as well, because how the star will evolve depends so sensitively on mass. It is entirely possible for a "large" ($>\sim$ 10 $M_\odot$) star main sequence to undergo significant mass loss as it reaches later stages of evolution. If we considered the star at the beginning of its life we would assume that it had enough mass to end its life with a a Type II supernova, but it is entirely possible for this star to lose enough mass late in life that it will end up evolving like a low-to-intermediate mass star. Rather than exploding in fiery supernova, these stars shed their outer envelope in beautiful filaments called planetary nebula that surround the inert core, called a white dwarf.

1.2.2 Stellar Interiors

Once a star begins shining it enters into a tenuous truce with gravity. The star will live as long as it generates enough energy to remain in hydrostatic equilib-

[1]It is common to write parameters such as mass, size, and luminosity compared to the Sun, which is represented with $\odot$

rium with gravity. This energy is generated from nuclear fusion and is how stars forge heavier elements in their cores. Deducing that stars generate their luminosity using fusion was one of the most remarkable scientific breakthroughs of this century. This discovery, published only 63 years ago in Burbidge et al. (1957) fundamentally changed how we describe stellar interiors and launched an entire branch of astrophysics. Each stage of evolution is governed by different nucleosynthesis; here we will briefly describe nucleosynthesis and stellar interiors specific to low-to-intermediate mass stars. For full discussions on nucleosynthesis see Burbidge et al. (1957); Wallerstein et al. (1997); Karakas (2019); Clayton (1968) while stellar interiors are described in Hansen et al. (2004); Kippenhahn et al. (2012); Hubeny & Mihalas (2014). The nuclear products that we discuss here will play a critical role in the discussion of AGB nucleosynthesis and surface chemistry in Sections 1.3.1 and 1.3.3.

A star spends the majority of its life burning hydrogen to helium in its core. There are two ways the hydrogen can burn. The first is called the proton-proton chain (p-p chain) and is predominant source of energy in stars ≤ 1.2 $M_\odot$ (Hubeny & Mihalas 2014). The p-p chain takes 4 protons and after 3 branches the reaction creates He^4.

$$
\begin{aligned}
&p + p \longrightarrow H^2 + \beta^+ + \nu, \\
&H^2 + p \longrightarrow He^3 + \gamma, \\
&He^3 + He^3 \longrightarrow He^4 + 2p
\end{aligned}
$$

The second is the carbon-nitrogen-oxygen (CNO) cycle which is the predominant source of energy in stars > 1.3 $M_\odot$ (Salaris & Cassisi 2005). This cycle involves 6 reactions to create He^4. It begins with carbon and creates nitrogen, then oxygen, and finally arrives at helium.

$$
\begin{aligned}
&C^{12} + p \longrightarrow N^{13} + \gamma, && N^{13} \longrightarrow C^{13} + \beta^+ + \nu, \\
&C^{13} + p \longrightarrow N^{14} + \gamma, && N^{14} + p \longrightarrow O^{15} + \gamma, \\
&O^{15} \longrightarrow N^{15} + \beta + \nu, && N^{15} + p \longrightarrow C^{12} + He^4 + 2p
\end{aligned}
$$

The CNO cycle is particularly important for evolved stars because it affects surface composition, as will be seen in Section 1.3.3. Both of these reactions produce helium ash in the core of the star, and when when the hydrogen (protons) becomes depleted, the star's primary source of energy becomes helium burning to carbon. This takes place via the triple-α process where 3 helium nuclei, or "alpha" particles, fuse to create a carbon atom.

$$
\begin{aligned}
&He^4 + He^4 \longrightarrow Be^8 \\
&Be^8 + He^4 \longrightarrow C^{12} + 2\gamma
\end{aligned}
$$

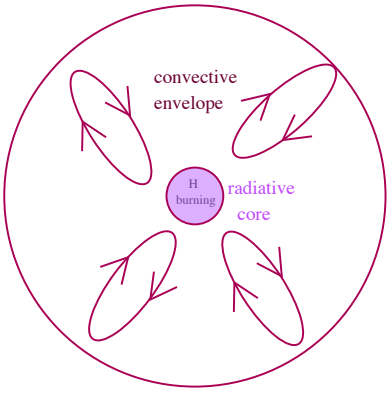

Figure 1.1: Interior of low-to-intermediate mass stars. For stars < 1.2 $M_\odot$ the hydrogen burning is done via the p-p chain and for stars above 1.2 $M_\odot$ the hydrogen burns via the CNO cycle.

Under certain conditions additional "α elements" such as O, Ne, Mg, Si, and Ca can also be produced from this chain by successively adding a α particles (He nuclei); i.e. $C^{12} + \alpha \longrightarrow O^{16}, O^{16} + \alpha \longrightarrow Ne^{20}$ etc. (Hubeny & Mihalas 2014). Higher mass stars (above 10 $M_\odot$ on main sequence) will continue to burn heavier and heavier elements i.e. carbon to oxygen, oxygen to silicon etc., but we will not discuss these processes here.

Detailed modeling of stellar interiors indicate that different stages of nucleosynthesis each have specific thresholds in terms of densities and temperatures. The mass above the core of the star determines which thresholds are met, and therefore what type of nucleosynthesis takes place and what the interior structure is like. Much work has been done recently on calculating specific conditions in low-to-intermediate mass stars stars(e.g. Lattanzio & Boothroyd (1997)). Stars with mass ≤ 1.2 $M_\odot$ are burning hydrogen via the p-p chain, and the temperatures in their cores is low enough for the core to be in radiative equilibrium and the emission and absorption of photons carries energy outwards. As these photons emerge from the core into the surrounding envelope they experience an increase in opacity, and the radiative energy transport becomes inefficient. Convection becomes the primary energy mechanism. Figure 1.1 provides a schematic of the stellar interior for low-to-intermediate mass stars. For giants and supergiants that are hundreds of times larger than the Sun it is possible for the entire envelope to be convective (imagine convective cells larger than the Sun!). In the next section, we will see how the star's evolution is tied to its nucleosynthesis.

1.2.3 Evolution of Low-to-Intermediate Mass Stars

Evolutionary stages can be found in the Hertzsprung-Russell (HR) diagram presented in Figure 1.2 which plots a star's luminosity vs. its temperature. This

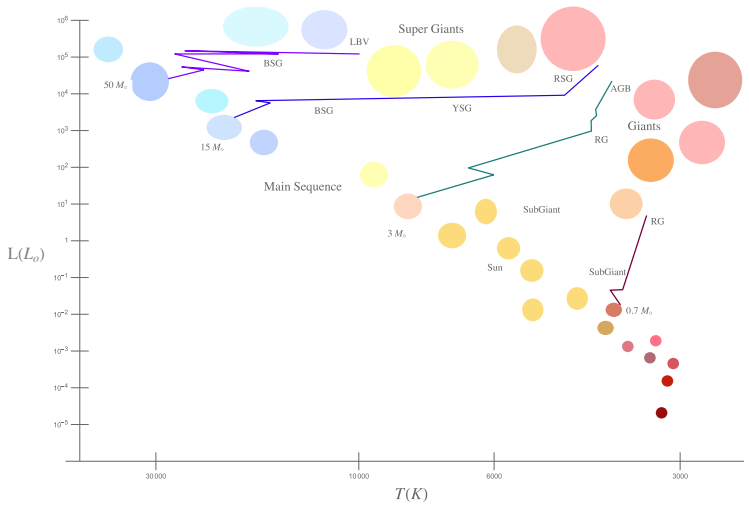

Figure 1.2: The Hertzprung-Russell (HR) diagram provides a "snapshot" of local stars. It plots the relationship between a star's luminosity and temperature. We can track a star's evolution through changes in its luminosity and temperature. A low-to-intermediate mass star remains on the main sequence core hydrogen is depleted. Then it will expand and cool, moving up and to the right as it ascends the red giant branch (RGB), followed by the asymptotic giant branch (AGB).

provides astronomers with a snapshot of local stars and allows us to track different stages of evolution. The main sequence is where stars spend the majority of their lives, and as they evolve they move off the main sequence in evolution tracks governed by their mass. Figure 1.2 provides examples of tracks for a variety of initial masses. The stars we focus on here are low-to-intermediate mass, $\sim 0.8 - 9$ $M_\odot$ on the main sequence.

A star is born in a giant molecular cloud. Gravity condenses the gas and dust until the density reaches ~ 100 g cm^{-3} and the temperature $\sim 10^6$ K (Hansen et al. 2004), conditions under which hydrogen begins fusing to helium. The star enters the main sequence where it will spend the majority of its life burning hydrogen to helium in its core. When the hydrogen supply becomes exhausted, only a thin shell continues burning around the helium-enriched core. The star loses luminosity and hydrostatic equilibrium can longer be maintained; gravity begins to gain the upper hand and contracts the star. If the star is ≥ 2.5 $M_\odot$ the gravitational contraction increases the temperature to rise to 10^8 K, which ignites helium burning in the core (Kippenhahn et al. 2012).

If the star is < 2.5 $M_\odot$ there is not enough mass to reach the necessary temperature to ignite helium burning from gravitational contraction alone. In the cores of these stars the electrons have become degenerate. Electron degeneracy arises because electrons are Fermions, and consequently cannot occupy the same quantum mechanical state. This creates a degeneracy pressure that is strong enough to withstand gravitational contraction as long as the core is smaller than

the Chandrasekhar limit of 1.4 $M_\odot$. Degenerate matter has a unique behavior where an increase in temperature does not initiate a change in volume, until the thermal pressure exceeds the degeneracy pressure. This feature allows the core to increase in temperature, but not volume until the thermal pressure exceeds the degeneracy pressure. Helium fusion ignites, increasing the temperature, which further increases the fusion rate, which continually drives the temperature higher, eventually causing a runaway reaction. This thermal nuclear runaway is called a heliumflash and the peak luminosity it can produce is 10^{11} $L_\odot$ which can outshine our entire galaxy; this peak only lasts a few-to-hundreds of seconds (Kippenhahn et al. 2012). This explosion of energy lifts most of the degeneracy of the core and it can now thermally expand once again. This expansion then absorbs the majority of the photons released so most of the energy never reaches the surface of the star.

After helium-burning is ignited in the core, the outer envelope of the star expands and cools in response to the core contraction and increase in temperature; this reaction is referred to as the "mirror principle" of radial motion (Kippenhahn et al. 2012; Hubeny & Mihalas 2014). The star has now moved off the main sequence into the Red Giant Branch (RGB). It will remain a red giant for approximately a factor of 10 less time than it was on the main sequence. When the helium in the core also becomes depleted, then the star evolves onto the Asymptotic Giant Branch.

1.3 Asymptotic Giant Branch Stars

Asymptotic Giant Branch (AGB) stars are highly evolved low-to-intermediate mass stars (≤ 8 $M_\odot$). They are characterized by nuclear shell burning, large convective envelopes, and remarkable mass loss rates. Highly extended envelopes with cool temperatures make them molecule and dust factories; strong stellar winds return this enriched material to the surround interstellar medium (ISM). Their evolution is highly complicated, and numerical models that fully account for all these details are currently in production. Descriptions of AGB evolution and nucleosynthesis can be found in Herwig (2005); Busso et al. (1999); Iben & Renzini (1983), and pulsation and mass loss models are described in Bowen (1988); Willson (2000); Höfner & Olofsson (2018).

1.3.1 Phases of Evolution

As a star reaches the end of the red giant phase it transitions to an AGB star. While on the RGB He burning increased C/O as in the core. When the He becomes depleted the star is not massive enough to ignite carbon burning. Instead, helium-burning continues in a shell below the hydrogen-burning shell. We characterize the early-AGB (E-AGB) phase as when the hydrogen-burning shell continues to burn outward, until the temperature in the shell drops enough the hydrogen shell

becomes extinguished. The star's luminosity now depends on the helium-shell burning.

The helium shell burns outward until it reaches the bottom of the extinguished H shell. Because helium burns at 10^8 K and H burns at 10^6 K the close proximity to the bottom of the hydrogen-shell re-ignites hydrogen-burning. The luminosity is now driven by hydrogen-burning and the He shell is extinguished. The star now enters the Thermal-Pulsing AGB (TP-AGB) phase characterized by instabilities driven by the interaction between the hydrogen-burning and helium-burning shells as follows. The hydrogen-burning shell creates additional He until the bottom of the helium-shell reaches conditions to re-ignite in a partial He flash. At the onset of the helium-shell burning, the star's luminosity sharply increases causing the star to expand and cool, until the hydrogen-burning shell once again is mostly extinguished. The helium-shell burns its way outward until it becomes extended enough that the conditions are no longer favorable for fusion. Gravity causes the star to contract, and the hydrogen-shell once again ignites. The entire cycle repeats roughly every 10^4 years (Karakas et al. 2002). How many thermal pulses it will undergo is strictly dependent on its mass and mass-loss rate. The thermal pulses are connected to convective overshoot events called "dredge ups" and are necessary for the creation of carbon stars (see Section 1.3.3). The star will remain in this TP-AGB phase until it suffers a final instability in hydrostatic equilibrium. The star ejects its outer envelope, ultimately ending its life as a white dwarf surrounded by a planetary nebula.

1.3.2 Nucleosynthesis

All metals heavier than hydrogen and helium are forged in the hearts of stars during nucleosynthesis. Here we provide a very brief description of just a few different nuclear processes specific to AGB stars to provide an idea of how they produce heavier elements to enrich the ISM. For full discussions of these process see Iben (1967); Herwig (2005); Karakas & Lattanzio (2014) and references therein. As seen in the previous section, AGB stars are characterized by nucleosynthesis of hydrogen and helium burning shells. The helium-shell undergoes partial runaway events, or partial He-flashes, that lead to thermal pulses. This causes a convective overshoot called a dredge up that brings material from the core of the star to the outer envelopes. This particular behavior of AGB stars makes their nucleosynthesis quite intriguing and complicated. Nuclei can be exposed to first hydrogen-burning, then helium-burning, and then have cyclic repeat exposures with every thermal pulse.

AGB stars create heavier elements in a variety of ways. Carbon is generated via the triple-α process during the helium-shell flash. Deep within the shell oxygen is also produced. After a partial helium-flash is over the hydrogen-shell resumes burning creating helium and nitrogen, which is a leftover product of the CNO cycle. Eventually this nitrogen is transformed first into oxygen and then neon via alpha capture. During a thermal pulse temperatures may reach 3×10^8

K, which can marginally activate neon to burn to magnesium via alpha capture (Gallino et al. 1998). This reaction creates extra neutrons as one of the nucleosynthesis products. Additional neutrons are also developed with the production of ^{13}C within the helium-shell as helium is converted to carbon and oxygen. These neutrons play a vital role in creating elements past the iron peak via the slow-process or s-process, which creates heavy elements via neutron capture. The process is designated "slow" compared to beta decay. This process is responsible for half of all elements heavier than iron (Arlandini et al. 1999), and AGB stars are the main producers of s-process elements in the universe (Bisterzo et al. 2014).

1.3.3 Dredge Ups and Surface Composition

The elements produced inside an AGB star will eventually affect the star's surface composition. Three large convective events (creatively) named the first, second, and third dredge up bring material from the heart of the star to the outer envelope. The first dredge up actually occurs as the star moves off the main sequence. When the hydrogen-burning in the core transitions to hydrogen-shell burning, large thermal instabilities drive the convective cells in the outer envelope toward the core. When the star is in hydrostatic equilibrium an opacity barrier exists between the radiatively-driven core and the convectively-driven envelope. Large temperature instabilities are generated when the star briefly moves out of hydrostatic equilibrium as core hydrogen-burning evolves to hydrogen-shell burning; these instabilities energetically drive the convective cells past this barrier into the shells surrounding the core. As the star regulates, material is then "dredged" up, and allowed to mix with the outer envelope. In this first dredge up event the most significant change to the surface composition is the nitrogen abundance which is approximately doubled (Iben & Renzini 1983).

The second dredge-up is similar to to the first dredge up and occurs when core He burning transitions to helium-shell burning. This dredge up event only happens for stars above 3-5 $M_\odot$ (Kippenhahn et al. 2012). The surface composition will be altered by the addition of carbon, oxygen, and nitrogen. The third dredge up is created from thermal instabilities arising from the alternate shell burning during a thermal pulse. This is the primary way the surface composition is altered in AGB stars. A low-mass AGB star can dredge up 5×10^{-3} $M_\odot$ per thermal pulse (Herwig 2005). For a star at the beginning of the AGB phase the C/O ratio is well below unity and it is classified as an oxygen-rich or M-type star. Enough dredge ups can alter the star because the region between the hydrogen-shell and helium-shell has 5 times more carbon than oxygen (Herwig 2005). If the star is massive enough to undergo sufficient thermal pulses and subsequent dredge ups, enough carbon is brought to the surface to change the C/O ratio to more than unity and it evolves to a C-type star.

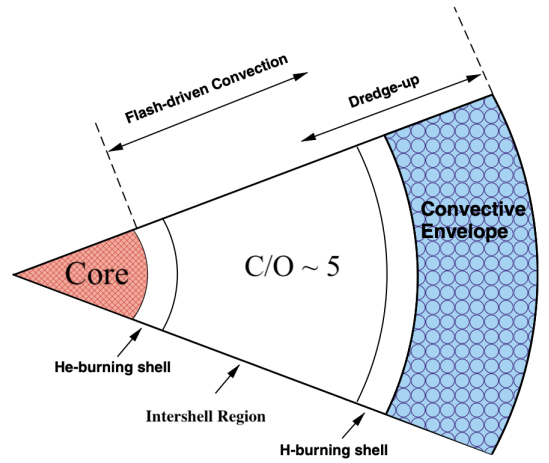

Figure 1.3: Interior of AGB star during the third dredge up (not drawn to scale). After a thermal pulse the convective envelope may reach down to the region between the hydrogen-burning shell and the helium-burning shell, called the inter-shell region. Multiple dredge ups lead to the formation of a C-type star because in the inter-shell region carbon is 5 times more abundant than oxygen and is brought to the surface during the dredge up. Figure adapted from Karakas et al. (2002).

1.3.4 Stellar Atmospheres

The circumstellar environment surround an AGB star is rich is dust and gas. As the star evolves off the main sequence to become first a red giant and then an an AGB star, it undergoes an extreme transformation. In response to the luminosity dips when hydrogen and subsequent helium become depleted in the core, gravity contracts the star. This contraction turns on helium-core burning at the onset of the red giant phase and then shell burning when the star becomes an AGB. This contraction also has another consequence; it causes the outer envelope of the star to massively expand (due to the mirror principle discussed in Section 1.2.3) until the star is several hundred $R_\odot$ in diameter (Herwig 2005). For context, this means if an average AGB star replaced the Sun, it would fill in the space out to Mars' orbit. The highly expanded envelope has low surface gravity near the edge allowing material to escape with the stellar wind. A typical AGB star experiences an astonishingly high mass loss rates of $10^{-6} - 10^{-4}\ M_\odot \mathrm{yr}^{-1}$ (Olofsson 1997). The escaped material is helped along with a "gentle" wind ~ 10 km s^{-1} creating an even larger atmosphere.

Here we will pause for a moment to define a stellar atmosphere. Up to this point we have described internal processes of the star, but the focus of this dissertation is actually the stellar atmosphere. In their book, Hubeny & Mihalas

(2014) define a stellar atmosphere as "the layers of star from which the photons escape freely into space and can be measured by an outside observer." A common reference point in the atmosphere is the *photosphere*, where photons have roughly a 50% chance of escape. The majority of emitted photons in the envelope and interior are re-absorbed before they can escape, making these regions extremely difficult to observe; thus the vast majority of our information is provided by the star's atmosphere, where light can escape and travel to our telescopes. For main sequence stars, the depth range over which material transitions from optically thick (opaque) to optically thin (transparent) is much smaller than the radius of the photosphere. For example, the Sun's photosphere is 10^{10} cm, and the depth range where the material becomes transparent is 10^{7} cm (Hubeny & Mihalas 2014) which means the radius of the Sun is well defined. This does not hold true for evolved stars. For giant and supergiants like AGB stars with highly extended envelopes the depth range over which material transitions from optically thick to optically becomes significantly larger that the size of the photosphere. The boundary between optically thick and optically thin now depends on the wavelength of the photon trying to escape, making the concept of a definite radius impossible.

The effective temperature (temperature of perfect blackbody with the observed flux) of an AGB star ranges is $\sim$2000-3500 K, which allows the atmosphere to be quiet cool (for a star). As material escapes from the envelope into the atmosphere, it subsequently cools to form molecules and dust grains. The condensation process of dust is extraordinarily complex and requires a detailed description of a gas-to-solid phase change in a low-density environment. This can only happen in regions of the atmosphere where the local temperature drops below the dust condensation temperature. As the molecules and dust escape in the stellar wind they form the the expanding circumstellar environment (CSE) that surrounds the star. The CSE primarily consists of molecular hydrogen, H_2, but 90 additional molecular species have been identified in AGB atmospheres (Höfner & Olofsson 2018), indicating that these stars are prolific molecule factories. The chemical composition of the CSE depends strongly on the C/O ratio. An AGB star first evolves as an M-type (oxygen-rich) with C/O $<$1. The majority of the carbon quickly becomes bound in CO molecules that form deep in the atmosphere. The surrounding CSE is then characterized by oxygen-rich chemistry although the presence of molecules like CO_2 indicate that the dis-equilibrium chemistry from shocks in the atmosphere also play a role in creating molecules (e.g. Cherchneff (2006)). The dust species are dominated by silicates and include familiar species such as olivine and pyroxene (Waters et al. 1996; Gail & Sedlmayr 1999).

If an AGB star survives enough thermal pulses and subsequent dredge ups, then enough carbon is dredged up then the star evolves to a C-type (carbon-rich) with C/O $>$ 1. The CSE is now characterized by "sooty" species including polycyclic aromatic hydrocarbons (PAHs) (Buss et al. 1993) and fullerenes (C_{60} & C_{70}) (Sloan et al. 2014). The dust lacks the variety seen with the silicate species in the M-types, but includes amorphous carbon and SiC (Höfner & Olofsson 2018). On

the way to becoming a C-type the atmospheric chemistry will reach an intermediate phase where C/O $\sim$1 and the star is classified as an S-type. The surrounding CSE then shows characteristics of intermediate chemistry (Danilovich et al. 2014; Höfner & Olofsson 2018).

We will now turn our attention to a specific type of AGB star called a Mira variable, characterized by everything described in this section with the addition of recurrent, regular pulsations that greatly affect their atmospheres.

1.4 Mira Variables

Mira variables are named for their prototype *Mira*, which means "wonderful" in Latin . Mira received its name in 1622 from Johannes Hevelius for acting like no other star in the sky because it would greatly brighten and then disappear from view much like a nova, but unlike novas the star seemed to repeat this pattern.

1.4.1 Pulsation

Mira variables are a sub-set of AGB stars that pulsate roughly every 200-500 days. These pulsations are accompanied by an astonishing change in magnitude[2]. They can change up to 8 magnitudes in the visual and 2-3 magnitudes in the infrared (Reid & Goldston 2002; Olofsson 1997). These pulsations are thought to be driven by changes in opacity, κ, which we refer to as the κ-mechanism. Mira variables have variable ionization of hydrogen and helium in their envelope (Reid & Goldston 2002) making them vulnerable to pulsation. The variability can cause a layer inside the star to increase in opacity, making it harder for photons to escape. This drives the temperature up in deeper layers which then undergo thermal expansion and swell outward. As the star expands, it cools and falls back inward and the process is repeated (Kippenhahn et al. 2012; Hansen et al. 2004). As the pulsation emerges from the envelope to the atmosphere, the density and temperature drop allowing the speed to become greater than the local speed of sound. A shock wave of $\sim$10 km s^{-1} then propagates through the atmosphere (Slutz 1976; Reid & Goldston 2002). This pulsation cycle is what creates the magnificent changes in a Mira's magnitude. We track the pulsation with *phase*, which finds the difference between the observation date (t) to a date where the star was determined to be at maximum brightness (t_o) and then this difference is then divided by the star's period (P).

$$\phi = \frac{t - t_o}{P} \tag{1.1}$$

[2]A stars apparent magnitude is tracked on a reverse logarithmic scale so stars with smaller magnitudes are brighter. One order of magnitude difference is 2.5 times brighter, two orders of magnitude is 6.3 times brighter etc.

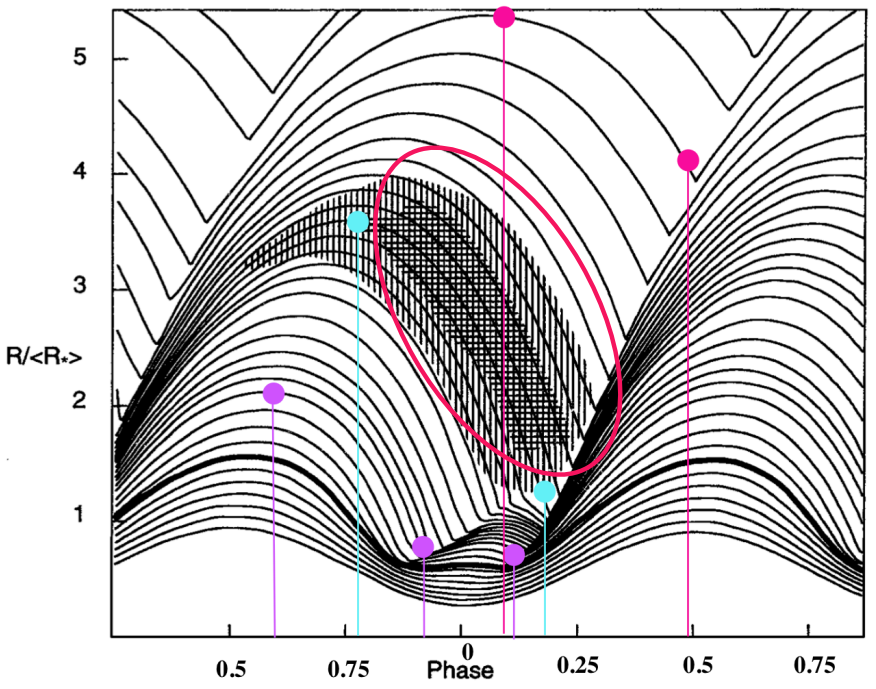

Figure 1.4: Pulsation model calculated by George H. Bowen tracing out the radius as a function of time. The purple dots trace a layer in the atmosphere near $2R_\star$; the layer is smallest close to $\phi = 0$ and largest near $\phi = 0.5$. The teal dots trace a layer near $3.5R_\star$ which is largest near $\phi = 0.75$, and smallest near $\phi = 0.2$. The pink dots trace a layer near $5R_\star$, which is largest near $\phi = 0.1$ and smallest at $\phi = 0.5$. The outer layers show a marked delay in response to the pulsation indicating a complicated interaction between smaller layers moving outward while more extended layers are falling inward. The hatched region circled in red is named the "dust factory" in (Willson 2000), where dust nucleation is expected to be rapid. Figure adapted from Willson (2000).

This lets us compare the pulsation cycle of different Mira variables in a systematic way and allows us to track how behavior in the atmosphere changes with the pulsation of the star.

We believe the photosphere is smallest and hottest at maximum phase, or $\phi = 0 = 1$. This corresponds to the maximum optical brightness; the maximum infrared brightness typically lags behind approximately $\sim$0.2 phase, which we see from light curves plotted in databases like the American Association of Variable Star Observers (AAVSO). The pulsation begins as the star expands. The photosphere reaches maximum expansion at minimum phase, $\phi = 0.5$; this corresponds to when the star is largest, and coolest. The star then begins to contract and heat up as it moves towards maximum phase and the cycle repeats.

Looking at Figure 1.4, we notice that as we move further out in the atmosphere, the minimum and maximum sizes substantially lag the photosphere's behavior. Around $2R_\star$ it reaches maximum expansion at $\phi \sim 0.6$ and minimum expansion in a range from $\phi = 0$ to ~ 0.2. Further out around $3.5R_\star$ the atmosphere is largest near $\phi = 0.8$ and smallest near $\phi = 0.2$, and at $5R_\star$ it is largest just after $\phi = 0$ and smallest at $\phi = 0.5$. This suggests the atmosphere has a complicated response to the phase of the star.

1.4.2 Mira Circumstellar Environments

The pulsations greatly affect the circumstellar environment surrounding the star. Mira variables have 3 chemistries as described in Section 1.3.4. M-types are oxygen rich, C-types are carbon-rich, and S-types have intermediate chemistry. Their cool atmospheres allow for molecule and dust growth and the pulsations help loft this material into the surrounding circumstellar environment (CSE) and contribute to high mass loss rates. Figure 1.5 provides a diagram of a Mira variable and its CSE. A major difference between the M-types and C-types is that M-types have a variety of maser[3] activity including emission from SiO, OH, and H_2O masers, but C-types typically only have HCN masers (Menten et al. 2018). In the M-types, the three masers appear to originate from different layers in the atmosphere with SiO masers originating nearest the photosphere, the H_2O masers residing further out, and the OH masers originating furthest out in the CSE (Reid & Moran 1981). The HCN masers in C-types originate roughly 2-4 $R_\star$ (Smith et al. 2014). Masers provide great tools for studying Mira CSEs because the emission is extremely bright and consistent; modeling the conditions that create the lines yields valuable information about the star such as distance and mass loss rates.

Mira atmospheres are characterized by their high mass loss rates which create high extended CSE's enriched with molecules and dust. Unfortunately, mass loss rates are extremely hard to calculate because they depends so sensitively on fundamental stellar parameters like mass and luminosity, which are quite difficult to accurately determine. Our simplistic description of mass loss is a major shortcoming in stellar evolution models, because mass loss has such a profound influence on a star's evolution (Lattanzio & Karakas 2016; Karakas & Lattanzio 2014). Full reviews on mass loss and how it affects stellar evolution can be found in Willson (2000) and Höfner & Olofsson (2018). The working insight to Mira atmospheres we do have is due to extensive work with modeling pulsations and its effect on mass loss as seen in Bowen (1988). We know that pulsation acts like a piston in the atmosphere, that contracts and expands regions in the atmosphere. The shock drives up the density as it propagates until values in dust forming regions are high enough to drive a dust driven wind with efficient mass loss (Bowen 1988). Regions in the atmosphere may experience a departure from radiative equilibrium that can lead to "refrigerated zones" where dust condensation can occur within a few stellar radii (Willson 2000); this region is circled in red

[3]Maser stands for microwave amplification by stimulated emission of radiation.

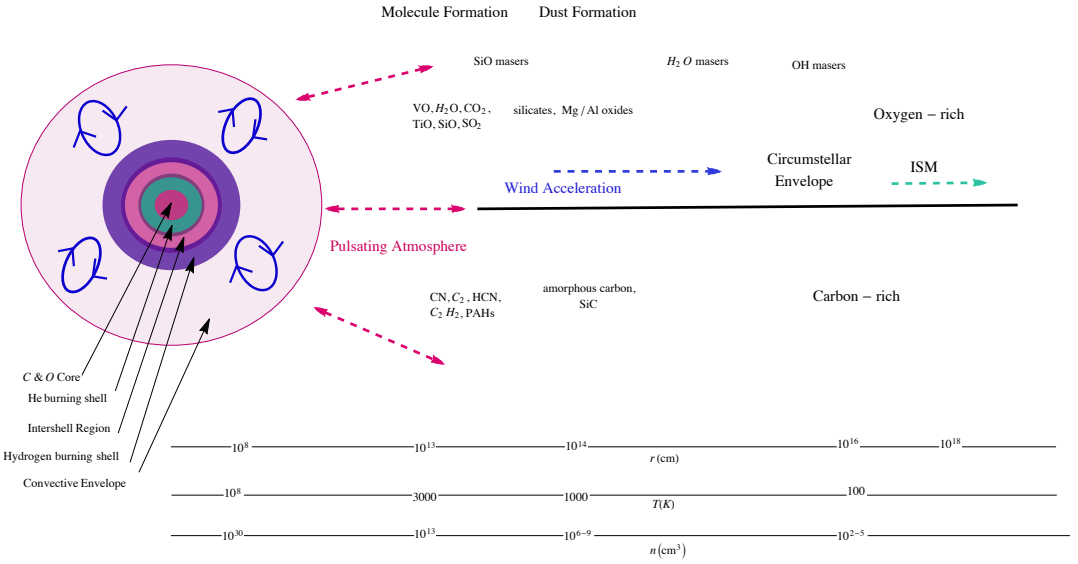

Figure 1.5: Schematic of Mira with circumstellar environment. The Mira has alternate shell burning around its core that create thermal pulses causing dredge up events. The star pulsates every 200-500 days which helps loft material into the atmosphere that eventually becomes molecules and then dust. The stellar wind pushes on the dust grains driving efficient mass loss. The top half of the diagram is specific to M-type Miras, and the bottom half is specific to C-types. Figure adapted from Uttenthaler (2007).

in Figure 1.4. The work provided in this dissertation is part of the ongoing effort in the community to characterize how molecules behave in this environment.

1.5 Mid-IR and Molecular Spectroscopy

This work focuses on analyzing mid-infrared (mid-IR) spectral features of Mira variables. Mira atmospheres are dominated by dust and molecules, and are thus best observed in the mid-IR ($\sim$2-100 μm); this region of the electromagnetic spectrum is prevalent to fundamental bending and stretching modes of vibrations. Unfortunately, this band of the electromagnetic spectrum is quite difficult to observe from the ground due to telluric interference. Our atmosphere is filled with molecules like H_2O, CO_2, N_2, O_2, O_3 etc. (Smette et al. 2015) all of which have dozens on transitions in the infrared which lead to significant drops in transmission through Earth's atmosphere as can be seen in Figure 1.6 (transmission data calculated with ATRAN[4](Lord 1992)). These drops in transmission are most effectively dealt with by using spaced-based instruments to make observations.

[4]`https://atran.arc.nasa.gov/cgi-bin/atran/atran.cgi`

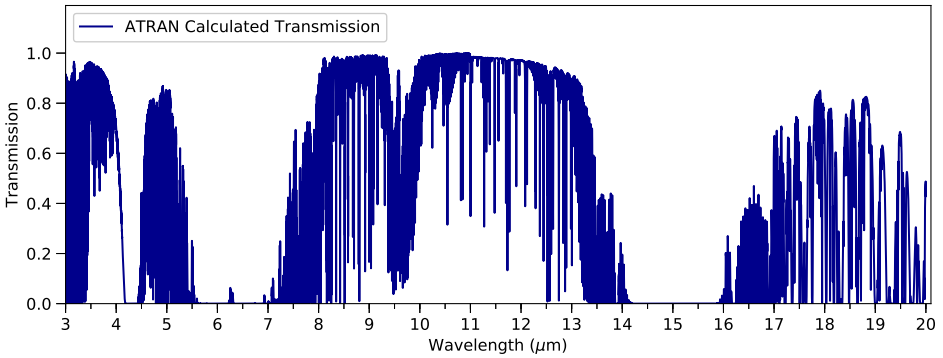

Figure 1.6: Atmospheric Transmission from 3-20 μm. Common telluric molecules that interfere significantly are H_2O, CO_2, and O_3, with lesser contributions from N_2O, CH_4, CO and OCS (Smette et al. 2015). The significant drops in transmission are best addressed by using space-based instruments to make observations. Transmission data calculated with ATRAN (Lord 1992).

Temperatures in Mira atmospheres are a few hundred to few thousand Kelvin making them perfect environments to excite molecules vibrationally. The modes that can be excited are determined by a molecule's symmetry. To make a spectral line the molecule must emit a photon, which means something must perturb the molecule. The strength of the spectral line is proportional to the molecule's electric dipole moment. Symmetric molecules like H_2 have no permanent dipole moments making them much more difficult to observe because only perturbations that break their symmetry create strong transitions.

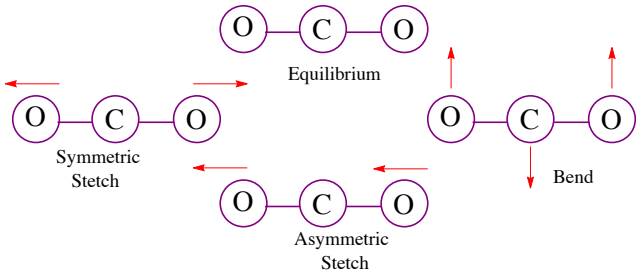

Figure 1.7: Vibrational modes for linear triatomic molecules include a symmetric stretch, an asymmetric stretch, and bending. Note the molecule could bend up and down or in and out of the page. Each bend will release the same amount of energy creating degeneracy.

The number of vibrational modes a molecule has depends on its number of atoms, N, and its degrees of freedom. Polyatomic molecules have 3 degrees of freedom associated with translational motion in the x, y, or z direction, and 3 associated with the molecule's rotation. If the molecule is linear the rotational

degrees of freedom drop to 2 because a rotation about the molecular axis does not displace any of the atoms. A non-linear polyatomic molecule will then have $3N-6$ vibrational modes while a linear molecule will have $3N-5$ modes. These modes arise from the molecules symmetrically stretching, asymmetrically stretching, bending, and combinations of all three as shown in Figure 1.7.

Molecular energy levels can be though of as Russian nesting dolls. Each electronic state contains a ladder of vibrational levels, and each vibrational level then has a ladder of rotational levels. Which "doll" you observe depends on which part of the electromagnetic spectrum you are using for the observation. Electronic transitions require the most energy and are observed at shorter wavelengths like the UV. Vibrational transitions require less energy and are seen in the infrared to millimeter. Pure rotational transitions require the least amount of energy, and are observed in the sub-millimeter to radio.

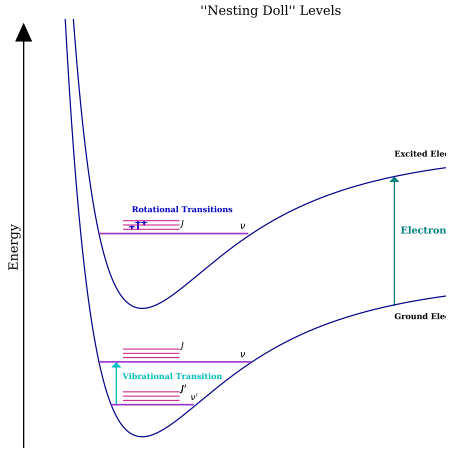

Figure 1.8: "Nesting Doll" energy levels. Each electronic state contains vibrational levels, and each vibrational state contains rotational levels. Ro-vibrational transitions occur from level J in state ν to a rotational level J$'$ in a different vibrational state ν'.

A transition in mid-IR spectroscopy is then technically a ro-vibrational transition, although it is common to shorten this to just vibration, where the transition occurs from one rotational level J in state ν to a rotational level J' in a different vibrational state ν' as seen in Figure 1.8. It is common to see ro-vibrational transitions labeled as $(\nu, J) - (\nu', J')$. If the spectrometer has moderate resolution it is not possible to separate out each rotational transition and we just see one broad spectral feature called a "bandhead" (imagine how the outside nesting doll does not reveal how many dolls lie inside). Ro-vibrational transitions are governed by selection rules which arise when calculating the probability a transition will occur. The selection rules for angular momentum, l, include:

1. $\Delta l = 0$, called a parallel transition and only allows rotational transitions of $\Delta J = \pm 1$.

2. $\Delta l = \pm 1$, called a perpendicular transition and allows rotational transitions of $\Delta J = \pm 1$ and $\delta J = 0$

3. $\Delta l = \pm 1$, with $l \neq 0$.

In this work we are primarily concerned with perpendicular transitions of CO_2. The spectral lines created by perpendicular transitions have 3 components: transitions that satisfy $\Delta J = +1$ create an R-branch, transitions satisfying $\Delta J = -1$ create a P-branch, and transitions that satisfy $\Delta J = 0$ create a Q-branch. The Q-branch is significantly stronger than the P and R branches (Herzberg 1945), as can be seen in Figure 1.9.

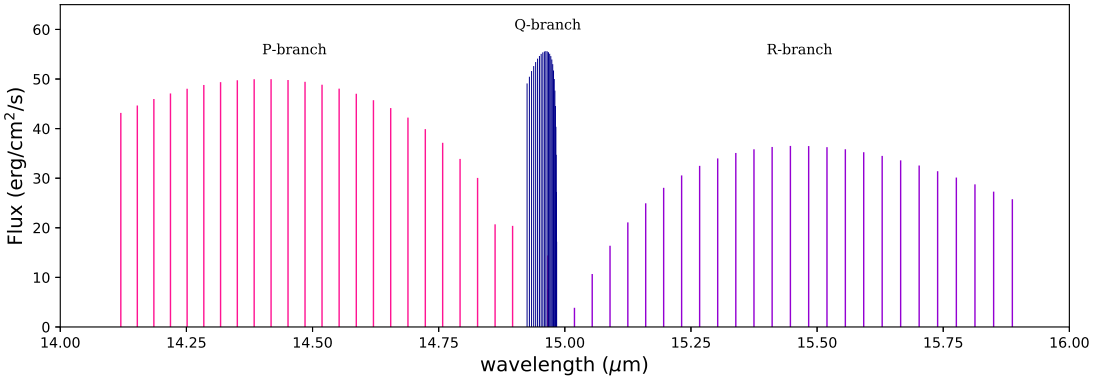

Figure 1.9: Perpendicular band of CO_2 centered at 15 μm. The Q-branch transitions are closely grouped together in the center, with the P-branch to the left and the R-branch to the right.

1.6 Current Questions

Mira atmospheres are perfect laboratories for studying how AGB stars enrich their surrounding environment. The cool temperatures and regular pulsations create an ideal environment for molecule and dust production. However, what makes Miras so interesting to study also makes them quite difficult and there are still large gaps in our understanding of these dynamic stars. Open questions within the astronomical community include:

- Atmospheric Structure: We know that Miras have large extended atmospheres that are cool enough for molecules to form which eventually create dust grains. What is still missing is a detailed structural understanding. We know there is a molecular layer and "further" out a dust production zone, but specific locations are still under debate.

- Dust nucleation: Observations show that Miras create prolific amounts of dust, but which species condenses out first and under what conditions is still not fully understood. Where the dust can begin to nucleate depends on the local temperature; are there "refrigeration zones" that allow dust to form within a few stellar radii? The results of the doctoral work presented in Güth (2017) indicate that the dust species in M-type Miras change with phase, does this behavior also occur for S-types and C-types? Is it possible for the refrigeration zone to develop at certain phases of the pulsation?

- Pulsation: How do the different layers of gas and dust respond to the shocks propagating through the atmosphere? Is there a phase dependent variability that shows the layers are responding to the undulating atmosphere?

- Mass Loss: We can estimate mass loss rates for Miras with strong maser activity, but we still lack a generalized approach to mass loss that applies to both M-types and C-types. Not every Mira exhibits maser activity. Are atmospheric conditions that are favorable for maser emission related to higher mass loss rates? Do Miras undergo a constant mass-loss rate, or is the mass-loss rate periodic?

- Pulsation Period: Miras with longer periods have stronger shocks. Can we observe any significant difference between Miras with long and short periods? Does period affect the mass loss rate?

Gaining insight to these topics requires detailed, multi-wavelength, and time-resolved observations. Multiple observations at different phases are required to understand the time-dependent nature of Mira atmospheres.

1.7 In this Thesis

The work presented in this thesis involves analyzing gas features in the mid-IR spectra of 22 Mira variables spanning all 3 chemistries. Chapter 2 describes the experiment and data used for this work. In Chapter 3 we provide a discussion on line identification and behavior for all 3 chemical subclasses in our sample. Chapter 4 provides details on modeling five CO_2 lines identified in the M-types, and also includes a discussion of the new 17.62 μm feature seen in all 3 chemistries. Chapter 5 is the initial publication associated with this work which focuses on modeling the CO_2 features in the M-type R Tri. The results from the CO_2 models can be found in Chapter 6, and accompanying plots are found in Appendix I. Insights to Mira atmospheres gained from these models and future work are discussed in Chapter 7.

"Measure what can be measured, and make measureable what cannot be measured."

— Galileo Galilei

Chapter 2

DATA OVERVIEW

This Chapter describes and organizes the data used in this work. An introduction to the experiment is provided Section 2.1. Details on data acquisition and reduction are provided in Sections 2.1.1 and 2.1.3. Information about the target sample and individual Miras is provided in Sections 2.1.2 and 2.2.

2.1 Experiment

The analysis of mid-infrared (mid-IR) spectra presented in this dissertation is part of a larger experiment described in Creech-Eakman et al. (2012). The experiment endeavors to characterize the circumstellar environments (CSE) surrounding Mira variables. These environments are incredibly complex and dynamic. Observing them at multiple wavelengths is necessary to fully understand the interaction between the star's photosphere, atmosphere and surrounding CSE. In an effort to accomplish this Creech-Eakman used the ground-based Palomar Testbed Interferometer (PTI) (Colavita et al. 1999) to repeatedly observe a set of Miras at K-band (centered at 2.2 μm). These observations are to be used in conjunction with observations taken with the space-based Spitzer Space Telescope's Infrared Spectrograph (IRS) (Houck et al. 2004) in the mid-IR (10-35 μm). The optical and near-IR interferometric data constrain the angular size of the atmosphere at 2.2 μm (recall that the size of the atmosphere is wavelength dependent), see Section 1.3. If the distance to the star is known we can derive fundamental information about the star including its physical size, effective temperature, and bolometric flux. Using this approach to calculate the temperature is typically more accurate than using one approximated from spectral typing.

In contrast, the mid-IR spectra taken with Spitzer's IRS examines cooler molecule and dust production zones in the atmosphere that lie in layers on top of the photosphere. Spectra for this project were taken approximately once a month in an effort to span multiple phases across the pulsational cycle of the target stars.

These spectra span a wavelength range containing atomic and molecular transitions that is difficult to observe from the ground, and in the case of specific molecules, like CO_2 impossible because of telluric interference.

2.1.1 Data Acquisition

The data were acquired during Spitzer GO program 50717 from mid-2008 until early 2009. This was the final year of the cold mission for Spitzer. A subset of Miras from the sample stars in the PTI set were chosen based on three main criteria. 1) The M-type stars had been categorized by dust spectral sub-type according to Little-Marenin & Little (1990) or Sloan & Price (1998) by using Low Resolution Spectra (LRS) from IRAS[1]. 2) The stars had optimal observation windows for Spitzer to observe them several times during Cycle 5. 3) The stars would be bright enough for excellent SNR, but not so bright that would saturate the IRS detectors.

The IRS instrument has four modules: 1) low-resolution, short wavelength (SL, 5.3-14 μm); 2) low-resolution, long-wavelength (LL, 14-40 μm); 3) high-resolution, short-wavelength (SH, 10-19.5 μm); 4) high-resolution, long-wavelength (LH, 19-37 μm) (Houck et al. 2004). Data was taken in all 4 modes for our sample; the work presented in this thesis focuses on both the SH and LH (R$\sim$ 600) spectra. Both the SH and LH each have ten orders (bands that span a certain wavelength range) that are stitched together to give a final, continuous spectrum from 9.98-36.83 μm for each observation in the sample. During Cycle 5 Spitzer was nearing the end of its supply of cryogen to cool all its instruments, which can create instability in the mid-infrared detectors; in response to this the IRS instrument team recommended observing dedicated backgrounds for all the stars. Normally, the stars in this sample are bright enough not to require backgrounds, but this was done in an effort to minimize issues arising from low supply of coolant.

2.1.2 Target Sample

The Miras analyzed in this work were chosen to coincide with an ongoing study with the Palomar Testbed Interferometer (PTI), as explained above. Target stars originally picked for the PTI study were thought to have angular diameters near 2 mas; this was the ideal size for PTI to have maximum sensitivity. Assuming the target Miras all have a typical radius of $\sim$1 AU this places them within $\sim$1 kpc of Earth. Approximately 40 stars were chosen for the Spitzer study, however, the requirement of dedicated backgrounds and other observational constraints limited final sample of stars observed to 25. The focus of this dissertation is on

[1]The Infrared Astronomical Satellite (IRAS) was a space-based telescope that operated from February-November 1983. This was the first instrument to perform an all sky survey at infrared wavelengths. The Low Resolution Spectrometer (LRS) took spectra from 8-22 μm for $\sim$5000 objects.

analyzing several spectral features in the 13 M-type Miras from this data set; we also include analysis of a new feature at 17.62 μm that is seen in all three chemical sub-classes throughout the entire sample .

Table 2.1 presents the 13 M-type Miras and associated parallaxes measured with Gaia (Gaia Collaboration 2018) and Hipparcos (van Leeuwen 2007) and Table 2.2 provides angular diameters and physical radii computed with these distances. There is clearly a discrepancy between the parallaxes determined from the Gaia survey vs the Hipparcos survey. It should be noted that difficulty determining parallaxes in Miras is a known issue (e.g. van Belle et al. (2002); Thompson et al. (2002b)). If we compare the parallaxes with the angular diameters reported in Table 2.2 we note that most of the angular diameters of the stars are larger than stars' parallax. This can lead to a disparity in the calculation of the light photocenter. These stars also have large convective cells and potential spots on their surface which can also make it difficult for accurate position of the photocenter; the effects on parallax from surface granulation in red supergiant stars like Betelgeuse is discussed in Chiavassa et al. (2011). The ambiguity in the calculation of the photocenter means that there are larger error bars on the distances than you would expect to see for a star of this magnitude.

In an effort to minimize the discrepancy between the Gaia and Hipparcos parallaxes we estimated a distance calculated from the point where error bars overlap (for applicable targets). For R Tri the error bars do not overlap and we will continue to use a distance of 294 pc as used in Baylis-Aguirre et al. (2020). For S Peg they overlap starting at 1.4231 mas which gives a distance of 703 pc. For SS Cas they overlap at 2.1272 mas which gives a distance of 470 pc. For R Cet they overlap at 1.8642 mas which gives a distance of 536 pc. For S Lac they overlap at 1.4817 mas which gives a distance of 675 pc. These distances will be used

Parallax Data and Calculated Distances				
Target	Gaia Plx[1] (mas)	Gaia Distance (pc)	Hipparcos Plx[2] (mas)	Hipparcos Distance (pc)
R Tri	1.0714 ± 0.2941	934^{+354}_{-200}	3.40 ± 1.51	294^{+235}_{-90}
S Peg	1.2886 ± 0.13545	776^{+91}_{-74}	2.52 ± 2.26	397^{+3449}_{188}
S Ser	NA	NA	3.17 ± 1.49	315^{+280}_{-100}
SS Cas	2.2862 ± 0.1590	437^{+33}_{-28}	1.33 ± 2.59	$752^{+\infty}_{-496}$
W Her	0.6404 ± 0.0812	1562^{+226}_{-176}	NA	NA
RT Cyg	1.1261 ± 0.0569	888^{+15}_{-43}	NA	NA
R Cet	1.7554 ± 0.1088	570^{+37}_{-34}	2.92 ± 1.86	342^{+601}_{-133}
Z Zyg	1.5293 ± 0.0807	654^{+36}_{-34}	NA	NA
Y Del	0.9940 ± 0.4510	1006^{+836}_{-314}	NA	NA
S Lac	1.5906 ± 0.1089	629^{+46}_{-41}	1.19 ± 1.44	$840^{+\infty}_{-460}$
S Psc	0.5336 ± 0.2001	1874^{+1125}_{-511}	NA	NA
U Cvn	0.9210 ± 0.1670	1086^{+240}_{-167}	NA	NA
UX Cyg	0.1764 ± 0.1674	$5669^{+105442}_{-2760}$	NA	NA

Table 2.1: Parallax data and subsequent calculated distances for our 13 M-type Miras.[1]Gaia Collaboration (2018), [2]van Leeuwen (2007)

in subsequent analysis for these particular stars. The remaining stars with the exception of S Ser only have Gaia parallaxes reported. In the case of UX Cyg the estimated distance is unrealistically large because we believe all targets are within $\sim$1 kpc, and therefore suspicious as it will yield non-physical answers in later calculations; we will use a distance estimated from maser emission. Nakashima & Deguchi (2007) using SiO maser emission place UX Cyg at 590 pc, far more reasonable than 5700 pc.

Angular Sizes and Calculated Radii		
Target	Angular Diameter (mas)	R($R_\odot$)
R Tri	4.631	150[2]
S Peg	4.2676	323*
S Ser	4.2041	142*
SS Cas	1.804	91.2*
W Her	2.4136	405[1]
RT Cyg	2.380	227[1]
R Cet	3.0909	178*
Z Cyg	3.5164	247[1]
Y Del	3.1796	342[1]
S Lac	2.9547	214*
S Psc	3.935	793[1]
U Cvn	3.397	397[1]
UX Cyg	3.878	246**

Table 2.2: Interferometric measurements of angular diameters were observed with PTI, and were shared via private communication with Michelle Creech-Eakman. The physical sizes are then determined by the distance. [1]Calculated with Gaia data, [2]Calculated with Hipparcos data, * Calculated using overlap from Gaia and Hipparcos as described in previous paragraph. ** Calculated with maser distance.

2.1.3 Data Reduction

The Spitzer Data Analysis Cookbook [2], published by the Spitzer team, was used to guide the data reduction. I would like to note that each spectrum presented in this work was reduced individually, by hand, by Dr. Tina Güth as part of her doctoral work. This section provides an overview of the data reduction steps. For full details see Creech-Eakman et al. (2012) and Güth (2017).

The data were downloaded from the Spitzer Heritage Archive (SHA); this included IRS data for all targets and their dedicated backgrounds. Individual ob-

[2]https://irsa.ipac.caltech.edu/data/SPITZER/docs/dataanalysistools/cookbook/

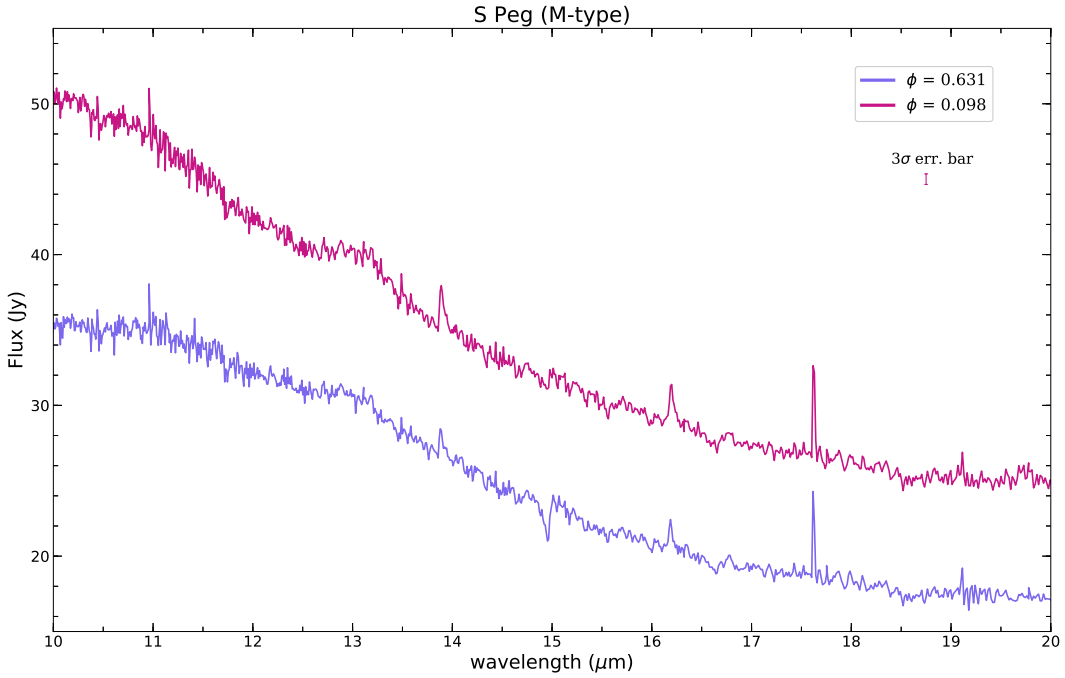

Figure 2.1: Mid-IR spectra of the M-type Mira variable S Peg. The top spectrum is artificially offset by an additional 5 Jy for clarity. The spectral features are discussed in Chapter 3.

servations with their respective backgrounds were unzipped in their own folders. The first step was to subtract the dedicated sky background using IDL codes written by Güth. Next, IRSCLEAN was used to remove bad pixels in the data. This is an IDL program provided by the Spizer team that automatically flags bad/rougue pixels, and also allows the user to flag additional bad/rough pixels the program may have overlooked. The Spitzer IRS Custom Extractor (SPICE) program is then used to extract the spectrum after the data is clean; this program extracts the flux and corresponding uncertainties. The stars in the sample were all bright enough to potentially introduce interference fringes inside Spitzer. To account for these fringes the IRSFRINGE package was used to "defringe" the spectra after it was extracted. The order-overlaps, provided by the IRS Instrument Handbook[3] were removed, and subsequently the individual orders were stitched together to create a complete spectrum. The resulting data product was an ascii file containing wavelength (μm), flux (Jy), and flux uncertainty (Jy). An example of a fully reduced spectrum is provided in Figure 2.1.

[3] `https://irsa.ipac.caltech.edu/data/SPITZER/docs/irs/`

2.2 Mira Data

The chemical subclass of a Mira is determined by its carbon-to-oxygen ratio in molecules and dust in its surround circumstellar environment. If $C/O < 1$ it is classified as oxygen-rich (M-type), if $C/O \sim 1$ it is classified as intermediate (S-type), and if $C/O > 1$ it is classified as carbon-rich (C-type). For additional details see Section 1.4. Each Mira in this dataset was observed at least twice and Table 2.3 provides the chemistries and observations of the stars used in this work. There are two stars worth additional discussion in regards to their assigned chemical sub-class. First, the M-type Y Del had very weak CO_2 spectral features, and possible emission of C_2H_2 at 13.7 μm and HCN at 14 μm, both of which are indicative species of C-types. It is possible that Y Del is actually much closer to an S-type than the rest of the M-types in our sample. Second, the S-type LX Cyg had strong, clear absorption of C_2H_2 at 13.7 μm and HCN at 14 μm and 14.3 μm; the strength of the features indicate that LX Cyg is actually a C-type, and we have put the results of its analysis with the other C-types.

Star	Chemistry	Obs.	Phase
R Tri	M-type	2	0.153, 0.222
S Peg	M-type	2	0.631, 0.098
S Ser	M-type	2	0.620,0.671
SS Cas	M-type	3	0.029, 0.169, 0.368
W Her	M-type	5	0.473, 0.604, 0.725, 0.794, 0.919
RT Cyg	M-type	7	0.654, 0.780, 0.983, 0.114, 0.276, 0.459, 0.584
R Cet	M-type	2	0.850, 0.019
Z Cyg	M-type	7	0.725, 0.859, 0.961, 0.054, 0.170, 0.309, 0.391
Y Del*	M-type	3	0.280, 0.539, 0.579
S Lac	M-type	3	0.279, 0.383, 0.819
S Psc	M-type	2	0.990, 0.042
U Cvn	M-type	2	0.948, 0.036
UX Cyg	M-type	4	0.225, 0.276, 0.454, 0.487
R Cyg	S-type	6	0.544, 0.612, 0.696, 0.782, 0.884, 0.919
S Lyr	S-type	5	0.758, 0.815, 0.022, 0.086, 0.168
S Uma	S-type	3	0.039, 0.152, 0.874
X And	S-type	2	0.598, 0.701
LX Cyg**	C-type	4	0.326, 0.369, 0.532, 0.957
RZ Peg	C-type	3	0.451, 0.258, 0.750
U Lyr	C-type	6	0.572, 0.653, 0.710, 0.784, 0.819,0.909
V Crb	C-type	3	0.960, 0.073, 0.127
ZZ Gem	C-type	2	0.720, 0.786

Table 2.3: Observations and Phases of Miras. The mathematical definition of the phase, ϕ, is given in Section 1.4.1. * Possible S-type, ** Previously classified as S-type.

Star	SE Class	Period[1] (days)	Distance (pc)	Masers		
				OH	SiO	H_2O
R Tri	SE3	275.3	294	N[6]	Y[7]	Y[7]
S Peg	SE1	312.2	703	Y[6]	N[3]	N[3]
S Ser	SE3	389	315	Y[6]	Y[7]	Y[7]
SS Cas	*	143.1	470	N[6]	NA	N[4]
W Her	"no feature"[1]	273.7	1562	N[6]	N[5]	N[5]
RT Cyg	*	191.4	888	N[6]	N[4]	N[4]
R Cet	SE8	165.8	536	N[6]	Y[7]	Y[7]
Z Cyg	SE8	267	654	Y[6]	Y[7]	Y[7]
Y Del	SE4	475.1	1006	N[6]	N[5]	N[5]
S Lac	"no feature"[1]	240.6	675	N[6]	N[4]	N[4]
S Psc	SE4	422.7	1874	N[6]	N[5]	N[5]
U Cvn	SE7	307.9	1086	Y[6]	Y[7]	Y[7]
UX Cyg	SE8	546.3	590	Y[6]	Y[7]	Y[7]

Table 2.4: Information used in analysis for M-type Miras. Maser activity is designated with a Y for reported detection and N for no detection. * no IRAS LRS data [1]Creech-Eakman et al. (2012),[2]Sivagnanam et al. (1988), [3]Cho & Kim (2012), [4]Benson & Little-Marenin (1996), [5]Benson et al. (1990), [6]Engels & Bunzel (2015), [7]Kim et al. (2014)

The majority of this work focuses on analysis of molecular features in the M-type Miras and we now provide more specific details of the M-type Miras in this dataset. Using low-resolution spectroscopy these stars can be further classified according to their broad solid-state or dust features. Little-Marenin & Little (1990) originally classified oxygen-rich AGB stars using Low Resolution Spectrometer (LRS) data from IRAS. Their method involved subtracting the underlying stellar continuum in order to focus on the dust components;sd they created five identification classes. 1) Sil: clear emission feature at 9.8 μm; 2) Sil+: emission at 9.8 μm plus a developing feature at $\sim$ 11 μm; 3) Sil++ identical to Sil+, but with pronounced emission at 11 μm; 4) S: 10.5-10.8 μm emission peak instead of 9.8 μm; 5) Broad: wide feature from 9-15 μm centered at 12 μm. Several years later Sloan & Price (1998) modified these five main classes to include three sub-classes and this "SE" class system was adopted to categorize different M-types. The system is divided from SE1-SE8 and relates to the original classification in the following way. SE1-SE2 correspond to the Broad class (5), SE3-SE4 combined the Sil++ and Sil classes (3,1); SE3-SE6 are referred to as a subcategory called "structured silicate emission". Finally, SE1-SE2 spectra show broad dust emission, while SE7-SE8 spectra show narrow "classic" silicate emission (Sloan & Price 1998). The M-types in this sample that were previously observed with IRAS have SE classifications, and those lacking LRS data were categorized in Creech-Eakman et al. (2012). In Table 2.4 we provide basic information for each M-type Mira including SE clas-

sification, periods, distances that will be used in all subsequent calculations, and maser activity.

The observational study of Mira variables using the interferometric and spectroscopic data discussed in this chapter demonstrates a concerted effort to characterize the highly complicated environments surrounding these stars. The large error bars associated with parallax measurements for every star in our sample suggest that a new approach to parallax measurements for stars with extended atmospheres is greatly needed.

"What's in a name? that which we call a rose
By any other name would smell as sweet."

— William Shakespeare

Chapter 3

LINE IDENTIFICATION AND BEHAVIOR

This chapter discusses the identification of prominent spectral features seen in our IRS spectra. Because all the molecular features were initially identified using the literature Section 3.1 outlines the historical context of these molecules in AGB stars. Sections 3.2, 3.3, and 3.4 discuss molecular features specific to each chemistry, and Section 3.5 describes a feature not previously observed before this Spitzer experiment.

3.1 Historical Context

The molecule and dust enriched regions in a Mira's circumstellar environment (CSE) are best studied in the near and mid-infrared. This region of the electromagnetic spectrum is home to many atomic and molecular transmissions that are inaccessible to ground-based instruments due to telluric absorption. For example, Figure 3.1 shows a transmission spectrum from 3-20 μm calculated with ATRAN[3] (Lord 1992) showing wide bands centered at $\sim$ 4.5 μm, $\sim$ 6.5 μm, and 15 μm where the transmission drops to 0. These large gaps are mainly due to telluric H_2O and CO_2, but other molecules such as ozone (O_3) also significantly contribute.

Space-borne instruments remove the complications affecting ground-based observations at these wavelengths. One key astronomical instrument used throughout the late 90's and early 2000's was the Infrared Space Observatory (ISO) (Kessler et al. 1996). Notable gas-phase molecules observed include H_2O, CO, CO_2, CH_2, HCN, OH, and PAHs, while solid-state observations include both amorphous and crystalline silicates, several oxides, sulfides and carbonates (van Dishoeck

[3] `https://atran.arc.nasa.gov/cgi-bin/atran/atran.cgi`

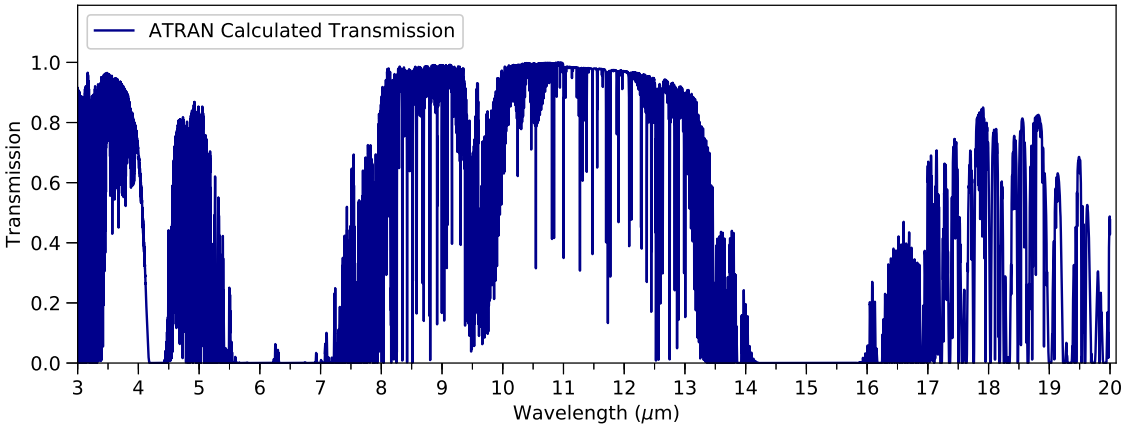

Figure 3.1: Atmospheric Transmission from 3-20 μm. The drops in transmission are primarily caused by absorption of H_2O, O_3, and CO_2, with lesser contributions from N_2O, CH_4, CO and OCS (Smette et al. 2015). Transmission data calculated with ATRAN[3] (Lord 1992).

2004). ISO observations of C-type AGB stars frequently showed a complicated spectrum near 14 μm which could include a broad absorption of C_2H_2 at 13.7 μm and both emission and absorption of HCN at 14 μm (Aoki et al. 1999). Some stars also showed a sharp emission feature of HCN at 14.3 μm (Yamamura & de Jong 2000; Cernicharo et al. 1999; Aoki et al. 1999).

A striking discovery was several CO_2 emission lines in M-type AGB atmospheres (Justtanont et al. 1998; Ryde et al. 1998); before ISO observations it was believed that the carbon in Mira atmospheres was primarily locked in CO molecules (Cherchneff 2006). Five spectral features were initially reported at 13.87 μm, 16.18 μm, 14.97 μm, 13.48 μm, and 15.40 μm in several Miras and semi-regular variable stars. The features at 13.87 μm and 16.18 μm were always seen in emission, but the feature at 14.98 μm was observed in both emission and absorption. Stars with these prominent CO_2 features also had the mysterious unidentified 13 μm "dust" feature (Little-Marenin & Price 1986; Little-Marenin & Little 1988; Sloan et al. 1996), and there was a correlation between the strength of the CO_2 lines and the 13 μm feature (Justtanont et al. 1998; Sloan et al. 2003a). Further studies demonstrated that CO_2 is extended throughout the atmosphere and that a minimum of 2 "slabs" of gas (see Section 4.4.1) is required to recreate the observed features (Markwick & Millar 2000; Cami et al. 2000; Yamamura & de Jong 2000). Multiple observations of T Cep in Yamamura (2003) and Yamamura & de Jong (2000) hinted at variations in the features with phase, but unfortunately ISO only observed 1.4 periods which was not sufficient to determine if these variations were transient or tied to the pulsation. The ISO discoveries demonstrated that molecular layers in Mira CSE's are dynamic, but lacked enough observations to tie gas behavior to the phase of the Mira.

3.2 M-types

The M-type Miras show several strong features at 13.49 μm, 13.87 μm, 14.98 μm, 16.18 μm, and 16.76 μm. We identify these features as un-resolved, ro-vibrational Q-branch bandheads of CO_2, according to labeled transitions in Herzberg (1945) and HITRAN (Gordon et al. 2017). Table 3.1 provides the specific ro-vibrational transitions associated with each feature. Each vibrational level is designated as $\nu_1\nu_2^l\nu_3$ with ν_1 referring to a symmetric stretch, ν_2 refers to a doubly degenerate bending mode, and ν_3 refers to an asymmetric stretch. For further details and a diagram of these modes see Section 4.3.2.

Band Center (μm)	Transition
13.49	$11^10(1)$ - $02^20(1)$
13.87	$10^00(1)$ - $01^10(1)$
14.98	$01^10(1)$ - $00^00(1)$
16.18	$10^00(2)$ - $01^10(1)$
16.76	$11^10(2)$ - $02^20(1)$

Table 3.1: Observed CO_2 ro-vibrational transitions. A vibrational state is designated as $\nu_1\nu_2^l\nu_3$, with three "modes" that contribute to the vibration of the molecule: ν_1 refers to a symmetric stretch, ν_2 refers to bending, and ν_3 refers to an asymmetric stretch. More details can be found in Section 4.3.

The features at 13.87 μm and 16.18 μm are a Fermi degenerate pair, as are the features at 13.49 μm and 16.76 μm; full details on Fermi degeneracy can be found in Section 4.3. As discussed in Section 3.1 most of these CO_2 transitions were previously observed with ISO and e.g. Justtanont et al. (1998); Ryde et al. (1998); Markwick & Millar (2000); Cami et al. (2000); Yamamura & de Jong (2000), however the majority of the ISO studies include single observations and no phase dependent discussions. This work builds off the ISO observations by including observations across multiple phases; the 13 Mira variables analyzed here have 2-7 repeat observations with changing phase. Figures 3.2-3.4 provide examples of IRS spectra for 3 of our M-type Miras. The 5 CO_2 Q-branch bandheads of interest in this study are labeled with arrows, and the phase of each star is also provided. It is quickly apparent that though the spectra share similarities they are far from uniform.

The most noticeable feature is the ν_2 band at 14.98 μm which is seen in both emission and absorption. Yamamura & de Jong (2000) reported identical behavior of the ν_2 band of SO_2 at 7.2 μm in several Miras. The hot bands at 13.49 μm, 13.87 μm, 16.18 μm, and 16.76 μm are always in emission. The 14.98 μm feature is quite dynamic in this dataset, and can be seen in very weak emission transitioning to absorption in S Lac. In S Peg the absorption feature is so weak as to be in the noise limit in one observation and could be considered a non-detection, but in the next observation it is strong absorption. In SS Cas the line is in emission, and

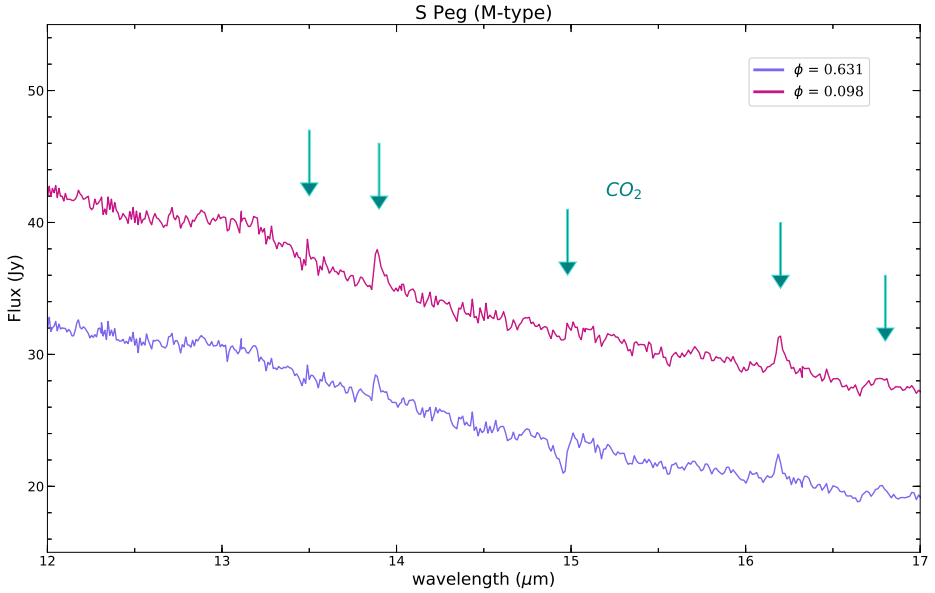

Figure 3.2: Mid-IR spectra of the M-type Mira variable S Peg. The top spectrum is artificially offset by an additional 5 Jy for clarity. Modeling of the CO_2 is discussed in Chapter 4.

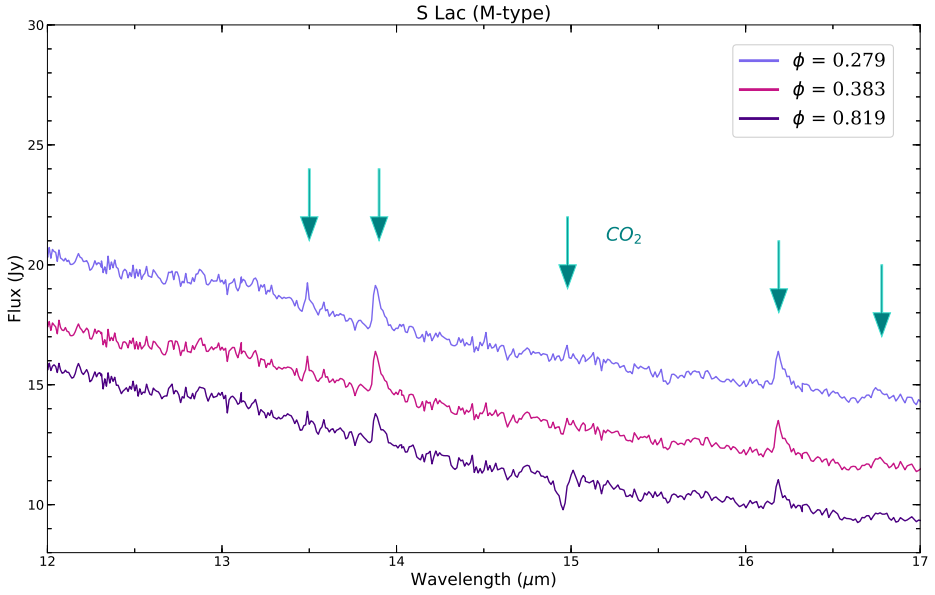

Figure 3.3: IRS spectra of the M-type Mira variable S Lac. The top spectrum is artificially offset by an additional 4 Jy and the middle spectrum is offset by an additional 2 Jy for clarity. Note the dynamic change of the fundamental ν_2 band at 14.98 μm.

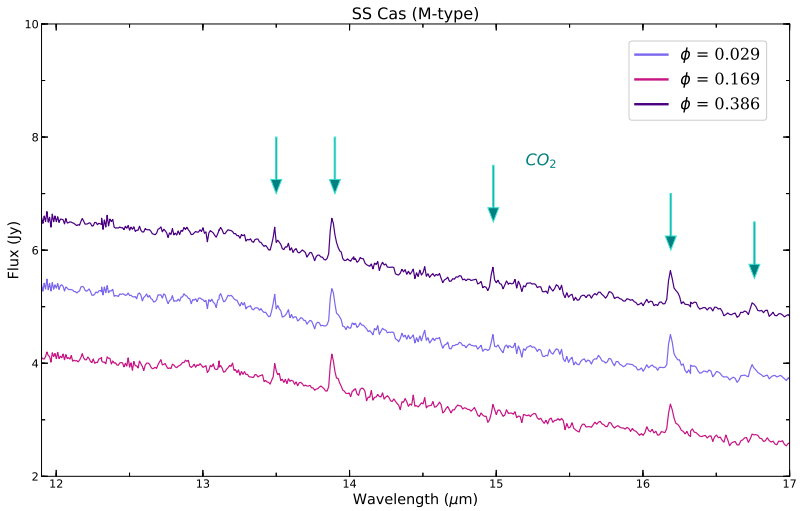

Figure 3.4: IRS spectra of the M-type Mira variable SS Cas. The top spectrum is artificially offset by an additional 2 Jy and the middle spectrum is offset by an additional 1 Jy for clarity. Note here the fundamental ν_2 band at 14.98 μm is seen in emission compared to the spectra in Figure 3.2.

then as with S Lac it grows so weak it is a possible a non-detection. The spectra of these three stars are characteristic of the whole M-type data set. We can clearly see that the CO_2 gas is dynamic across the stellar pulsation cycle. Chapter 4 describes how we created synthetic spectra to determine the temperature, density, and location of the CO_2 gas within the CSE.

3.3 C-types

The C-type Miras show several features at $\sim$14 μm. We identify these features as HCN and C_2H_2 according to labeled transitions in Herzberg (1945) and HITRAN (Gordon et al. 2017). Identifying specific bands is not as straightforward for these species as it was with CO_2. Multiple Q-branches overlap near 14 μm and the IRS resolution of $\sim$ 600 is not high enough to unambiguously differentiate specific transitions. Tables 3.2 and 3.3 provide a list of bands possibly contributing to the features seen in the spectra.

The labeling scheme for vibrational levels of HCN is quite similar to that of CO_2, with some variations because HCN is not symmetric. The ν_1 stretch refers to a CN stretch, ν_2 is still a double degenerate bend of the molecule, and ν_3 refers to HC stretch (Shimanouchi 1977). Figure 3.5 provides a sketch of the modes. The labeling scheme for C_2H_2 is different from that of CO_2 and HCN because it has an additional atom, and its vibrational modes are thus more complicated. There are 7 modes that can vibrate the molecule: ν_1 refers to a symmetric stretch of CH,

HCN	
Band Center (μm)	Transition
14.04	$01^{1}0(1)$-$00^{0}0(1)$
14.30	$02^{0}0(1)$-$01^{1}0(1)$
13.99	$02^{2}0(1)$-$01^{1}0(1)$
14.24	$03^{1}0(1)$-$02^{0}0(1)$
14.55	$03^{1}0(1)$-$02^{2}0(1)$
13.94	$03^{3}0(1)$-$02^{2}0(1)$

Table 3.2: HCN ro-vibrational transitions. A vibrational state is designated as $\nu_1\nu_2^l\nu_3$, with four modes that contribute to the molecule's vibration: ν_1 refers to C-N stretch, ν_2 refers to a degenerate bending, and ν_3 refers to H-C stretch.

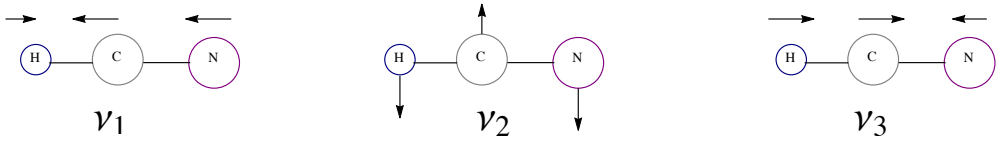

Figure 3.5: Diagram of vibrational modes for HCN. The four vibrational modes include the ν_1 stretch of CN, ν_2 is a doubly degenerate bend of the molecule, and ν_3 refers to HC stretch.

C_2H_2	
Band Center (μm)	Transition
13.71	$\nu_5(l=1)$ - 0
13.72	$\nu_4+\nu_5(l=0)$ - $\nu_4(l=1)$
13.68	$\nu_4+\nu_5(l=2)$ - $\nu_4(l=1)$
13.89	$2\nu_5(l=0)$ - $\nu_5(l=1)$
13.71	$2\nu_5(l=2)$ - $\nu_5(l=1)$

Table 3.3: C_2H_2 ro-vibrational transitions. C_2H_2 is labeled $\nu_1\nu_2^l\nu_3\nu_4\nu_5$ and has 7 modes that can vibrate the molecule (see Figure 3.6): ν_1 refers to a symmetric stretch of CH, ν_2 refers to a symmetric stretch of CC, ν_3 refers is an asymmetric stretch of CH, ν_4 is a degenerate symmetric bend, and lastly, ν_5 is a degenerate asymmetric bend. Lastly (l) describes the vibrational angular momentum and arises from degenerate bending modes.

ν_2 refers to a symmetric stretch of CC, ν_3 refers is an asymmetric stretch of CH, ν_4 is a degenerate symmetric bend, and lastly, ν_5 is a degenerate asymmetric bend. These modes are illustrated in Figure 3.6. We are labeling transitions according to HITRAN conventions described in Jacquemart et al. (2003). The eigenfrequencies

for C_2H_2 have coincidental degeneracy such that $\omega_1 \simeq \omega_3 \simeq 5\omega_4 \simeq 5\omega_5$ and $\omega_2 \simeq 3\omega_4 \simeq 3\omega_5$. It becomes useful to organize vibrational levels into "polyads" described with a pseudo-quantum number, P, where $P = 5\nu_1 + 3\nu_2 + 5\nu_3 + \nu_4 + \nu_5$. A transition is then described from a $n\nu_5$ polyad to $(n+1)\nu_5$ polyad.

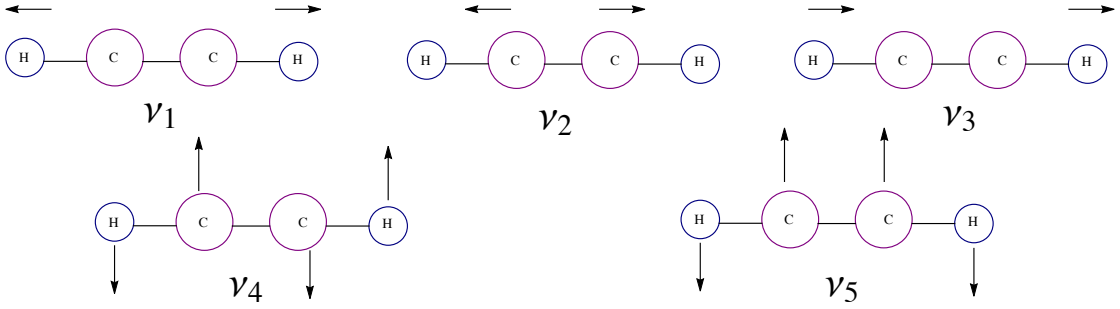

Figure 3.6: Vibrational modes of C_2H_2. The 7 modes include ν_1 which is a symmetric stretch of CH, ν_2 refers to a symmetric stretch of CC, ν_3 refers is an asymmetric stretch of CH, ν_4 is a doubly degenerate symmetric bend, and lastly, ν_5 is a doubly degenerate asymmetric bend.

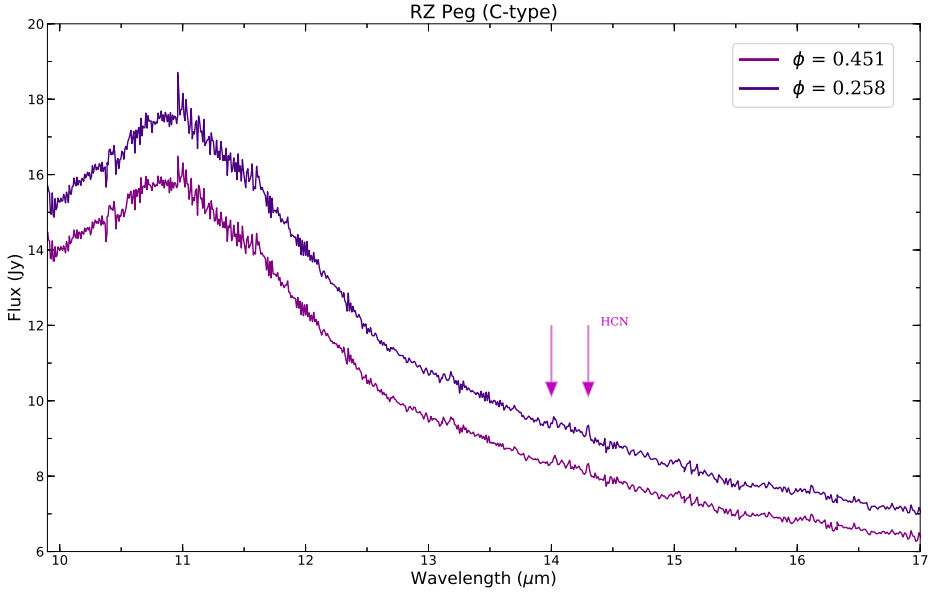

Figure 3.7: IRS spectra of the C-type Mira variable RZ Peg. The spectra are notably missing the broad C_2H_2 feature at 13.7 μm, but show HCN emission at 14.04 μm and 14.3 μm.

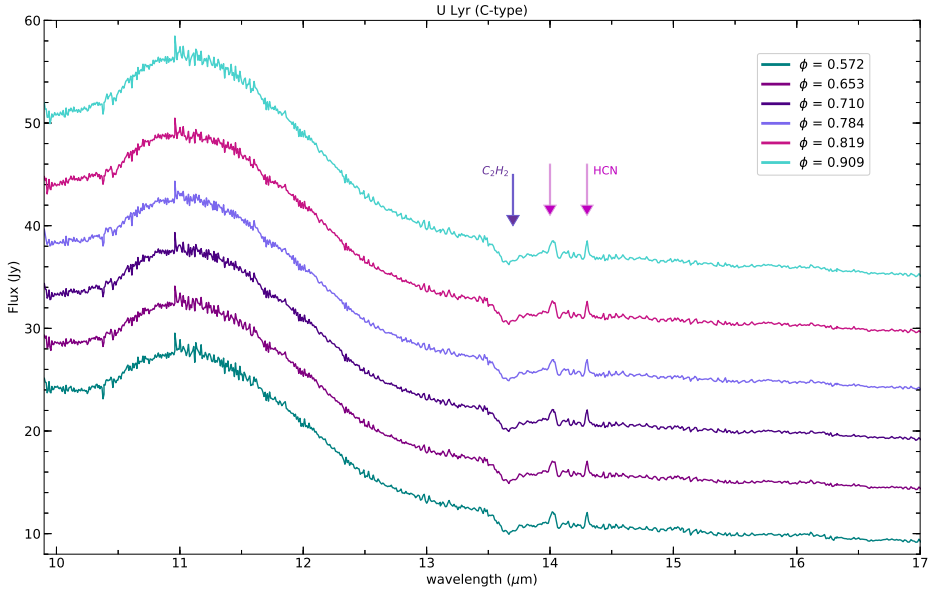

Figure 3.8: IRS spectra of the C-type Mira variable U Lyr. The top spectrum is artificially offset by an additional 8 Jy and the middle spectrum is offset by an additional 5 Jy for clarity. U Lyr shows a HCN feature that the other C-types do not.

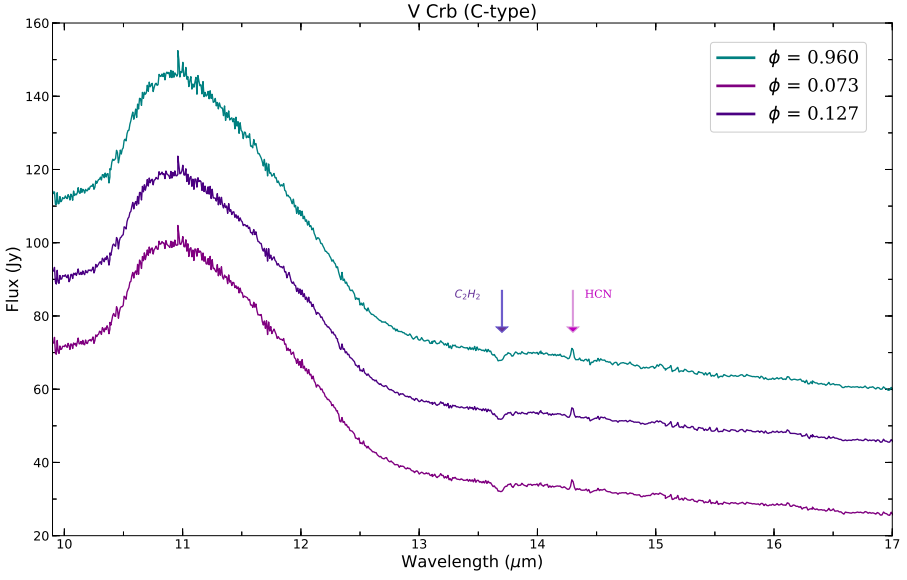

Figure 3.9: IRS spectra of the C-type Mira variable V Crb. The top spectrum is artificially offset by an additional 30 Jy and the middle spectrum is offset by an additional 20 Jy for clarity. V Crb is lacking the HCN feature at 14.04 μm compared to U Lyr.

Most of the C-types in our sample show these classic features near 14 μm. Figures 3.8, 3.9 and 3.7 show the IRS spectra for U Lyr, V Crb, and RZ Peg. The broad absorption seen at 13.7 μm is most likely a combination of several transitions of C_2H_2. The clear emission lines at 14.04 μm and 14.3 μm are HCN, although it is likely that additional HCN transitions also affect the spectrum between 13.7-14 μm. It is also possible that there are additional contributions from HCN near 14 μm that were not resolved with IRS; for example Aoki et al. (1999) observed HCN in absorption at 14 μm in V Crb, but the ISO Short Wavelength Spectrometer (SWS) setting used for that experiment had R $\sim$ 1500 compared to R $\sim$ 600 for IRS. RZ Peg is lacking a clear C_2H_2 feature at 13.7 μm compared to other C-types in the set. It is possible that it is just evolving into a C-type and has not dredged up enough carbon to create an abundance of carbon-rich molecules.

3.4 S-types

The S-types in our data set run the gamut in terms of spectral features. These stars have an "intermediate" chemistry where it is thought that $C/O \sim 1$. This actually makes it difficult to systematically categorize their features. If they are just entering the S-type phase they will not have produced enough carbon to create carbon-rich species like C_2H_2, but the oxygen has been depleted via silicate dust production so oxygen-rich species like CO_2 are weak or absent.

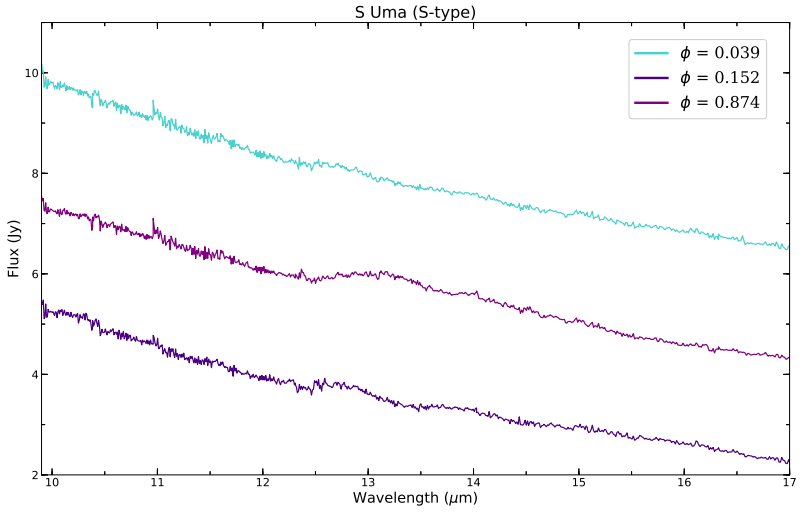

Figure 3.10: IRS spectra of the S-type Mira variable S Uma. The upper spectrum is artificially offset by an additional 4 Jy and the middle spectrum is offset by an additional 4 Jy for clarity. S Uma provides an example of how ambiguous an S-type spectrum can be compared to the spectra presented in Sections 3.2 and 3.3.

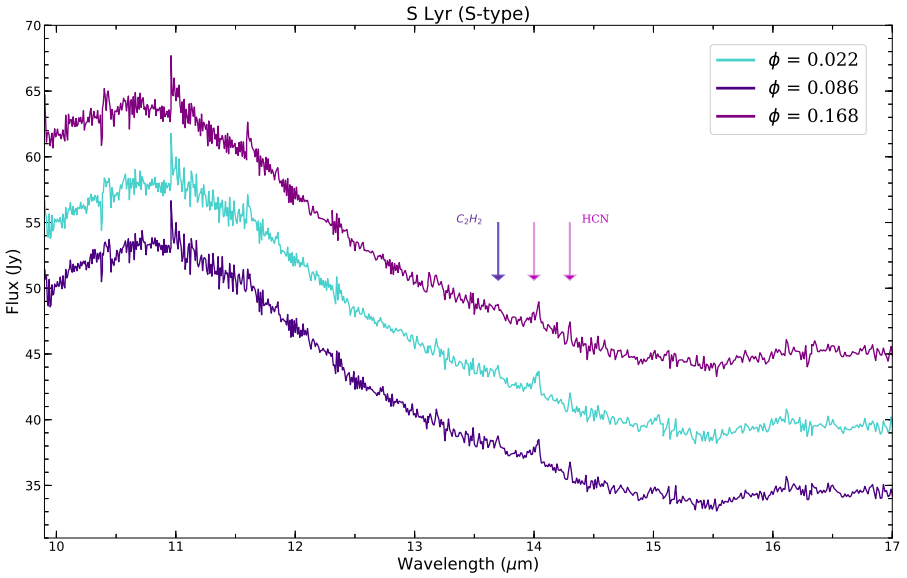

Figure 3.11: IRS spectra of the S-type Mira variable S Lyr. The top spectrum is artificially offset by an additional 12 Jy and the middle spectrum is offset by an additional 6 Jy for clarity. The spectra show additional un-identified bandheads near 11 μm and 13 μm that require further study for identification.

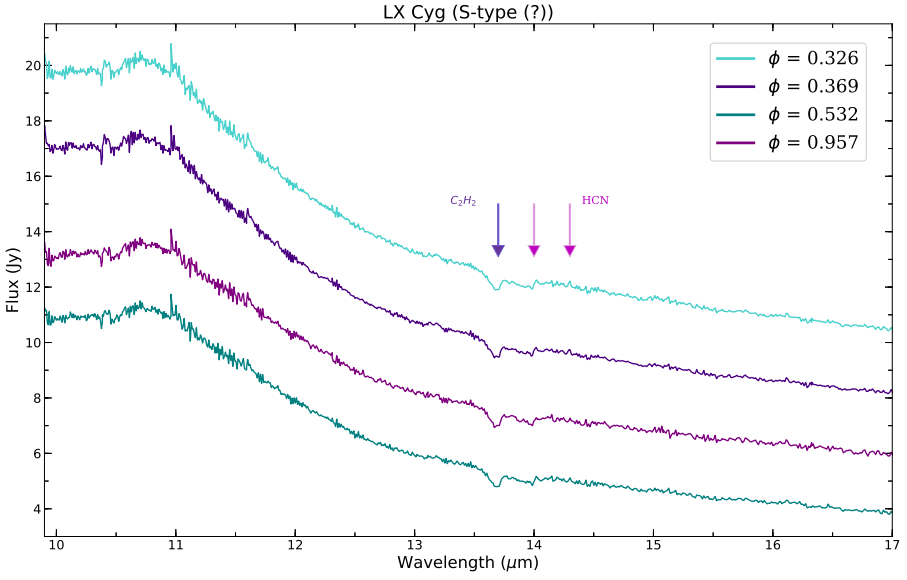

Figure 3.12: IRS spectra of the S-type Mira variable LX Cyg. The top spectrum is artificially offset by an additional 6 Jy, the next spectrum down is offset by an additional 4 Jy, and the second spectrum down is offset by an additional 2 Jy for clarity.

The intermediate chemistry in S-type Miras can lead to fairly ambiguous looking spectra as in Figure 3.10. There are no prominent emission or absorption features of CO_2, HCN, or C_2H_2. In contrast, the spectra of S Lyr and LX Cyg in Figures 3.11 and 3.12 are much more interesting. S Lyr shows HCN emission at 14 μm and 14.3 μm as well as a weak emission feature near 13.7 μm, possibly from C_2H_2. It is reasonable to question if the emission line at 14 μm could potentially be the $10^00(1)$ - $01^10(1)$ transition from CO_2, but when we examine both features we notice that the CO_2 feature gets broad towards longer wavelengths, while the HCN feature gets broad towards shorter wavelengths (see Figure 3.13). This is a consequence of their individual quantum mechanics driving the Q-branch transitions. In LX Cyg the HCN is actually in absorption near 14 μm and weak emission at 14.3 μm. What is quite surprising is the strength of the C_2H_2 absorption which is unlike the rest of the S-type spectra. It is possible LX Cyg received the wrong chemical sub-class and should be classified a C-type.

3.5 Novel Feature at 17.62 μm

All the Miras in our sample show a previously un-observed emission line at 17.62 μm. Since this feature was not observed with ISO we first consulted the IRS

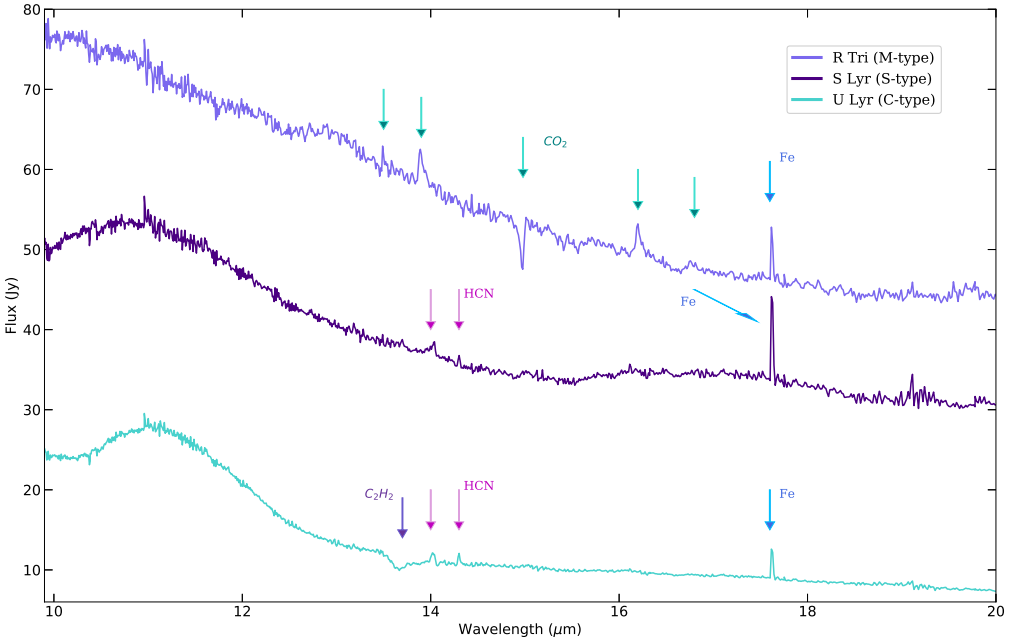

Figure 3.13: IRS spectra of 3 Mira variables with different chemistries. The top spectrum has been artificially offset by 20 Jy for clarity. Each spectrum shows the strong emission feature at 17.62 μm.

Instrument Handbook[1] and the "Features and Caveats"[2] for instrumental affects. No spurious features near 17.62 μm were reported, and additionally no reports of instrumental affects at this wavelength were ever found in the literature. If there was an obvious instrumental affect then observations of this line taken on the same day in different stars should produce identical features, but we do not observe this effect, as can be seen in Tables 6.4, 6.5, and 6.6.

We believe this observation is a consequence of how the spectra were taken. We have dedicated backgrounds *for every observation of every target in the sample target*, and the telescope nodded completely off-slit for the observations. A "nod" refers an offset applied to the telescope pointing, which is usually along a long slit such that the pair of pointings in the nod together can be used to increase the total SNR of the observation without wasting telescope time integrating on blank sky. Taking the difference between the pair removes background emission from the sky and the instrument; without the nod even space-based telescopes produce too much background radiation and it is nearly impossible to acquire decent sensitivity. When on-slit nodding is used the target remains in the slit the entire time, whereas in off-slit nodding the telescope moves off target for the second observation. If the source is extended then on-slit nodding has the risk of subtracting the feature from itself when the difference is taken, thus on-slit nodding is generally avoided for targets that are known to be extended. Miras have extremely extended atmospheres and it is possible on-slit nodding in previous observing programs would have missed observing this new feature.

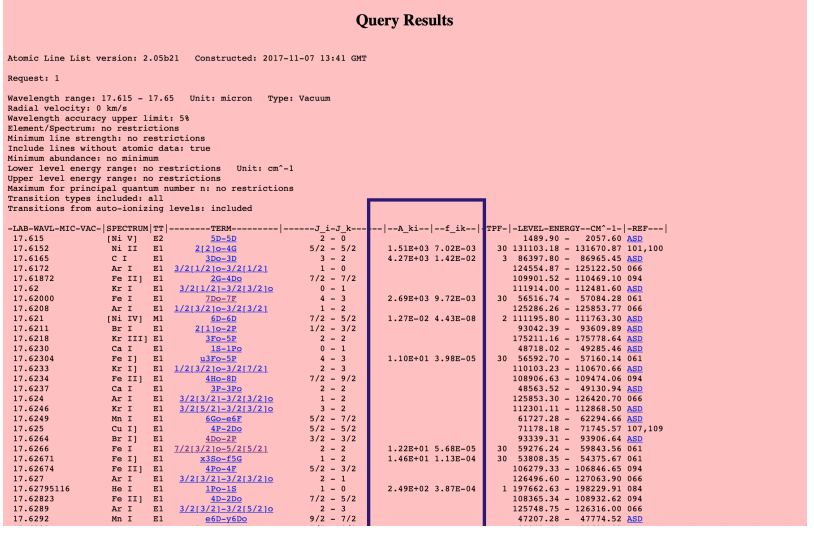

Query Results

Atomic Line List version: 2.05b21 Constructed: 2017-11-07 13:41 GMT

Request: 1

Wavelength range: 17.615 - 17.65 Unit: micron Type: Vacuum
Radial velocity: 0 km/s
Wavelength accuracy upper limit: 5%
Element/Spectrum: no restrictions
Minimum line strength: no restrictions
Include lines without atomic data: true
Minimum abundance: no minimum
Lower level energy range: no restrictions Unit: cm^-1
Upper level energy range: no restrictions
Maximum for principal quantum number n: no restrictions
Transition types included: all
Transitions from auto-ionizing levels: included

-LAB-WAVL-MIC-VAC-	SPECTRUM	TT	--------TERM---------	------J_i-J_k------	--A_ki--	--f_ik--	TPF-	-LEVEL-ENERGY-CM^-1-	-REF---
17.615	[Ni V]	E2	5D-5D	2 - 0				1489.90 - 2057.60	ASD
17.6152	Ni II	E1	2[2]o-4G	5/2 - 5/2	1.51E+03	7.02E-03	30	131103.18 - 131670.87	101,100
17.6165	C I	E1	3Do-3D	3 - 2	4.27E+03	1.42E-02	3	86397.80 - 86965.45	ASD
17.6172	Ar I	E1	3/2[1/2]o-3/2[1/2]	1 - 0				124554.87 - 125122.50	066
17.61872	Fe II]	E1	2G-4Do	7/2 - 7/2				109901.52 - 110469.10	094
17.62	Kr I	E1	3/2[1/2]-3/2[3/2]o	0 - 1				111914.00 - 112481.60	ASD
17.62000	Fe I	E1	7Do-7F	4 - 3	2.69E+03	9.72E-03	30	56516.74 - 57084.28	061
17.6208	Ar I	E1	1/2[3/2]o-3/2[3/2]	1 - 2				125286.26 - 125853.77	066
17.621	[Ni IV]	M1	6D-6D	7/2 - 5/2	1.27E-02	4.43E-08	2	111195.80 - 111763.30	ASD
17.6211	Br I	E1	2[1]o-2P	1/2 - 3/2				93042.39 - 93609.89	ASD
17.6218	Kr III]	E1	3Fo-5P	2 - 2				175211.16 - 175778.64	ASD
17.6230	Ca I	E1	1S-1Po	0 - 1				48718.02 - 49285.46	ASD
17.62304	Fe I]	E1	u3Fo-5P	4 - 3	1.10E+01	3.98E-05	30	56592.70 - 57160.14	061
17.6233	Kr I]	E1	1/2[3/2]o-3/2[7/2]	2 - 3				110103.23 - 110670.66	ASD
17.6234	Fe II]	E1	4Ho-8D	7/2 - 9/2				108906.63 - 109474.06	094
17.6237	Ca I	E1	3P-3Po	2 - 2				48563.52 - 49130.94	ASD
17.624	Ar I	E1	3/2[3/2]-3/2[3/2]o	1 - 2				125853.30 - 126420.70	066
17.6246	Kr I	E1	3/2[5/2]-3/2[3/2]o	3 - 2				112301.11 - 112868.50	ASD
17.6249	Mn I	E1	6Go-6F	5/2 - 7/2				61727.28 - 62294.66	ASD
17.625	Cu I]	E1	4P-2Do	5/2 - 5/2				71178.18 - 71745.57	107,109
17.6264	Br I]	E1	4Do-2P	3/2 - 3/2				93339.31 - 93906.64	ASD
17.6266	Fe I	E1	7/2[3/2]o-5/2[5/2]	2 - 2	1.22E+01	5.68E-05	30	59276.24 - 59843.56	061
17.62671	Fe I]	E1	x3So-f5G	1 - 2	1.46E+01	1.13E-04	30	53808.35 - 54375.67	061
17.62674	Fe II]	E1	4Po-4F	5/2 - 3/2				106279.33 - 106846.65	094
17.627	Ar I	E1	3/2[3/2]-3/2[3/2]o	2 - 1				126496.60 - 127063.90	066
17.62795116	He I	E1	1Po-1S	1 - 0	2.49E+02	3.87E-04	1	197662.63 - 198229.91	084
17.62823	Fe II]	E1	4D-2Do	7/2 - 5/2				108365.34 - 108932.62	094
17.6289	Ar I	E1	3/2[3/2]-3/2[5/2]o	2 - 3				125748.75 - 126316.00	066
17.6292	Mn I	E1	e6D-y6Do	9/2 - 7/2				47207.28 - 47774.52	ASD

Figure 3.14: Sample output from search in the Atomic Line List (van Hoof 2018). The rectangle enclosing the Einstein A coefficients and the oscillator strengths shows how many transitions are missing these data.

[1] https://irsa.ipac.caltech.edu/data/SPITZER/docs/irs/irsinstrumenthandbook/

[2] https://irsa.ipac.caltech.edu/data/SPITZER/docs/irs/features/

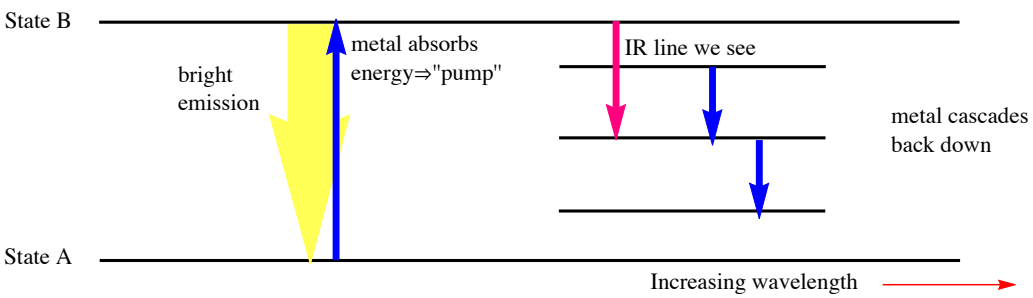

Figure 3.15: Diagram illustrating fluorescence. A very strong emission line at a higher energy (shorter wavelength) is coincident with a transition that has matching quantum numbers. This allows the prominent emission to serve as a "pump" to the adjacent transition. The metal then emits photons of lower energy than the pumping transition, which we see as fluorescence features at lower energies (longer wavelengths).

This feature is characteristically different than the molecular features discussed in Sections 3.2, 3.3, and 3.4, indicating the species is atomic instead of molecular. It is markedly narrow, at the limit of the instrumental resolution, and always seen in emission. Identifying this feature is not straightforward, but there are several guidelines we can use as a starting point. 1) Possible originating species must be available to both oxygen-rich and carbon-rich environments. Eliminating possibilities is not as straightforward as it would be for a main sequence star because Miras undergo massive dredge-up events that contribute to the production of heavier elements via the s-process and α process (as discussed in Section 1.3.1). 2) The atmosphere is "cool" ($\sim$2000-3000 K) so we expect a neutral metal over an ionized metal. 3) The emission is extremely bright ($\sim$ 10's of Jy) in many observations. 4) The strength of the feature appears to be tied to the phase of the star.

We consulted the Atomic Line List [3] (van Hoof 2018) for identification. Figure 3.14 shows a screen shot of part of the search output in our wavelength range. An obstacle in the identification process can be seen in the rectangle enclosing the Einstein A coefficients and oscillator strengths. Both of these are related to the probability a transition will occur, the larger the number the stronger the transition. Few transitions in this wavelength regime have measured or calculated values for these parameters making it difficult use a minimum oscillator strength to narrow the search results.

Based upon the reported oscillator strengths and all our other considerations above, we identify this new feature as Fe I. It is reasonable to expect Fe as a metal

[3] `http://www.pa.uky.edu/~peter/newpage/`

present in both chemistries. This would not be the first time Fe I was present in all observations in a set; in a study of phase dependent emission line behavior of six Mira variables that included 3-7 observations for each star, Richter & Wood (2001) reported optical transitions of Fe I were present in every spectrum. Finally, due to its sharpness, consistent brightness and lack of additional multiplet transitions (a multiplet consists of nearby transitions that arise from fine-structure splitting) we believe this is a fluorescence feature. Fluorescence is common in Mira atmospheres and Fe I fluorescence has been previously identified in both M-types (Luttermoser 2000) and C-types (Johnson et al. 1995). Possible pumping mechanisms for this feature are discussed in Section 4.7. The line strength is changing with the phase of the star as can be seen in Figure 3.16, and its periodicity may indicate the feature probes shock behavior in the CSE.

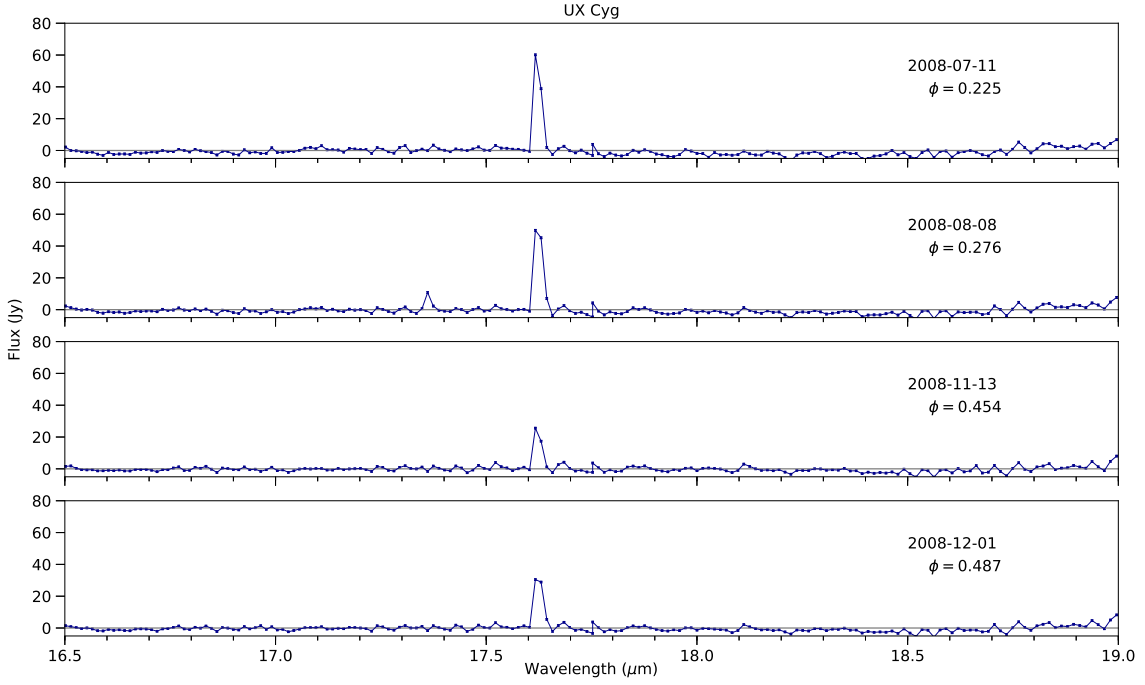

Figure 3.16: Phase dependent behavior of the 17.62 μm feature in the M-type Mira variable UX Cyg. Note a background subtraction has been performed and is described in the following chapter.

"The spectra of more than 200,000 stars have been studied. The results will help to unravel some of the mysteries of the great universe, visible to us, in the depths above. They will provide material for investigation of those distant suns of which we nothing except as revealed by the rays of light, traveling for years with great velocity through space, to be made at last to tell their magical story on our photographic plate. "

— Annie Jump Cannon

Chapter 4

SPECTRAL ANALYSIS

In this chapter, we present analysis of the five CO_2 Q-branch bandheads identified in the M-types in Chapter 3. This involved subtracting a background and modeling the lines with a radiative transfer code called RADEX. Results from these models are presented in Table 6.3 and plots of the spectra with the fits are provided in Appendix A.1. Additionally, analysis and discussion of the Fe fluorescence feature includes background subtractions and Gaussian profile fitting for each observation. These results are presented in Tables 6.4, 6.5, and 6.6 for the M-types, S-types, and C-types, respectively, and plots of the profiles are included in Appendix B.1.

4.1 Background Subtractions

Before we modeled the spectral features we needed to subtract the background emission, called the continuum; if the line profiles we are trying to match with synthetic spectra have any extra emission from background sources the model calculations can return poor physical conditions for the features being fit. The backgrounds were all subtracted in a similar fashion using the Python package

Sherpa[1] (Burke et al. 2020). Once the backgrounds were subtracted, an ASCII file of the residuals was saved and used for further modeling.

4.1.1 Subtraction 13-17 μm

The five Q-branch lines of CO_2 lie at 13.49, 13.87, 14.98, 16.18, and 16.76 μm and we decided to search for global fits that would model all 5 lines simultaneously. We therefore performed a background subtraction from 13-17 μm. Mira atmospheres have significant dust, which often makes a simple blackbody background insufficient. We adopted a "graybody" where we added a power-law function in addition to the blackbody function. An example of this background is shown in Figure 4.1.

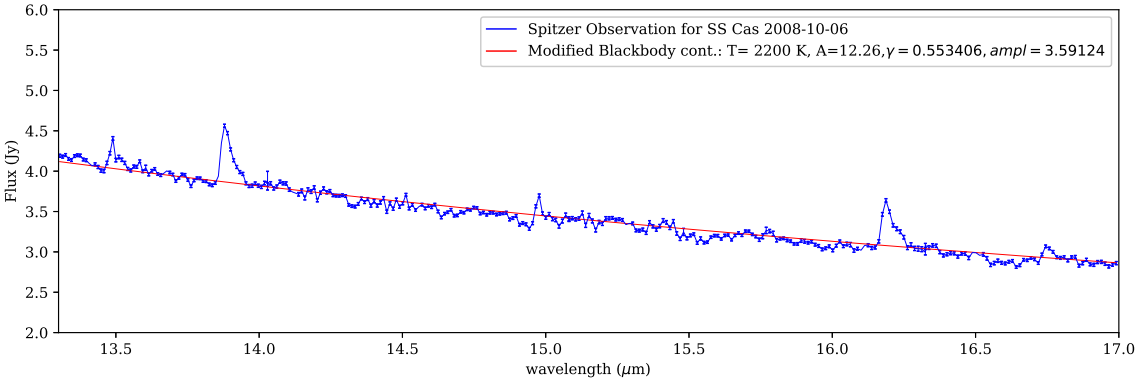

Figure 4.1: Graybody subtraction between 13-17 μm in the M-type Mia variable SS Cas. The graybody is created by adding *Sherpa's* built in power-law function to the blackbody.

For the Miras that had significant dust emission from 15-20 μm, even the graybody failed and we did the subtraction in two sections. The dust starts contaminating the spectrum near 15 μm and after several fitting iterations we decided to fit a graybody from 13 - 15 μm, and then a power-law from 15-17 μm. Ideally we would prefer to fit the graybody past 15 μm because of the CO_2 feature at 14.98 μm, but attempts to fit the graybody at longer wavelengths yielded poor results. The separate residuals were then joined at overlap point to create a final, continuous residual from 13-17 μm. An example of this is shown below in Figure 4.2.

After the backgrounds were subtracted, *Sherpa* saved the residuals as an ASCII file. However, *Sherpa* only saves the wavelength and flux in the residuals, and we want to include the flux uncertainty as part of the radiative transfer modeling. The uncertainty in the flux does not show great fluctuation in our

[1] `https://cxc.cfa.harvard.edu/contrib/sherpa/`

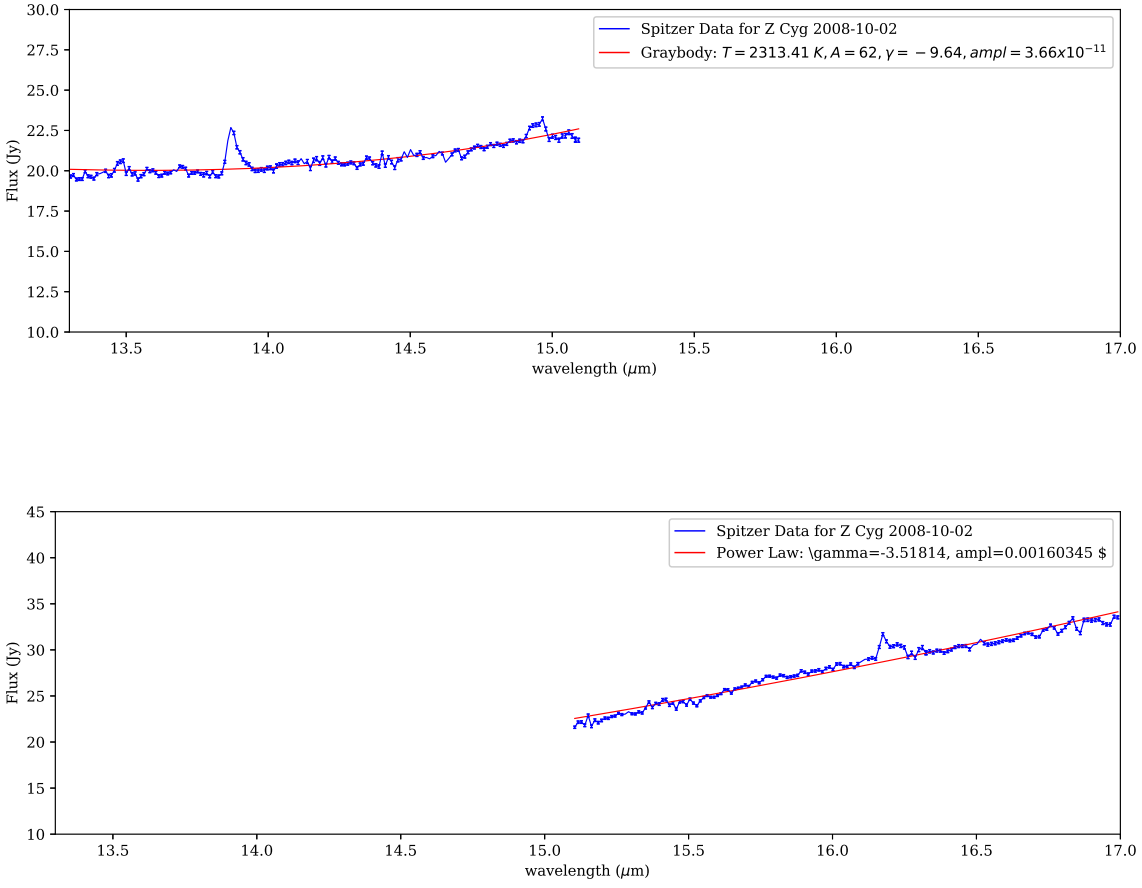

Figure 4.2: Background subtraction for the M-type Mira Z Cyg which had significant dust emission and required the background be split into two sections.

data, and the SNR throughout our dataset is quite high, and we do not anticipate a large difference in and out of the line. For example, a typical flux uncertainty value for R Tri was 150 mJy, while CO_2 line strengths in question range from 4-6 Jy. We calculated the average flux uncertainty between 13-17 μm as a representative value of the uncertainty; we propagated this value through each point to create a final residual file that contains wavelength, flux, and flux uncertainty.

4.1.2 Subtraction 16-19 μm

The subtractions for the Fe feature at 17.62 μm were performed in an identical fashion as described above. Here, we only applied a power-law continuum because at these wavelengths, most of the targets appeared to be well-fit using a Rayleigh-jeans tail assumption, and were thus insensitive to changes in temperature. The cases where this fails are the M-type Miras that have significant dust emission between 15-20 μm as discussed in Güth (2017), and for these targets, we replaced the power-law with a polynomial. One of the outstanding questions we had at the beginning of this work was if the strength of the 17.62 μm feature was tied to the strength of the continuum. To keep track of this behavior we picked a section 0.5 μm away from the line that was not near any possible features and recorded the value of the continuum. Figures 4.3 and 4.4 provide examples of the power-law and polynomial backgrounds, respectively.

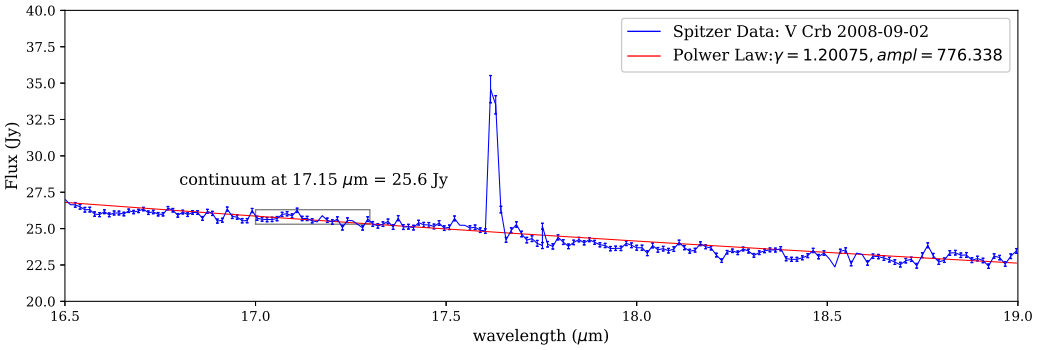

Figure 4.3: Background subtraction for the C-type Mira V Crb. The linear nature of the continuum indicates it is approaching the Rayleigh-Jeans tail.

4.1.3 Offset and Alignment Issues

Several of the spectra in our sample had "offset" issues where the spectrum had large, artificial jumps in the flux. These arise from mis-matching the flux when joining the orders together to make a continuous spectrum. The offsets made

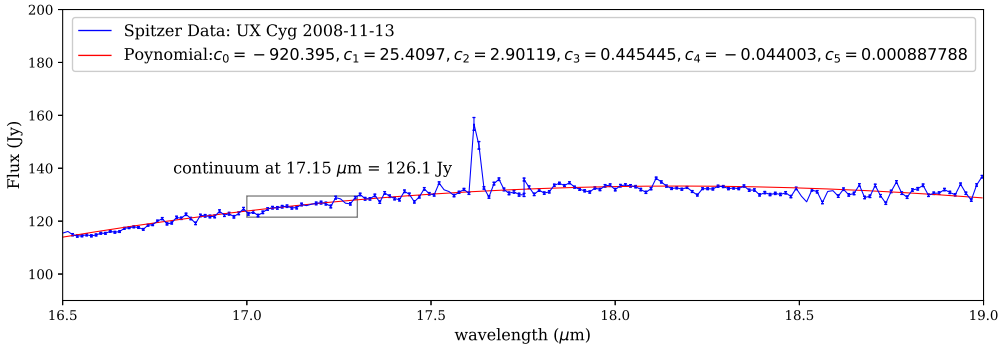

Figure 4.4: Background subtraction for the M-type Mira UX Cyg. Note this spectrum of UX Cyg is quite different from V Crb in Figure 4.3, due to significant dust emission. The continuum was then better fit with a polynomial rather than a power-laws.

background subtractions difficult because the shape of the continuum was artificially jumpy. When we encountered a spectrum with an offset issue, we corrected the jump in flux by shifting longer wavelengths up to meet the shorter wavelengths before the drop. This never shifted the overall spectrum by more than $\sim$1 Jy and had no affect on the actual line strengths.

One target in the sample of stars included in the CO_2 analysis showed a possible alignment issue; that is the slit may have not been properly aligned on the star as the spectrum was taken. We noticed this was a possible issue in the spectra of M-type Mira Z Cyg before we began modeling the CO_2 lines. Furthermore, Güth (2017) described "odd hitches" in the spectra of Z Cyg while modeling the dust composition and attributed it to possible saturation of the detector, or a misalignment of the slit. Initial models were consistently finding line centers that indicated a temperature much cooler than previous models from other stars, and at these temperatures, the line would become saturated at the column densities necessary to re-create the line intensities. We decided to adjust the spectrum using the width of the uncertainty of the IRS instrument, $\Delta\lambda \simeq 0.025\mu$m, as an upper limit. Using the maximum shift of 0.025 μm, the spectrum shifted so far right that the models were then coming back with temperatures too high. When compared to the other stars in the sample, the most consistent model results were produced when we adjusted the spectrum 0.019 μm to the right. The 16.18 μm and 16.76 μm lines are potentially under shifted, but this shift was able to adjust all the lines so they could be fit without colder temperatures that saturate at the densities required to match the line intensities.

In the following sections, we discuss the analysis of the 5 CO_2 Q-branch bandheads.

4.2 Building the Model Infrastructure

The CO_2 bands observed in the M-types show remarkable variability (see Figures 3.2, 3.3, and 3.4 in Chapter 3). The fundamental bending mode at 14.98 μm is seen in both absorption and emission while the excited bands at 13.49, 13.87, 16.18, and 16.76 μm are in emission. These clues indicate the CO_2 lines are being created in a minimum of two regions in the atmosphere. Historically, most models were calculated assuming local thermodynamic equilibrium (LTE) (e.g. Cami et al. (2000)). We wanted to test if this assumption was valid because Mira atmospheres are dynamic with shocks driven by pulsations continually perturbing the environment. We chose to model the CO_2 lines with the radiative transfer code, RADEX, which can solve the radiative transfer under non-local thermodynamic equilibrium (NLTE) conditions.

4.2.1 RADEX

RADEX[2] (van der Tak et al. 2007) is a radiative transfer code written originally by John Black that is available for public use as part of the Leiden Atomic and Molecular Database (LAMDA) (Schöier et al. 2005). It is offered as both an online version[3] for quick estimates of physical conditions as well as a source code[4] to create grids of calculations.

We chose to model the lines with RADEX for several key reasons.

1. The code uses the Sobolev approximation approach for expanding stellar envelopes (Sobolev 1960). This method for calculating radiative transfer is strongly recommended in Hubeny & Mihalas (2014) for dynamic stellar atmospheres.

2. RADEX is capable of running under NLTE conditions which is crucial for these lines because we do not know if they are formed under equilibrium conditions; indeed, our intuition about pulsations in Mira atmospheres suggests that NLTE should be precluded, and studies done by Cherchneff (2006) and Duari et al. (1999) revealed that the CO_2 molecules are created with disequilibrium chemistry.

3. RADEX includes collisional effects in the calculations making it a step up in model sophistication from previous studies that created radiative transfer models only using spectroscopic and dipole moment data. The majority of previous studies fit lines separately, but RADEX simultaneously calculates the radiative transfer for all lines in a specified wavelength range. The ability to fit multiple bands at once in "global" fits creates stronger constraints on the atmospheric conditions.

[2] `https://home.strw.leidenuniv.nl/~moldata/radex.html`

[3] `http://var.sron.nl/radex/radex.php`

[4] `https://personal.sron.nl/~vdtak/radex/index.shtml`

4. RADEX provides flexibility by allowing us to create and upload custom molecular data files for the calculation. This will allow us to update models as we add further transitions.

4.2.2 Molecular File

RADEX calculates the radiative transfer using a data file specific to the desired molecule that includes Einstein coefficients, detailed level energies, and collisional rate coefficients for state-to-state transitions. The LAMDA database (Schöier et al. 2005) has over two dozen molecular and atomic files ready for modeling, however, the majority of these files are designed for modeling pure rotational spectra observed in the radio. We needed to be able to model ro-vibrational transitions in the mid-IR, which meant creating our own data file. We followed the instructions provided in the RADEX documentation[4] for creating custom molecular files.

We created an original data file for ro-vibrational transitions of CO_2 in the 10-20 μm range. The file is built around 8 ro-vibrational bands shown in Figure 4.5; five of these bands are for the five strong Q-branch bandheads, and the remaining 3 were included for possible contributions, e.g. the $02^20(1) - 01^10(1)$ transition at 14.97 μm was contributing to the ν_2 band at 14.98 μm in the work done in Markwick & Millar (2000). Inside each of these vibrational levels we included a rotational ladder up to $J = 50$. The file contains over 700 radiative transitions combined with more than 18,000 collision interactions with H_2. Assembling the necessary data required multiple data bases and published studies of CO_2.

The Einstein A coefficients and transition wavenumbers were provided by the HITRAN[5] database (Gordon et al. 2017). The wavenumbers were eventually converted to frequencies for the final molecular file. Currently, RADEX provides 7 possible collision partners for the calculations: H_2, p-H_2, o-H_2, e^-, atomic H, He, and H^+. We chose to use H_2 as the collision partner in all our calculations for two reasons. We expect H_2 to be a dominant molecule in AGB atmospheres (Duari et al. 1999), and most published laboratory data necessary to calculate rate coefficients are from collisions with H_2.

Rate coefficients are temperature dependent; we needed to account for Mira atmospheres which vary between several thousand and several hundred Kelvin. A study of CO_2 collisions with H_2 from Nevdakh et al. (2003) examined the temperature dependence of the vibrational rate coefficient in the 01^10-0^00 transition, and we used their results to extrapolate the temperature dependence of the remaining vibrational rate coefficients from 100-1000 K in 50 K steps.

[5] `https://hitran.org`

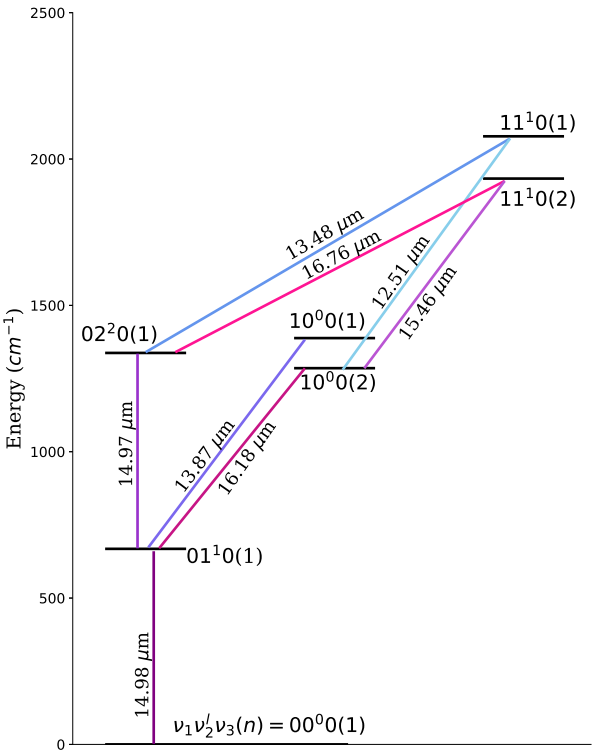

Figure 4.5: Grotrian diagram of CO_2 transitions included our RADEX models. Levels are labeled according to HITRAN's conventions. The colors of the transitions match the corresponding band in the slab spectrum calculated with RADEX shown in Figure 5.3.

4.2.3 Collisional Rate Coefficients

We found no evidence in the literature for pure rotational transitions induced by CO_2 colliding with other species, and this lack of data is also reported in Bosman et al. (2017), who used rotational rate coefficients of CO colliding with H_2 in their calculations of state-to-state coefficients. In an effort to preserve as much ro-vibrational behavior as possible in our models, we used data from Castro et al. (2017) which examined ro-vibrational transitions up to $J = 30$ of CO colliding with H_2. Rates for the remaining J = 31-50 transitions were then calculated using data from pure rotational transitions provided on the LAMDA database. Rates for J=31-40 were taken from (Yang et al. 2010) and rates for J=41-50 were taken from (Neufeld 2012). We followed methods similar to those in several papers (Bosman et al. 2017; Bruderer et al. 2015; Faure & Josselin 2008; Chandra & Sharma 2001) to calculate full state-to-state transitions. We combined vibrational rates with rotational rates to estimate the full state-to-state, ro-vibrational rate coefficients. Vibrational rate coefficients were taken from Bosman et al. (2017), Table A.1, or were calculated according to the relationship derived in Chandra &

Sharma (2001) for $\nu > \nu'$:

$$k(\nu \rightarrow \nu') = \nu \frac{2\nu' + 1}{2\nu + 1} k(\nu = 1 \rightarrow \nu' = 0). \tag{4.1}$$

To calculate full ro-vibrational collisional rates from initial state ν, J to final state ν', J′ we used the method suggested in Bosman et al. (2017) and Faure & Josselin (2008) which assumes the vibrational level can be decoupled from the rotational levels. Then the rotational levels are used to calculate a proportionality constant, $P_{J,J'}(T)$ which acts as a scaling factor on the vibrational rate. T

$$k(\nu, J \rightarrow \nu', J') = P_{J,J'}(T) k(\nu \rightarrow \nu') \tag{4.2}$$

This proportionality constant can be derived as followed. In thermal equilibrium, the transition rate from $i \rightarrow j$ must be balanced.

$$N_i^* C_{ij} = N_j^* C_{ji}$$

where C_{ij} is the collisional rate and the * indicates the level population in LTE (Hubeny & Mihalas 2014). Then, when we consider the Boltzmann equation we have a relationship between the Boltzmann ratio and the collision rate.

$$\frac{N_i^*}{N_j^*} = \frac{g_i}{g_j} e^{-(E_i - E_j)/kT}$$

$$\frac{N_i^*}{N_j^*} = \frac{C_{ji}}{C_{ij}} = \frac{g_i}{g_j} e^{-(E_i - E_j)/kT}$$

$$\frac{C_{ij}}{C_{ji}} \frac{g_i}{g_j} e^{-(E_i - E_j)/kT}$$

$$C_{ij} = C_{ji} \frac{g_j}{g_i} e^{(E_i - E_j)/kT}$$

This equals Faure & Josselin (2008), Equation 10. We will now express the collisional rate coefficients as as $C_{ij} = k(\nu, J \rightarrow \nu', J'; T)$ and $C_{ji} = k(\nu', j \rightarrow \nu, i; T)$.

$$k(\nu, J \rightarrow \nu', J'; T) = \frac{g_J'}{g_J} e^{(E_J - E_{J'})/kT} k(\nu', J' \rightarrow \nu, J; T)$$

Continuing to follow Faure & Josselin (2008), we next write the rotationally summed and average vibrational rate as

$$k(\nu \rightarrow \nu'; T) = \frac{\sum_J (g_J \exp[-E_{\nu,J}/kT] \sum_{J'} k(\nu, J \rightarrow \nu', J'; T))}{\sum_J g_J \exp[-E_{\nu,J}/kT]}$$

and assume that $E_{\nu',i} = E_{\nu,J} + \Delta E_{\nu\nu'}$. With these last 2 assumptions in place then

$$P_{J,J'}(T) = \frac{k(1, J \rightarrow 0, J')\Sigma_J g_J \exp(-E_{\nu,J}/kT)}{\Sigma_J(g_J \exp(-E_{\nu,J}/kT)\Sigma_{J'} k(1, J \rightarrow 0, J'; T))}. \tag{4.3}$$

satisfies the balance requirements in Equation 4.2. This result is slightly different than the original expressions because those assumed the full rates are proportional to the rotational transitions inside the ground vibrational state (e.g. Bosman et al. (2017); Bruderer et al. (2015)). We assumed the rates are proportional to ro-vibrational transitions from the $\nu = 1 \rightarrow \nu' = 0$ state in our efforts to maintain ro-vibrational behavior for the models.

This summation basically provides the conditional probability that a transition will occur. The numerator provides the the rate for the transition of interest and the denominator sums up all the rates from other possible transitions. A diagram of this conditional probability is provided in Figure 4.6. All calculations for these values were done with Python. Once we had the necessary $P_{JJ'}$ values for a desired band, we multiplied them by the vibrational rate coefficient, and the final step was to scale these results according to temperature to produce full, temperature dependent, state-to-state collisional rate coefficients. A sample slab spectrum calculated with our CO_2 file is provided in Figure 4.7 with model parameters: T_{kin} = 750 K, H_2 density = 10^{12} cm^{-3}, CO_2 column density = 10^{16} cm^{-2}, background temperature = 300 K, linewidth = 1 km s^{-1}. Our spectrum reproduced consistent behavior to the one calculated in Bosman et al. (2017) under similar parameters.

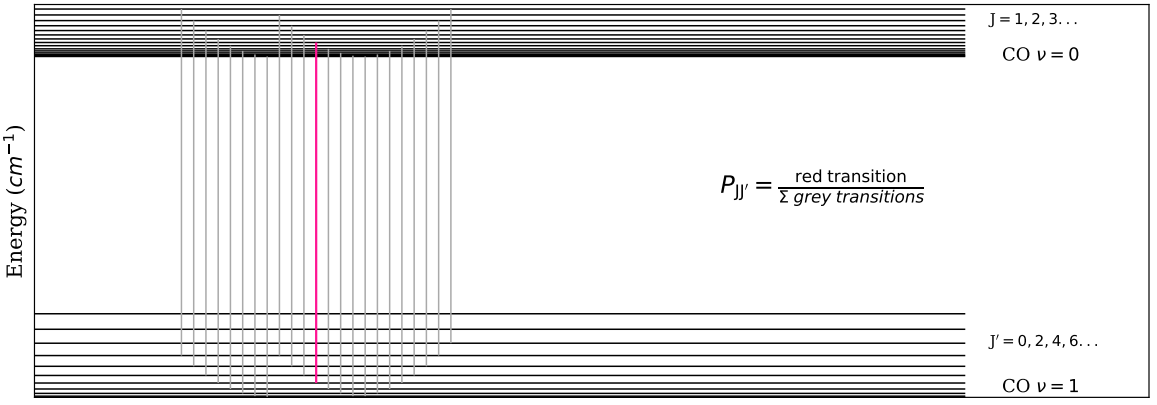

Figure 4.6: Here we illustrate the conditional probability that is calculated with $P_{JJ'}$. The red line represents the transition of interest, and the gray lines represent all other possible transitions governed by the selection rules described in Section 4.3.2. The final rate coefficient of the state-to-state transition is then proportional to rate of the red transition divided by the sum of the rates of all the transitions.

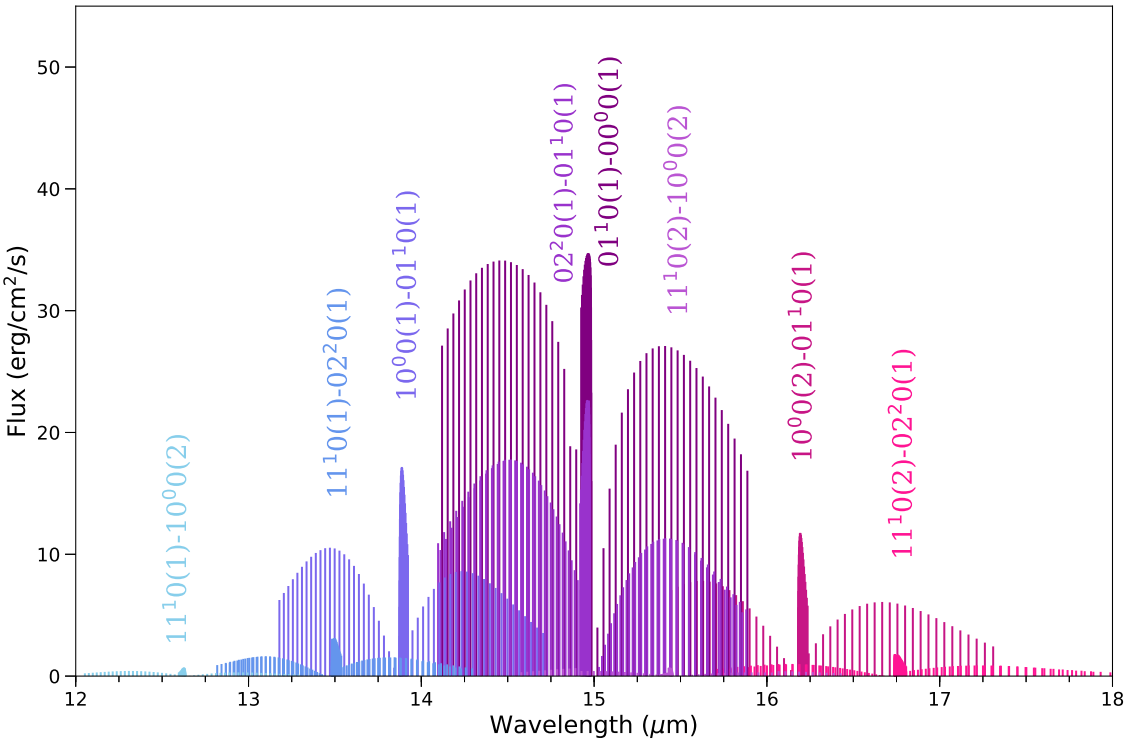

Figure 4.7: Sample slab spectrum of CO_2 calculated with RADEX using our original molecular file. The colors of the bands match their corresponding transitions shown in the energy level diagram in Figure 4.5.

4.3 The CO_2 Molecule

The CO_2 molecule is a fully symmetric, linear molecule and it lacks a permanent dipole moment. The chemical reactions that create CO_2 in M-type Mira atmospheres are complex and depend on shock chemistry tied to the pulsation of the star; for a full discussion of CO_2 reactions see Cherchneff (2006). From Section 1.5 we know the lack of a dipole moment will affect what spectral features it produces. Because it is a linear molecule, the number, N, of available vibrational modes is $3N - 5 = 3(3) - 5 = 4$. These include a symmetric stretching mode, ν_1 at 1337 cm^{-1} (7.48 μm), a doubly degenerate bending mode, ν_2, at 667 cm^{-1} (14.98 μm), and an anti-symmetric stretching mode, ν_3, at 2349 cm^{-1} (4.26 μm). These vibrational modes are illustrated in 4.8. The ν_1 band creates a Raman line while the ν_2 and ν_3 bands create infrared lines. Raman lines arise from a change in polarization in the molecule, while infrared lines are created when there is a change in the dipole moment. The symmetric stretch does not alter the dipole moment, but it does alter polarization; the bending and anti-symmetric stretch alter the dipole moment, but not the polarizability. Under the rule of *mutual exclusion* for molecules with a center of symmetry transitions that are allowed in a Raman

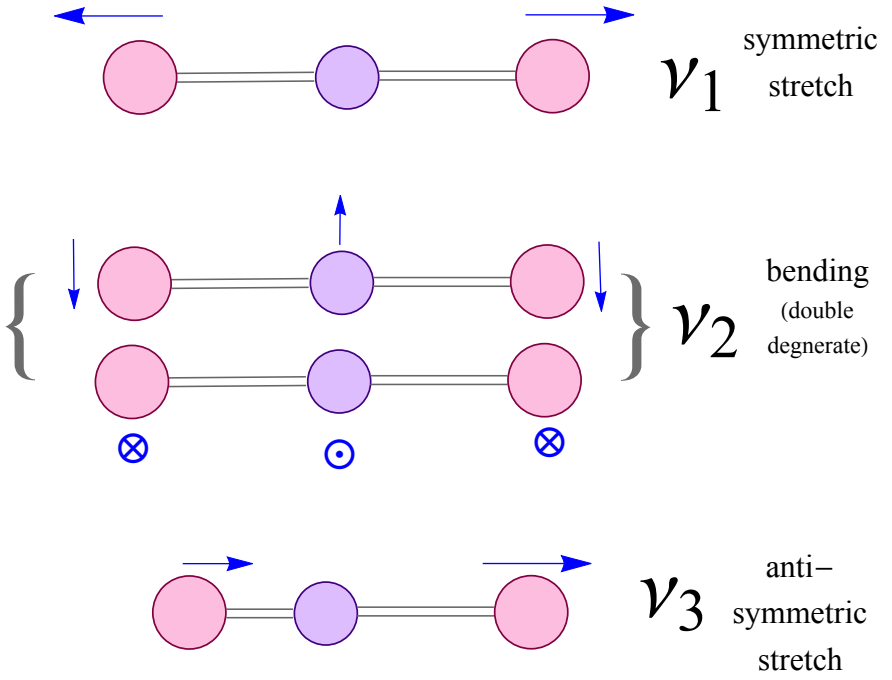

Figure 4.8: Vibrational modes of CO_2.

spectrum are forbidden in an infrared spectrum, and conversely, transitions allowed in an infrared spectrum are forbidden in a Raman spectrum (Herzberg 1945). This means for CO_2 the ν_1 band is infrared inactive, and ν_2 and ν_3 are Raman inactive.

We label a vibrational state according to contributions from each of the fundamental modes: $\nu_1\nu_2^l\nu_3$, where l denotes angular momentum. Upon closer inspection of the fundamental transitions, we notice that $\nu_1 \approx 2\nu_2$. This "accidental" degeneracy was discovered by Enrico Fermi (Fermi 1931) and allows the eigenstates of $2\nu_2$ to perturb the eigenstates of ν_1, provided they have identical angular momentum (Herzberg 1945). The Fermi degeneracy adds a layer of complication to specifying vibrational levels because states that have the same value of $2\nu_2 + \nu_1$ mix to the point that we can no longer unambiguously distinguish the original levels. The result, called Fermi splitting, is two vibrational levels with slightly different energies. For example, the vibrational level $\nu_1\nu_2\nu_3 = 020$ has two sub-levels 02^00 and 02^20 for $l = 0$ and $l = 2$ respectively that could potentially interact with the 10^00 state. Fermi resonances only occur for states of the same species (identical symmetry) (Herzberg 1945; Bernath 2020) so only the 02^00 can perturb and mix with the 10^00 level (both have $l = 0$). To account for Fermi splitting in our labeling scheme, we make an addition to the original notation: $\nu_1\nu_2^l\nu_3(n)$, where n specifies a Fermi pair. In our example, with the Fermi levels created by the mixing of the 02^00 and the 10^00 states are then labeled as $10^00(1)$ and $10^00(2)$ following HITRAN's convention that ν_1 in Fermi split levels is deter-

mined by the state with the largest symmetric stretch quantum number. We have 2 sets of Fermi pairs on our Spitzer spectra; the bands at 13.48 and 16.76 μm are transitions from the Fermi split levels $11^10(1)$ and $11^10(2)$ to the $02^20(1)$ level, and similarly, the bands at 13.87 and 16.18 are transitions from Fermi split levels $10^00(1)$ and $10^00(2)$ to the $01^10(1)$ level, as can be seen in Figure 4.5.

4.3.1 Rotational Structure

In its ground electronic state, CO_2 has a fully symmetric wavefunction. This alters the structure of some of the rotational ladders inside the vibrational levels, because every state needs to be fully symmetric to satisfy Bose-Einstein statistics (Bosman et al. 2017). This symmetry requirement results in some vibrational levels missing all odd J levels while others miss all even J levels. We will briefly summarize rotational structures specific to vibrational levels; complete discussions on rotational structure can be found in Herzberg (1945); Bernath (2020); Bosman et al. (2017).

- The ground state, 00^00 and all subsequent levels with $\nu_2 = \nu_3 = 0$ only contain even J values and start with $J = 0$.
- The first excited state 01^10 contains both even and odd levels starting at $J = 1$. In general, for states with $\nu_2 \neq 0$ but $\nu_3 = 0$ the ladder starts at $J = \nu_2$; for example the 03^30 state starts at $J = 3$ and then continues on $J = 4, 5, 6....$
- If $\nu_2 = 0$ and $\nu_3 \neq 0$ and is odd, then only odd J levels exist, and similarly, if ν_3 is even then only even J levels exist.
- If $\nu_2 \neq 0$ and $\nu_3 \neq 0$ the rotational ladder starts at ν_2 and contains both even and odd J values.

4.3.2 Ro-vibrational Transitions

The structure of CO_2 spectral features is determined by the transitions between rotational ladders inside each vibrational state. The selection rules govern these transitions. From Section 1.5 we know that parallel bands obey $\Delta J = \pm 1$ and create P and R branches. Perpendicular bands obey $\Delta J = 0$, $\Delta J = \pm 1$ creating a strong Q-branch in addition to the P and R branches. If we look at the spectrum in Figure 4.7, we notice that P and R transitions from adjacent bands overlap; these will then overlap and blend together creating a "forest" of lines. In this work we focused on modeling the macroscopic behavior of the five strong Q-branches at 13.49, 13.87, 14.98, 16.18, and 16.76 μm, because the IRS resolution of ~ 600 is not sufficient to properly model all the nuances of the forests of P and R branches blending together. The individual Q-branch transitions build to the left or the

right based on whether or not the rotational constant is larger in the upper state or the lower state (Ryde et al. 1999). In the case of the ν_2 band at 14.98 μm the rotational constant of the upper level is slightly larger than that of the lower level so transitions from higher J values occur at slightly shorter wavelengths, making the band grow to the left. This is opposite for the remaining for bands; their upper level rotational constants are slightly smaller than those of the lower levels so higher level J transitions occur at longer wavelengths and their bands grow to the right. This trend is reflected in the slab spectrum we produced with RADEX in Figure 4.7 and can be seen observationally in the spectra shown in Figures 3.2, 3.3, and 3.4.

When we examine Figure 4.11 we notice that the lines are artificially "peaky", as a result of the perceived hard cut-off of rotational levels at $J = 50$ included in our molecular file. This behavior can lead to perceived mismatches between the RADEX models and the Spitzer spectra. Including additional rotational levels may alleviate some of the "peaky" behavior, but a cut-off point will always exist in the model that we must be aware of when we create models.

4.4 Model

We chose to use a slab model approach for modeling the CO_2 in the Mira atmosphere. This is a common approach for describing Mira atmospheres (e.g. Matsuura et al. (2002); Yamamura et al. (1999b)). The atmospheric structure is modeled as plane-parallel slabs that lie on top of each other to create an "onion" like structure. The conditions of each specific slab of gas can are determined separately, and then the results are combined to produce a macroscopic model of the atmosphere. The major weakness of this approach is that it is not entirely realistic to break up the atmosphere into discrete slabs and model one at a time; however attempting to calculate the radiative transfer of multiple molecules across the whole Mira atmosphere which can stretch several AU, is nearly impossible. RADEX offers two other geometries for the calculations, but neither of them include contributions from stellar winds or shocks so we decided to stick with the plane-parallel approach. We also wanted to verify our results by checking their consistency with previous models, all of which used a plane-parallel slab.

4.4.1 Slab Model

After running initial models it became clear that the five CO_2 features resulted from different atmospheric conditions implying multiple slabs would be needed to model all the features. We have adopted 3-slabs for modeling the CO_2 emission seen in the M-type Miras by assuming the Fermi pair at 13.49 and 16.76 μm lines are created in the first slab, the second Fermi pair at 13.87 and 16.18 μm lines are created in a second slab, and the 14.98 μm line is created in the third slab. Fitting the pairs of lines together creates stronger constrains on the physical

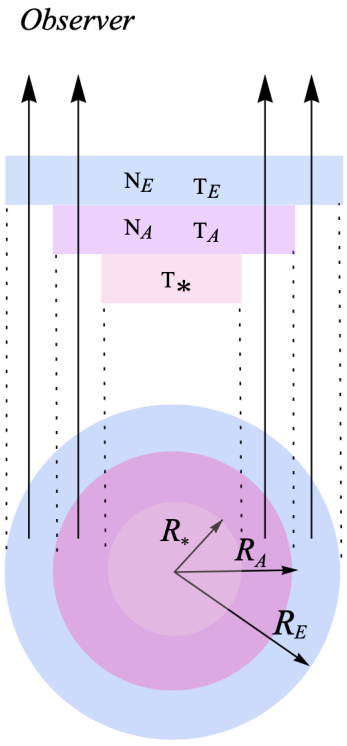

Figure 4.9: Conceptual slab model with an emitting layer sitting above an absorbing layer (not to scale). RADEX models provide the column densities, N_A and N_E as well as the temperatures T_A and T_E. The emitting regions R_A and R_E can be estimated according to steps provided in Section 4.4.2.

parameters than if they were fit individually. For stars that showed the 14.98 μm feature in absorption, we were able to create a global fit for the 13.87, 14.98, and 16.18 μm lines by adding 2 slabs together. The radiative transfer in each slab was calculated in RADEX and the results were superimposed to fit all three bands simultaneously; that is the flux result from the absorbing slab was directly added to the flux result from the emitting slab to produce a final model that was fitted the spectrum. This multi-slab approach was suggested in Ryde et al. (1998) who noticed that the temperature structure required to produce absorption at 14.98 μm with simultaneous emission at 13.87 μm and 16.18 μm indicated both a warm dense layer within a few stellar radii, and an extended slightly cooler layer.

The models focus on using the Q-branch bands to derive basic physical parameters for the CO_2 layer. Each layer is described with three main parameters derived with RADEX model: the kinetic temperature, T, the column density N, and the optical depth τ. These can then be used to estimate the size of slab of CO_2.

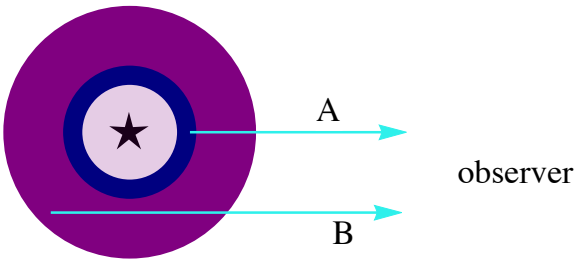

Figure 4.10: Different paths of light considered in the estimation of the emitting regions of CO_2. Ray A considers the path of a layer only slightly large than the star, while Ray B considers the path of a an extended layer.

4.4.2 Emitting Region

Estimating the emitting region of the CO_2 gas will provide insight into the atmospheric structure in the M-types. Previous studies like Cami et al. (2000) built in the emitting region as one of the parameters in their radiative transfer calculations where they solved for flux density directly. RADEX calculates a flux that we must convert to flux density (F_ν, Jy) to fit our spectra, and does not include the size of the slab in the calculations. We devised a way to estimate the size of the emitting region of CO_2, R_{CO_2}, using results from RADEX in conjunction with the flux density values from the observed lines. Here, we derive the two expressions used in these estimates.

We place layers of gas above the star. The first absorbing layer is only slightly larger than the star, while the second layer is much more extended. The general solution to the radiative transfer equation is:

$$I_\nu = I_\nu^o \, e^{-\tau} + S_\nu (1 - e^{-\tau}).$$

For the CO_2 gas in absorption near the star, we follow path A in Figure 4.10. The initial intensity I_ν^o comes as blackbody radiation from the star and the source function is blackbody radiation from the gas.

$$I_g = B_\star \, e^{-\tau} + B_g (1 - e^{-\tau})$$

The flux density in the absorption line can be estimated by considering the difference between the gas intensity and the star's intensity.

$$\Delta I = I_g - I_\star$$

$$\Delta I = B_\star \, e^{-\tau} + B_g (1 - e^{-\tau}) - B_\star$$

$$\Delta I = -B_\star (1 - e^{-\tau}) + B_g (1 - e^{-\tau})$$

To finish backing out the flux density multiply by the solid angle on the sky.

$$\Delta F = \pi \left(\frac{R_\star}{D}\right)^2 \left[-B_\star(1-e^{-\tau}) + \left(\frac{R_{CO_2}}{R_\star}\right)^2 B_g(1-e^{-\tau})\right] \tag{4.4}$$

$$\frac{\Delta F}{\left(\frac{R_\star}{D}\right)^2 (1-e^{-\tau})} + \frac{B_\star}{B_g} = \left(\frac{R_{CO_2}}{R_\star}\right)^2 \tag{4.5}$$

For the larger emitting region we follow path B in Figure 4.10. Here there is no initial intensity from the star because $R_{CO_2} > R_\star$, that is the emitting layer is large enough that light traveling through the layer just depends on the blackbody of the gas.

$$I_g = B_g(1-e^{-\tau})$$

$$\Delta I = I_g - I_\star$$

$$\Delta I = B_g(1-e^{-\tau}) - B_\star$$

As before, multiply by the solid angle to back out the flux.

$$\Delta F_\nu = \pi \left(\frac{R_\star}{D}\right)^2 \left[-B_\star + \left(\frac{R_{CO_2}}{R_\star}\right)^2 B_g(1-e^{-\tau})\right] \tag{4.6}$$

$$\frac{\Delta F}{\left(\frac{R_\star}{D}\right)^2 (1-e^{-\tau})} + \frac{B_\star}{B_g(1-e^{-\tau})} = \left(\frac{R_{CO_2}}{R_\star}\right)^2 \tag{4.7}$$

We used Equations 4.5 and 4.7 to estimate the R_{CO_2} for all the lines seen in the M-type Miras. Equation 4.5 was used for absorption lines and Equation 4.7 for emission lines. We find ΔF by considering the difference from the peak of the desired line to the continuum. The distances, D, to the stars used in the calculations are presented in Table 2.4, the stellar radii are calculated using infrared interferometric data presented in Table 2.2, the stars' blackbody temperatures are determined using the blackbody subtraction discussed in Section 4.1.1, and RADEX calculates the optical depth, τ and the temperature of the gas. Previous CO_2 models indicate that CO_2 can be quite extended in Mira atmospheres ranging from $\sim$2-10 $R_\star$ (see Table 6.1) and our results presented in Table 6.3 confirm this.

4.5 RADEX Parameters

RADEX's input parameters include kinetic temperature, collision partner species, collision partner density, column density, background radiation temperature, and linewidth. We performed all our calculations with H_2 as the colliding partner (see Section 5.4.0.1). We performed test calculations with H_2 densities ranging from 10^{10}-10^{12} cm^{-3} based on the density profile presented in Reid & Menten (1997). Models calculated with an H_2 density of 10^{10} cm^{-3} did not adequately reproduce the ν_2 absorption feature. We noticed no significant differences in the models calculated using 10^{11} cm^{-3} vs 10^{12} cm^{-3}; we therefore set the H_2 density at 10^{12} cm^{-3} for all calculations, because Reid & Menten (1997) reported this as the gas density near the molecular photosphere in AGB stars. The linewidth includes thermal and turbulent effects and was assumed to be the same for all calculations. We set the width to 1 km s^{-1} for all calculations since we do not expect significant Doppler or turbulence broadening in the lines because the stellar wind is $\sim$10 km s^{-1} and the shocks range from 10-40 km s^{-1}.

4.5.1 Kinetic Temperature

The kinetic temperature of the CO_2 gas greatly influences line shapes. When the temperature increases, higher rotational levels within the band can become more populated and transitions from these higher levels cause the Q-branches to effectively broaden. The line centers for the 14.98 μm line will shift toward shorter wavelengths at higher temperatures while the line centers for the 13.49 μm, 13.87 μm, 16.18 μm, and 16.76 μm shift toward longer wavelengths. This behavior is the result of additional Q-branch transitions building to the left for the 14.98 μm line and building to the right for remaining four lines (see Section 4.3.2). An example of this behavior in the ν_2 band is presented in Figure 4.11. All lines were calculated with the same column density (10^{14} cm^{-2}), background temperature (100 K), H_2 density (10^{12} cm^{-3}), and linewidth (1 km s^{-1}). As the temperature moves from 400 K to 600 K to 1000 K, the line center shifts towards shorter wavelengths. This behavior was critical in helping us constrain the temperature in the RADEX calculations.

4.5.2 Column Density

The model spectra is sensitive to the column density. Figure 4.12 demonstrates how increasingly higher column densities produce more pronounced affects in the model spectra. All four spectra in this example were calculated with the same kinetic temperature (750 K), background temperature (300 K), H_2 density (10^{12} cm^{-3}), and linewidth (1 km s^{-1}). The column density increases from 5 to 500×10^{16} cm^{-2} which significantly alters the line intensities in the corresponding spectra. An increase in column density precipitates an increase in optical depth.

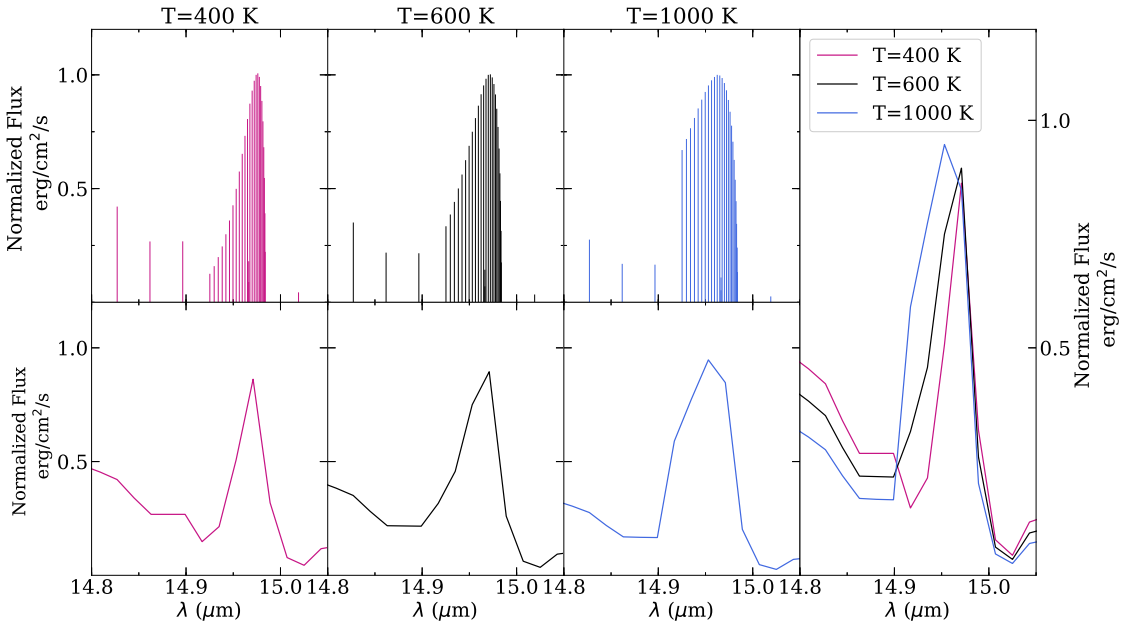

Figure 4.11: Temperature panel demonstrating how temperature affects the behavior of the 14.98 μm feature. All calculations were done at the same column density, background temperature, and linewidth. The three bands were calculated at 400 K, 600 K, and 1000 K. The bottom and right side panel are the RADEX spectra smoothed to Spitzer's IRS resolution. The temperature increase adds Q-branch transitions to the left causing the line center to shift towards shorter wavelengths (see Section 4.3.2).

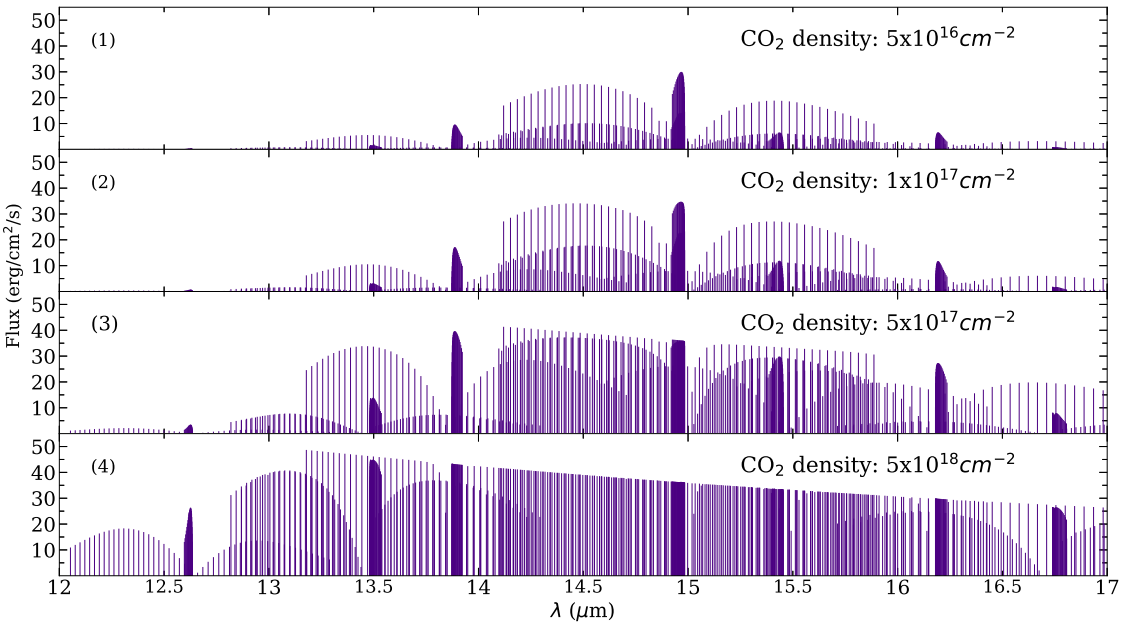

Figure 4.12: Density panel demonstrating the affects of larger column densities on line intensity. All slab spectra were calculated at the same kinetic temperature, background temperature, and linewidth. Panel (1) was calculated at density 5×10^{16} cm^{-2}, panel (2) at 1×10^{17} cm^{-2}, panel (3) at 5×10^{17} cm^{-2}, and panel (4) at 5×10^{18} cm^{-2}. Higher densities create increases in optical depth; the fundamental ν_2 band is the first line to become optically thick; as can be seen in panel (3). Eventually, the column density reaches a point where the whole spectrum flattens into a continuum as seen in panel (4).

The fundamental ν_2 band at 14.98 μm is the first line to become optically thick (see panel (3) in Figure 4.12); further increases in column density make more lines optically thick, until eventually, the spectrum flattens into a continuum-like effect (panel (4) in Figure 4.12).

4.6 Model Procedures

Now we take all the elements described in Sections 4.1.1, 4.4.1, and 4.5 and describe how we fit the M-type spectra. First, the background was subtracted. The resulting residuals were fit with initial RADEX models. To create a RADEX spectrum, we input a "guess" of good physical parameters. We took the RADEX output and converted it to flux density in Jy to directly match our observations. The RADEX spectra was then re-binned using the Python package *spectres* (Carnall 2017) to match the IRS resolution of R$\sim$ 600, which corresponded to a bin size of 0.019 μm. Re-binning the RADEX output at this resolution created prominent

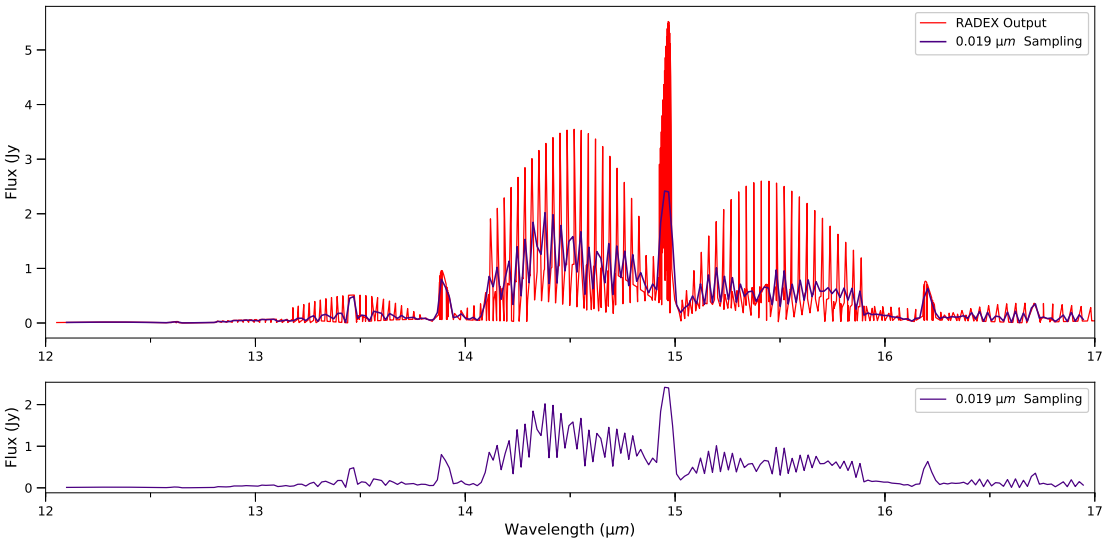

Figure 4.13: Example of RADEX output rebinned at R∼600 to match the Spitzer spectrum. The original RADEX result is shown in the top spectrum and the rebinned spectra is shown below. Notice the artificial jumps in the spectra caused by the truncation of rotational levels as discussed in Section 4.3.2.

Q-branch bandheads surrounded by a blend of weaker P and R branches as can be seen in Figure 4.13. Once we had our final output file, we fit it to the Spitzer spectrum using the Python package *Sherpa*. The fit was evaluated based upon the χ^2 results and "by-eye" fitting. This procedure was iterated through until a the line was satisfactorily fit. When calculating the fit(s) for the 13.87 μm, 14.98 μm, and 16.18 μm lines simultaneously, the fit from the emission layer was combined with the fit of the absorption layer to produce a global fit for all three lines. We built individual grids for each observation. For the 13.87 μm, 14.98 μm, and 16.18 μm lines, the temperature range was built in 50 K steps. The 13.49 μm and 16.76 μm proved fairly insensitive to temperature; their grids varied between 100-200 K, and often we just report a minimum bound for their temperature. The column density for the 13.87 μm and 16.18 μm lines was built in steps that ranged $0.05 - 0.15 \times 10^{17}$ cm^{-2}. The column density for the 13.49 μm and 16.76 μm lines was built in steps that ranged $0.1 - 0.5 \times 10^{16}$ cm^{-2}. When the 14.98 μm line was seen in absorption, the column density step size was 0.05×10^{16} cm^{-2}, but when it was in emission, the step size had a much larger range from 0.5×10^{15} - 0.5×10^{16} cm^{-2}. This wide range is because the emission ranged from extremely weak to fairly strong. The step sizes determine the uncertainties in kinetic temperature and column density reported in Table 6.3. Observations for every M-type Mira and their corresponding RADEX fits are provided in Appendix A.1.

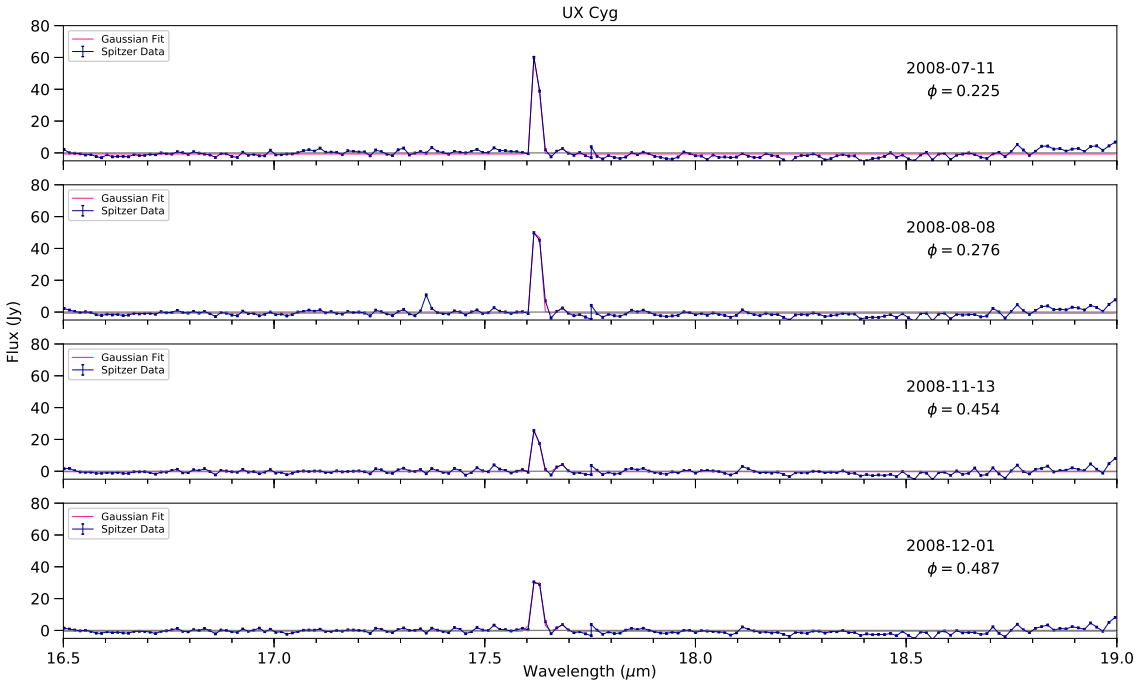

Figure 4.14: Gaussian profile fitting of the 17.62 μm feature for the M-type Mira variable UX Cyg.

4.7 17.62 μm Feature

The novel feature at 17.62 μm required a different approach than the CO_2 analysis. We have tentatively identified this feature as Fe I. For discussion on the process of how the line was identified see Section 3.5. Because of the unknown nature of the emission we first wanted to investigate if this feature fluctuated with the phase of the star. The continuum was subtracted as described in Section 4.1.2. The residuals were fit using the Python package *Sherpa*. We chose to model the lines with a Gaussian profile, because the line was extremely narrow, just slightly larger than the wavelength uncertainty of the instrument, and we do not expect large effects of collisional broadening to justify a Lorenztian profile. The profile fitting with *Sherpa* provided us with an amplitude, full-width-half-maximum (FWHM) width, and a line center. An example of the profile fitting for the M-type UX Cyg is provided in Figure 4.14. We fit this feature for all the spectral types in our sample. This allowed us to build a table to look for patterns with phase; these are included as Tables 6.4, 6.6, and 6.5 for the M-types, C-types, and S-types, respectively. Panels of the fits for every star are included in Appendix B.1.

In addition to tracking the line behavior with phase we also searched for possible fluorescence mechanisms. This involved searching for Fe I transitions

that share the same quantum state as the upper state of the 17.62 μm line, that are also adjacent to strong emission lines. There are several classic examples of Fe I fluorescing in the atmospheres of late-type stars, including Fe I lines at 4202$\AA$ and 4308 $\AA$ fluoresced by the Mg II, *k* line (Willson 1972), and Fe I lines at 2823.3 $\AA$, 2844.0 $\AA$, and 2355.9 also by the Mg II, *k* line (Carpenter et al. 2013). The *Atomic Line List* was consulted for Fe I transitions that shared the same upper level energy as the 17.62 μm feature. The task was then to find a coincident bright emission feature near one (or more) of the transitions on this list. We first checked for bright lines in our spectra that could serve as the pump, but none were identified. We then turned to the bright emission lines reported in the literature and to Charlotte Moore's UV tabel Moore (1950). We have compiled a list of pumps that overlap with an Fe I transition that shares the same upper state (7F, J = 3) as our 17.62 μm line. This list includes: Al II (UVI) at at 2669 $\AA$, Fe II (UV60) at 2933 $\AA$, Fe II (UV60) at 2940 $\AA$, Fe I (UV120) 2950 $\AA$, Fe I (UV134) at 2996 $\AA$, K I at 2942 $\AA$, and Ti I (UV1) at 2933 $\AA$. These possibilities are summarized in Figure 6.1 presented in Chapter 6.

"The reward of the young scientist is the emotional thrill of being the first person in the history of the world to see something or to understand something. Nothing can compare with that experience. The reward of the old scientist is the sense of having seen a vague sketch grow into a masterly landscape."'

— Cecilia Payne-Gaposchkin

Chapter 5

MID-IR SPECTRA OF THE M-TYPE MIRA VARIABLE R TRI OBSERVED WITH THE SPITZER IRS

In this chapter we present the publication of the analysis for the M-type Mira variable *R Tri* (Baylis-Aguirre et al. 2020). The article was originally published in the *Monthly Notices of the Royal Astronomical Society*; permission for use in this dissertation is found in Appendix C.

Abstract

We present analysis of mid-IR spectra of the oxygen-rich Mira variable R Tri. The data were taken with the Spitzer Infrared Spectrometer (IRS) as part of a study tracking how Mira variables' regular pulsations affect circumstellar envelopes. We detected strong emission lines at 13.87 μm, 16.18 μm, and 17.6 μm, and one strong absorption feature at 14.98 μm. The emission features at 13.87 μm and 16.18 μm are excited vibrational bands of CO_2, while the absorption feature is the fundamental ν_2 band. The 17.6 μm emission feature has a completely different character than the molecular lines and we report its identification as Fe I fluorescence. We used a 2-slab model with the radiative transfer code RADEX to model the CO_2 Q-branch bandheads. Our results indicate a slab of gas with T$\sim$600 K

located at ∼3-4 R_*. The cool temperature discrepancy with the radius provides observational evidence for the previously theoretical "refrigeration zone".

Keywords

stars: Mira Variables — stars: variable — stars: atmospheres — stars: circumstellar matter — stars: late-type — astrochemistry — line: formation

5.1 Introduction

5.1.1 Background and Motivation

A fundamental topic in stellar physics is how stars create molecules and dust and return them back to the interstellar medium (ISM). Understanding this process affects many facets across astrophysics from star and planet formation to galaxy evolution. Molecules and dust contribute significantly to circumstellar environments, but our understanding of their creation is, at best, still rudimentary. We know a large fraction of material returned to the ISM is preferentially formed at the latest stages of stellar evolution (i.e. red giants, AGB stars, and supernovae), and that mass loss is a requisite activity throughout stellar evolution (Romano et al. 2010).

Asymptotic Giant Branch (AGB) stars are low-to-intermediate mass ($0.8 - 8M_\odot$) stars in the final stages of their evolution. They are characterized by hydrogen and helium shell burning on top of a degenerate carbon and oxygen core. Mira variables are AGB stars that pulsate regularly (periods of 100-500 days) with their visual amplitudes varying by up to several magnitudes. Miras variables have three chemical subclasses: oxygen rich, C/O <1 (M-type), carbon rich, C/O >1 (C-type), and intermediate, C/O ∼ 1 (S-type). The cool temperatures (2500-3500 K) of their photopsheres allow for the creation of molecules and dust in the atmosphere and the pulsations help loft this material into the surrounding environment. These conditions make Mira atmospheres perfect laboratories for studying how evolved stars enrich the ISM.

Near and mid-infrared spectroscopy provide the best opportunities for studying extended atmospheres surrounding Mira variables. Space-borne observations allow a study of wavelengths that are impossible to view with ground-based instruments due to telluric absorption. In the late 90's and early 2000's the Infrared Space Observatory (ISO) (Kessler et al. 1996) made several crucial discoveries about molecules in Mira atmospheres. Yamamura et al. (1999b) reported the discovery of ro-vibrational band of SO_2 at 7.3 μm in 3 M-type Miras, which had previously only been observed in the millimeter (Lucas et al. 1986; Omont et al. 1993). T Cep had SO_2 bands that showed time variation moving from emission to absorption, but unfortunately the ISO observations only caught

1.4 periods and it was not determined if this was periodic behavior or a transient event. Justtanont et al. (1998) and Ryde et al. (1998) independently reported the discovery of several ro-vibrational bands of CO_2 between 13 and 17 μm in several oxygen-rich AGB stars. The ν_2 fundamental band (bending mode) was sometimes observed in absorption while the excited bands were always seen in emission, but the variability could not be tied to the pulsation cycle. Justtanont et al. (1998) also noted that for AGB stars that exhibited the 13 μm dust feature the strength of this feature appeared to be correlated to the strength of the CO_2 emission features. Yamamura et al. (1999a) reported ro-vibrational bands of H_2O between 2.4 and 4 μm with variability that seemed to follow the pulsation cycle. These ISO observations clearly demonstrate that molecular layers surrounding Mira variables are dynamic, but more observations are required to understand what drives the observed variability.

The discovery of CO_2 in oxygen rich sources is particularly interesting because until the ISO observations it was believed that the majority of the carbon was locked in CO molecules. Most contemporary models assumed thermal equilibrium in AGB and Mira atmospheres, and did not take into account how pulsation driven shock waves could affect circumstellar chemistry. Duari et al. (1999) suggested that the CO_2 forms in a region close to the photosphere of the star under non-equilibrium conditions created by shocks. To test this idea they created a model for the inner wind that experienced periodic shock waves from stellar pulsation and examined the chemistry in the cooling layers left behind in the post-shock region. The calculated abundances indicated that CO_2 was a product of shock chemistry after CO molecules were destroyed by OH radicals. Cherchneff (2006) used this wind model for the oxygen rich Mira TX Cam and reported consistent CO_2 abundances. The model also showed CO_2 is a good candidate for discriminating between M-type and C-type Mira variables because CO_2 stops forming in regions >1 R_* for C-types due to a lack of OH molecules. The authors point out that time-resolved observations are needed to provide additional insight crucial to understanding how the periodic shocks affect the chemistry.

In this paper we present analysis of mid-IR observations of the M-type Mira variable R Tri taken with the Spitzer Infrared Spectrometer (IRS) (Houck et al. 2004). These observations are part of an observing campaign of 25 Mira variables designed to study phase dependent behavior in their circumstellar environment (Creech-Eakman et al. 2012). This study provides the first opportunity since ISO to investigate Mira atmospheres in a wavelength range not permissible for ground-based instruments, and it provides an opportunity to study time-dependent behavior of spectral lines as suggested by previous studies (e.g. Yamamura (2003); Cherchneff (2006)). For data reduction see Section 5.2.2.1, and for resulting spectra see Section 5.3. The Spitzer observations were done in conjunction with a decade long study of AGB stars using the Palomar Testbed Interferometer (PTI) (Creech-Eakman & Thompson 2009). Combining results from these two observational studies provides us with an unprecedented detail of the molecule and dust forming region in R Tri's atmosphere.

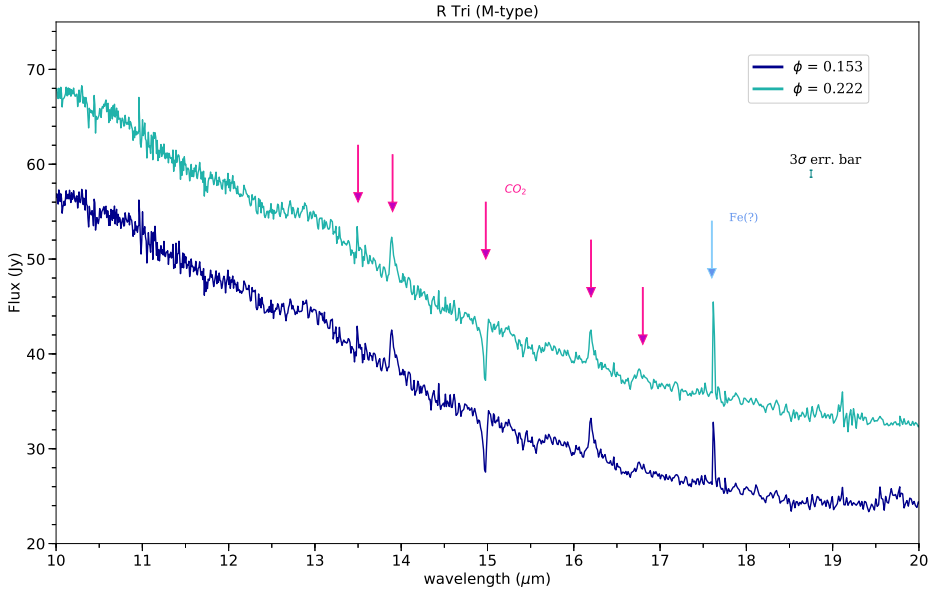

Figure 5.1: Spitzer IRS high resolution (R ∼600) spectra of the M-type Mira variable R Tri. The top spectrum has been artificially offset upward 8 Jy for clarity.

5.2 Observational Data

5.2.1 R Tri

This paper focuses on the oxygen-rich Mira variable R Tri, which has a fairly short period of 266 days and ranges from spectral type M3.5 to M8 over the pulsation cycle. Originally classified as "featureless" in the 8-21 μm region in the IRAS Low Resolution Spectrometer catalog (Olnon et al. 1986) R Tri was later determined to have modest silicate and dust emission by Sloan & Price (1998) and classified as an "SE3". Benson et al. (1990) detected both H_2O and SiO masers, and Jura (1994) determined a mass loss rate of 1.1×10^{-7} $M_\odot$ yr^{-1}. Using the results from the improved Hipparcos data reduction (van Leeuwen 2007) we estimate its distance at 294 pc.

5.2.2 Spitzer Observations

The observations presented in this paper are part of a larger study done with the Spitzer Space Telescope's IRS (Houck et al. 2004) to characterize circumstellar environments surrounding Mira variables (Creech-Eakman et al. 2012). The data were acquired during Spitzer GO program 50717 during 2008-09; for data reduction see Section 5.2.2.1. This study provides an opportunity to address questions previously raised by ISO observations about the dynamics of Mira atmospheres in a wavelength regime that is inaccessible from the ground. The stars included in

this study were chosen based on two conditions: 1) multiple observations were possible during Spitzer Cycle 5, and 2) the stars were bright enough to obtain high SNR spectra, but not so bright as to saturate the detector. This high stellar flux required defringing algorithms in the data reduction therefore each star in the sample has a dedicated background. A "typical" period for a Mira variable is roughly one year so observations were made approximately every month for a sampling rate of $\sim$0.1 of a pulsation phase. In the case of R Tri two observations were obtained on 2008-09-07 and 2008-10-02, and resulted in two spectra at phases $\phi = 0.153$ and $\phi = 0.222$, respectively (see Figure 5.1).

5.2.2.1 Data Reduction

Each spectrum in our dataset was reduced individually by hand. This data reduction process is fully described in Creech-Eakman et al. (2012). First, a sky subtracted stellar spectral image was created by subtracting a dedicated background spectral image from the stellar spectral image. The Spitzer IDL package IRSCLEAN[1] was used to remove rogue/bad pixels including bad pixels found by hand in each spectra in addition to those automatically flagged by the program. The "Spitzer IRS Custom Extractor" (SPICE)[2] tool was used to extract the stellar spectral orders from the spectral images by assuming an extraction of a point source. The SPICE package used calibration data from the observations which was specific to the orbits and our GO program, along with the bad pixel masks to extract and calibrate the flux from the IRS spectra. Because all of our stars were bright, fringes created internally from the spacecraft could have polluted the observations. To account for this possibility the Spitzer IRSFRINGE[3] tool was used to "defringe" each spectrum. The individual spectral orders were sewn together into one complete high-resolution (R$\sim$600) spectrum, combining individual nods of each module to create the final spectrum. Figure 5.1 shows the resulting spectra for R Tri.

[1] `https://irsa.ipac.caltech.edu/data/SPITZER/docs/dataanalysistools/tools/irsclean/`

[2] `https://irsa.ipac.caltech.edu/data/SPITZER/docs/dataanalysistools/tools/spice/`

[3] `https://irsa.ipac.caltech.edu/data/SPITZER/docs/dataanalysistools/tools/irsfringe/`

5.3 Spectra

5.3.1 Line Identification

5.3.1.1 Molecular Features

The spectra in Figure 5.1 show two strong emission features at 13.87 μm and 16.18 μm, a strong absorption feature at 14.98 μm, and two weaker emission features at 13.49 μm and 16.78 μm. We have identified these features as unresolved rovibrational Q-branch bands of $^{12}CO_2$; the absorption feature at 14.98 μm is due to the fundamental ν_2 mode, while the emission lines are created by excited states (Herzberg 1945; Gordon et al. 2017). An energy level diagram for CO_2 including the observed transitions are given in Figure 5.2. The continuum between Q-branches is dominated by a plethora of much weaker P and R transitions. Strong Q-branch lines of $^{12}CO_2$ were first observed in AGB stars with ISO by Justtanont et al. (1998) and Ryde et al. (1998).

5.3.1.2 Atomic Features

There is a bright emission feature centered at 17.6 μm seen in both phases and the narrowness of the line indicates that it is an atomic feature. We have consulted the Atomic Line List (van Hoof 2018) for identification and have preliminary identified this feature as Fe I fluorescence based on the available oscillator strengths and the strength of the emission. Fe fluorescence is commonly observed at other wavelengths in Mira atmospheres (Willson 1972; Luttermoser 1996, 2000). Further analysis of this feature will be presented in a later paper.

5.4 RADEX

We have chosen to model the CO_2 Q-branch bandheads using the radiative transfer code, RADEX (van der Tak et al. 2007) which is available as part of the Leiden Atomic and Molecular Database (LAMDA) (Schöier et al. 2005). We chose this this code for several reasons. First, it solves the radiative transfer using the Sobolev's approximation for expanding stellar envelopes (Sobolev 1960) an approach recommended strongly in Hubeny & Mihalas (2014) for stars with dynamic atmospheres such as Miras. Second, the code works under NLTE conditions, and this capability is vital because *a priori* we do not know if the CO_2 lines are formed under equilibrium conditions. Previous work done by Cherchneff (2006) and Duari et al. (1999) indicate the CO_2 gas must be created with dis-equilibrium conditions. Third, RADEX provides a step up in model sophistication because it includes collisional affects where older models only required spectroscopic and dipole moment data for radiative transfer calculations. Most

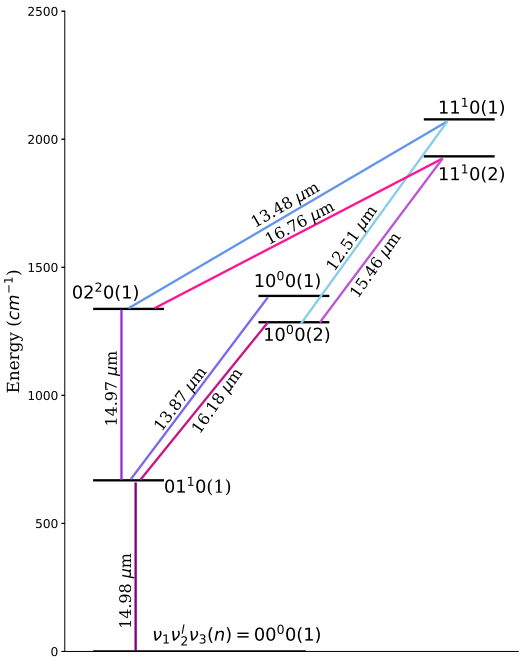

Figure 5.2: Vibrational energy diagram of CO_2 transitions included in RADEX model. The vibrational levels and Fermi split levels are labeled according to HITRAN's notation. The colors of the transitions match the bands calculated with RADEX that are shown in Figure 5.3.

previous models fit lines separately, but RADEX calculates the radiative transfer for all lines included in the desired wavelength range. This allows us to fit multiple lines simultaneously which provides stronger constraints on the physical conditions creating the features. RADEX also provides flexibility by allowing the user to upload original molecular files for the calculations. We have created a custom molecular file for CO_2 that allows us to calculate the ro-vibrational transitions in Figure 5.2 from 10-20 μm (for file details see Sections 5.4.0.1 and 5.4.0.2 below). A sample slab spectrum is presented in Figure 5.3.

5.4.0.1 Molecular File

RADEX data files require detailed level energies, Einstein coefficients, and rate coefficients for collisional de-excitation for state-to-state transitions. There are data files of many molecules ready for modeling on the Leiden Atomic and Molecular Database (LAMDA) (Schöier et al. 2005), but most of these files are created for pure rotational transitions at longer wavelengths. We built a a custom data file for ro-vibrational transitions of CO_2 going up to J=50, in the 10-20 μm range which includes over 700 radiative transitions and more than 18,000 collisional interactions with H_2 as the colliding partner. An energy level diagram of the CO_2 bands included in our file is presented in Figure 5.2. Einstein A coefficients, and

transition frequencies for CO_2 were taken from the HITRAN database (Gordon et al. 2017). Of the seven collision partners provided in the RADEX code (H_2, p-H_2, o-H_2, e^-, atomic H, He, and H^+) we have chosen H_2 as the colliding partner in all our calculations for two reasons: 1) H_2 is a dominant molecule in Mira atmospheres (Duari et al. 1999), 2) most of the published laboratory data required to calculate the collisional rate coefficients were derived from experiments with H_2 collisions. Circumstellar environments surrounding Miras vary between several hundred and several thousand Kelvin. The collisional rate coefficients depend on temperature, thus, to account for the wide range of temperatures needed in Mira atmospheres we have used the results of CO_2 colliding with H_2 from Nevdakh et al. (2003) to extrapolate the temperature dependence of the 01^10-0^00 vibrational rate for temperatures up to 1000K. This temperature dependence was then applied to the remaining vibrational bands included in the file to create collisional rate coefficients for temperatures ranging from 100-1000 K in 50 K steps.

5.4.0.2 Collisional Rate Coefficients

As with Bosman et al. (2017), we found no evidence of pure rotational transitions caused by CO_2 colliding with other species in the literature. To preserve ro-vibrational behavior for our calculations we used ro-vibrational data of CO colliding with H_2 taken from Castro et al. (2017) which included transitions up to J=30. For the remaining transitions, J=31 to J=50 were calculated using rotational data of CO colliding with H_2 taken from the LAMDA database. Rates for J=31-40 were taken from (Yang et al. 2010) while rates for J=41 to J=50 were taken from the highydrogen-J extrapolation file (Neufeld 2012). To calculate full state-to-state transitions we followed methods similar to those presented in Bosman et al. (2017); Bruderer et al. (2015); Faure & Josselin (2008); Chandra & Sharma (2001). Vibrational rates were combined with rotational rates to create full ro-vibrational rate coefficients. Rate coefficients between vibrational levels were taken from Table A.1 in Bosman et al. (2017) or were calculated according to the relationship derived in Chandra & Sharma (2001) for $\nu > \nu'$:

$$k(\nu \rightarrow \nu') = \nu \frac{2\nu' + 1}{2\nu + 1} k(\nu = 1 \rightarrow \nu' = 0). \tag{5.1}$$

To calculate the full ro-vibration collisional rates from initial state ν, J to final state ν', J' we used the method suggested in Bosman et al. (2017) and Faure & Josselin (2008) to assume the vibrational levels can be decoupled from the rotational levels, that is, the rotational levels can be used to calculate a proportionality constant, $P_{J,J'}(T)$, that acts as a scaling factor on the vibrational rates:

$$k(\nu, J \rightarrow \nu', J') = P_{J,J'}(T) k(\nu \rightarrow \nu') \tag{5.2}$$

$$P_{J,J'}(T) = \frac{k(1, J \rightarrow 0, J') \Sigma_J g_J \exp(-E_{\nu,J}/kT)}{\Sigma_J (g_J \exp(-E_{\nu,J}/kT) \Sigma_{J'} k(1, J \rightarrow 0, J'; T))}. \tag{5.3}$$

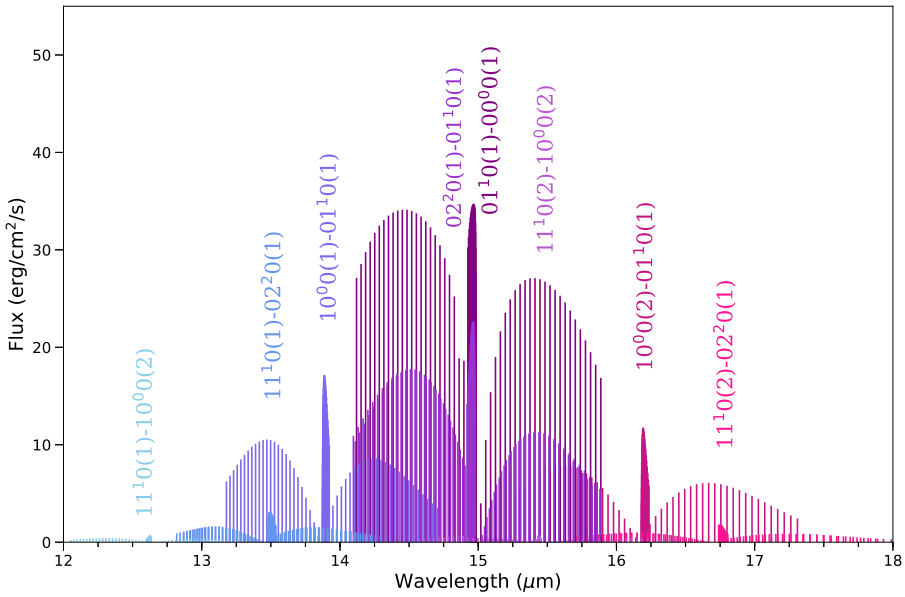

Figure 5.3: Sample slab spectrum of CO_2 calculated with RADEX. The colors of the bands match corresponding transitions shown in the energy level diagram in Figure 5.2. Note the Q-branches build to the left or right according to the discussion in Section 5.5.0.1.

Our proportionality equation differs slightly from the original expressions because we are not assuming the full rates are proportional to the rotational transitions inside the ground vibrational state as was done previously (e.g. Bosman et al. (2017); Bruderer et al. (2015)). Instead, we assume the rates are proportional to rotational transitions from the $\nu = 1 \rightarrow \nu' = 0$ state in an effort to preserve as much ro-vibrational behavior as possible for our model calculations. A sample slab spectrum calculated with RADEX is presented in Figure 4.7 with model parameters: kinetic temperature = 750 K, H_2 density = 10^{12} cm^{-3}, CO_2 column density = 10^{16} cm^{-2}, background temperature = 300 K, linewidth = 1 km s^{-1}. This spectrum reproduces consistent behavior to the one calculated in Bosman et al. (2017) which uses similar parameters.

5.5 CO_2 Molecule

CO_2 is a fully symmetric linear molecule without a permanent dipole moment. It has four vibrational modes: a symmetric stretching mode (ν_1) at 1337 cm^{-1} , a doubly degenerate bending mode (ν_2) at 667 cm^{-1}, and an anti-symmetric stretching mode (ν_3), at 2349 cm^{-1}. A vibrational state is then written as $\nu_1\nu_2^l\nu_3$, where l denotes angular momentum. The symmetric stretch is IR inactive be-

cause of CO_2's lack of a permanent dipole moment. Coincidentally $\nu_1 \approx 2\nu_2$ and this accidental degeneracy allows for the eigenstates of $2\nu_2$ to perturb the eigenstates of ν_1, if they have identical angular momentum (Herzberg 1945). The vibrational states that have the same value of $2\nu_2 + \nu_1$ mix to the point that we can no longer unambiguously separate the individual levels. This mixing creates two vibrational levels that have slightly different energies in a phenomena called Fermi splitting. For example, the vibrational level $\nu_1\nu_2\nu_3 = 020$ has sub-levels 02^00 and 02^20 for $l = 0$ and $l = 2$ respectively. Only 02^00 can perturb and mix with the 10^00 level (both have $l = 0$) and vice versa , which creates two vibrational levels with distinct energies (Herzberg 1945). To account for Fermi splitting the vibrational state notation becomes $\nu_1\nu_2^l\nu_3(n)$; the Fermi levels created by the mixing of the 02^00 and the 10^00 states are then labeled as $10^00(1)$ and $10^00(2)$ following HITRAN's convention that ν_1 in Fermi split levels is determined by the state with the largest symmetric stretch quantum number. A vibrational level energy diagram for transitions included in our model is given in Figure 5.2. The colors of the transitions match the corresponding bands shown in Figure 5.3.

5.5.0.1 Ro-vibrational Transitions

The structure of CO_2 emission is governed by transitions between the rotational ladders inside each vibrational level. Selection rules govern which transitions are permitted. Parallel bands obey $\Delta J = \pm 1$ and create P and R branches only. Perpendicular bands obey $\Delta J = 0$, $\Delta J = \pm 1$ creating a strong Q-branch in addition to the P and R branches. The P and R branches from adjacent bands overlap and blend together affecting the continuum. We are only modelling the macroscopic behavior of the three strong CO_2 Q-branches at 13.87 μm, 14.98 μm and 16.18 μm because we do not have the resolution to properly model all the nuances created with the P, R transitions blending together. The Q-lines build to the left or the right depending on whether the rotational constant is larger in the upper state or the lower state (Ryde et al. 1998). Hence, the Q-transitions build to the left for the 14.98 μm line, but build to the right for the 13.87 and 16.18 μm lines. This trend is reflected in the slab spectrum produced using RADEX in Figure 5.3.

5.6 Model

5.6.1 Slab Model

We have chosen a slab model approach because although RADEX provides the expanding sphere as an option for the escape probability calculation this option does not include contributions from stellar winds or shocks. RADEX does provide a step up in sophistication from previous slab models for CO_2 which were not calculated in NLTE nor included collisions. We have adopted 2-slabs for modelling the CO_2 lines. The radiative transfer in each slab is calculated using

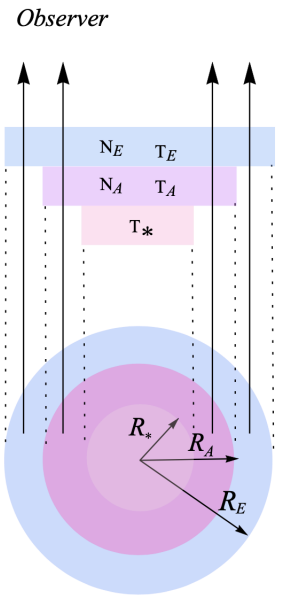

Figure 5.4: Conceptual two layer slab model with an emitting layer sitting above an absorbing layer (not to scale). The layers are described by column density and kinetic temperature, which are calculated from RADEX models.

RADEX and then the results are added to create a global fit all for all three features, rather than fitting each line individually. Ryde et al. (1998) suggest a multi-slab approach because the temperature structure needed to produce absorption at 14.98 μm in conjunction with satellite emission lines at 13.87 μm, 16.18 μm etc., requires a warm dense layer within several stellar radii in addition to an extended slightly cooler layer. Our model is focused on using the Q-branch bands to derive basic physical parameters for the CO_2 layers. We assume two adjacent uniform plane-parallel CO_2 layers superimposed on the stellar background source, as seen in Figure 5.4. If the first slab is roughly the same size as the star it creates an absorbing layer (except when $T > T_*$) while the second layer is more extended and creates an emitting layer. The layers are described with two main parameters derived from the RADEX results, T_A and T_E; the kinetic temperatures of the absorbing and emitting layers, and N_A and N_E; the column densities of the absorbing and emitting layers. These are then used along with the optical depth calculated by RADEX to estimate the size of the slab of CO_2 gas as a function of R_*.

5.6.2 Stellar Parameters

A simple blackbody did not fit the continuum well in the region of interest, most likely due to extra contribution from circumstellar dust species (Güth 2017). We therefore approximated the stellar background with a graybody continuum com-

prised of the sum of a blackbody function and a power law. The derived background temperatures for the first and second observations of R Tri are 2232 K and 2462 K, respectively. The angular size of R Tri was determined to be 5.22 $\pm$ 0.30 mas using optical interferometric measurements taken with the Palomar Testbed Interferometer (Thompson et al. 2002a). Using this result with parallax data from Hipparcos (van Leeuwen 2007) we calculate the resulting stellar radius for R Tri to be 165 $R_\odot$ $\pm$ 10 $R_\odot$.

5.6.3 RADEX Parameters

RADEX requires several input parameters including, kinetic temperature, collision partner species, collision partner density, column density, background radiation temperature, and linewidth. We tested a range of H_2 densities from 10^{10}-10^{12} cm^{-3} based on the density profile presented in Reid & Menten (1997). We found that a density of 10^{10} cm^{-3} did not adequately reproduce the ν_2 absorption feature. There was not a significant difference in the calculation results between using a density of 10^{11} cm^{-3} and 10^{12} cm^{-3}, therefore we set the H_2 density at 10^{12} cm^{-3} for all calculations because this is the gas density reported in Reid & Menten (1997) near the molecular photosphere in AGB stars. The linewidth is assumed to be the same for all transitions included in the calculation and includes thermal and turbulent effects. We set the linewidth to 1 km s^{-1} for all calculations because the winds in Mira atmospheres are on the order of one to tens of km s^{-1} which will not create significant Doppler or turbulence broadening of the lines.

5.6.3.1 Kinetic Temperature

The temperature of the CO_2 gas plays a vital role in determining line behavior. As the temperature increases higher rotational levels within a band become more populated causing the Q-branches to effectively broaden. This temperature dependence will shift the line center either right or left, depending on if additional Q-branch transitions build to the left or right (see Section 5.5.0.1). This can be seen in Figure 5.5 for the fundamental ν_2 band at 14.98 μm. All lines were calculated with the same column density (10^{14} cm^{-2}), background temperature (100 K), H_2 density (10^{12} cm^{-3}), and linewidth (1 km s^{-1}). As the temperature increases additional Q-branch transitions broaden the line and shift the band center towards shorter wavelengths. Using this behavior allows us to constrain the temperature in fits from RADEX.

5.6.3.2 Column Density

The CO_2 column density also greatly affects the model spectra. Figure 5.6 demonstrates how increasing the column density affects the calculated spectra. All three spectra were calculated using the same kinetic temperature (750 K), background

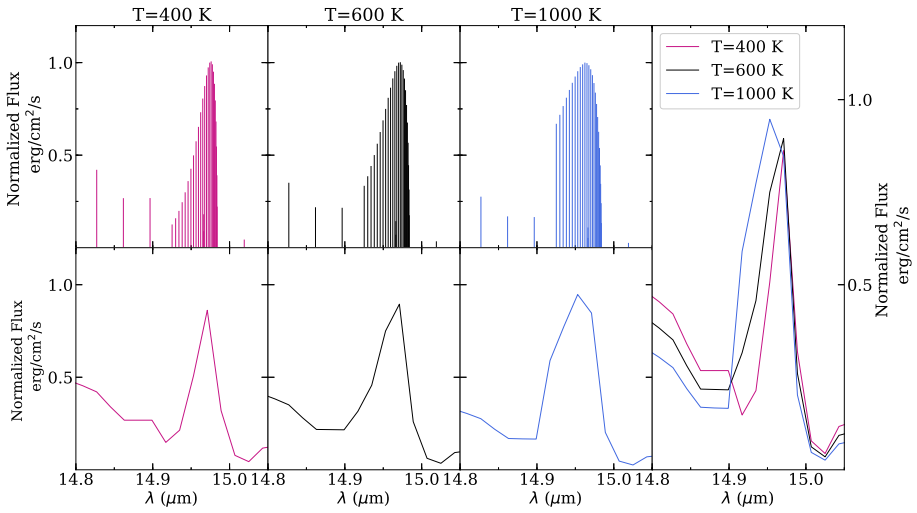

Figure 5.5: Temperature panel to demonstrate how temperature affects the behavior of the 14.98 μm feature. Each calculation was done at the same column density, background temperature, and linewidth. Bands were calculated at 400 K, 600 K, and 1000 K. The bottom and right side panels are the RADEX spectra smoothed to Spitzer's IRS resolution. The temperature increase adds Q-branch transitions to the left causing the line center to shift towards shorter wavelengths.

temperature (300 K), H_2 density (10^{12} cm^{-3}), and linewidth (1 km s^{-1}). As the column density increases from 5 to 500$\times 10^{16}$ cm^{-2} the resulting spectra show excited bands beginning to contribute and increasing line intensity. Increasing the column density also increases the optical depth and allows higher rotational levels to become populated. This causes line intensity to increase and the additional transitions also cause the lines to broaden. The first line to become optically thick is the fundamental ν_2 band at 14.98 μm (panel (3) in Figure 5.6); increasing the column density past this point causes the spectrum to flatten into a continuum-like effect (panel (4) in Figure 5.6).

5.7 Results

The RADEX spectra calculated for the two R Tri observations are presented in Figures 5.7 and 5.8. The models targeted the ν_2 bending mode at 14.98 μm and the two excited bands at 13.87 and 16.18 μm. The strong absorption at 14.98 μm is not well reproduced from one single slab of CO_2; it requires contributions from both the absorbing layer close to the star and a surrounding emitting layer (see Figure 4.9). The grid for the absorbing layer was built in 50 K steps in T_A and 0.05 $\times$ 10^{16} cm^{-2} steps in N_A, and the grid for the emitting layer had 50 K steps in T_E and 0.5 $\times$ 10^{17} cm^{-2} steps in N_E. These step sizes determine the

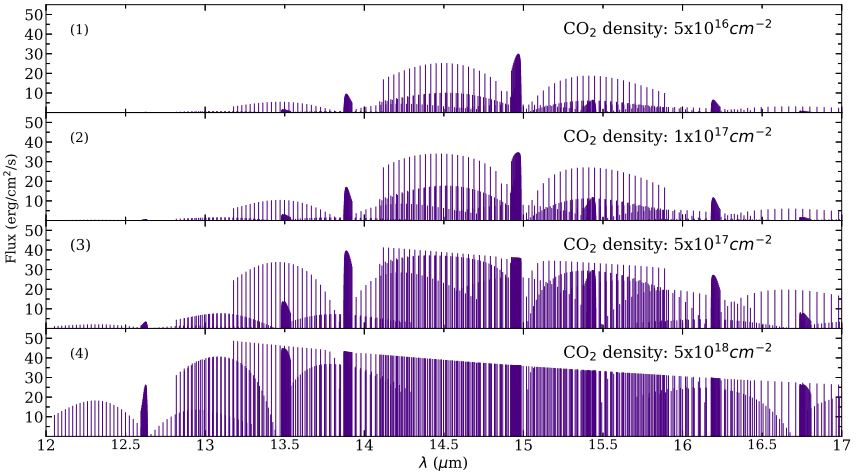

Figure 5.6: Density panel to demonstrate how the column density of CO_2 changes the intensity of the lines. All slab spectra were calculated at the same kinetic temperature, background temperature, and linewidth. Panel (1) was calculated at density 5×10^{16} cm^{-2}, panel (2) at 1×10^{17} cm^{-2}, panel (3) at 5×10^{17} cm^{-2}, and panel (4) at 5×10^{18} cm^{-2}. The optical depth increases with the density; the fundamental ν_2 band is the first line to become optically thick, this can be seen in panel (3). Eventually, the column density reaches a point where the whole spectrum flattens into a continuum as seen in panel (4).

uncertainties in temperature and column density. The step size for N_E is larger than N_A because the emission lines have greater optical depth and are thus higher up their respective curve of growth, making them less sensitive to changes in density. The fits were evaluated with eye-fitting and a χ^2 test. The slab model results and their uncertainties are presented in Tables 5.1 and 5.2. The results are almost identical because the star is in almost the same pulsational phase in both observations. The absorbing layer has $T_{kin} = 550$ K, $N_A = 2.25 - 2.4 \times 10^{16}$ cm^{-2}, and $\tau \approx 0.9$, while the emitting layer has $T_{kin} = 600$ K, $N_E = 4.5 - 5.0 \times 10^{17}$ cm^{-2}, and $\tau \approx 1.8$. Using the the RADEX parameters from both layers combined with the stellar size, we estimate the radius of the of the slabs to be R$\sim 3 - 4R_*$.

5.8 Discussion

The CO_2 Q-branch bandheads at 13.87 μm, 14.98 μm, and 16.18 μm seen in Figures 6.1.1 and 6.1.1 are well reproduced by the RADEX slab spectra. The regions between the Q-branches are dominated by P and R transitions blending together to create a forest of lines; it is impossible to distinguish individual P and R bands at Spitzer's resolution and thus no attempt was made to reproduce their behavior in this work. The two absorption features at 15.3 μm and 15.6 μm are likely

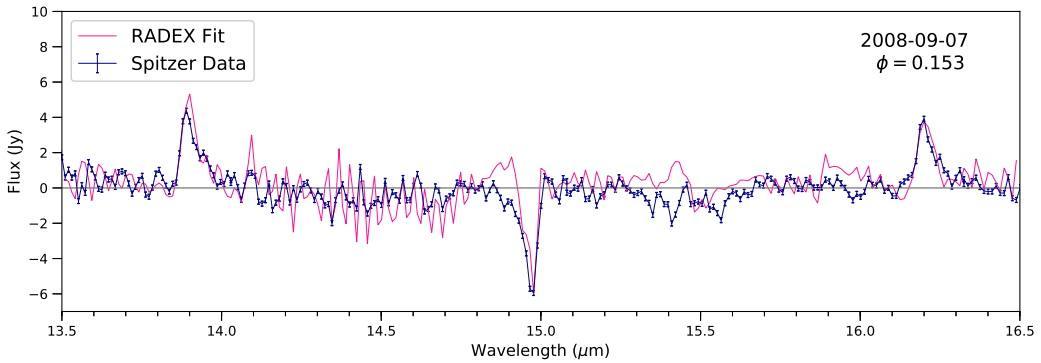

Figure 5.7: Result from 2 layer slab model calculation performed with RADEX for R Tri.

Table 5.1: RADEX slab spectrum model results for R Tri 2008-09-07. The 2 layer slab model has a cooler, denser absorbing layer close to the star with a warmer less dense layer laying above it. The optical depth for the emitting contribution is taken as the average of the optical depths of the 13.87 and 16.18 μm bands.

RADEX Results R Tri 2008-09-07					
λ μm		T_{kin}(K)	N (cm^{-2})	T_{exc}	τ
14.98		550 ± 50	$2.25\times10^{16} \pm 0.05\times 10^{16}$	607^{+46}_{-49}	$0.850^{+0.04}_{-0.02}$
13.87		600 ± 50	$5.0\times10^{17} \pm 0.5\times 10^{16}$	597^{+49}_{-50}	$1.91^{+0.19}_{-0.19}$
16.18		600 ± 50	$5.0\times10^{17} \pm 0.5\times 10^{16}$	597^{+49}_{-50}	$1.87^{+0.19}_{-0.18}$

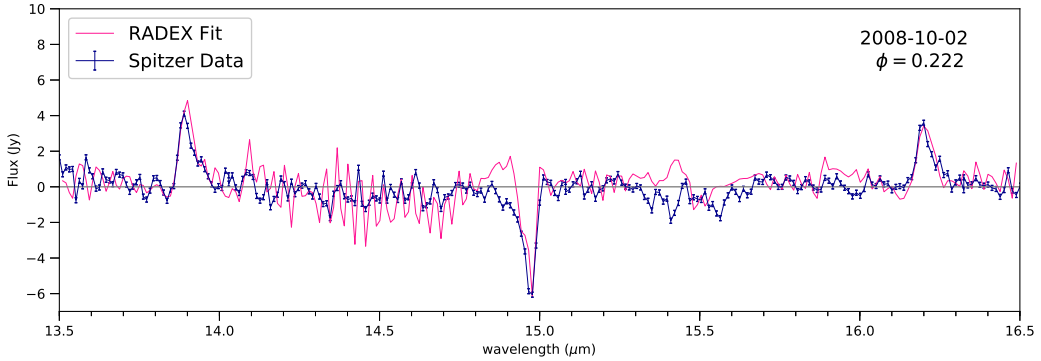

Figure 5.8: Result from 2 layer slab model calculation performed with RADEX for R Tri.

Table 5.2: RADEX slab spectrum model results for R Tri 2008-10-02. The results are almost identical to those presented in Table 5.1 because the star is nearly the same phase as the previous observation. The optical depth for the emitting contribution is taken as the average of the optical depths of the 13.87 and 16.18 μm bands.

RADEX Results R Tri 2008-10-02					
λ μm		T_{kin}(K)	N (cm^{-2})	T_{exc}	τ
14.98		550 ± 50	$2.40\times10^{16} \pm 0.05\times 10^{16}$	605^{+46}_{-49}	$0.911^{+0.02}_{-0.02}$
13.87		600 ± 50	$4.50\times10^{17} \pm 0.5\times 10^{16}$	596^{+49}_{-50}	$1.72^{+0.19}_{-0.19}$
16.18		600 ± 50	$4.50\times10^{17} \pm 0.5\times 10^{16}$	596^{+49}_{-50}	$1.69^{+0.18}_{-0.19}$

due to transitions from additional excited bands not included in our RADEX file, while the feature at 15.4 μm could be the ν_2 bending mode for $^{13}CO_2$. Averaging the results from both sets of observations the column density for the absorbing layer is $N_A \sim 2 \times 10^{16}$ cm^{-2}, and the column density for the emitting layer is an order of magnitude higher $N_E \sim 5 \times 10^{17}$ cm^{-2}. The layers have an average excitation temperature, $T_{ex} \sim 600$ K. These results are consistent with previous models of CO_2 in AGB stars and Mira variables presented in Table 5.3. Markwick & Millar (2000) results are of particular interest because their observations of R Cas showed the 14.98 μm feature in absorption with two excited emission bands at 13.5 μm and 13.87 μm and this was the only model of the three presented in Table 5.3 that attempted to fit multiple lines simultaneously rather than individually. The absorption feature could only be well fit if the model deviated from a thermal population of the 01^10 level and the authors argue that this deviation could be the result of collisional de-excitation with H_2, preferential formation of excited states, or an unknown pumping mechanism.

5.9 Conclusion

Spitzer observations of the M-type Mira variable R Tri show several Q-branch band heads of CO_2 and a new bright emission feature at 17.6 μm. We built a molecular file of ro-vibrational transitions of CO_2 between 12-17 μm that can be used with RADEX to model CO_2 in the mid-IR. RADEX's capabilities of calculating the radiative transfer under NLTE conditions with collisional de-excitation with H_2 creates an advance in model sophistication. We used a 2-slab RADEX model to simultaneously fit the three CO_2 Q-branches at 13.87 μm, 14.98 μm, and 16.18 μm. The model results indicate an extended layer of CO_2 gas located from $\sim$3-4 R_* with a kinetic temperature of $\sim$600 K. It is possible that this is observational evidence for a refrigeration zone which would permit silicate dust condensation within a few stellar radii. We will use RADEX to analyze the CO_2

Table 5.3: Results on CO_2 from previous studies conducted with ISO. Specific lines are denoted (E) for emission and (A) for absorption. [1]Yamamura et al. (1999a), [2]Cami et al. (2000), [3]Markwick & Millar (2000)

Previous Model Results			
Target	T_{exc}(K)	N (cm^{-2})	R(R_*)
o Cet[1]			
4.3 μm (A)	800	2.0×10^{17}	2.3
Z Cas[1]			
4.3 μm (A)	800	1.5×10^{18}	1.7
EP Aqr[2]			
λ = 13.48 μm (E)	700	3.2×10^{18}	4.4
λ = 13.87 μm (E)	500	3.2×10^{18}	8.6
λ = 14.98 μm (E)	350	1.0×10^{19}	9
λ = 16.18 μm (E)	550	3.2×10^{18}	7.2
R Cas[3]			
13.48 μm & 13.87 μm (E)	1100	2.0×10^{16}	3.2
14.98 μm (A)	900	5.0×10^{16}	NA
IRC+10011[3]			
14.98 μm (A)	650	3.0×10^{16}	7

lines in the remaining M-type Miras from the Spitzer study which will allow us to determine if the CO_2 gas undergoes any phase dependent behavior. We will use EXES on board SOFIA to observe a subset the M-type Miras included in the Spitzer study as part of SOFIA's Cycle 8 campaign. The higher resolution provided by EXES will allow us to put stronger constraints on the temperature and column density. SOFIA provides the first opportunity since Spitzer to observe CO_2 at these wavelengths, and the results from this work will provide an excellent starting point for future studies of CO_2 with SOFIA and JWST.

Acknowledgements

The authors wish to thank the referee for their comments and discussion. We also wish to thank A. Bosman for the private communication and discussion about collisional rate coefficients. This work was originally supported through a NASA Spitzer grant for Program GO 50717, funded through NASA-JPL under contract 1344355. This research has made use of NASA's Astrophysics Data System.

"The most exciting phrase to hear in science, the one that heralds new discoveries, is not 'Eureka!' (I found it!) but 'That's funny ...'"

— Isaac Asimov

Chapter 6

RESULTS AND DISCUSSION

Here we present results of the models of the five CO_2 Q-branch bandheads described in Chapter 4. Each M-type Mira has a brief description of their specific results, and Table 6.3 provides results of every RADEX calculation. Plots of the Spitzer data overlaid with the RADEX models are provided in Appendix A.1. We also discuss the results of the 17.62 μm feature.

6.1 RADEX Results for the M-type Miras

We used RADEX to fit every M-type Mira spectrum from 13-17 μm. We ran three slab models for each observation (if all five lines were present). When the 14.98 μm line was seen in absorption, we were able to create a 2-slab model by adding the contributions from the 13.87 and 16.18 μm slab to the 14.98 μm slab thereby creating a model that fit all three lines at once.

The goal of the models was to fit the Q-branch bandheads at 13.45 μm, 13.87 μm, 14.98 μm, 16.18 μm, and 16.76 μm. We do not have the resolution to accurately fit the forest of P and R branches, though the models do seem to track the macroscopic behavior. We noticed some consistent trends in the models that we will describe here to prevent repetition for every star's results. When the 14.98 μm feature was seen in absorption, the models considerably overfit the shoulder at shorter wavelengths, that is the model produces too much flux near 14.9 μm, and this makes the synthetic spectrum appear to have an extra feature that the Spitzer spectrum does not. This could arise from the truncation to $J = 50$ in the molecular file, it is possible that the additional transitions would alleviate the sharp jump in the synthetic spectra. Another possible explanation could be be additional excited bands near 14.95 μm that were not included in our molecular file that would provide absorption to fit that shoulder better. Similarly, features

near 15.5 μm (both absorption and emission) that are clearly not fit well could also be additional transitions not included in our molecular file. Occasionally, we see a weak feature near 15.4 μm that could be $^{13}CO_2$. We consistently struggled with the 13.5 μm and 16.8 μm fits. These fits were insensitive to temperature, making it difficult to accurately determine a line center. The fits all returned extremely low optical depths with the strongest depths being 0.07 and 0.06, which could explain the insensitivity to temperature. The gas is too thin to be a decent "thermometer". Because of this insensitivity, we only estimated emitting regions for results that had optical depths greater than 0.01. Specific model parameters for every fit are included in Table 6.3.

Before we discuss the results for each individual M-type Mira, recall that $\phi = 0 = 1$ corresponds to when the photosphere is smallest and hottest and the star is brightest in the optical, and $\phi = 0.5$ corresponds to when the photosphere is largest and coolest. Figure 1.4 indicates that larger layers in the atmosphere lag in their response to the pulsation, and suggests the atmosphere has a complicated response to the phase of the star. The following results for the individual M-type Miras confirm this complicated relationship with the pulsational phase.

6.1.1 R Tri

R Tri has two observations at $\phi = 0.153$ and $\phi = 0.222$, and showed deep absorption at 14.98 μm. We were able to fit the 13.87 μm, 14.98 μm and 16.18 μm with a two slab model. Models for both observations are given in Figures A.1 and A.2.The grid for the absorbing layer was built in 50 K steps in T_A and 0.05×10^{16} cm^{-2} steps in N_A, and the grid for the emitting layer had 50 K steps in T_E and 0.5×10^{17} cm^{-2} steps in N_E. The absorbing layer has T_{kin} = 550 K, and the emitting layer has T_{kin} = 600 K for both phases. Additional specific values of the fits are provided in Table 6.3. The model overfits the spectrum at the left shoulder of the 14.98 μm band. This is most likely caused by additional excited transitions near 14.98 μm not included in the molecular file. Similarly, the two absorption features at 15.3 μm and 15.6 μm are also likely due to excited transitions not included in the molecular file, while the feature at 15.4 μm could be the ν_2 bending mode for $^{13}CO_2$.

The line behavior of the 14.98 μm line varies only slightly between the two phases. The absorption grows slightly stronger from $\phi = 0.153$ to $\phi = 0.222$. The optical rises from τ=0.850 to τ=0.911 accordingly. The kinetic temperature was 550 K for both observations. The excitation temperature for this layer is 57 K higher than the kinetic temperature, indicating that the ν_2 band is experiencing more NLTE effects from the shock than the two excited bands at 13.87 μm and 16.18 μm. We estimate the absorbing region to be 4.4R$_\star$, for both phases. The line behavior of the two emission lines at 13.87 μm and 16.18 μm was opposite to the absorption feature. Their intensities decreased from $\phi = 0.153$ to $\phi = 0.222$ and the average optical depth of the emitting layer drops from τ=1.89 to τ=1.71. The

kinetic temperature was 600 K for both observations. The emitting region for the emission lines at ϕ = 0.153 was R_E = 3.6$R_\star$, and at ϕ = 0.222 it was R_A = 3.8$R_\star$.

None of the results are significantly different in the two observations, most likely because they are at nearly the same phase. Structurally we can say that at near $\phi = 0.2$ the atmosphere has a region of CO_2 that stretches from ∼3.5-4 $R_\star$ with an average kinetic temperature of 600 K. This is several hundred Kelvin cooler than we would expect at this part of the atmosphere.

6.1.2 S Peg

S Peg has two observations at $\phi = 0.631$ and $\phi = 0.098$, and showed a dynamic change in the absorption at 14.98 μm. We fit additional excited bands at 13.49 μm and 16.76 μm. The grid for the absorbing layer was built in 50 K steps in T_A and 0.05×10^{16} cm^{-2} steps in N_A, and the grid for the first emission layer had 50 K steps in T_E and 0.5×10^{17} cm^{-2} steps in N_E, while the second emission layer had 50 K steps in T_E and $(0.25 - 0.5) \times 10^{17}$ cm^{-2} steps in N_E. The absorbing layer has T_{kin} = 750 K, and the emission layers have T_{kin} = 500 K and 1400 K. The three bands at 13.87 μm, 14.98 μm and 16.18 μm were fit by adding the absorbing layer with the first emission layer. We attempted to add the second emission layer to create a 3-slab model, but no suitable fit was found. The second emission layer was left as independent of the two layers that created the 2-slab model. The S Peg spectra show similar issues as R Tri with the ν band overfit on the left shoulder and absorption features at 15.4 μm and 15.6 μm are not fit; all of which require additional bands in the molecular file.

The feature changes from deep absorption in the ϕ =0.631 observation to weak absorption in the $\phi = 0.098$ observation. This change is reflected in the RADEX results. The optical depth in the absorbing layer drops from τ = 0.627 at $\phi = 0.631$ to τ = 0.346 at $\phi = 0.098$. Meanwhile, the emission lines increase in intensity, but the optical depth in the emitting layer remains constant at $\tau = 1.86$. As with R Tri, there is $\sim$ 50 K difference between T_{kin} and T_{exc}, indicating this layer is experiencing more NLTE effects. We estimate the absorbing region at 2.7 $R_\star$ for $\phi = 0.631$, and at 2.5 $R_\star$ for $\phi = 0.098$. The emission region of the 13.87 μm and 16.18 μm lines is estimated at 3.7-4.1 $R_\star$ for $\phi = 0.631$ and 3.5-3.7 $R_\star$ for $\phi = 0.631$. The emission region for the 13.49 μm and 16.76 μm lines is estimated at 5.3 $R_\star$ for $\phi = 0.631$ and 5.6 $R_\star$ for $\phi = 0.631$.

The drop in optical depth and size of the absorbing layer track with the radial behavior of the atmosphere responding to the pulsation near 2.5$R_\star$ in Figure 1.4. The emission layer lies farther out near 4$R_\star$ which means it might have expanded farther than what was seen in the $\phi = 0.631$ observation because it does not reach maximum expansion until near $\phi = 0.8$. We cannot say if this layer tracks the pulsation as cleanly as the inner absorbing layer without an observation near $\phi = 0.8$. The observations do tell us that there is CO_2 gas near 2.5 $R_\star$ and 3.5-4 $R_\star$ at 750 K and 500 K, respectively. These are right in the dust production zone theorized by Bowen (1988) and Willson (2000).

6.1.3 S Ser

S Ser has two observations at $\phi = 0.620$ and $\phi = 0.671$. The grid for the absorbing layer was built in 50 K steps in T_A and 0.05×10^{16} cm^{-2} steps in N_A, and the grid for the first emission layer had 50 K steps in T_E and 0.5×10^{17} cm^{-2} steps in N_E, and the second emitting layer also had 50 K steps in T_E and 0.5×10^{17} cm^{-2} steps in N_E. The absorbing layer has T_{kin} = 700 K, and the emitting layers have T_{kin} = 500 K and 1400 K.

The features do not vary greatly between the two observations, most likely because they are near in phase. The greatest change comes from the excited bands at 13.49 μm and 16.76 μm. The optical depth rises from $\tau \sim 0.03$ - $\tau \sim 0.05$ and the emission region drops from 7 $R_\star$ to 6.5$R_\star$. This could indicate that this outer layer of the atmosphere has stopped expanding and is beginning to fall back. This fallback has not yet reached the inner layers of the atmosphere because the next emission layer for the 13.87 μm and 16.18 μm features, showed a drop in optical depth and an increase of the emission region from 3.6 $R_\star$ to 3.8 $R_\star$ which tracks the pulsation near 4$R_\star$ in Figure 1.4; this layer is nearing maximum expansion at $\phi = 0.671$. Similarly, the strength of the ν_2 band absorption does slightly drop from $\phi = 0.620$ and $\phi = 0.671$, while the optical depth drops from $\tau \sim 0.7$ to $\tau \sim 0.6$, and the absorption region remains virtually constant at from 2.9 $R_\star$. These observations are quite similar to S Peg and tell us that the CO_2 gas lies at 2.9$R_\star$ and 3.5-4$R_\star$ with kinetic temperatures of 700 K and 550 K, respectively, which are favorable for dust condensation.

6.1.4 SS Cas

SS Cas has three observations at $\phi = 0.029$, $\phi = 0.169$ and $\phi = 0.386$. Its spectra are notably different than the previous three stars. The fundamental ν_2 band is always seen in emission. The first emission layer corresponding to the 14.98 μm feature was built in 50 K steps in T_{E1} and 0.25×10^{15} cm^{-2} steps in N_{E1}. The second emission layer corresponding to the 13.87 μm and 16.18 μm features was built in 50 K steps in T_{E2} and 0.1×10^{17} cm^{-2} steps in N_{E2}. We attempted to fit the 14.98 μm feature in absorption, but the line center of the absorption seen in SS Cas is 14.95 μm and the temperature required to match this line center required $\sim$ 2000 K; it is more likely that this absorption arises from excited bands that are not included in our molecular file.

The kinetic temperatures of the layers of CO_2 in SS Cas are much cooler than those found for R Tri, S Peg, and S Ser, ranging from 350-400 K. The excitation temperatures of the 14.98 μm features only differ from the kinetic temperature by about 15 K, indicating this layer is nearly in LTE compared to when the line is seen in absorption. The estimated emitting region for the first emission layer ranges from 11-14 $R_\star$, and the emitting region for the second emission layer ranges from 12-14 $R_\star$. These observations seem to show cooler thinner gas much farther out than the first three stars showed. The emitting regions for the two emission slab

calculations overlap so we can think of a large extended layer of CO_2 sitting at 11-14$R_\star$ with a temperature of $\sim$400 K. This is far enough from the star that the stellar wind is possibly pushing on the gas causing it to thin and drop its optical depth.

6.1.5 W Her

W Her has five observations at $\phi = 0.473$, $\phi = 0.604$, $\phi = 0.725$, $\phi = 0.794$, and $\phi = 0.919$. The fundamental ν_2 band was seen in emission in all five observations. As with SS Cas, we created 3 layers to fit the five CO_2 features. The first emission layer corresponding to the 14.98 μm feature was built in 50 K steps in T_{E1} and $0.25 - 0.5 \times 10^{15}$ cm^{-2} steps in N_{E1}. The second emission layer corresponding to the 13.87 μm and 16.18 μm features was built in 50 K steps in T_{E2} and 0.1×10^{17} cm^{-2} steps in N_{E2}. The third emission layer corresponding to the 13.49 μm and 16.76 μm was again problematic to fit. The grid was built in 100 K steps in T_{E3} and 0.1×10^{16} cm^{-2} steps in N_{E3}.

The model results for W Her are quite similar to SS Cas. Having the fundamental ν_2 band in emission resulted in a much cooler gas farther out in the atmosphere. The kinetic temperature from of the two emission layers ranges from 350-400 K and both layers lie beyond 10 $R_\star$. As the star moved from $\phi = 0.473$ to $\phi = 0.794$ the layer associated with the 14.98 μm feature expanded from 10 $R_\star$ to 15 $R_\star$. The layer associated with the 13.87 μm and 16.18 μm shows only minor changes across the first four phases. Both layers show a compression in size from $\phi = 0.794$ to the $\phi = 0.919$. As with SS Cas the emission regions overlap and we can consider a large slab of CO_2 at 10-15$R_\star$ with temperature $\sim$400 K.

6.1.6 RT Cyg

RT Cyg has seven observations at $\phi = 0.654$, $\phi = 0.780$, $\phi = 0.983$, $\phi = 0.114$, $\phi = 0.276$, $\phi = 0.459$, and $\phi = 0.584$. The fundamental ν_2 band was seen in emission the first 5 observations, but then it flips to absorption in the final two observations. The excited bands at 13.49 μm and 16.76 μm were too weak to fit. For the first five phases we created two emission layers. The first emission layer corresponding to the 14.98 μm feature was built in 50 K steps in T_{E1} and $0.2 - 0.5 \times 10^{15}$ cm^{-2} steps in N_{E1}. The second emission layer corresponding to the 13.87 μm and 16.18 μm features was built in 50 K steps in T_{E2} and $0.05 - 0.1 \times 10^{17}$ cm^{-2} steps in N_{E2}. When the 14.98 μm line was seen in absorption, the grid was built in 50 K steps in T_A and $0.05 - 0.1 \times 10^{15}$ cm^{-2} steps in N_A. This absorbing layer was then added to the second emission layer (E2) to produce a simultaneous fit of the 13.87 μm, 14.98 μm, and 16.18 μm features.

The observations that showed the 14.98 μm band in emission traced regions farther out in the atmosphere, similar to SS Cas and W Her. As with the other

stars, the emission region for the 13.87 μm and 16.18 μm remains fairly constant with minor fluctuations in size. The layer for the 14.98 μm region expands from 11.7 $R_\star$ to 12.5 $R_\star$ and then contracts to 10 $R_\star$ at $\phi = 0.654, 0.780$, and 0.983, respectively; this layer then expanded to 11.2 $R_\star$ and 14.5 $R_\star$ for ϕ = 0.114, ϕ = 0.276. The feature flips to absorption for $\phi = 0.459$ and $\phi = 0.584$, and this feature traces a region at 3.3 $R_\star$. The layer for the 13.87 μm and 16.18 μm feature also moves closer to the star at these phases. We seem to be tracing different regions of the atmosphere based upon whether or not the ν_2 band is seen in emission or absorption. When this feature is seen in emission, we see the cooler thinner gas farther out in the atmosphere. When we see it in absorption, we see a region much closer to the star. The change in behavior makes it difficult to tease out a pattern because we suddenly move from probing the outer layers to layers much closer to the star. These observations do tell us that CO_2 is highly extended in RT Cyg's atmosphere tracing regions from 3-14$R_\star$.

6.1.7 R Cet

R Cet has two observations at $\phi = 0.850$, and $\phi = 0.019$. The fundamental ν_2 band is seen in strong emission in both cases. We created three layers to fit the five CO_2 features. The first emission layer corresponding to the 14.98 μm feature was built in 50 K steps in T_{E1} and $0.15 - 0.3 \times 10^{16}$ cm^{-2} steps in N_{E1}. The second emission layer corresponding to the 13.87 μm and 16.18 μm features was built in 50 K steps in T_{E2} and 0.1×10^{17} cm^{-2} steps in N_{E2}. The third emission layer corresponding to the 13.49 μm and 16.76 μm features was built in 100 K steps in T_{E3} and 0.5×10^{16} cm^{-2} steps in N_{E3}. This layer proved difficult to fit for the $\phi = 0.019$ observation; we only put a bound on the temperature of 5000 K and the optical depth was too low to estimate an emitting region.

The intensity of 14.98 μm feature strengthens from the $\phi = 0.850$ to the $\phi = 0.019$ observation and this is reflected in the optical depth as it moves from $\tau = 1.32$ to $\tau = 2.38$. The kinetic temperature shows only a slight increases from 450 K to 500 K; the excitation temperature deviates only slightly from the kinetic temperature and does not indicate the feature is experiencing strong NLTE effects. The estimated emission region for the feature came back at $\sim$ 5 $R_\star$, much closer than the previous stars that also showed the 14.98 μm in emission, but this line quite optically thick compared to the other observations. The column density doubles from $\phi = 0.850$ to $\phi = 0.019$.

These trends are also reflected in the layer associated with the 13.87 μm and 16.18 μm features; the line intensities increase from $\phi = 0.850$ to the $\phi = 0.019$, with high optical depths of $\tau \sim$1.2. We estimate the emission region at $\sim$ 6 $R_\star$. The second emission layer for the 13.49 μm and 16.76 μm showed a decrease in line intensity and this is reflected in the optical depth as it drops from $\tau = 0.05$ to $\tau = 0.01$. Column densities for both these layers drop from $\phi = 0.850$ to $\phi = 0.019$, opposite to what the 14.98 μm feature does. The layer associated with the 14.98 μm feature near 5 $R_\star$, appears to get perturbed between $\phi = 0.850$ and

$\phi = 0.019$ which caused the column density and optical depth to increase, but this perturbation does not appear to yet affect the second emission layer further out near $6R_\star$. Unlike SS Cas, W Her, and RT Cyg, the 14.98 μm line in emission for R Cet does not trace cool, thinner gas past $10R_\star$; rather R Cet appears to have an optically thick layer of CO_2 between 5-$6R_\star$ with a kinetic temperature of 500 K, optimal conditions for silicate dust nucleation.

6.1.8 Z Cyg

Z Cyg has seven observations at $\phi = 0.725$, $\phi = 0.859$, $\phi = 0.961$, $\phi = 0.054$, $\phi = 0.170$, $\phi = 0.309$, and $\phi = 0.280$. The ν_2 band was seen in emission in all observations. We created three layers to fit the CO_2 features. Longwards of 16 μm suffered from severe contamination from dust emission which greatly affected the CO_2 lines at 16.18 μm and 16.76 μm. The first emission layer corresponding to the 14.98 μm feature was built in 100 K steps in T_{E1} and $0.05 - 0.5 \times 10^{16}$ cm^{-2} steps in N_{E1}. The second emission layer corresponding to the 13.87 μm and 16.18 μm features was built in 100 K steps in T_{E2} and $0.1 - 0.25 \times 10^{17}$ cm^{-2} steps in N_{E2}. The third emission layer corresponding to the 13.49 μm and 16.76 μm features was built in 100-200 K steps in T_{E3} and $0.25 - 0.5 \times 10^{16}$ cm^{-2} steps in N_{E3}. The temperature uncertainties are higher for Z Cyg because it appeared to have a systemic alignment issue that we addressed by shifting the spectrum 0.019 μm to the right, as described in Section 4.1.3. As with the other stars, the third layer for the 13.49 μm and 16.76 μm bands proved difficult to fit, especially when the 16.76 μm feature was extremely weak in several of the observations. For observations with significant dust contamination, we only estimated the emitting layers for the short wavelength bandheads.

Tracking the 14.98 μm line behavior, we see it is definitely sensitive to the phase of the star. We see the line intensity increase from $\phi = 0.725$ to $\phi = 0.859$ then the intensity drops from $\phi = 0.961$ through $\phi = 0.309$ and remains the same for $\phi = 0.391$. The optical depth of the line increased from $\phi = 0.725$ to $\phi = 0.859$, decreased from $\phi = 0.859$ to $\phi = 0.0.170$, and finally increased from $\phi = 0.0.170$ to $\phi = 0.391$. The estimated emission region for this layer ranges from 4.5-6.7 $R_\star$. It is smallest at $\phi = 0.859$ and largest at $\phi = 0.170$, corresponding the largest and smallest optical depths, as can be seen in Table 6.3.

Tracking the 13.87 μm behavior we also see a change with phase. The line strength increases from $\phi = 0.725$ to $\phi = 0.859$ then decreases from $\phi = 0.859$ to $\phi = 0.391$. The optical depth of the line increased from $\phi = 0.725$ to $\phi = 0.859$, decreased from $\phi = 0.859$ to $\phi = 0.961$, then increased from $\phi = 0.961$ to $\phi = 0.309$. This layer is slightly out of step with the 14.98 μm layer, but the macroscopic behavior is the same. The estimated emission region for the layer ranges from 4.4-8 $R_\star$. It is smallest at $\phi = 0.391$ and largest at $\phi = 0.961$ corresponding to largest and smallest optical depths. This second layer overlaps with the estimated layer of the 14.98 μm feature, and we can think of one large slab of CO_2, extending 4.4-8 $R_\star$. These results are similar to R Cet; when the 14.98 μm is in strong emis-

sion and the line is optically thick, it traces gas closer to the star than when it is optically thin. The average kinetic temperature of this slab is ∼500 K; for the inner portion of the slab near 4 $R_\star$ this is fairly cool, and it would allow for rapid silicate dust condensation.

6.1.9 Y Del

Y Del has three observations at $\phi = 0.280$, $\phi = 0.539$, and $\phi = 0.579$. The lines were fairly weak compared to the other stars in the sample; the excited bands at 13.49 μm and 16.76 μm were too weak too fit.We created two layers to fit the remaining three CO_2 features. The first emission layer corresponding to the 14.98 μm feature was built in 50 K steps in T_{E1} and 1×10^{15} cm^{-2} steps in N_{E1}. The second emission layer corresponding to the 13.87 μm and 16.18 μm features was built in 50 K steps in T_{E2} and 1×10^{17} cm^{-2} steps in N_{E2}.

The spectra for Y Del have a much different character than those of the other M-types. The CO_2 lines are much weaker, and there are features near 14 μm that could be from carbon species like HCN and C_2H_2. The line behavior of the 14.98 μm features still does appear to change with phase. The intensity is strongest at $\phi = 0.280$, then it weakens at $\phi = 0.539$, and then it strengthens at $\phi = 0.579$. The optical depth tracks this behavior and is largest at $\phi = 0.280$, then it decreases at $\phi = 0.539$, but then increases at $\phi = 0.579$. The kinetic temperature was 450 K for all three observations. We estimate the emission region to be 6.4-7.2 $R_\star$, with the smallest value occurring at $\phi = 0.280$ and the largest value occurring at $\phi = 0.539$.

The features at 13.87 μm and 16.18 μm have minimal changes in intensity across the three phases. The optical depth increases from $\phi = 0.280$ to $\phi = 0.539$ and remains the same at $\phi = 0.579$. The kinetic temperature was 300 K for all three observations. We estimate the emission region to be 11-14 $R_\star$. The layer is smallest at $\phi = 0.579$ and largest at $\phi = 0.280$. The two layers do not appear to overlap. The first layer is smallest at $\phi = 0.280$ while the second layer is largest. This confirms that the second emission layer is more extended than the first layer, because its behavior lags behind significantly. The addition of possible carbon species features, and the relative weakness of the lines, could indicate that Y Del is evolving toward an S-type chemistry.

6.1.10 S Lac

S Lac has three observations at $\phi = 0.279$, $\phi = 0.383$ and $\phi = 0.819$. The absorbing layer for $\phi = 0.383$ and $\phi = 0.819$ was built in 50 K steps in T_A and 0.05×10^{16} cm^{-2} steps in N_A. For the $\phi = 0.279$ observation, the step size for the column density decreased to 0.5×10^{15} cm^{-2}. The first emission layer for the 13.87 and 16.18 μm lines had steps of 50 K and 0.1×10^{17} cm^{-2}. The second emission layer for the 13.49 μm and 16.76 μm lines was so optically thin that fits were extremely

difficult. We place an upper bound on the temperature of 4000 K, and the column density was built in 0.25×10^{16} cm^{-2} steps.

S Lac shows a dynamic change of the ν_2 band. At $\phi = 0.279$ the feature is in emission, but by $\phi = 0.383$ it is weak absorption, and the $\phi = 0.819$ observation shows stronger absorption. The kinetic temperature for the emission is 400 K, but when it flips to absorption, it rises to $\sim$ 800 K. The densities also change by an order of magnitude when the line flips from emission to absorption. The estimated emission region for the line is 9.04 R$_\star$, while the absorbing region is much closer to the star at $\phi = 0.383$, it is 2.80 R$_\star$ and at $\phi = 0.819$, it is 3.39 R$_\star$. The different line behavior must be letting us see two completely different regions of the atmosphere. When the line is in emission, we see thin cool gas much farther out in the atmosphere; when the line is in absorption we see warmer gas closer to the photosphere.

The emission region for the 13.87 μm and 16.18 μm lines also appear to trace a wider range compared to the results for the other M-type Miras in this dataset. When the ν_2 band is in emission, and we do not add an absorbing layer contribution, we find the emission region at $\sim$ 8.8 R$_\star$, just under the distance estimated for the ν_2 band. For the $\phi = 0.383$ and $\phi = 0.819$ observations, when we can add an absorbing layer to these lines, we find a smaller layer at 7.3 R$_\star$ and 7.0 R$_\star$, respectively. We seem to be tracing different portions of the atmosphere depending on whether or not the 14.98 μm line was seen in emission or absorption. When the line is in emission, we trace two layers farther out in the atmosphere; when the line is in absorption we trace this layer near the star, and the second emission layer moves inward. This again tells us that CO_2 is quite extended in the atmosphere from $\sim$3-9R$_\star$ and has conditions favorable for dust production.

6.1.11 S Psc

S Psc has two observations at $\phi = 0.990$ and $\phi = 0.042$. These observations provide an opportunity to check for shock behavior, because they are both just on either side of $\phi = 0$ when the pulsation cycle starts over. The ν_2 band was seen in absorption for both observations. The grid was built in 100 K steps for T$_A$ and 0.25×10^{16} cm^{-2} for N$_A$. The first emission layer for 13.87 μm and 16.18 μm was built in 50 K steps for T$_{E1}$ and 0.5×10^{17} cm^{-2} for N$_{E1}$. The second emission layer for 13.49 μm and 16.76 μm was not sensitive to temperature and we found an upper bound of 3000 K; the column density was built in steps of 0.25×10^{16} cm^{-2}.

The spectra look almost identical, and this is reflected in the fits. The kinetic temperature of the ν_2 band 1000 K, roughly 200 K hotter than the rest of the stars that show ν_2 in absorption. Both observations are right on top of $\phi = 0$, indicating this layer is near its smallest and hottest point. The optical depth for the 14.98 μm feature increased from $\tau = 0.8$ to $\tau = 1$, while the optical depth of the first emission layer dropped from $\tau = 2.02$ to $\tau = 1.86$. The second emitting region

had $\tau = 0.01$ for both observations. The absorbing layer lies at 2.2 $R_\star$, the first emitting layer lies at just under 5 $R_\star$. The second emitting layer result does not seem physical with the upper bound temperature; as with other stars these lines are so optically thin that the models become insensitive to temperature.

It is difficult to back out any change atmospheric dynamics from these observations, because they are almost identical phases; but we can say that near maximum phase, S Psc has an absorbing layer of CO_2 at 2.2 $R_\star$, and an emission layer slightly further out at 5 $R_\star$. Both layers are cool enough for dust production.

6.1.12 U Cvn

U Cvn has two observations at phase $\phi = 0.948$ and $\phi = 0.036$. Here is another opportunity to check for behavior near maximum phase. The ν_2 band is seen in absorption in both observations. The grid was built in 50 K steps for T_A and 0.05×10^{16} cm^{-2} for N_A. The first emission layer for 13.87 μm and 16.18 μm was built in 50 K steps for T_{E1} and 0.1×10^{17} cm^{-2} for N_{E1}. We found a fit for all three lines by adding the absorbing layer to this first emission layer. The second emission layer for 13.49 μm and 16.76 μm was not sensitive to temperature and we place an upper bound of 3000 K; the column density was built in steps of 0.25×10^{16} cm^{-2}. The optical depths were so small that we did not estimate an emitting region for this layer.

The line behavior did fluctuate between the two phases. The intensity of the 14.98 μm absorption increased from $\phi = 0.948$ to $\phi = 0.036$. The optical depth rose from 0.392 to 0.533, and the column density also increased. We estimate the absorbing region to be 2.6 $R_\star$ at $\phi = 0.948$ and 2.8 $R_\star$ at $\phi = 0.036$. The intensity of the emission features at 13.87 μm and 16.18 μm also increased from $\phi = 0.948$ to $\phi = 0.036$. The optical depth rose slightly, from 1 to 1.08, while the density remained constant. The slight increase in optical depth is likely from the kinetic temperature rising slightly from 450 K to 500 K. We estimate the emitting region of this layer to be 5.4-6 $R_\star$ at $\phi = 0.948$ and 5.1-5.4 $R_\star$ at $\phi = 0.036$.

As with S Psc and other stars that have two phases measurements close together, it is difficult to determine if the atmosphere underwent any significant changes. The absorbing region shows a slight expansion, while the emitting region shows a slight contraction, but additional phase observations are needed to confirm these small changes are consistent. We can say that near maximum phase U Cvn has an absorbing layer of CO_2 gas at 2.6-2.8 $R_\star$ that is 750-800 K, and slightly farther out it has an emission region of CO_2 at 5-6 $R_\star$ that is 450-500 K. These are both cool for their locations and thus create favorable conditions for dust production.

6.1.13 UX Cyg

UX Cyg has four observations at $\phi = 0.225$, $\phi = 0.276$, $\phi = 0.454$, and $\phi = 0.484$. The ν_2 band is seen in absorption for all four observations, but the emission lines are incredibly weak. Only the $\phi = 0.454$, and $\phi = 0.484$ show the emission lines at 13.87 μm and 16.18 μm, and none of the observations show the features at 13.49 μm and 16.76 μm. The grid was built in 50 K steps for T_A and 0.5×10^{16} cm^{-2} for N_A. The first emission layer for 13.87 μm and 16.18 μm was built in 50 K steps for T_{E1} and 0.5×10^{17} cm^{-2} for N_{E1}. As with Z Cyg, there is significant dust contamination near 16 μm, disrupting the fit of the 16.18 μm line. The fits for the 13.87 μm are poor and are should be considered as upper bounds on the conditions.

The absorption line shows variability with phase. The intensity decreases from $\phi = 0.225$ through $\phi = 0.276$ to $\phi = 0.454$, then increases at $\phi = 0.487$. The optical depth decreases from $\phi = 0.225$ to $\phi = 0.276$ then increases from $\phi = 0.454$ to $\phi = 0.487$. The column density also follows this pattern. We estimate the absorbing region at increasing phase to be 4.75, 4.77, 4.21, and 4.29 $R_\star$. The column density increased significantly from the early phases to the later phases, increasing the optical depth allowing us to see deeper into the atmosphere. UX Cyg shows similar behavior to R Cet, Z Cyg and U Cvn. All these stars showed strong, optically thick emission lines which traces a layer of CO_2 gas near $5R_\star$ at temperatures favorable to silicate dust formation.

6.2 Discussion

6.2.1 Model Results

We were successful in modeling the CO_2 Q-branch bandheads seen in the M-types. The regions between the Q-branches are dominated by a forest of P and R transitions blending together; it is impossible to distinguish individual P and R transitions at Spitzer's resolution, and thus no attempt was made to reproduce their behavior in this work. The slab models seemed to overfit the left shoulder when the ν_2 band was seen in absorption, which may be caused by missing excited bands near 14.95 μm in our molecular file. Similarly, features in the Spitzer spectra seen near 15.5 μm may also be additional excited bands of CO_2 not included in the molecular file. We also did not include any transitions of $^{13}CO_2$. Future work will include updating the molecular file with additional bands and creating a file for $^{13}CO_2$.

Our results are consistent with previous studies of CO_2 in AGB stars observed with ISO. A summary of previous results is presented in Table 6.1. Our temperatures, column densities and radii all are in reasonable agreement with the those in the table. When the 4.3 μm band was seen in absorption in Z Cas and *o* Ceti, it traced a region near 2 $R_\star$ (Yamamura et al. 1999a) while emission lines

Previous Model Results			
Target	T_{exc}(K)	N (cm^{-2})	R(R_*)
***o* Cet**[1]			
4.3 μm (A)	800	2.0×10^{17}	2.3
Z Cas[1]			
4.3 μm (A)	800	1.5×10^{18}	1.7
EP Aqr[2]			
$\lambda = 13.48$ μm (E)	700	3.2×10^{18}	4.4
$\lambda = 13.87$ μm (E)	500	3.2×10^{18}	8.6
$\lambda = 14.98$ μm (E)	350	1.0×10^{19}	9
$\lambda = 16.18$ μm (E)	550	3.2×10^{18}	7.2
R Cas[3]			
13.48 μm & 13.87 μm (E)	1100	2.0×10^{16}	3.2
14.98 μm (A)	900	5.0×10^{16}	NA
IRC+10011[3]			
14.98 μm (A)	650	3.0×10^{16}	7

Table 6.1: Results of CO_2 from previous studies conducted with ISO. Specific lines are denoted (E) for emission and (A) for absorption. [1]Yamamura et al. (1999a), [2]Cami et al. (2000), [3]Markwick & Millar (2000)

traced regions further out from 4-9 $R_\star$ (Cami et al. 2000). Our stars show similar behavior; when seen in absorption the 14.98 μm line traced regions near 2 $R_\star$, while the emission lines at 13.87 μm and 16.18 μm traced regions father out near 5 $R_\star$. The only substantial discrepancy comes from previous results for the 13.49 μm feature in Ep Aqr, which fit a much cooler, denser gas than any of our models showed. That study was done with the SWS on ISO which had R$\sim$1000-3000, contributing to more sensitive fits. Markwick & Millar (2000) results are particular interesting, because their observations had the 14.98 μm feature in absorption with two emission lines at 13.49 μm and 13.87 μm. They also attempted fit multiple lines simultaneously in a similar fashion to our models, and their models only fit well if there was a deviation from LTE in the 01^10 level. The authors argued this deviation could be the result of collisional de-excitation with H_2, which was not included in their models, preferential formation of excited states, or an unknown pumping mechanism. We saw in several stars that the 14.98 μm line had excitation temperatures $\sim$50 K larger than the kinetic temperatures, indicating that the line was feeling some NLTE affects. RADEX provides a tool that allows H_2 collisions and will solve the radiative transfer under NLTE; these address many of the difficulties seen in previous CO_2 models.

Star	SE Class	Period[1] (days)	Masers OH	SiO	H_2O	14.98 μm Line
SS Cas	*	143.1	N[6]	NA	N[4]	E, w
W Her	"no feature"[1]	273.7	N[6]	N[5]	N[5]	E, w
RT Cyg	*	191.4	N[6]	N[4]	N[4]	E, w ; A, w
R Cet	SE8	165.8	N[6]	Y[7]	Y[7]	E, s
Z Cyg	SE8	267	Y[6]	Y[7]	Y[7]	E, s
Y Del	SE4	475.1	N[6]	N[5]	N[5]	E, w
S Lac	"no feature"[1]	240.6	N[6]	N[4]	N[4]	E, w; A, w
S Peg	SE1	312.2	Y[6]	N[3]	N[3]	A
R Tri	SE3	275.3	N[6]	Y[7]	Y[7]	A
S Ser	SE3	389	Y[6]	Y[7]	Y[7]	A
S Psc	SE4	422.7	N[6]	N[5]	N[5]	A
U Cvn	SE7	307.9	Y[6]	Y[7]	Y[7]	A
UX Cyg	SE8	546.3	Y[6]	Y[7]	Y[7]	A

Table 6.2: M-type Mira periods, spectral classifications, maser activity, and ν_2 band behavior (E indicates emission, A indicates absorption, s and w indicate strong, and weak). The shorter period Miras show the ν_2 band in emission, while the longer period Miras show it in absorption. There also appears to be a correlation between maser activity and the ν_2 band behavior. * no IRAS LRS data [1]Creech-Eakman et al. (2012),[2]Sivagnanam et al. (1988), [3]Cho & Kim (2012), [4]Benson & Little-Marenin (1996), [5]Benson et al. (1990), [6]Engels & Bunzel (2015), [7]Kim et al. (2014)

6.2.2 Line Behavior

Our results indicate that the CO_2 features are quite dynamic; we were able to trace some behavior with phase, but not every star showed a clear pattern. Key differences arose in stars that showed the fundamental ν_2 band at 14.98 μm in absorption vs. those that showed this feature in emission and if the emission was weak or strong. We add these results to the other basic data we have for the stars including their silicate emission (SE) class (Sloan & Price 1998), period, and maser activity in Table 6.2.

The stars with the ν_2 band in emission in our sample all have shorter periods ranging from 143-273 days. Y Del is the only exception with a period of 475 days. We will ignore Y Del's results for this discussion because we believe Y Del may be evolving toward an S-type; its lines were extremely weak, and we see features near 14 μm in its spectra that may be carbon species. W Her has the next longest period at 273 days, which is very close to R Tri's period of 275 days, but R Tri shows maser activity and W Her does not, indicating the two stars are behaving differently. The stars with the ν_2 band in absorption all had maser activity, while

most of the stars with the ν_2 band in weak emission have no maser activity. A striking difference can be noted if we consider all the SE7 and SE8 Miras which includes R Cet, Z Cyg, U Cvn, and UX Cyg. We notice that R Cet and Z Cyg have shorter periods of 166 days and 267 days, and exhibit the ν_2 band in emission; U Cvn and UX Cyg have longer periods of 308 and 546 days and show the the ν_2 band in absorption. The stars in this sample seem to show the ν_2 band in emission for the shorter periods, and show this band in absorption for the longer periods. It has been theorized that Miras with shorter periods pulsate in the first overtone mode rather than the fundamental mode (van Leeuwen et al. 1997), but this presents problems with observations, because the shocks generated in the first overtone are not strong enough to produce bright emission lines seen in Mira spectra (Willson 2000). Mira light curves are also asymmetric with a sharp rise near maximum phase, and these curves are characteristic of fundamental mode models (Willson 2000). We cannot completely disregard the possibility of different pulsation modes, because the modes are determined using stellar radii and mass values (e.g. Ostlie & Cox (1986)) that are derived using distance estimates, most often from parallax data, which is incredibly fickle for Miras. We saw the huge dispersion of distances from parallax measurements taken with Gaia and Hipparcos presented in Table 2.1. Until we have consistent distance measurements and a reasonable estimate of the mass the Mira pulsation modes are not set in stone. The M-type Miras in our sample clearly show different atmospheric dynamics between the shorter and longer periods.

6.2.3 Atmospheric Structure

Our results indicate that CO_2 is highly extended in Mira atmospheres. This is consistent with previous models in Table 6.1. When the 14.98 μm line was seen in absorption, we traced a region 2-4 $R_\star$, and the emission lines traced a region 3.5-5 $R_\star$. When all three lines were seen in emission, we traced a region from 7-15 $R_\star$. The kinetic temperatures of the gas in regions near the star 2-5 $R_\star$ were typically 500-750 K, except for S Psc where it peaked at 1000 K (possibly due to a shock). This results are also consistent with chemical abundances calculated in Agúndez et al. (2020) that show CO_2 as one of the most abundant molecules in M-type AGB atmospheres from 1-10 $R_\star$. The Agúndez calculations were performed under chemical equilibrium conditions and it is likely that the true CO_2 abundance is higher based upon observational results of SO_2, CS, NH_3, and HCN reported with the calculated equilibrium abundances in Agúndez et al. (2020). Indeed, Cherchneff (2006) reports a CO_2 abundance 2 orders of magnitude higher at 5 $R_\star$ due to the addition of shocks to the abundance calculations and argues strongly that equilibrium conditions are not sufficient to interpret observational results.

The molecule and dust forming region in Mira atmospheres is thought to lie near 2-5 R$\star$ (e.g. Reid & Menten (1997); Wong et al. (2016)), therefore the stars that show the absorption feature allow us to peak inside this unique part of the atmosphere. The low kinetic temperatures are evidence the CO_2 gas is creating a "refrigeration zone" at several $R_\star$. This is theorized in Willson (2000)

who describe how a departure from radiative equilibrium following the shock would allow the temperature to drop in a region at several R_*. This drop in temperature could precipitate silicate dust closer to the star than previous LTE models would allow, because silicate dust grains may require the temperature to be below 600 K for condensation (Gail & Sedlmayr 1998). The CO_2 might actually be contributing to the refrigeration. If we look at Figure 4.7, we notice there are hundreds of transitions available to CO_2 between 10-20 μm, and we only included eight bands that contained up to $J = 50$. There are likely hundreds of more transitions at these wavelengths. These all offer a plethora of radiative paths that could efficiently cool photons escaping from the photosphere, making it possible for silicates to nucleate at a few stellar radii.

Wong et al. (2016) placed the inner dust formation radius at $\sim$4-5 $R_\star$ for *o* Ceti. Silicate growth near the star is problematic because it requires lower temperatures than we would initially think is possible for this part of the atmosphere. Gail et al. (2013) argue that gas-phase SiO molecules nucleate into clusters and then condense onto grains, and that SiO gas is depleted at temperatures ranging from 600-800 K (for mass loss rates of $10^{-6} - 10^{-4}$ $M_\odot$ yr^{-1} respectively). Assuming the dust temperature is equivalent to the gas temperature at the inner boundary of the shell, this would allow silicate nucleation at closer distances than previously thought. However, models in Wong et al. (2016) showed that the SiO molecules will not deplete onto grains within 4 $R_\star$. If the CO_2 is providing a "refrigeration zone" this would allow silicate dust to develop in the inner regions of the atmosphere.

Some of the layers appeared to trace the pulsation of the star, but not every star had a clear trend. It could be that the more extended layers do not respond to the pulsation as much as layers near the photosphere do.

Table 6.3: Table of Results from RADEX fits. Line behavior is marked with an *A* for absorption, *E* for emission, with *w* and *vw* for weak and very weak, respectively. ^{A}possible no detection, ^{B}dust contamination ^{C}possible absorption

Target	$\mathbf{T_{kin}}$**(K)**	**N (cm^{-2})**	$\mathbf{T_{exc}}$ **(K)**	τ	**R (R$_*$)**	ϕ
R Tri 2008-09-07						
13.87 μm (E)	600 ± 50	$5\times10^{17} \pm 0.5\times 10^{17}$	597^{+49}_{-50}	$1.91^{+0.19}_{-0.19}$	3.6	0.153
14.98 μm (A)	550 ± 50	$2.25\times10^{16} \pm 0.05\times 10^{16}$	607^{+46}_{-49}	$0.850^{+0.04}_{-0.02}$	4.45	0.153
16.18 μm (E)	600 ± 50	$5\times10^{17} \pm 0.5\times 10^{17}$	597^{+49}_{-50}	$1.87^{+0.19}_{-0.18}$	3.5	0.153
R Tri 2008-10-02						
13.87 μm (E)	600 ± 50	$4.50\times10^{17} \pm 0.5\times 10^{17}$	596^{+49}_{-50}	$1.72^{+0.19}_{-0.19}$	3.8	0.222
14.98 μm (A)	550 ± 50	$2.40\times10^{16} \pm 0.05\times 10^{16}$	607^{+46}_{-49}	$0.911^{+0.02}_{-0.02}$	4.45	0.222
16.18 μm (E)	600 ± 50	$4.50\times10^{17} \pm 0.5\times 10^{17}$	596^{+49}_{-50}	$1.69^{+0.18}_{-0.19}$	3.7	0.222
S Peg 2008-12-08						
13.49 μm (E)	1400 ± 50	$7.5\times10^{16} \pm 0.5\times 10^{16}$	1390^{+45}_{-53}	$0.0499^{+0.0034}_{-0.0034}$	5.20	0.631
13.87 μm (E)	500 ± 50	$5.5\times10^{17} \pm 0.5\times 10^{17}$	498 ± 50	1.86 ± 0.17	3.67	0.631
14.98 μm (A)	750 ± 50	$2.40\times10^{16} \pm 0.05\times 10^{16}$	796 ± 47	0.627 ± 0.013	2.69	0.631
16.18 μm (E)	500 ± 50	$5.5\times10^{17} \pm 0.5\times 10^{17}$	498 ± 50	1.85 ± 0.17	3.56	0.631
16.76 μm (E)	1400 ± 50	$7.5\times10^{16} \pm 0.5\times 10^{16}$	1370^{+50}_{-53}	$0.0463^{+0.0031}_{-0.0032}$	5.31	0.631
S Peg 2009-01-05						
13.49 μm (E)	1400 ± 50	$1.0\times10^{17} \pm 0.25\times 10^{17}$	1390 ± 50	$0.0669^{+0.0017}_{-0.0017}$	5.60	0.098
13.87 μm (E)	500 ± 50	$5.50\times10^{17} \pm 0.5\times 10^{17}$	498 ± 50	1.86 ± 0.17	4.07	0.098
14.98 μm (A, vw)	750 ± 50	$1.55\times10^{16} \pm 0.05\times 10^{16}$	808 ± 45	0.346 ± 0.014	2.52	0.098
16.18 μm (E)	500 ± 50	$5.50\times10^{17} \pm 0.5\times 10^{17}$	498 ± 50	1.85 ± 0.17	3.94	0.098
16.76 μm (E)	1400 ± 50	$1.0\times10^{17} \pm 0.25\times 10^{17}$	1370^{+50}_{-50}	$0.0620^{+0.016}_{-0.0016}$	5.43	0.098

Continued on next page

Target	T_{kin}(K)	N (cm^{-2})	T_{exc} (K)	τ	R (R_*)	ϕ
S Ser 2008-08-13						
13.49 μm (E)	1400 $\pm$ 50	$5.5\times10^{16} \pm 0.5\times 10^{16}$	1380 $\pm$50	0.0357 $\pm$0.0034	6.97	0.620
13.87 μm (E)	550 $\pm$ 50	$4.0\times10^{17} \pm 0.5\times 10^{17}$	546 $\pm$49	1.46 $\pm$0.18	3.60	0.620
14.98 μm (A)	700 $\pm$ 50	$2.55\times10^{16} \pm 0.05\times 10^{16}$	747 $\pm$ 48	0.729 $\pm$ 0.015	2.85	0.620
16.18 μm (E)	550 $\pm$ 50	$4.0\times10^{17} \pm 0.5\times 10^{17}$	547 $\pm$49	1.44 $\pm$0.18	3.50	0.620
16.76 μm (E)	1400 $\pm$ 50	$5.5\times10^{16} \pm 0.5\times 10^{16}$	1340$\pm$50	0.0334$\pm$0.0034	6.86	0.620
S Ser 2008-09-02						
13.49 μm (E)	1400 $\pm$ 50	$8.0\times10^{16} \pm 0.5\times 10^{16}$	1380 $\pm$50	0.0525 $\pm$0.0034	6.52	0.671
13.87 μm (E)	550 $\pm$ 50	$4.0\times10^{17} \pm 0.5\times 10^{17}$	546 $\pm$49	1.46 $\pm$0.18	3.92	0.671
14.98 μm (A)	700 $\pm$ 50	$2.20\times10^{16} \pm 0.05\times 10^{16}$	751 $\pm$ 48	0.625 $\pm$ 0.015	2.92	0.671
16.18 μm (E)	550 $\pm$ 50	$4.0\times10^{17} \pm 0.5\times 10^{17}$	547 $\pm$49	1.44 $\pm$0.18	3.81	0.671
16.76 μm (E)	1400 $\pm$ 50	$8.0\times10^{16} \pm 0.5\times 10^{16}$	1350$\pm$50	0.0490$\pm$0.0031	6.25	0.671
SS Cas 2008-08-15						
13.49 μm (E)	$\sim$ 12,000	$5\times10^{15} \pm 1\times 10^{15}$	10,900 $\pm$?	0.00105 $\pm$ 0.00014		0.029
13.87 μm (E)	350 $\pm$ 50	$1.4\times10^{17} \pm 0.1\times 10^{15}$	346 $\pm$ 49	0.27 $\pm$0.020	13.31	0.029
14.98 μm (E, w)	350 $\pm$ 50	$3.5\times10^{15} \pm 0.25\times 10^{15}$	339 $\pm$ 46	0.220 $\pm$ 0.018	12.20	0.029
16.18 μm (E)	350 $\pm$ 50	$1.4\times10^{17} \pm 0.1\times 10^{15}$	347 $\pm$ 49	0.28 $\pm$ 0.020	11.78	0.029
16.76 μm (E)	$\sim$12,000	$5\times10^{15} \pm 1\times 10^{15}$	8200 $\pm$?	0.000814 $\pm$ 0.00016		0.029
SS Cas 2008-09-04						
13.49 μm (E)	2400 $\pm$ 100	$5.5\times10^{15} \pm 0.5\times 10^{15}$	2340 $\pm$ 100	0.00276 $\pm$ 0.00025		0.169
13.87 μm (E)	350 $\pm$ 50	$1.3\times10^{17} \pm 0.1\times 10^{15}$	346 $\pm$ 49	0.250 $\pm$0.02	13.74	0.169
14.98 μm (E, w)	350 $\pm$ 50	$2.30\times10^{15} \pm 0.25\times 10^{15}$	339 $\pm$ 46	0.146 $\pm$ 0.016	14.28	0.169
16.18 μm (E)	350 $\pm$ 50	$1.3\times10^{17} \pm 0.1\times 10^{15}$	347 $\pm$ 49	0.260 $\pm$0.02	11.93	0.169
16.76 μm (E)	2400 $\pm$ 100	$5.5\times10^{15} \pm 0.5\times 10^{15}$	2200 $\pm$ 80	0.00260 $\pm$ 0.00023		0.169

Continued on next page

Target	T_{kin}(K)	N (cm^{-2})	T_{exc} (K)	τ	R (R_*)	ϕ
SS Cas 2008-10-06						
13.49 μm (E)	$\sim$ 10,000	$4.5\times10^{15} \pm 0.5\times 10^{15}$	9420^{+880}_{-900}	0.000734 ± 0.000082		0.386
13.87 μm (E)	350 ± 50	$1.4\times10^{17} \pm 0.1\times 10^{15}$	346 ± 49	0.270 ± 0.020	13.79	0.386
14.98 μm (E, w)	400 ± 50	$3.25\times10^{15} \pm 0.25\times 10^{15}$	385 ± 46	0.191 ± 0.015	11.21	0.386
16.18 μm (E)	350 ± 50	$1.40\times10^{17} \pm 0.1\times 10^{15}$	347 ± 49	0.280 ± 0.020	12.02	0.386
16.76 μm (E)	$\sim$ 10,000	$4.5\times10^{15} \pm 0.5\times 10^{15}$	7210^{+510}_{-540}	0.000821 ± 0.000091		0.386
W Her 2008-06-05						
13.49 μm (E)	2000 ± 100	$1.0\times10^{16} \pm 0.1\times 10^{16}$	1960^{+880}_{-900}	0.000734 ± 0.00557		0.473
13.87 μm (E)	350 ± 50	$1.7\times10^{17} \pm 0.1\times 10^{17}$	346 ± 49	0.328 ± 0.020	12.84	0.473
14.98 μm (E, w)	400 ± 50	$4.5\times10^{15} \pm 0.5\times 10^{15}$	386 ± 46	0.263 ± 0.029	10.15	0.473
16.18 μm (E)	350 ± 50	$1.7\times10^{17} \pm 0.1\times 10^{17}$	347 ± 49	0.340 ± 0.020	11.25	0.473
16.76 μm (E)	2000 ± 100	$1.0\times10^{16} \pm 0.1\times 10^{16}$	1860^{+510}_{-540}	0.00521 ± 0.000091		0.473
W Her 2008-07-11						
13.49 μm (E)	2400 ± 100	$1.0\times10^{16} \pm 0.1\times 10^{16}$	2340 ± 100	0.00503 ± 0.00051		0.604
13.87 μm (E)	350 ± 50	$1.4\times10^{17} \pm 0.1\times 10^{17}$	346 ± 49	0.270 ± 0.020	13.49	0.604
14.98 μm (E, w)	400 ± 50	$2.75\times10^{15} \pm 0.25\times 10^{15}$	384 ± 45	0.161 ± 0.015	12.46	0.604
16.18 μm (E)	350 ± 50	$1.4\times10^{17} \pm 0.1\times 10^{17}$	347 ± 49	0.280 ± 0.020	11.83	0.604
16.76 μm (E)	2400 ± 100	$1.0\times10^{16} \pm 0.1\times 10^{16}$	2200 ± 80	0.00473 ± 0.00048		0.604
W Her 2008-08-13						
13.49 μm (E)	2000 ± 100	$1.0\times10^{16} \pm 0.1\times 10^{16}$	1960 ± 100	0.00557 ± 0.00057		0.725
13.87 μm (E)	350 ± 50	$1.35\times10^{17} \pm 0.05\times 10^{17}$	346 ± 49	0.260 ± 0.010	13.42	0.725
14.98 μm (E, vw)	400 ± 50	$2.1\times10^{15} \pm 0.4\times 10^{15}$	384 ± 45	0.123 ± 0.024	13.80	0.725
16.18 μm (E)	350 ± 50	$1.35\times10^{17} \pm 0.05\times 10^{17}$	347 ± 49	0.270 ± 0.010	11.89	0.725
16.76 μm (E)	2000 ± 100	$1.0\times10^{16} \pm 0.1\times 10^{16}$	1860 ± 100	0.00521 ± 0.00053		0.725

Continued on next page

Target	T_{kin}(K)	N (cm^{-2})	T_{exc} (K)	τ	R (R_*)	ϕ
W Her 2008-09-01						
13.49 μm (E)	2000 $\pm$100	$1.0\times10^{16} \pm 0.1\times 10^{16}$	1960 $\pm$ 100	0.00557 $\pm$ 0.00057		0.794
13.87 μm (E)	350 $\pm$ 50	$1.3\times10^{17} \pm 0.1\times 10^{17}$	346 $\pm$49	0.250 $\pm$0.020	13.31	0.794
14.98 μm (E, vw)	400 $\pm$ 50	$1.7\times10^{15} \pm 0.4\times 10^{15}$	383 $\pm$ 45	0.099 $\pm$ 0.023	14.82	0.794
16.18 μm (E)	350 $\pm$ 50	$1.3\times10^{17} \pm 0.1\times 10^{17}$	347 $\pm$49	0.260 $\pm$0.020	11.78	0.794
16.76 μm (E)	2000 $\pm$ 100	$1.0\times10^{16} \pm 0.1\times 10^{16}$	1860 $\pm$ 100	0.00521 $\pm$ 0.00053		0.794
W Her 2008-10-05						
13.49 μm (E)	2500 $\pm$100	$9.1\times10^{16} \pm 0.1\times 10^{16}$	2440 $\pm$ 100	0.00447 $\pm$ 0.00005		0.919
13.87 μm (E)	350 $\pm$ 50	$1.55\times10^{17} \pm 0.1\times 10^{17}$	346 $\pm$49	0.299 $\pm$0.020	12.91	0.919
14.98 μm (E, w)	400 $\pm$ 50	$4.5\times10^{15} \pm 0.5\times 10^{15}$	386 $\pm$ 45	0.263 $\pm$ 0.029	10.26	0.919
16.18 μm (E)	350 $\pm$ 50	$1.55\times10^{17} \pm 0.1\times 10^{17}$	347 $\pm$49	0.310 $\pm$0.020	11.44	0.919
16.76 μm (E)	2500 $\pm$ 100	$9.1\times10^{16} \pm 0.1\times 10^{16}$	2280 $\pm$ 90	0.00420 $\pm$ 0.00005		0.919
RT Cyg 2008-06-05						
13.49 μm (E)						0.654
13.87 μm (E)	350 $\pm$ 50	$1.2\times10^{17} \pm 0.1\times 10^{17}$	346 $\pm$49	0.231 $\pm$0.020	12.02	0.654
14.98 μm (E, vw)	400 $\pm$ 50	$2\times10^{15} \pm 0.2\times 10^{15}$	384 $\pm$ 46	0.117 $\pm$ 0.012	11.69	0.654
16.18 μm (E)	350 $\pm$ 50	$1.2\times10^{17} \pm 0.1\times 10^{17}$	347 $\pm$49	0.240 $\pm$0.020	10.48	0.654
16.76 μm^A						0.654
RT Cyg 2008-06-29						
13.49 μm (E)						
13.87 μm (E)	350 $\pm$ 50	$1.35\times10^{17} \pm 0.05\times 10^{17}$	346 $\pm$49	0.260 $\pm$0.010	12.05	0.780
14.98 μm (E, vw)	400 $\pm$ 50	$1.9\times10^{15} \pm 0.2\times 10^{15}$	383 $\pm$ 46	0.112 $\pm$ 0.012	12.47	0.780
16.18 μm (E)	350 $\pm$ 50	$1.35\times10^{17} \pm 0.05\times 10^{17}$	347 $\pm$49	0.270 $\pm$0.010	10.63	0.780
16.76 μm^A						0.780

Continued on next page

Target	T_{kin}(K)	N (cm^{-2})	T_{exc} (K)	τ	R (R_*)	ϕ
RT Cyg 2008-08-07						
13.49 μm (E)						0.983
13.87 μm (E)	350 ± 50	$1.45\times10^{17} \pm 0.1\times 10^{17}$	346 ± 49	0.279 ± 0.020	12.68	0.983
14.98 μm (E)	550 ± 50	$2.5\times10^{15} \pm 0.25\times 10^{15}$	518 ± 45	0.112 ± 0.012	9.75	0.983
16.18 μm (E)	350 ± 50	$1.45\times10^{17} \pm 0.1\times 10^{17}$	347 ± 49	0.290 ± 0.020	11.10	0.983
16.76 μm[C]						0.983
RT Cyg 2008-09-01						
13.49 μm (E)						0.114
13.87 μm (E)	350 ± 50	$1.3\times10^{17} \pm 0.1\times 10^{17}$	346 ± 49	0.250 ± 0.020	12.96	0.114
14.98 μm (E, w)	550 ± 50	$1.7\times10^{15} \pm 0.2\times 10^{15}$	517 ± 45	0.0766 ± 0.009	11.23	0.114
16.18 μm (E)	350 ± 50	$1.3\times10^{17} \pm 0.1\times 10^{17}$	347 ± 49	0.260 ± 0.020	11.30	0.114
16.76 μm[A]						0.114
RT Cyg 2008-10-02						
13.49 μm (E)						0.276
13.87 μm (E)	350 ± 50	$1.05\times10^{17} \pm 0.05\times 10^{17}$	346 ± 49	0.202 ± 0.010	12.92	0.276
14.98 μm (E, vw)	400 ± 50	$1.2\times10^{15} \pm 0.3\times 10^{15}$	383 ± 45	0.0706 ± 0.018	14.57	0.276
16.18 μm (E)	350 ± 50	$1.05\times10^{17} \pm 0.05\times 10^{17}$	347 ± 49	0.209 ± 0.010	11.35	0.276
16.76 μm[A]						0.276
RT Cyg 2008-11-06						
13.49 μm (E)						0.459
13.87 μm (E)	350 ± 50	$2.1\times10^{17} \pm 0.1\times 10^{17}$	347 ± 49	0.405 ± 0.020	9.26	0.459
14.98 μm (A, w)	600 ± 50	$3.3\times10^{15} \pm 0.05\times 10^{15}$	$694\ ^{+44}_{-40}$	0.106 ± 0.003	3.34	0.459
16.18 μm (E)	350 ± 50	$2.1\times10^{17} \pm 0.1\times 10^{17}$	347 ± 49	0.420 ± 0.020	8.23	0.459
16.76 μm (E, vw)						0.459

Continued on next page

Target	T_{kin}(K)	N (cm^{-2})	T_{exc} (K)	τ	R (R_*)	ϕ
RT Cyg 2008-11-30						
13.49 μm (E)						0.584
13.87 μm (E)	350 ± 50	$2.1\times10^{17} \pm 0.1\times 10^{17}$	347 ± 49	0.405 ± 0.020	9.45	0.584
14.98 μm (A, w)	600 ± 50	$3.2\times10^{15} \pm 0.1\times 10^{15}$	695^{+43}_{-39}	0.103 ± 0.003	3.30	0.584
16.18 μm (E)	350 ± 50	$2.1\times10^{17} \pm 0.1\times 10^{17}$	347 ± 50	0.420 ± 0.020	8.44	0.584
16.76 μm^A						0.584
R Cet 2008-09-03						
13.49 μm (E)	1400 ± 100	$8.5\times10^{16} \pm 0.5\times 10^{16}$	1430 ± 90	0.0508 ± 0.0003	7.46	0.850
13.87 μm (E)	450 ± 50	$4.1\times10^{17} \pm 0.1\times 10^{17}$	446 ± 50	1.23 ± 0.030	6.28	0.850
14.98 μm (E, S)	450 ± 50	$2.5\times10^{16} \pm 0.15\times 10^{16}$	441 ± 48	1.32 ± 0.08	5.15	0.850
16.18 μm (E)	450 ± 50	$4.1\times10^{17} \pm 0.1\times 10^{17}$	447 ± 50	1.24 ± 0.030	5.91	0.850
16/76.49 μm (E)	1400 ± 100	$8.5\times10^{16} \pm 0.5\times 10^{16}$	1400 ± 90	0.0473 ± 0.0003	7.10	0.850
R Cet 2008-10-01						
13.49 μm (E)	≥ 5000	$3.75\times10^{16} \pm 0.1\times 10^{16}$	≥ 4530	0.0102 ± 0.0003		0.019
13.87 μm (E)	500 ± 50	$3.6\times10^{17} \pm 0.1\times 10^{17}$	495 ± 50	1.22 ± 0.030	6.36	0.019
14.98 μm (E, S)	500 ± 50	$5\times10^{16} \pm 0.3\times 10^{16}$	493 ± 49	2.38 ± 0.14	4.94	0.019
16.18 μm (E)	500 ± 50	$3.6\times10^{17} \pm 0.1\times 10^{17}$	496 ± 50	1.21 ± 0.030	6.05	0.019
16/76.49 μm (E)	≥ 5000	$3.75\times10^{16} \pm 0.1\times 10^{16}$	≥ 4010	0.00998 ± 0.0003		0.019
Z Cyg 2008-06-05						
13.49 μm (E)	1600 ± 200	$5\times10^{16} \pm 0.5\times 10^{16}$	1610 ± 180	0.0284 ± 0.0003	8.35	0.725
13.87 μm (E)	500 ± 100	$1.3\times10^{17} \pm 0.15\times 10^{17}$	492 ± 98	0.438 ± 0.034	7.37	0.725
14.98 μm (E, S)	500 ± 100	$3.\times10^{16} \pm 0.5\times 10^{16}$	491 ± 96	1.67 ± 0.24	4.59	0.725
16.18 μm^B (E)	500 ± 100	$1.3\times10^{17} \pm 0.15\times 10^{17}$	493 ± 98	0.438 ± 0.033		0.725
16.76 μm (E, vw)	1600 ± 200	$5\times10^{16} \pm 0.5\times 10^{16}$	1560 ± 170	0.0265 ± 0.0003		0.725

Continued on next page

Target	T_{kin}(K)	N (cm^{-2})	T_{exc} (K)	τ	R (R_*)	ϕ
Z Cyg 2008-07-11						
13.49 μm (E)	1600 $\pm$ 200	$4.5\times10^{16} \pm 0.5\times 10^{16}$	1610 $\pm$ 180	0.0255 $\pm$ 0.0003	6.45	0.859
13.87 μm (E)	500 $\pm$ 100	$1.35\times10^{17} \pm 0.1\times 10^{17}$	492 $\pm$98	0.455 $\pm$0.034	7.26	0.859
14.98 μm (E, S)	500 $\pm$ 100	$4.25\times10^{16} \pm 0.5\times 10^{16}$	492 $\pm$96	2.03 $\pm$ 0.23	4.50	0.859
16.18 μm^B (E)	500 $\pm$ 100	$1.35\times10^{17} \pm 0.1\times 10^{17}$	493 $\pm$98	0.455 $\pm$0.033		0.859
16.76 μm (E, vw)	1600 $\pm$ 200	$4.5\times10^{16} \pm 0.5\times 10^{16}$	1560 $\pm$ 170	0.0238 $\pm$ 0.0003		0.859
Z Cyg 2008-08-07						
13.49 μm (E)	2400 $\pm$ 200	$2.5\times10^{16} \pm 0.25\times 10^{16}$	2310 $\pm$ 170	0.0115 $\pm$ 0.0003	10.58	0.961
13.87 μm (E)	500 $\pm$ 100	$9\times10^{16} \pm 0.5\times 10^{16}$	491 $\pm$98	0.303 $\pm$0.017	8.08	0.961
14.98 μm (E, S)	450 $\pm$ 100	$2.75\times10^{16} \pm 0.5\times 10^{16}$	441 $\pm$95	1.45 $\pm$ 0.26	4.97	0.961
16.18 μm^B (E)	500 $\pm$ 100	$9\times10^{16} \pm 0.5\times 10^{16}$	492 $\pm$98	0.302 $\pm$0.017		0.961
16.76 μm^A (E, vw)	2400 $\pm$ 200	$2.5\times10^{16} \pm 0.25\times 10^{16}$	2190 $\pm$ 150	0.0108 $\pm$ 0.0003		0.961
Z Cyg 2008-09-01						
13.49 μm (E)	2400 $\pm$ 200	$1.5\times10^{16} \pm 0.25\times 10^{16}$	2320 $\pm$ 180	0.00689 $\pm$ 0.0012		0.054
13.87 μm (E)	450 $\pm$ 100	$1.5\times10^{17} \pm 0.25\times 10^{17}$	443 $\pm$98	0.449 $\pm$0.075	7.62	0.054
14.98 μm (E, S)	500 $\pm$ 100	$1.2\times10^{16} \pm 0.05\times 10^{16}$	482 $\pm$93	0.583 $\pm$ 0.024	5.56	0.054
16.18 μm (E,)	450 $\pm$ 100	$1.5\times10^{17} \pm 0.25\times 10^{17}$	445 $\pm$98	0.453 $\pm$0.076	7.09	0.054
16.76 μm^A (E, vw)	2400 $\pm$ 200	$1.5\times10^{16} \pm 0.25\times 10^{16}$	2190 $\pm$ 150	0.00647 $\pm$ 0.0011		0.054
Z Cyg 2008-10-02						
13.49 μm (E)	3000 $\pm$ 200	$1.5\times10^{16} \pm 0.25\times 10^{16}$	2840 $\pm$ 180	0.00596 $\pm$ 0.001		0.170
13.87 μm (E)	450 $\pm$ 100	$1.75\times10^{17} \pm 0.25\times 10^{17}$	444 $\pm$98	0.524 $\pm$0.075	6.58	0.170
14.98 μm (E, S)	500 $\pm$ 100	$1\times10^{16} \pm 0.2\times 10^{16}$	480 $\pm$93	0.487 $\pm$ 0.096	6.74	0.170
16.18 μm^B (E)	450 $\pm$ 100	$1.75\times10^{17} \pm 0.25\times 10^{17}$	445 $\pm$98	0.529 $\pm$0.076		0.170
16.76 μm^A (E, vw)	3000 $\pm$ 200	$1.5\times10^{16} \pm 0.25\times 10^{16}$	2630 $\pm$ 150	0.00564 $\pm$ 0.001		0.170

Continued on next page

Target	T_{kin}(K)	N (cm^{-2})	T_{exc} (K)	τ	R (R_*)	ϕ
Z Cyg 2008-11-08						
13.49 μm (E)	2400 $\pm$ 200	$1.75\times10^{16} \pm 0.25\times 10^{16}$	2310 $\pm$ 180	0.00805 $\pm$ 0.0012		0.309
13.87 μm (E)	650 $\pm$ 100	$1.4\times10^{17} \pm 0.1\times 10^{17}$	645 $\pm$97	0.549 $\pm$0.039	4.78	0.309
14.98 μm (E, S)	450 $\pm$ 100	$0.95\times10^{16} \pm 0.05\times 10^{16}$	434 $\pm$92	0.508 $\pm$ 0.026	6.40	0.309
16.18 μm^B (E)	650 $\pm$ 100	$1.4\times10^{17} \pm 0.1\times 10^{17}$	646 $\pm$97	0.533 $\pm$0.076		0.309
16.76 μm^A (E)	2400 $\pm$ 200	$1.75\times10^{16} \pm 0.25\times 10^{16}$	2190 $\pm$ 150	0.00755 $\pm$ 0.0012		0.309
Z Cyg 2008-11-30						
13.49 μm (E, vw)	2000 $\pm$ 200	$1.25\times10^{16} \pm 0.25\times 10^{16}$	1960 $\pm$ 180	0.00634 $\pm$ 0.0013		0.391
13.87 μm (E)	650 $\pm$ 100	$1.7\times10^{17} \pm 0.1\times 10^{17}$	645 $\pm$97	0.667 $\pm$0.04	4.37	0.391
14.98 μm (E, S)	400 $\pm$ 100	$1.2\times10^{16} \pm 0.2\times 10^{16}$	389 $\pm$93	0.698 $\pm$ 0.116	6.56	0.391
16.18 μm (E)	650 $\pm$ 100	$1.7\times10^{17} \pm 0.1\times 10^{17}$	646 $\pm$97	0.647 $\pm$0.076	4.25	0.391
16.76 μm^A (E, vw)	2000 $\pm$ 200	$1.25\times10^{16} \pm 0.25\times 10^{16}$	1880 $\pm$ 150	0.00594 $\pm$ 0.0012		0.391
Y Del 2008-07-11						
13.49 μm (E,vw)						0.280
13.87 μm (E, w)	300 $\pm$ 50	$2.5\times10^{17} \pm 1\times 10^{17}$	297 $\pm$50	0.327 $\pm$0.13	13.90	0.280
14.98 μm (E,w)	450 $\pm$ 50	$9\times10^{15} \pm 1\times 10^{15}$	434 $\pm$45	0.481 $\pm$ 0.053	6.39	0.280
16.18 μm (E, w)	300 $\pm$ 50	$2.5\times10^{17} \pm 1\times 10^{17}$	298 $\pm$50	0.344 $\pm$0.14	12.06	0.280
16.76 μm (E, vw)						0.280
Y Del 2008-11-11						
13.49 μm (E,vw)						0.539
13.87 μm (E, w)	300 $\pm$ 50	$3\times10^{17} \pm 1\times 10^{17}$	297 $\pm$50	0.392 $\pm$0.13	12.69	0.539
14.98 μm (E,w)	450 $\pm$ 50	$6\times10^{15} \pm 1\times 10^{15}$	432 $\pm$46	0.322 $\pm$ 0.053	7.2	0.539
16.18 μm (E, w)	300 $\pm$ 50	$3\times10^{17} \pm 1\times 10^{17}$	298 $\pm$50	0.413 $\pm$0.14	10.92	0.539
16.76 μm (E, vw)						0.539

Continued on next page

Target	T_{kin}(K)	N (cm^{-2})	T_{exc} (K)	τ	R (R_*)	ϕ
Y Del 2008-30-11						
13.49 μm (E,vw)						0.579
13.87 μm (E, w)	300 $\pm$ 50	$3\times10^{17} \pm 1\times 10^{17}$	297 $\pm$50	0.392 $\pm$0.13	12.67	0.579
14.98 μm (E,w)	450 $\pm$ 50	$7\times10^{15} \pm 1\times 10^{15}$	432 $\pm$46	0.375 $\pm$ 0.053	6.82	0.579
16.18 μm (E, w)	300 $\pm$ 50	$3\times10^{17} \pm 1\times 10^{17}$	298 $\pm$50	0.413 $\pm$0.14	10.75	0.579
16.76 μm (E, vw)						0.579
S Lac 2008-08-07						
13.49 μm (E)	$\simeq$ 4000	$1.5\times10^{16} \pm 0.25\times 10^{16}$	$\sim$ 3700	0.00482 $\pm$ 0.0008		0.279
13.87 μm (E)	400 $\pm$ 50	$1.8\times10^{17} \pm 0.1\times 10^{17}$	395 $\pm$50	0.451 $\pm$0.025	8.55	0.279
14.98 μm (E)	400 $\pm$ 50	$6.5\times10^{15} \pm 0.5\times 10^{15}$	386 $\pm$46	0.380 $\pm$ 0.029	9.04	0.279
16.18 μm (E)	400 $\pm$ 50	$1.8\times10^{17} \pm 0.1\times 10^{17}$	396 $\pm$50	0.461 $\pm$0.026	8.84	0.279
16.76 μm (E)	$\simeq$ 4000	$1.5\times10^{16} \pm 0.25\times 10^{16}$	$\sim$ 3340	0.00465 $\pm$ 0.0008		0.279
S Lac 2008-09-01						
13.49 μm (E)	$\simeq$ 4000	$1.5\times10^{16} \pm 0.25\times 10^{16}$	$\sim$ 3700	0.00482 $\pm$ 0.0008		0.383
13.87 μm (E)	400 $\pm$ 50	$4.2\times10^{17} \pm 0.1\times 10^{17}$	397 $\pm$50	1.05 $\pm$0.03	7.25	0.383
14.98 μm (A,w)	800 $\pm$ 50	$1.1\times10^{16} \pm 0.05\times 10^{16}$	856 $\pm$45	0.259 $\pm$ 0.012	2.80	0.383
16.18 μm (E)	400 $\pm$ 50	$4.2\times10^{17} \pm 0.1\times 10^{17}$	398 $\pm$50	1.08 $\pm$0.03	6.55	0.383
16.76 μm (E)	$\simeq$ 4000	$1.5\times10^{16} \pm 0.25\times 10^{16}$	$\sim$ 3340	0.00465 $\pm$ 0.0008		0.383
S Lac 2008-12-15						
13.49 μm (E)	$\simeq$ 4000	$1\times10^{16} \pm 0.25\times 10^{16}$	$\sim$ 3710	0.00321 $\pm$ 0.0008		0.819
13.87 μm (E)	400 $\pm$ 50	$4.2\times10^{17} \pm 0.1\times 10^{17}$	397 $\pm$50	1.05 $\pm$0.03	7.01	0.819
14.98 μm (A)	750 $\pm$ 50	$1.4\times10^{16} \pm 0.05\times 10^{16}$	710 $\pm$45	0.425 $\pm$ 0.015	3.39	0.819
16.18 μm (E)	400 $\pm$ 50	$4.2\times10^{17} \pm 0.1\times 10^{17}$	398 $\pm$50	1.08 $\pm$0.03	6.41	0.819
16.76 μm (E)	$\simeq$ 4000	$1\times10^{16} \pm 0.25\times 10^{16}$	$\sim$ 3350	0.00311 $\pm$ 0.0008		0.819

Continued on next page

Target	T_{kin}(K)	N (cm^{-2})	T_{exc} (K)	τ	R (R_*)	ϕ
S Psc 2008-08-12						
13.49 μm (E)	$\simeq$ 3000	$3\times10^{16} \pm 0.25\times 10^{16}$	$\sim$ 2830	0.0120 $\pm$ 0.001		0.990
13.87 μm (E)	500 $\pm$ 50	$6\times10^{17} \pm 0.5\times 10^{17}$	497 $\pm$50	2.02 $\pm$0.17	5.0	0.990
14.98 μm (A)	1000 $\pm$ 100	$4.75\times10^{16} \pm 0.25\times 10^{16}$	1030 $\pm$107	0.829 $\pm$ 0.045	2.17	0.990
16.18 μm (E)	500 $\pm$ 50	$6\times10^{17} \pm 0.5\times 10^{17}$	497 $\pm$50	2.02 $\pm$0.17	4.72	0.990
16.76 μm (E)	$\simeq$ 3000	$3\times10^{16} \pm 0.25\times 10^{16}$	$\sim$ 2640	0.0113 $\pm$ 0.001		0.990
S Psc 2008-09-03						
13.49 μm (E)	$\simeq$ 3000	$3\times10^{16} \pm 0.25\times 10^{16}$	$\sim$ 2830	0.0120 $\pm$ 0.001		0.042
13.87 μm (E)	500 $\pm$ 50	$5.5\times10^{17} \pm 0.5\times 10^{17}$	497 $\pm$50	1.86 $\pm$0.17	4.89	0.042
14.98 μm (A)	1000 $\pm$ 100	$5.75\times10^{16} \pm 0.25\times 10^{16}$	1030 $\pm$110	1.01 $\pm$ 0.045	2.18	0.042
16.18 μm (E)	500 $\pm$ 50	$5.5\times10^{17} \pm 0.5\times 10^{17}$	497 $\pm$50	1.85 $\pm$0.17	4.67	0.042
16.76 μm (E)	$\simeq$ 3000	$3\times10^{16} \pm 0.25\times 10^{16}$	$\sim$ 2640	0.0113 $\pm$ 0.001		0.042
U Cvn 2008-06-05						
13.49 μm (E)	$\simeq$ 2500	$2.25\times10^{16} \pm 0.25\times 10^{16}$	$\sim$ 2410	0.0101 $\pm$ 0.0012		0.948
13.87 μm (E)	450 $\pm$ 50	$3.3\times10^{17} \pm 0.1\times 10^{17}$	445 $\pm$50	0.989 $\pm$0.031	5.96	0.948
14.98 μm (A)	800 $\pm$ 50	$1.65\times10^{16} \pm 0.05\times 10^{16}$	850 $\pm$46	0.392 $\pm$ 0.012	2.55	0.948
16.18 μm (E)	450 $\pm$ 50	$3.3\times10^{17} \pm 0.1\times 10^{17}$	446 $\pm$50	0.999 $\pm$0.031	5.43	0.948
16.76 μm (E)	$\simeq$ 2500	$2.25\times10^{16} \pm 0.25\times 10^{16}$	$\sim$ 2270	0.00949 $\pm$ 0.0011		0.948
U Cvn 2008-07-02						
13.49 μm (E)	$\simeq$ 3000	$2.25\times10^{16} \pm 0.25\times 10^{16}$	$\sim$ 2830	0.00897 $\pm$ 0.001		0.036
13.87 μm (E)	500 $\pm$ 50	$3.2\times10^{17} \pm 0.1\times 10^{17}$	495 $\pm$50	1.08 $\pm$0.03	5.44	0.036
14.98 μm (A)	750 $\pm$ 50	$2.05\times10^{16} \pm 0.05\times 10^{16}$	800 $\pm$47	0.533 $\pm$ 0.014	2.84	0.036
16.18 μm (E)	500 $\pm$ 50	$3.2\times10^{17} \pm 0.1\times 10^{17}$	496 $\pm$50	1.08 $\pm$0.03	5.10	0.036
16.76 μm (E)	$\simeq$ 3000	$2.25\times10^{16} \pm 0.25\times 10^{16}$	$\sim$ 2640	0.00847 $\pm$ 0.001		0.036

Continued on next page

Target	T_{kin}(K)	N (cm^{-2})	T_{exc} (K)	τ	R (R_*)	ϕ
UX Cyg 2008-07-11						
14.98 μm (A)	550 ± 50	$3.5\times10^{16} \pm 0.5\times 10^{16}$	592 ± 50	1.36 ± 0.2	4.75	0.225
UX Cyg 2008-08-08						
14.98 μm (A)	550 ± 50	$3\times10^{16} \pm 0.5\times 10^{16}$	597 ± 50	1.15 ± 0.2	4.77	0.276
UX Cyg 2008-11-13						
13.87 μm (E, w)	600 ± 50	$4\times10^{17} \pm 0.5\times 10^{17}$	595 ± 49	1.53 ± 0.20	3.49	0.454
14.98 μm (A)	550 ± 50	$5\times10^{16} \pm 0.5\times 10^{16}$	581 ± 49	1.98 ± 0.21	4.21	0.454
16.18 μm^B (E)						0.454
UX Cyg 2008-12-01						
13.87 μm (E)	600 ± 50	$5\times10^{17} \pm 0.5\times 10^{17}$	596 ± 49	1.91 ± 0.21	3.49	0.487
14.98 μm (A)	550 ± 50	$5\times10^{16} \pm 0.5\times 10^{16}$	581 ± 49	1.98 ± 0.21	4.29	0.487
16.18 μm^B (E)						0.487

6.3 17.62 μm Fe Feature

Every observation showed the 17.62 μm feature, across all three chemical subclasses; to check for behavior unique to chemical subclass we fit every line in our dataset. We fit the lines with Gaussian profiles and the results for the M-types C-type, and S-type Miras are presented in Tables 6.4, 6.6, and 6.5, respectively. Panels of the fits for each star are also provided in Appendix B.1. We notice that observations of different stars taken on the same day have different fit parameters which is evidence that this is a real feature. If it was an instrumental effect we would expect observations taken on the same day to result in identical fits.

We have tentatively identified this feature as Fe I as discussed in Section 3.5. When we track the line strength we notice the line is always seen in emission and the amplitude changes with the phase of the Mira, for example see Figure 3.16. Even observations close in phase show a dynamic change; R Tri had observations at $\phi = 0.153, 0.222$ and the amplitude increased from 8.8 Jy to 13.2 Jy, and for S

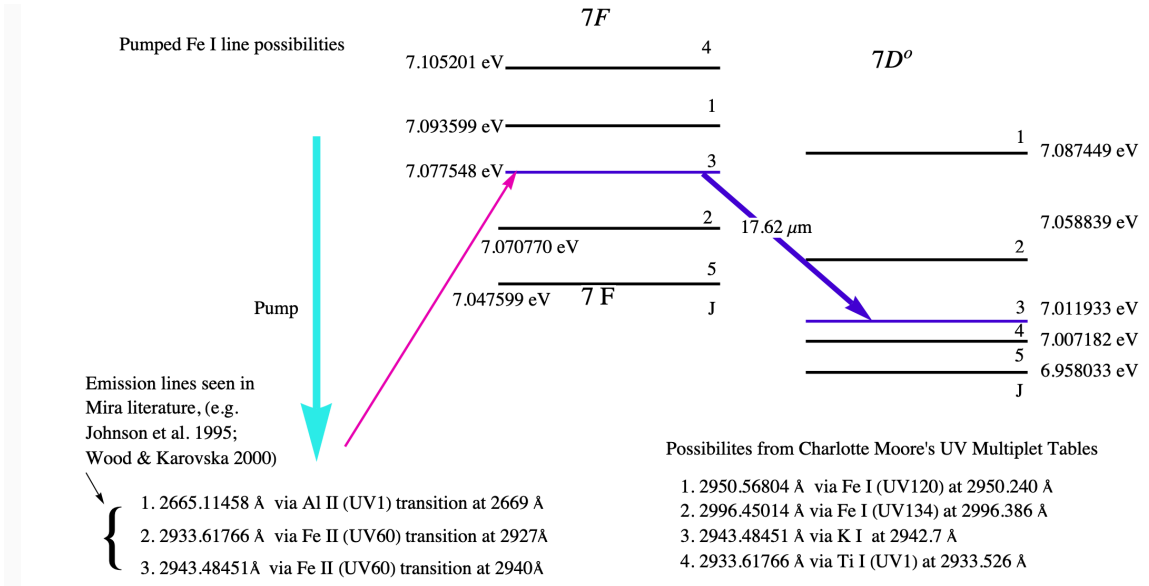

Figure 6.1: Partial Energy level diagram of Fe I. Bright emission lines previously observed in Mira atmospheres that could serve as pumps include an Al II transition and several Fe II transitions. Other possible pumps taken from Moore (1950) include Fe I, K, or Ti. One (or more) of these transitions could pump the Fe I up to the J = 3 level in the 7F state. The possible candidates all have J = 3 in their upper state, which allows them to exchange energy with 7F, J = 3 level. This extra energy is dumped into our fluoresced line at 17.62 μm.

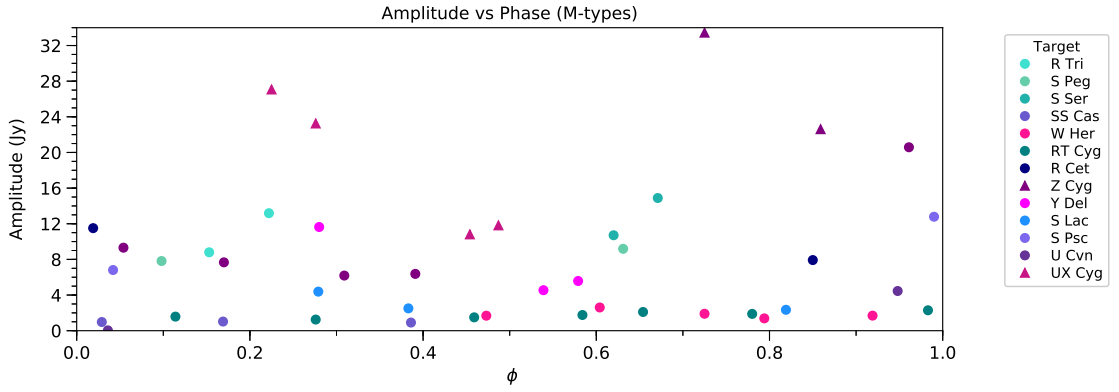

Figure 6.2: Amplitude of the 17.62 μm line vs. phase for the M-type Miras. The points marked with a triangle and square have been re-scaled to fit the frame.

Psc the amplitude dropped from 12.8 Jy to 6.9 Jy just from $\phi = 0.990$ to $\phi = 0.042$. These rapid changes with phase hint that the line might be formed in a region close to the photosphere that responds strongly to the pulsation. The amplitude of the line also spans a wide range; varying from $\sim$1 Jy to upwards of 50 Jy.

One possible explanation for the variable emission strengths is fluorescence. This involves a "pump" that highly excites Fe I atoms that then radiate photons of lower energy than the photons that came from the pump. Similar fluorescence features have been previously observed in Mira atmospheres (e.g. Willson (1972); Johnson et al. (1995); Luttermoser (2000, 1996)), but only at shorter wavelengths. Several fluorescent paths using bright emission lines previously observed in Mira variables include: 1) the Fe I transition at 2665.1 $\AA$ lies near a bright Al II] (UVI) line at 2669 $\AA$, 2) the Fe I transition at 2933.6 $\AA$ that lies near the Fe II (UV60) transition at 2933 $\AA$, 3) the Fe I transition at 2943.5 $\AA$ that lies near the Fe II (UV60) transition at 2940 $\AA$. Both Al II] and Fe II have bee observed in M-types and C-

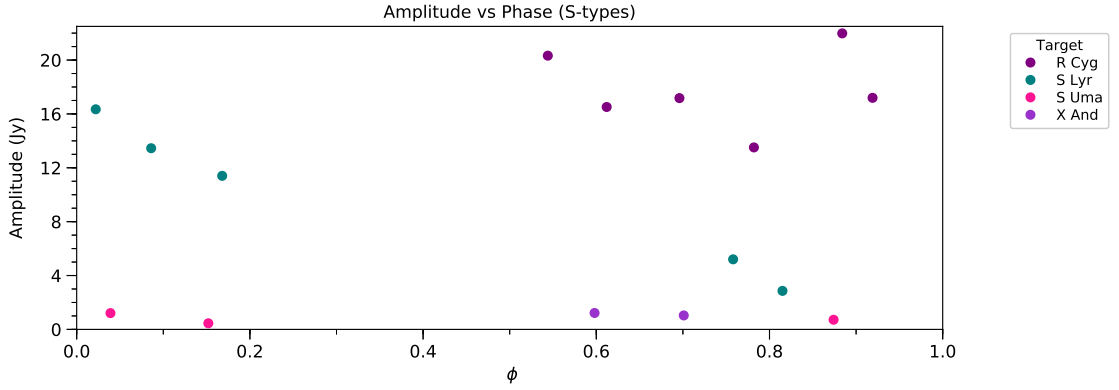

Figure 6.3: Amplitude of the 17.62 μm line vs. phase for the S-type Miras.

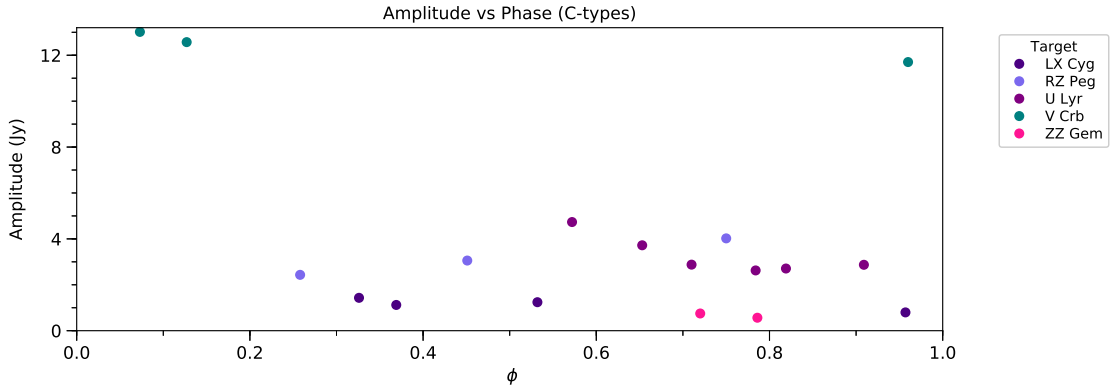

Figure 6.4: Amplitude of the 17.62 μm line vs. phase for the C-type Miras.

types (e.g. Wood & Karovska (2000); Johnson et al. (1995); Luttermoser (2000)) and so we cannot favor one over the other from a chemistry argument. These transitions are not as close in wavelengths space as previously reported pumps so we also consulted Moore (1950) for additional possibilities. These include: 1) the Fe I transition at 2950.5 $\AA$ that lies near the Fe I (UV120) line at 1950.3 $\AA$, 2) the Fe I transition at 2996.5 $\AA$ that lies near the Fe I (UV134) line at 2996.4 $\AA$, 3) the Fe I transition at 2943.5 $\AA$ that lies near the K I line at 2942.7 $\AA$, 4) the Fe I transition at 2933.6 $\AA$ that lies near the Ti I (UV1) line at 2933.5 $\AA$. The possible pumps with a partial energy diagram for Fe I are illustrated in Figure 6.1. The second set of possible fluorescent pathways includes pumps from emission lines that have not been previously reported in the literature for Mira variables, but the pumping transitions are closer in wavelength space that those in the first set

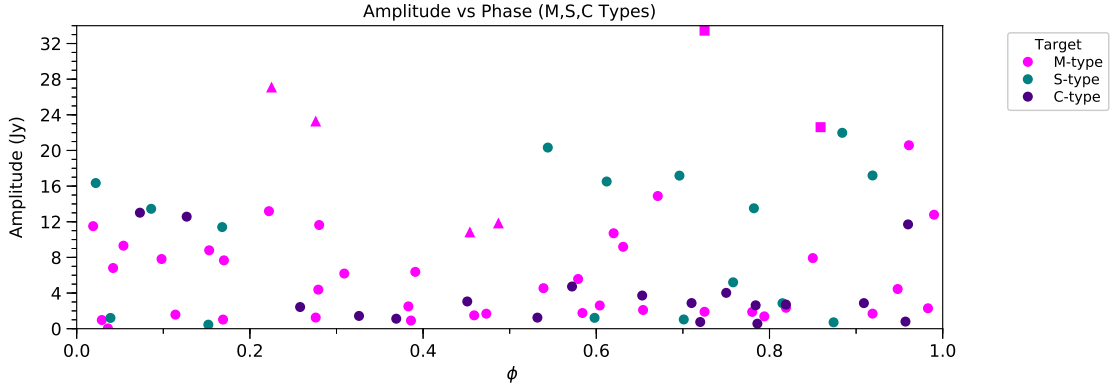

Figure 6.5: Amplitude of the 17.62 μm line vs. phase. The M-type Miras are shown in pink, the points marked with a triangle and square have been re-scaled to fit the frame. The C-type Miras are shown in purple, and the S-type Miras are shown in teal.

of possible pumps. To really narrow down the bright emission line possibilities we need UV and optical observations of our stars to check for the presence of any of these emission lines. Future work will involve diving into archives of UV and optical spectra to see if we can find more observational evidence. The UV lines peak flux occurs at $\phi = 0.3 - 0.4$ (Luttermoser 2000; Wood & Karovska 2000) and we checked our amplitudes at similar phases. We do not seem to consistently show this pattern, but we span a much broader range of phases than many of short wavelength studies done in Mira variables.

To check for a periodic pattern we plotted the amplitude vs. phase of the stars shown in Figures 6.2, 6.3, 6.4, which track the behavior of individual stars by color and 6.5 which tracks the whole set together. There is no clear phase dependence, but amplitudes above 5 Jy appear slightly more periodic. We took the data in Figure 6.5, and labeled the points according to the stars' period which is presented in Figure 6.5. Stars with periods greater than 300 days are shown with filled circles, and stars with periods less than 300 days are shown with triangles. Open circles and triangles represent reported maser activity. We notice that all but one of the maser observations lie above that 5 Jy line in the region with greater line strengths, and more variability. The stars with maser activity and longer periods show stronger emission for this Fe I line. This suggests that environments favorable to maser emission are also favorable for this Fe I transition.

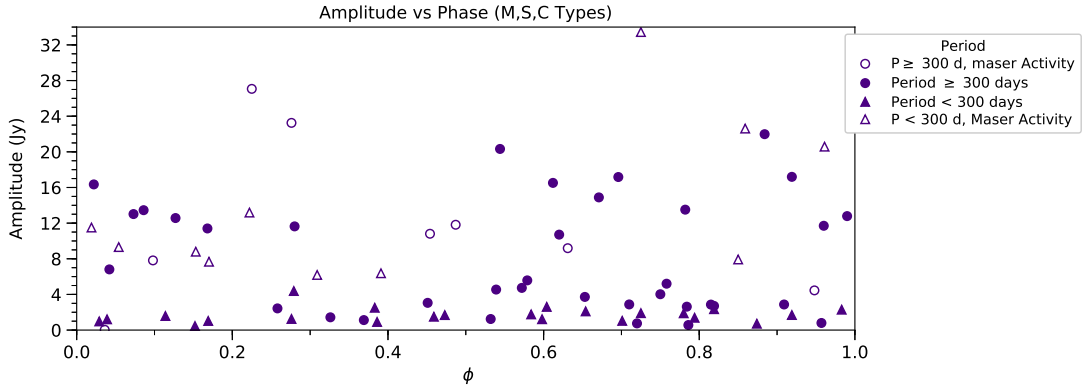

Figure 6.6: Amplitude of the 17.62 μm line vs. phase of Miras in our sample. Miras with periods greater than 300 days are shown with circles, and Miras with periods less than 300 days are shown with triangles with. R Tri, R Cet, and Z Cyg have periods less than 300 days, but show maser activity, unlike the other shorter period Miras in this sample and are indicated with open triangles.

Table 6.4: Results from Gaussian profile fitting of the 17.62 μm feature in M-type Miras. Continuum values with a * are within a dust feature.

Target	**Amplitude (Jy)**	**Line Center (μm)**	**FWHM (μm)**	**Continuum (Jy)**	ϕ
R Tri 2008-09-07	8.79662 $\pm$ 0.684783	17.6221 $\pm$ 0.000300584	0.0170067 $\pm$ 0.00146747	27.0	0.153
R Tri 2008-10-02	13.1868 $\pm$ 0.933348	17.6218 $\pm$ 0.000266262	0.0161057 $\pm$ 0.00118878	28.6	0.222
S Peg 2008-08-12	9.18918 $\pm$ 4.21907	17.6222 $\pm$ 0.000898797	0.013579 $\pm$ 0.00486961	19.1	0.631
S Peg 2009-01-05	7.81741 $\pm$ 0.237681	17.6234 $\pm$ 0.000219313 5	0.0207842 $\pm$ 0.000815364	22.3	0.098
S Ser 2008-08-13	10.7102 $\pm$ 0.251476	17.6233 $\pm$ 0.000181705	0.0212043 $\pm$ 0.000641286	26.2	0.620
S Ser 2008-09-02	14.8879 $\pm$ 0.497548	17.6232 $\pm$ 0.000126997	0.0183479 $\pm$ 0.000744561	29.2	0.671
SS Cas 2008-08-15	0.973398 $\pm$ 0.148894	17.6233 $\pm$ 0.000260826	0.0164878 $\pm$ 0.00265221	2.7	0.029
SS Cas 2008-09-04	1.02568 $\pm$ 0.0545661	17.6211 $\pm$ 0.000416583	0.0197357 $\pm$ 0.00128782	2.6	0.169
SS Cas 2008-10-06	0.913407 $\pm$ 0.102866	17.6215 $\pm$ 0.00048525	0.0161661 $\pm$ 0.00193431	2.8	0.386
W Her 2008-06-05	1.68405 $\pm$ 0.123956	17.622 $\pm$ 0.000300356	0.017249 $\pm$ 0.00143176	5.2	0.473
W Her 2008-07-11	2.606 $\pm$ 0.410464	17.6221 $\pm$ 0.000408382	0.0147399 $\pm$ 0.00209194	4.7	0.604
W Her 2008-08-13	1.900 $\pm$ 0.132214	17.6218 $\pm$ 0.000287178	0.0166602 $\pm$ 0.00126209	4.3	0.725
W Her 2008-09-01	1.38272 $\pm$ 0.0820885	17.6215 $\pm$ 0.000334428	0.0179735$\pm$ 0.00126048	4.1	0.794
W Her 2008-10-05	1.69103 $\pm$ 0.34026	17.622 $\pm$ 0.000560351	0.0149156 $\pm$ 0.00276781	4.5	0.919
RT Cyg 2008-06-05	2.1 $\pm$ 0.242406	17.6221 $\pm$ 0.000314908	0.0150796 $\pm$ 0.0016246	3.3	0.654
RT Cyg 2008-06-29	1.88472 $\pm$ 0.269381	17.6223 $\pm$ 0.000341903	0.0151734 $\pm$ 0.00202032	3.8	0.780
RT Cyg 2008-08-07	2.290 $\pm$ 0.231948	17.6223 $\pm$ 0.000269352	0.0157097 $\pm$ 0.00156655	4.4	0.983
RT Cyg 2008-09-01	1.580 $\pm$ 0.232435	17.622$\pm$ 0.000464809	0.015517 $\pm$ 0.00224107	3.9	0.114
RT Cyg 2008-10-02	1.24894 $\pm$ 0.110273	17.6223$\pm$ 0.000304514	0.0169897 $\pm$ 0.00165394	3.4	0.276
RT Cyg 2008-11-06	1.499 $\pm$ 0.348611	17.6222 $\pm$ 0.000539001	0.0146567 $\pm$ 0.00301461	3.2	0.459
RT Cyg 2008-11-30	1.7611 $\pm$ 0.250936	17.6222 $\pm$ 0.000356886	0.0152587 $\pm$ 0.00204797	3.5	0.584
R Cet 2008-09-03	7.92514 $\pm$ 0.492444	17.622 $\pm$ 0.000194038	0.0157475 $\pm$ 0.000977591	21.4*	0.850
R Cet 2008-10-01	11.5073 $\pm$ 0.346959	17.6218 $\pm$ 0.000131627	0.0170319 $\pm$ 0.000573697	31.7*	0.019

Continued on next page

Target	Amplitude (Jy)	Line Center (μm)	FWHM (μm)	Continuum (Jy)	ϕ
Z Cyg 2008-06-05	74.315 $\pm$ 2.14421	17.6219 $\pm$ 0.0000952775	0.0154143 $\pm$ 0.000435292	58.4*	0.725
Z Cyg 2008-07-11	50.2474 $\pm$ 0.820367	17.623 $\pm$ 0.0000600426	0.0181964 $\pm$ 0.000356267	60.3*	0.859
Z Cyg 2008-08-07	20.583 $\pm$ 0.594001	17.623 $\pm$ 0.000117138	0.0184907 $\pm$ 0.000649938	42.8*	0.961
Z Cyg 2008-09-01	9.31418 $\pm$ 0.918114	17.6218 $\pm$ 0.000379961	0.0161776 $\pm$ 0.00167486	28.2*	0.054
Z Cyg 2008-10-02	7.66944 $\pm$ 0.748351	17.6224 $\pm$ 0.000342246	0.0172953 $\pm$ 0.00190132	32.6*	0.170
Z Cyg 2008-11-08	6.18718 $\pm$ 0.270066	17.6219 $\pm$ 0.000349429	0.0209022 $\pm$ 0.00114656	27.9*	0.309
Z Cyg 2008-11-30	6.37443 $\pm$ 0.305448	17.6223 $\pm$ 0.00032572	0.0201711 $\pm$ 0.00122117	27.5*	0.391
Y Del 2008-07-11	11.6356 $\pm$ 0.350869	17.6232 $\pm$ 0.000148329	0.0191668 $\pm$ 0.000726181	24.2*	0.280
Y Del 2008-11-11	4.54593 $\pm$ 0.191791	17.6234 $\pm$ 0.000313092	0.020922 $\pm$ 0.00113907	16.0*	0.539
Y Del 2008-30-11	5.57663 $\pm$ 0.213308	17.623$\pm$ 0.000258187	0.0204774 $\pm$ 0.00100616	16.9*	0.579
S Lac 2008-08-07	4.38288 $\pm$ 0.231681	17.6219 $\pm$ 0.000196292	0.0163037 $\pm$ 0.000909857	10.3	0.279
S Lac 2008-09-01	2.50598 $\pm$ 0.11543	17.6216 $\pm$ 0.00025589	0.0180066 $\pm$ 0.000980682	9.4	0.383
S Lac 2008-12-15	2.34659 $\pm$ 0.252178	17.6219 $\pm$ 0.000383405	0.0160709 $\pm$ 0.00178802	9.2	0.819
S Psc 2008-08-12	12.7888 $\pm$ 0.577103	17.6217 $\pm$ 0.000202886	0.0169456 $\pm$ 0.000851854	22.0	0.990
S Psc 2008-09-03	6.8091 $\pm$ 0.330474	17.6218 $\pm$ 0.000298613	0.0189904 $\pm$ 0.0011293	20.2	0.042
U Cvn 2008-06-05	4.45378 $\pm$ 0.110964	17.6217 $\pm$ 0.000171175	0.0195932 $\pm$ 0.000604679	15.2	0.948
U Cvn 2008-07-02	4.371 $\pm$ 0.0927551	17.6226 $\pm$ 0.000184297	0.0219382 $\pm$ 0.00059515	18.8	0.036
UX Cyg 2008-07-11	90.221 $\pm$ 6.87582	17.6221$\pm$ 0.000188148	0.0146241 $\pm$ 0.000988533	132.7*	0.225
UX Cyg 2008-08-08	77.5 $\pm$ 2.94171	17.6231$\pm$ 0.0000694904	0.01657 $\pm$ 0.000666289	137.6*	0.276
UX Cyg 2008-11-13	36.025 $\pm$ 3.40722	17.6221 $\pm$ 0.000283292	0.0157731 $\pm$ 0.00148817	126.1*	0.454
UX Cyg 2008-12-01	39.3929 $\pm$ 0.656492	17.6235 $\pm$ 0.00013951	0.0216612 $\pm$ 0.000463531	124.2*	0.487

Table 6.5: Results from Gaussian profile fitting of the 17.62 μm feature in S-type Miras.

Target	**Amplitude (Jy)**	**Line Center (μm)**	**FWHM (μm)**	**Continuum (Jy)**	ϕ
R Cyg 2008-07-11	20.325 $\pm$ 1.62282	17.6219 $\pm$ 0.000248983	0.0153364 $\pm$ 0.00118386	35.3	0.544
R Cyg 2008-08-06	16.516 $\pm$ 2.13293	17.622 $\pm$ 0.000369937	0.0148651 $\pm$ 0.00176854	35.2	0.612
R Cyg 2008-09-07	17.174 $\pm$ 1.97662	17.6219 $\pm$ 0.000348825	0.0150881 $\pm$ 0.00164039	39.6	0.696
R Cyg 2008-10-16	13.5124 $\pm$ 0.983255	17.6218 $\pm$ 0.000299547	13.5124 $\pm$ 0.983255	45.9	0.782
R Cyg 2008-11-18	21.9813 $\pm$ 0.850354	17.6216 $\pm$ 0.000196656	0.0174743 $\pm$ 0.000778998	63	0.884
R Cyg 2008-12-01	17.1941 $\pm$ 0.796231	17.6217 $\pm$ 0.000245412	0.017903 $\pm$ 0.000975019	67.3	0.919
S Lyr 2008-06-05	5.20319 $\pm$ 0.243559	17.6214 $\pm$ 0.000322634	0.0191467 $\pm$ 0.00109839	17.1	0.758
S Lyr 2008-06-30	2.86051 $\pm$ 0.159967	17.622 $\pm$ 0.000551754	0.0227983 $\pm$ 0.00158421	16.8	0.815
S Lyr 2008-10-05	16.3448 $\pm$ 0.272689	17.6231 $\pm$ 0.000137283	0.0216163 $\pm$ 0.000463221	33.4	0.022
S Lyr 2008-11-06	13.4531 $\pm$ 0.258745	17.6235 $\pm$ 0.000169377	0.0220327 $\pm$ 0.000541675	34.3	0.086
S Lyr 2008-12-02	11.4022 $\pm$ 0.586221	17.6217 $\pm$ 0.000254319	0.0174363 $\pm$ 0.00102978	32.9	0.168
S Uma 2008-06-05	1.20792 $\pm$ 0.155771	17.6218 $\pm$ 0.000426124	0.0152892 $\pm$ 0.00191139	2.5	0.039
S Uma 2008-07-01	0.453011 $\pm$ 0.0476647	17.622 $\pm$ 0.000605501	0.0190222 $\pm$ 0.00246123	2.2	0.152
S Uma 2008-12-15	0.715916 $\pm$ 0.074821	17.6215 $\pm$ 0.000508794	0.0169895 $\pm$ 0.00199488	2.3	0.874
X And 2008-08-12	1.2187 $\pm$ 0.0379001	17.6237$\pm$ 0.000274143	0.0219577 $\pm$ 0.000873141	4.3	0.598
X And 2008-09-04	1.03699 $\pm$ 0.318024	17.6223 $\pm$ 0.00070107	0.0150074 $\pm$ 0.0042073	3.9	0.701

Table 6.6: Results from Gaussian profile fitting of the 17.62 μm feature in C-type Miras.

Target	**Amplitude (Jy)**	**Line Center (μm)**	**FWHM (μm)**	**Continuum (Jy)**	ϕ
LX Cyg 2008-08-07	1.43206 $\pm$ 0.196281	17.6219 $\pm$ 0.000473719	0.0158982 $\pm$ 0.00222186	4.4	0.326
LX Cyg 2008-09-01	1.122 $\pm$ 0.172057	17.6219 $\pm$ 0.000548288	0.0159772 $\pm$ 0.00251942	4.2	0.369
LX Cyg 2008-12-05	1.24137 $\pm$ 0.1007	17.6217 $\pm$ 0.000380755	0.0172641 $\pm$ 0.00159077	3.8	0.532
LX Cyg 2009-01-05	0.797165$\pm$ 0.119984	17.6214 $\pm$ 0.0015743	0.0229984 $\pm$ 0.00453021	3.9	0.957
RZ Peg 2008-07-04	3.05604 $\pm$ 0.252204	17.6218 $\pm$ 0.000283078	3.05604 $\pm$ 0.252204	6.4	0.451
RZ Peg 2008-08-06	2.43332 $\pm$ 0.219781	17.6218 $\pm$ 0.000326032	0.0159513 $\pm$ 0.00148071	7.0	0.258
RZ Peg 2008-11-12	4.0221 $\pm$ 0.411805	17.6221 $\pm$ 0.000308116	0.0157167 $\pm$ 0.00160229	10.9	0.750
U Lyr 2008-06-05	4.7335 $\pm$ 0.0728251	17.6231 $\pm$ 0.00010942	0.0207483 $\pm$ 0.000410677	9.2	0.572
U Lyr 2008-07-11	3.72102 $\pm$ 0.0610917	17.6233 $\pm$ 0.000137713	0.0217115 $\pm$ 0.000457346	9.3	0.653
U Lyr 2008-08-07	2.8774 $\pm$ 0.124723	17.6215 $\pm$ 0.00024052	0.0178045 $\pm$ 0.000905363	9.1	0.710
U Lyr 2008-09-10	2.62554 $\pm$ 0.148717	17.6218 $\pm$ 0.000259286	0.0172352 $\pm$ 0.00110573	9.1	0.784
U Lyr 2008-10-02	2.70871 $\pm$ 0.147857	17.6217 $\pm$ 0.000256009	0.0172811 $\pm$ 0.00107237	9.6	0.819
U Lyr 2008-11-06	2.87092 $\pm$ 0.161357	17.6218 $\pm$ 0.000251736	0.0171951 $\pm$ 0.00109102	10.0	0.909
V Crb 2008-07-01	11.7031$\pm$ 1.33046	17.6219 $\pm$ 0.000373714	0.0155466 $\pm$ 0.00174676	29.8	0.960
V Crb 2008-08-13	13.0169 $\pm$ 0.250321	17.6232 $\pm$ 0.000150601	0.0212884 $\pm$ 0.00052681	25.8	0.073
V Crb 2008-09-02	12.571$\pm$ 0.263426	17.6231 $\pm$ 0.000153519	0.0209095 $\pm$ 0.000563925	25.6	0.127
ZZ Gem 2008-11-11	0.749519 $\pm$ 0.0544047	17.6217 $\pm$ 0.000461628	0.0189582 $\pm$ 0.00169425	2.8	0.720
ZZ Gem 2008-12-02	0.564883 $\pm$ 0.0375204	17.6218 $\pm$ 0.000630542	0.0216287 $\pm$ 0.00185899	2.9	0.786

"Any new fact or insight that I may have found has not seemed to me as a 'discovery' of mine, but rather something that has always been there and that I had chanced to pick up."'

— P. V. Subrahmanyan Chandrasekhar

Chapter 7

CONCLUSIONS AND FUTURE WORK

In this thesis, we have contributed to the ongoing research of molecule and dust production in circumstellar environments around late-type variable stars. These stars are quite dynamic, and serve as perfect laboratories to study how stars enrich their environments. Here we will summarize our main conclusions and discuss future work that can be done to improve our understanding of these environments.

7.1 Summary

The spectra analyzed in this work are part of a larger study to characterize Mira atmospheres by combining mid-IR observations with interferometric observations (Creech-Eakman et al. 2012). The latter provide basic information about the stars such as radial size and effective temperature; these are difficult-to-impossible to determine without interferometry. The Spitzer part of this experiment was designed to look at dust composition across the stellar pulsation in all three chemical subclasses. Many experiments in physics yield unexpected results, and the Spitzer observations were no exception; the spectra showed the presence of more narrow molecular and atomic features in addition to the broad solid-state dust features. The dust was analyzed in a separate doctoral study and those results are presented in Güth (2017).

We were tasked with analyzing the unanticipated features, with identification as our first step. The spectra of the Miras in our sample showed a plethora of features; we focused on the features between 13-17 μm in the M-types, the features near 14 μm in the C-types, and the previously un-observed, sharp, bright

emission line at 17.62 μm common to all three chemical sub-classes. In the M-types we identified the features at 13.49 μm, 13.87 μm, 14.98 μm, 16.18 μm, and 16.76 μm as un-resolved Q-branch bandheads of CO_2. In the C-types, we identified features at 13.7 μm, 14 μm, and 14.3 μm as un-resolved Q-branch bandheads of C_2H_2 and HCN that will be modeled in future work. We tentatively identified the new feature at 17.62 μm as Fe I, with the possibility of it being a fluoresced feature.

7.2 Oxygen Rich Miras

Once the features were identified, the next step was to create synthetic spectra to reproduce the observed features. These synthetic spectra would provide information about atmospheric conditions that created the lines. We chose to model the CO_2 emission as plane parallel slabs of material and we then calculated the radiative transfer though the slabs using the publicly available radiative transfer code, RADEX. This code has many advantages, such as working under NLTE conditions and including collisions with H_2. We created three slab layers: one for the 14.98 μm feature, one for the Fermi degenerate pair at 13.87 μm and 16.18 μm, and one for the Fermi degenerate pair at 13.49 μm and 16.76 μm. When the ν_2 band at 14.98 μm was seen in absorption, we created a 2-slab model by adding the results of the absorption slab to the slab calculated for the 13.87 μm and 16.76 μm. Our RADEX models improved the results of previous studies of CO_2 done with ISO. The RADEX results were then combined with interferometric data to estimate the emitting regions of the CO_2 layers. We calculated the radial size of each star using angular diameters measured with the Palomar Testbed Interferometer and distances estimated with parallax. The distances reported in Table 2.1 indicate that parallax data for Mira variables is quite problematic. The large discrepancy between Gaia and Hipparcos data indicate our approach to parallax measurements for Miras is largely unsuitable for these stars; the distances are the dominant source of errors in understanding the atmospheres. Miras are so extended that often their angular diameter is approximately the same size of the parallax angle they create on the sky, which makes it incredibly difficult to accurately determine the photocenter. A more accurate approach for Mira variables would be to use the parallax measurement when the star is at maximum phase because this is when it is smallest, hottest, and brightest.

The models for the 13.49 μm and 16.76 μm features created the least physical results of the five lines. Most cases we could only place an upper bound on the temperature, and we did not estimate an emitting region size. The models all showed the gas to be quite optically thin, with the highest optical depth still less that 0.1. This could make the lines fairly insensitive to the temperature and make these lines poor "thermometers". Cami et al. (2000) calculated more physically realistic models based on their ISO SWS observations, which had higher resolution than our Spitzer IRS data. This suggests higher resolution observation could produce more accurate results. These lines are quite difficult to observe from the

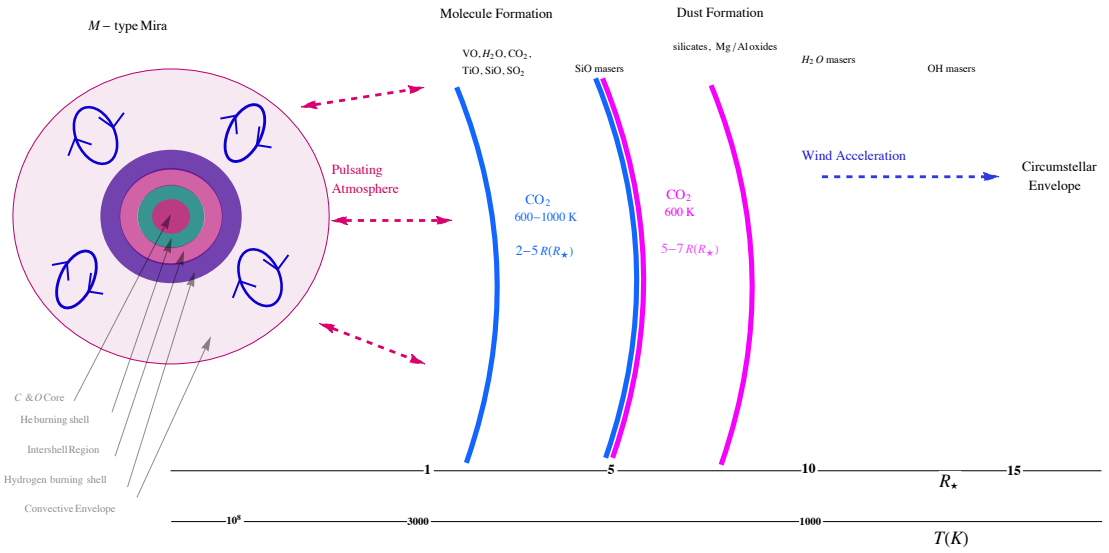

Figure 7.1: Summary of CO_2 layers for the M-type Miras in our sample that showed the 14.98 μm band in absorption.

ground, so future studies would need to be done with either the Stratospheric Observatory for Infrared Astronomy (SOFIA) or the James Web Space Telescope (JWST). The EXES instrument on board SOFIA provides R from $\sim$ 5000-100,000 and is currently operating, while JWST has yet to launch. We were awarded EXES observing time as part of SOFIA's Cycle 8, but unfortunately the observatory grounded due to the Covid-19 pandemic. We have proposed for Cycle 9, and are currently waiting for the panel decisions.

The models for the remaining three lines at 13.87 μm, 14.98 μm, and 16.18 μm produced more physical results. We will break the stars up into two categories based upon the behavior of the 14.98 μm band; those with this feature in absorption we will call the absorbing group, and those with that feature in emission we will call the emitting group.

The absorbing group was modeled with the 2-slab approach. The first layer was the absorbing layer that had kinetic temperatures that ranged from 600 K to 1000 K and we estimated the absorbing region to lie 2-5 $R_\star$. The second layer was the emitting layer that had kinetic temperatures $\sim$ 600 K, and we estimated the emitting region to lie 5-7 $R_\star$. Figure 7.1 provides an update to Figure 1.5 with the placement of the CO_2 for the absorbing group.

The emitting group was modeled with independent layers. The first layer had kinetic temperatures that ranged 400-500 K and a wide range of estimated emitting regions stretching from 5-15 $R_\star$. The second layer had kinetic temperatures 350-500 K with an estimated emitting region of 11-13 $R_\star$. Figure 7.2 places these regions in our Mira schematic. There is a bit of a mystery with the column densities in the absorbing group. The absorbing layer showed smaller column densities than the emitting layer even though it was closer to the star; we typi-

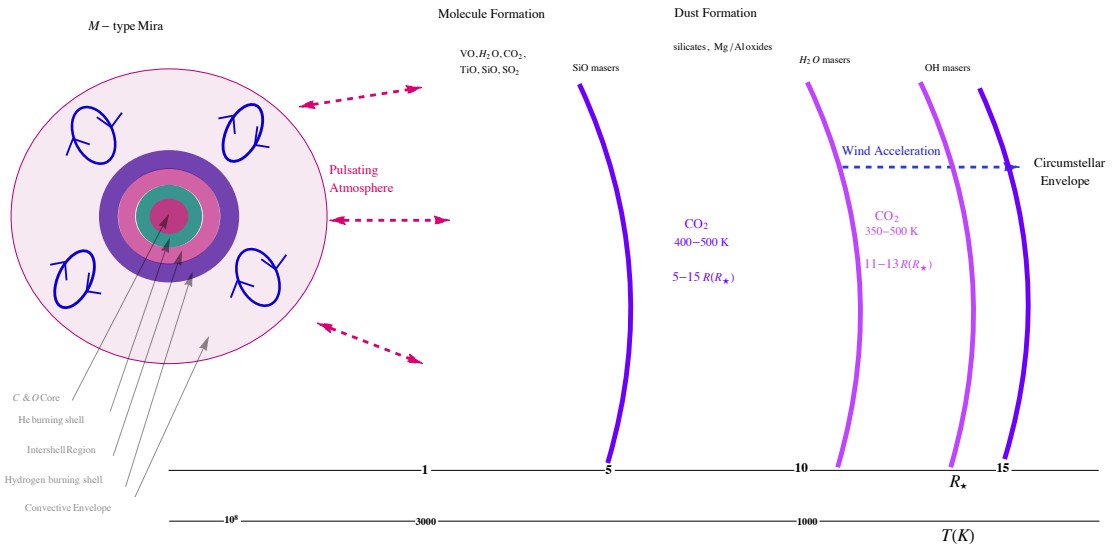

Figure 7.2: Summary of CO_2 layers for the M-type Miras in our sample that showed the 14.98 μm band in emission.

cally expect the column density to decrease at larger radii as the pulsations loft more and more material away. The increase in density could be a "snowplow" effect from the shocks moving though the atmosphere.

When we look at the CO_2 from both groups together, we conclude that CO_2 can be quite extended in the M-type atmospheres. What is most striking is the kinetic temperatures of the layers. Assuming radiative equilibrium conditions, we would expect gas at 2 $R_\star$ to be significantly warmer than even our hottest temperature of 1000 K. Willson (2000) suggest that deviations from radiative equilibrium, called "refrigeration zones" could lead to rapid dust nucleation at only a few $R_\star$. This is shown in Bowen's pulsation models as the hatched region that we have circled in red in Figure 1.4. Our CO_2 observations indicate the gas can be as cool as $\sim$600 K at 2-3 $R_\star$, which is a startling deviation from temperatures predicted from typical equilibrium calculations as can be seen in Figures 7.1 and 7.2. Our CO_2 results thus provide the first observational evidence for these "refrigeration zones".

The process of dust formation out of grains is still not fully understood. Grains can form when the local temperature drops below the condensation temperature of the specific grain. This is can begin roughly around 1500 K with grain formation radii that are typically 1.2-4 $R_\star$ (Lamers & Cassinelli 1999). It is not enough to simply condense the dust, however. In order for dust driven winds to efficiently drive mass loss, the dust must survive its journey through the atmosphere. As we follow a test grain though the atmosphere, if the local temperature exceeds the condensation temperature, the grain will sublimate rather than grow. The low kinetic temperatures of the CO_2 layers can strengthen dust production in two ways. First, it can provide an initial "refrigeration zone" to encourage

rapid dust condensation within a few $R_\star$. Then it can provide "protection" for the grains as they travel outward though the atmosphere. Part of the mass loss process involves coupling gas to dust grains, which then drag the gas along to the outer atmosphere. We can imagine a feedback process where the CO_2 protects new dust from sublimation, and this dust drags the CO_2 out to the outer atmosphere, where it continues to provide a cooling effect to further protect and encourage dust production.

A great experiment to test the relationship between CO_2 and dust nucleation can be performed by studying the 13 μm "dust" feature, which has proved difficult to identify for decades. This feature is broad like the solid state dust features, but no dust species has yet to produce satisfying fits. Currently, favored possible creators of the feature include crystalline alumina, crystalline silicates, and spinel (Sloan et al. 2003a), but crystalline dust creates sharper spectral features than what is seen in the 13 μm feature. As part of the discovery of CO_2 in AGB atmospheres, Justtanont et al. (1998) noticed that the strength of the 13 μm feature seemed to track with the strength of the CO_2 emission and they suggested that both were produced at the same location in the atmosphere under similar physical conditions. Sloan et al. (2003a) confirmed this correlation across several SE classes, and also noted that the 13 μm feature seemed to grow stronger as the 15 μm feature moved from absorption to emission. Our results indicate that when the 14.98 μm feature is seen in absorption, it is warmer and located ~ 3 $R_\star$, and when it is in emission, it is cooler and located ~ 5 $R_\star$. This suggests that the 13 μm feature grows stronger with a cooler CO_2 layer because the temperature is much more favorable for dust condensation. The 13 μm feature could be providing a peek into the condensation process. If the grains are nucleating in the CO_2 gas, then to properly account for the shape of the 13 μm feature, the addition of CO_2 emission to the sharp crystalline features could help explain why the feature appears more broad than a pure crystalline contribution would produce. In future work we can test this idea by combining results of dust spectra calculated with the DUSTY code, and combine them with our RADEX spectra to try and reproduce the 13 μm features that our in our sample of Miras.

The CO_2 lines showed dynamic behavior across the pulsation cycle as can be seen in Table 6.3. The 14.98 μm displayed the most variability and was seen in both emission and absorption. Table 6.2 tracks the 14.98 μm behavior with the stars' SE classification and period. We notice the stars that showed the ν_2 band in absorption all had periods longer than 300 days with two exceptions. R Tri has a period just short of 300 days, but unlike the other stars with shorter periods, it shows maser activity. Y Del has a period longer than 300 days, but we believe it is evolving toward an S-type so we will not include its results in this discussion. There appears to be a correlation between the pulsation period and the behavior of the ν_2 band. The longer period stars also all show maser activity from at least one molecule. This behavior was also reported in Cami (2002) who noticed that the stars that showed this band in absorption also appeared to have an optically thick emitting layer of water sitting just below the CO_2 layer. In that work, the stars that show the 14.98 μm band in absorption were all Miras with fairly long periods (> 300 days), while the stars that lacked the hot water layer and showed

the 14.98 μm band in emission were classified as Semi-regular variables, and had periods between 100-300 days. Our results are consistent with this picture; the Miras with periods less than 300 days showed the ν_2 band in emission. We have un-reduced low-resolution IRS spectra below 10 μm that can be used to check for the presence of a water features between 2-8 μm as was seen in Cami (2002); four of the six Miras that show the ν_2 band in absorption also have water masers, so it is reasonable to expect the presence of a water layer in their atmospheres. There is clearly a relationship between the pulsation period and the density of molecular layers surrounding the star.

There is much work yet to be done to fully characterize the CO_2 layers. We need additional observations across more phases to continue to tease out how the layers change within the pulsational cycle. We are planning to add several bandheads to our molecular file in an effort to address the features missed with our current file. We will also add higher J values to include more individual rovibrational transitions. The EXES mode that we proposed to use in Cycle 9 has R $\sim$ 50,000, and should be sufficient to help us determine how many additional rotational levels are needed. Higher resolution observations from SOFIA will also create tighter model constraints. We also need observations at shorter wavelengths. The region between 2-10 μm is home to transitions of several molecules including H_2O, SO_2, SiO, CO and CO_2. The features in this wavelength regime trace warmer gas closer to the star, and we need to understand these inner layers to help build a complete picture of the whole atmosphere. In particular, we would like to see if the longer period Miras in our sample show the hot water emission layer that was seen in Cami (2002) in conjunction with the ν_2 band in absorption.

We are also planning on making a file for $^{13}CO_2$ for those stars that showed features near 15.4 μm. Cami et al. (2000) also observed a feature at 15.4 μm in the ISO SWS spectrum of the semi-regular AGB star Ep Aqr and included transitions of $^{13}CO_2$ in their slab models of CO_2. When we examine energy levels of $^{13}CO_2$, we notice the largest shift from $^{12}CO_2$ is the fundamental ν_2 band at 15.4 μm, but the rest of the energy levels often overlap, e.g., the $10^00(2)$-$01^10(1)$ transition lies at 16.18 μm for $^{12}CO_2$ and at 16.20 μm for $^{13}CO_2$, which means the $^{13}CO_2$ could alter the line shapes, particularly in the wings. We will start by adding in contributions from the fundamental ν_2 band of $^{13}CO_2$ to the stars that showed a feature at 15.4 μm; if that addition strengthens the fit then we will add additional transitions to the molecular file. Adding contributions of $^{13}CO_2$ to our current models could help us estimate isotopic ratios of C^{12}/C^{13}. These ratios can then provide clues about the stellar evolution; if the ratio is small, it would suggest the star has undergone significant dredge up events, because C^{13} is created in the helium-burning shell and can only become available to alter atmospheric chemistry through dredge up (see Sections 1.3.1 and 1.3.3). A smaller ratio would then indicate a more-evolved Mira, or perhaps a Mira with more energetic convection.

7.3 Carbon Rich Miras

In addition to building more rigorous files to model CO_2 in the M-types, we also have plans to build files for HCN and C_2H_2 to model the features seen in the S and C types. The line behaviors do not seem to vary with phase as much as the CO_2 features in the M-types or the 17.62 μm do. However, we cannot confirm this lack of variability until we subtract the continuum; Aoki et al. (1999) observed a variety of carbon stars with ISO and point out that the continuum near 14 μm is difficult to determine due to contributions from SiC that peaks $\sim$ 11 μm. This study included V Crb, which is in our sample of C-type Miras. The ISO spectrum showed HCN absorption of ν_2 bands mixing with C_2H_2 near 14 μm as well as emission of the 02^00-01^10 band at 14.3 μm. Our spectra confirms the 14.3 μm feature, but we do not have the resolution to disentangle the absorption features. Aoki et al. (1999) suggest that the 02^00-01^10 band of HCN originates the circumstellar environment and is pumped by 7 μm photons emitted from the photosphere or a warm molecular layer surrounding the photosphere, and that the broad absorption of C_2H_2 originates in the photosphere or in the warm molecular layer. RADEX calculations will provide a more detailed picture of the physics behind these carbon features. We can use DUSTY to fit the SiC feature in our C-types and save the residuals in an effort to minimize the dust interference in the continuum before we perform radiative transfer calculations of the lines.

All the C-types in our sample show HCN features. This makes them great candidates to add to HCN maser surveys. Unlike the M-types, maser activity in C-types is much rarer, with vibrationally excited HCN lines accounting for most masers seen around carbon-rich stars (Menten et al. 2018). Ziurys & Turner (1986) suggested that HCN maser at 89.087 GHz maser can be pumped by 14 μm or 7 μm photons from its various ν_2 transitions. Work done in Smith et al. (2014) compared three sources of the 89 GHz maser to their respective ISO spectra presented in Sloan et al. (2003b), and found that the sources all exhibited emission at 14 μm and 14.3 μm, but two of the sources showed no emission at 7 μm. This suggests that the 14 μm photons are the more likely pump candidate. Adding the stars from our sample to maser surveys has two main advantages. We have multiple phase observations which could tease out phase dependent behavior between possible pumps and the masers. We also have interferometric data which we can use to derive the physical size of the star. This information, in addition to future RADEX models would provide a highly detailed description of the circumstellar environment that would greatly enhance our understanding of HCN masers in carbon-rich Miras.

7.4 Two Oddballs

When identifying the different features across the set, we came upon two Miras that did not necessarily match their assigned chemical subclass. The first is LX Cyg, which is classified as an S-type (C/O $\sim$1); we noticed strong absorption of

C_2H_2 at 13.7 μm as well as HCN features near 14 μm. These features indicate that it has much more carbon in its atmosphere than the other other S-types in our sample and we would classify it as a C-type. This is confirmed by Uttenthaler et al. (2016), who recently reported that LX Cyg underwent a dynamic period change from 460 days to 580 days along with a significant change in chemistry, and concluded that LX Cyg became a C-type sometime between 1975 and 2008. The next was Y Del, classified as an M-type Mira. It was originally classified by LML as a Sil++ according to IRAS LRS data, transferring to SE3-4 from Sloan & Price (1998). We noticed that the CO_2 lines were extraordinarily weak compared to the rest of the M-types, and that it showed features near 13.7 μm and 14 μm that could be from C_2H_2 or HCN. These features, when combined with the weak CO_2 lines, suggest that Y Del is an S-type rather than an M-type. Güth (2017) also reports Y Del as not fitting its assigned SE classification of SE4, and reported that the dust models indicated it behaved more like an SE7-8. The other SE4 star in our sample is S Psc and it showed completely different CO_2 behavior. Güth (2017) postulated that the SE classification provides information about how much annealing the dust has undergone; SE7-8 stars show crystalline Al_2O_3 while the other stars show amorphous Al_2O_3. Y Del being classified as an SE8 rather than an SE4 indicates older dust, and this, in conjunction with its weak CO_2 features and the presence of carbon species, all suggest that it is evolving toward an S-type star.

7.5 17.62 μm Fe Feature

One of the most unexpected results of this Spitzer study was the discovery of a new atomic feature at 17.62 μm in all three chemical subclasses. We believe this to be a real feature that may have been previously un-observed with other instruments because it was self-subtracted with on-slit nodding (see Section 3.5). The fact that we observed it with off-slit nodding and dedicated background suggests that its source is quite extended around the star. We have proposed to re-observe this feature with EXES on board SOFIA to confirm this Spitzer discovery.

We have tentatively identified this new feature as Fe I, based on available data. The line showed remarkable variability not only from star to star, but also across the pulsational phase. The strength of the feature and the lack of other nearby Fe I transitions suggests this may be a fluorescence feature. The search for possible pumping transitions has so far yielded several candidates including: one Al II (UV) transition, two Fe II (UV) transitions, two Fe I (UV) transitions, one K I (UV) transition, and one Ti I (UV) transition. The UV emission lines typically peak near $\phi = 0.4$ (Luttermoser 2000), suggesting that the 17.62 μm feature should also peak near this phase if a UV line was pumping it. The feature did not show peak strength at a consistent phase making it difficult to confirm UV lines as possible pump candidates. To continue chasing down potential pumping mechanisms, we will look through short wavelength archive data from Hubble, FUSE, GALEX, etc., to see if any of our stars were observed in the optical and

UV. Many of our sample stars only had 2-3 observations, which makes it difficult to track periodic behavior. Additional observations across more phases will help determine if variability can be tied to the stellar pulsation.

The line showed variability with the phase of the star, but when we examine Figure 6.5, we see no obvious periodic behavior. When we organize the Miras according to the length of their pulsation period, however, we do see an interesting trend. Stars that showed a stronger 17.62 μm feature ($>$ 5 Jy) all had periods above 300 days. The M-types with strong emission also all exhibited at least one maser detection. Miras with longer periods have stronger shocks and tend to have higher mass loss rates. The initial analysis of the 17.62 μm feature suggest it behaves similarly to a maser. We imagine an aurora effect where instabilities in the atmosphere excite the Fe I atoms that then "glow" throughout the entire pulsation. The longer the period, the stronger the atmospheric turbulence is from shocks which results in greater atmospheric lofting that provides more material to "glow". This could explain why the feature is present in every observation, and why it is strongest for the long period Miras.

7.6 Concluding Remarks

The Miras in our Spitzer sample are remarkably dynamic. The stars never present the same spectrum twice; observations taken only four weeks apart can show markedly different results. The results from the CO_2 analysis combined with the initial analysis of the 17.62 μm feature suggest the Miras with longer pulsation periods behave markedly differently than the shorter period Miras, leaving us with a new mystery to pursue in future work: *why*. If we truly wish to understand Mira circumstellar environments more emphasis must be placed on synoptic phase dependent studies across multiple wavelengths to study different parts of the atmosphere. We must also make an effort to make more accurate parallax measurements for these stars. The future of stellar physics lies in interferometry, but the fundamental stellar properties derived from directly measuring the stellar surface are only as good as the distance measurement to the star, which for Miras can often be rather poor. Our results with the M-type Miras serve as examples to how crucial interferometry is to studying circumstellar environments. The results of the RADEX models in conjunction with the physical size of the star allowed us to estimate emitting regions of the gas that suggest layers of CO_2 gas could serve as refrigeration zones that could efficiently drive dust condensation much closer to the star than radiative equilibrium calculations would allow. Combining the Spitzer observations with the PTI observations has provided us unprecedented access to the circumstellar environments around M-type Miras. Further studies of these remarkable stars will reveal yet more secrets hiding in their light, just waiting to be discovered.

REFERENCES

Agúndez, M., Martínez, J. I., de Andres, P. L., Cernicharo, J., & Martín-Gago, J. A. 2020, A&A, 637, A59

Aoki, W., Tsuji, T., & Ohnaka, K. 1999, A&A, 350, 945

Arlandini, C., Käppeler, F., Wisshak, K., et al. 1999, ApJ, 525, 886

Baylis-Aguirre, D. K., Creech-Eakman, M. J., & Güth, T. 2020, MNRAS

Benson, P. J. & Little-Marenin, I. R. 1996, ApJS, 106, 579

Benson, P. J., Little-Marenin, I. R., Woods, T. C., et al. 1990, ApJS, 74, 911

Bernath, P. F. 2020, Spectra of Atoms and Molecules

Bisterzo, S., Travaglio, C., Gallino, R., Wiescher, M., & Käppeler, F. 2014, ApJ, 787, 10

Bosman, A. D., Bruderer, S., & van Dishoeck, E. F. 2017, A&A, 601, A36

Bowen, G. H. 1988, ApJ, 329, 299

Bruderer, S., Harsono, D., & van Dishoeck, E. F. 2015, A&A, 575, A94

Burbidge, E. M., Burbidge, G. R., Fowler, W. A., & Hoyle, F. 1957, Reviews of Modern Physics, 29, 547

Burke, D., Laurino, O., wmclaugh, et al. 2020, sherpa/sherpa: Sherpa 4.12.2

Buss, R. H., J., Tielens, A. G. G. M., Cohen, M., et al. 1993, ApJ, 415, 250

Busso, M., Gallino, R., & Wasserburg, G. J. 1999, ARA&A, 37, 239

Cami, J. 2002, PhD thesis, University of Amsterdam

Cami, J., Bernard-Salas, J., Peeters, E., & Malek, S. E. 2010, Science, 329, 1180

Cami, J., Yamamura, I., de Jong, T., et al. 2000, A&A, 360, 562

Carnall, A. C. 2017, arXiv e-prints, arXiv:1705.05165

Carpenter, K. G., Nielsen, K. E., Kober, G. V., et al. 2013, in American Astronomical Society Meeting Abstracts, Vol. 221, American Astronomical Society Meeting Abstracts #221, 351.01

Castro, C., Doan, K., Klemka, M., et al. 2017, Molecular Astrophysics, 6, 47

Cernicharo, J., Yamamura, I., González-Alfonso, E., et al. 1999, ApJ, 526, L41

Chandra, S. & Sharma, A. K. 2001, A&A, 376, 356

Cherchneff, I. 2006, A&A, 456, 1001

Chiavassa, A., Pasquato, E., Jorissen, A., et al. 2011, A&A, 528, A120

Cho, S.-H. & Kim, J. 2012, AJ, 144, 129

Clayton, D. D. 1968, Principles of stellar evolution and nucleosynthesis

Colavita, M. M., Wallace, J. K., Hines, B. E., et al. 1999, ApJ, 510, 505

Creech-Eakman, M. J., Güth, T., Luttermoser, D. G., Jurgenson, C. A., & Speck, A. K. 2012, The Astronomical Review, 7, 4

Creech-Eakman, M. J. & Thompson, R. R. 2009, in Astronomical Society of the Pacific Conference Series, Vol. 412, The Biggest, Baddest, Coolest Stars, ed. D. G. Luttermoser, B. J. Smith, & R. E. Stencel, 149

Danilovich, T., Bergman, P., Justtanont, K., et al. 2014, A&A, 569, A76

Duari, D., Cherchneff, I., & Willacy, K. 1999, A&A, 341, L47

Engels, D. & Bunzel, F. 2015, A&A, 582, A68

Faure, A. & Josselin, E. 2008, A&A, 492, 257

Fermi, E. 1931, Zeitschrift fur Physik, 71, 250

Gaia Collaboration. 2018, VizieR Online Data Catalog, I/345

Gail, H. P. & Sedlmayr, E. 1998, Faraday Discussions, 109, 303

Gail, H. P. & Sedlmayr, E. 1999, A&A, 347, 594

Gail, H. P., Wetzel, S., Pucci, A., & Tamanai, A. 2013, A&A, 555, A119

Gallino, R., Arlandini, C., Busso, M., et al. 1998, ApJ, 497, 388

Gehrz, R. 1989, in Interstellar Dust, ed. L. J. Allamandola & A. G. G. M. Tielens, Vol. 135, 445

Gordon, I. E., Rothman, L. S., Hill, C., et al. 2017, J. Quant. Spec. Radiat. Transf., 203, 3

Güth, T. 2017, PhD thesis, New Mexico Institute of Mining and Technology

Hansen, C. J., Kawaler, S. D., & Trimble, V. 2004, Stellar interiors : physical principles, structure, and evolution

Herwig, F. 2005, ARA&A, 43, 435

Herzberg, G. 1945, Molecular spectra and molecular structure. Vol.2: Infrared and Raman spectra of polyatomic molecules

Höfner, S. & Olofsson, H. 2018, A&A Rev., 26, 1

Houck, J. R., Roellig, T. L., Van Cleve, J., et al. 2004, in Society of Photo-Optical Instrumentation Engineers (SPIE) Conference Series, Vol. 5487, Proc. SPIE, ed. J. C. Mather, 62–76

Hubeny, I. & Mihalas, D. 2014, Theory of Stellar Atmospheres

Iben, I., J. & Renzini, A. 1983, ARA&A, 21, 271

Iben, Icko, J. 1967, ARA&A, 5, 571

Jacquemart, D., Mandin, J. Y., Dana, V., et al. 2003, J. Quant. Spec. Radiat. Transf., 82, 363

Johnson, H. R., Ensman, L. M., Alexander, D. R., et al. 1995, ApJ, 443, 281

Jura, M. 1994, ApJ, 422, 102

Justtanont, K., Feuchtgruber, H., de Jong, T., et al. 1998, A&A, 330, L17

Karakas, A. I. 2019, IAU Symposium, 343, 79

Karakas, A. I. & Lattanzio, J. C. 2014, PASA, 31, e030

Karakas, A. I., Lattanzio, J. C., & Pols, O. R. 2002, PASA, 19, 515

Kessler, M. F., Steinz, J. A., Anderegg, M. E., et al. 1996, A&A, 500, 493

Kim, J., Cho, S.-H., & Kim, S. J. 2014, AJ, 147, 22

Kippenhahn, R., Weigert, A., & Weiss, A. 2012, Stellar Structure and Evolution

Lamers, H. J. G. L. M. & Cassinelli, J. P. 1999, Introduction to Stellar Winds

Lattanzio, J. & Karakas, A. 2016, in Journal of Physics Conference Series, Vol. 728, Journal of Physics Conference Series, 022002

Lattanzio, J. C. & Boothroyd, A. I. 1997, in American Institute of Physics Conference Series, Vol. 402, Astrophysical implications of the laboratory study of presolar materials, ed. T. J. Bernatowicz & E. Zinner, 85–114

Li, W., Chornock, R., Leaman, J., et al. 2011, MNRAS, 412, 1473

Little-Marenin, I. R. & Little, S. J. 1988, ApJ, 333, 305

Little-Marenin, I. R. & Little, S. J. 1990, AJ, 99, 1173

Little-Marenin, I. R. & Price, S. D. 1986, in Interstellar Processes: Abstracts of Contributed Papers, ed. D. J. Hollenbach & J. Thronson, H. A., 137–138

Lord, S. D. 1992, A new software tool for computing Earth's atmospheric transmission of near- and far-infrared radiation, NASA Technical Memorandum 103957

Lucas, R., Omont, A., Guilloteau, S., & Nguyen-Q-Rieu. 1986, A&A, 154, L12

Luttermoser, D. G. 1996, in Astronomical Society of the Pacific Conference Series, Vol. 109, Cool Stars, Stellar Systems, and the Sun, ed. R. Pallavicini & A. K. Dupree, 535

Luttermoser, D. G. 2000, ApJ, 536, 923

Markwick, A. J. & Millar, T. J. 2000, A&A, 359, 1162

Matsuura, M., Yamamura, I., Cami, J., Onaka, T., & Murakami, H. 2002, A&A, 383, 972

Menten, K. M., Wyrowski, F., Keller, D., & Kamiński, T. 2018, A&A, 613, A49

Moore, C. E. 1950, An ultraviolet multiplet table - Sect. 1-2

Nakashima, J.-i. & Deguchi, S. 2007, ApJ, 669, 446

Neufeld, D. A. 2012, ApJ, 749, 125

Nevdakh, V. V., Orlov, L. N., & Leshenyuk, N. S. 2003, Journal of Applied Spectroscopy, 70, 276

Olnon, F. M., Raimond, E., Neugebauer, G., et al. 1986, A&AS, 65, 607

Olofsson, H. 1997, Ap&SS, 251, 31

Omont, A., Lucas, R., Morris, M., & Guilloteau, S. 1993, A&A, 267, 490

Ostlie, D. A. & Cox, A. N. 1986, ApJ, 311, 864

Reid, M. J. & Goldston, J. E. 2002, ApJ, 568, 931

Reid, M. J. & Menten, K. M. 1997, ApJ, 476, 327

Reid, M. J. & Moran, J. M. 1981, ARA&A, 19, 231

Richter, H. & Wood, P. R. 2001, A&A, 369, 1027

Romano, D., Karakas, A. I., Tosi, M., & Matteucci, F. 2010, A&A, 522, A32

Rozwadowska, K., Vissani, F., & Cappellaro, E. 2021, New A, 83, 101498

Ryde, N., Eriksson, K., & Gustafsson, B. 1999, A&A, 341, 579

Ryde, N., Eriksson, K., Gustafsson, B., Lindqvist, M., & Olofsson, H. 1998, Ap&SS, 255, 301

Salaris, M. & Cassisi, S. 2005, Evolution of Stars and Stellar Populations

Schöier, F. L., van der Tak, F. F. S., van Dishoeck, E. F., & Black, J. H. 2005, A&A, 432, 369

Shimanouchi, T. 1977, Journal of Physical and Chemical Reference Data, 6, 993

Sivagnanam, P., Le Squeren, A. M., & Foy, F. 1988, A&A, 206, 285

Sloan, G. C., Kraemer, K. E., Goebel, J. H., & Price, S. D. 2003a, ApJ, 594, 483

Sloan, G. C., Kraemer, K. E., Price, S. D., & Shipman, R. F. 2003b, ApJS, 147, 379

Sloan, G. C., Kraemer, K. E., Wood, P. R., et al. 2008, ApJ, 686, 1056

Sloan, G. C., Lagadec, E., Zijlstra, A. A., et al. 2014, ApJ, 791, 28

Sloan, G. C., Levan, P. D., & Little-Marenin, I. R. 1996, ApJ, 463, 310

Sloan, G. C. & Price, S. D. 1998, ApJS, 119, 141

Slutz, S. 1976, ApJ, 210, 750

Smette, A., Sana, H., Noll, S., et al. 2015, A&A, 576, A77

Smith, C. L., Zijlstra, A. A., & Fuller, G. A. 2014, MNRAS, 440, 172

Sobolev, V. V. 1960, Moving envelopes of stars

Thompson, R. R., Creech-Eakman, M. J., & Akeson, R. L. 2002a, ApJ, 570, 373

Thompson, R. R., Creech-Eakman, M. J., & van Belle, G. T. 2002b, ApJ, 577, 447

Uttenthaler, S. 2007, PhD thesis, Institut für Astronomie der Universität Wien, Türkenschanzstrasse 17, A-1180 Wien, Austria; ESO Garching, Karl Schwarzschild Strasse 2, D-85748 Garching near Munich, Germany; Instituut voor Sterrenkunde, K. U. Leuven, Celestijnenlaan 200D, B-3001 Leuven, Belgium

Uttenthaler, S., Meingast, S., Lebzelter, T., et al. 2016, A&A, 585, A145

van Belle, G. T., Thompson, R. R., & Creech-Eakman, M. J. 2002, AJ, 124, 1706

van den Bergh, S. 1991, Phys. Rep., 204, 385

van der Tak, F. F. S., Black, J. H., Schöier, F. L., Jansen, D. J., & van Dishoeck, E. F. 2007, A&A, 468, 627

van Dishoeck, E. F. 2004, ARA&A, 42, 119

van Hoof, P. A. M. 2018, Galaxies, 6, 63

van Leeuwen, F. 2007, A&A, 474, 653

van Leeuwen, F., Feast, M. W., Whitelock, P. A., & Yudin, B. 1997, MNRAS, 287, 955

Wallerstein, G., Iben, Icko, J., Parker, P., et al. 1997, Reviews of Modern Physics, 69, 995

Waters, L. B. F. M., Molster, F. J., de Jong, T., et al. 1996, A&A, 315, L361

Willson, L. A. 1972, A&A, 17, 354

Willson, L. A. 2000, ARA&A, 38, 573

Wong, K. T., Kamiński, T., Menten, K. M., & Wyrowski, F. 2016, A&A, 590, A127

Wood, B. E. & Karovska, M. 2000, ApJ, 535, 304

Yamamura, I. 2003, in Astrophysics and Space Science Library, Vol. 283, Mass-Losing Pulsating Stars and their Circumstellar Matter, ed. Y. Nakada, M. Honma, & M. Seki, 173–180

Yamamura, I. & de Jong, T. 2000, in ESA Special Publication, Vol. 456, ISO Beyond the Peaks: The 2nd ISO Workshop on Analytical Spectroscopy, ed. A. Salama, M. F. Kessler, K. Leech, & B. Schulz, 155

Yamamura, I., de Jong, T., & Cami, J. 1999a, A&A, 348, L55

Yamamura, I., de Jong, T., Onaka, T., Cami, J., & Waters, L. B. F. M. 1999b, A&A, 341, L9

Yang, B., Stancil, P. C., Balakrishnan, N., & Forrey, R. C. 2010, ApJ, 718, 1062

Zhang, Y. & Kwok, S. 2013, Earth, Planets, and Space, 65, 1069

Ziurys, L. M. & Turner, B. E. 1986, ApJ, 300, L19

APPENDIX A

A.1 Spectra with RADEX fits.

Specific model parameters for each fit can be found in Table 6.3.

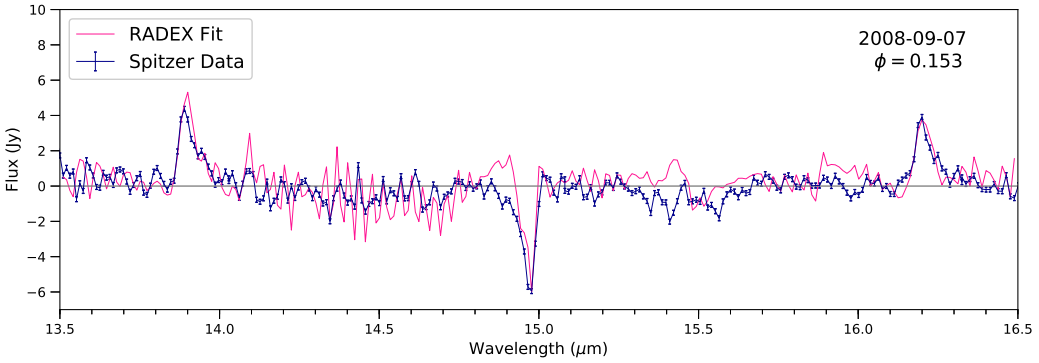

Figure A.1: Result from 2 layer slab model calculation performed with RADEX for R Tri 2008-09-07.

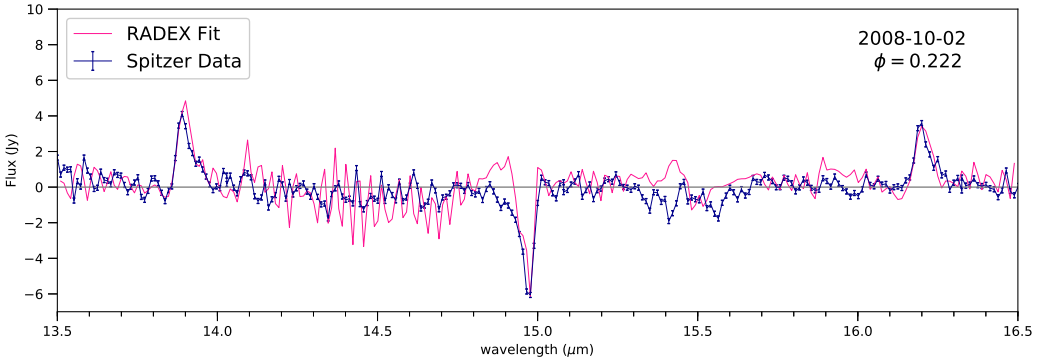

Figure A.2: Result from 2 layer slab model calculation performed with RADEX for R Tri 2008-10-02.

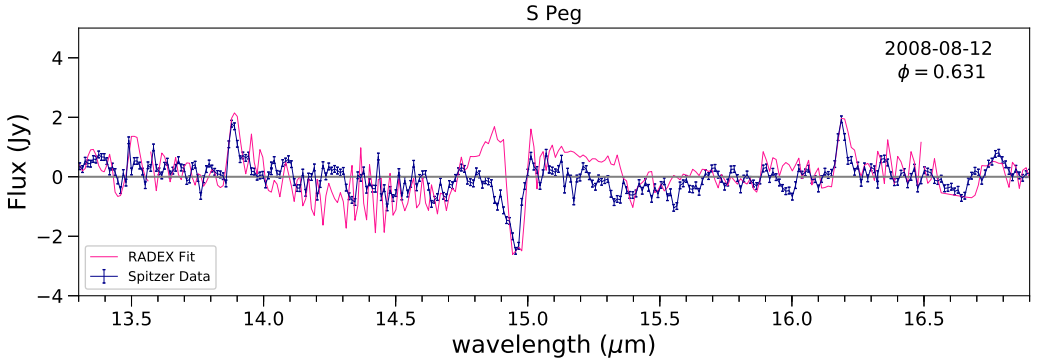

Figure A.3: Result from 2 layer slab model calculation performed with RADEX for S Peg 2008-08-12.

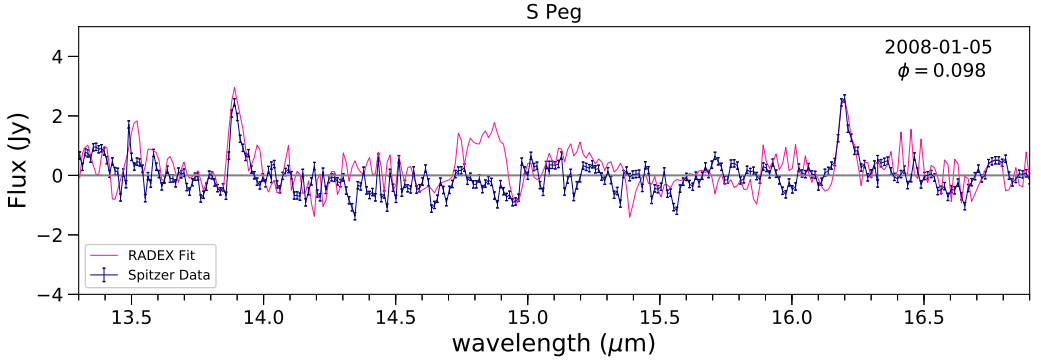

Figure A.4: Result from slab model calculation performed with RADEX for S Peg 2009-01-05.

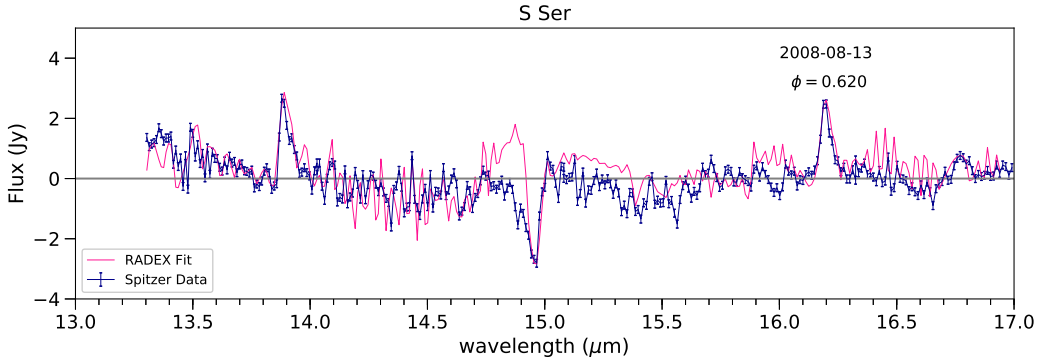

Figure A.5: Result from slab model calculation performed with RADEX for S Ser 2008-08-13.

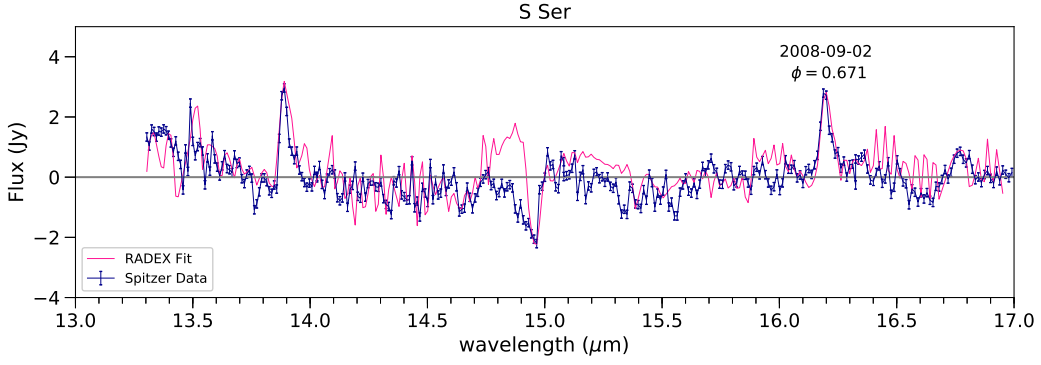

Figure A.6: Result from slab model calculation performed with RADEX for S Ser 2008-09-02.

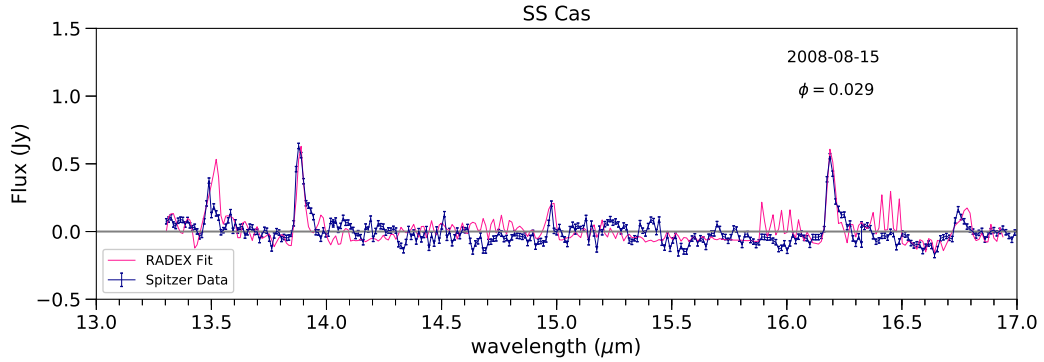

Figure A.7: Result from slab model calculations performed with RADEX for SS Cas 2008-08-15.

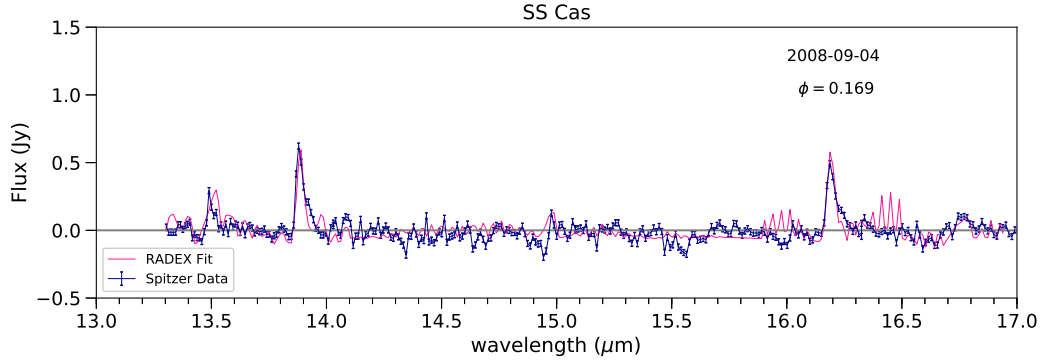

Figure A.8: Result from slab model calculations performed with RADEX for SS Cas 2008-09-04.

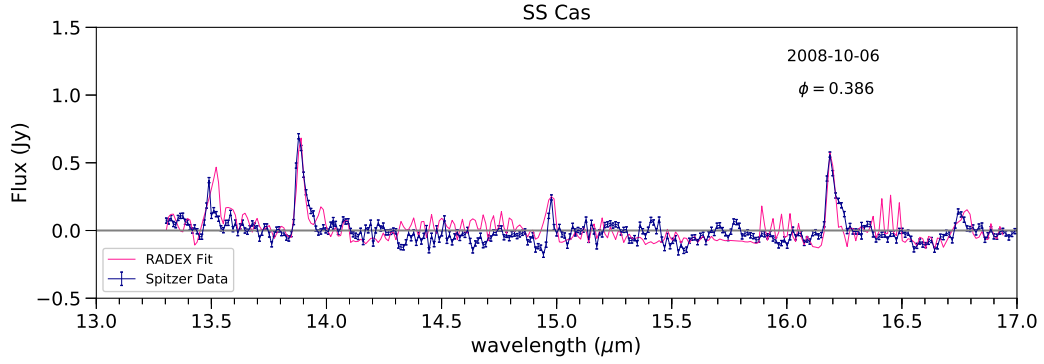

Figure A.9: Result from slab model calculations performed with RADEX for SS Cas 2008-10-06.

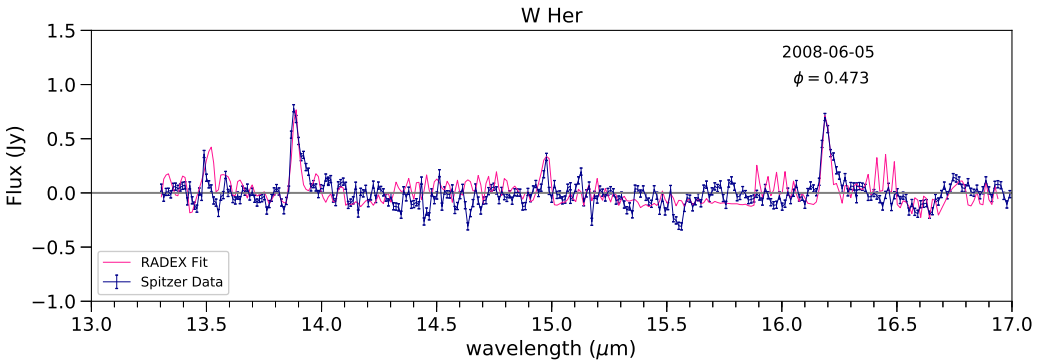

Figure A.10: Result from slab model calculations performed with RADEX for W Her 2008-06-05.

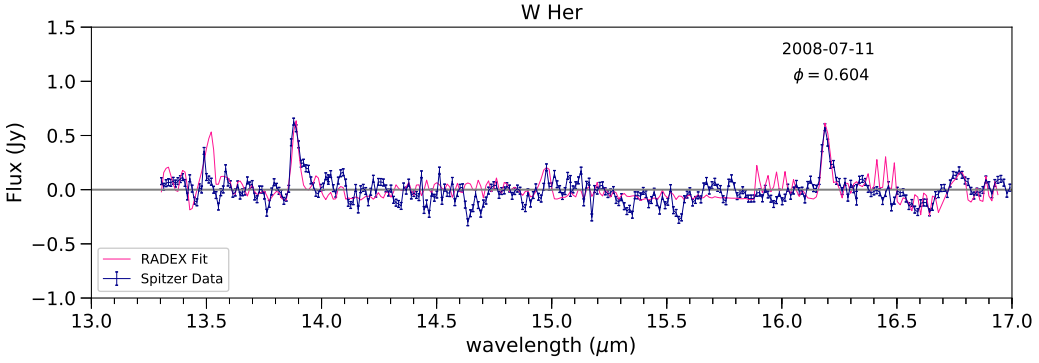

Figure A.11: Result from slab model calculations performed with RADEX for W Her 2008-07-11.

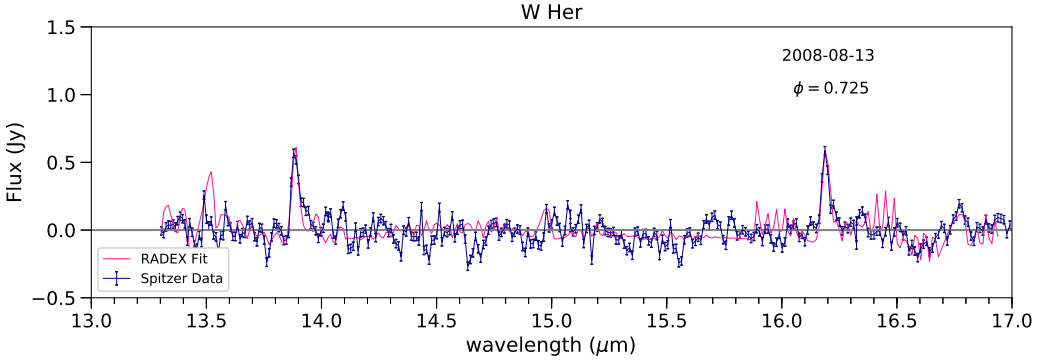

Figure A.12: Result from slab model calculations performed with RADEX for W Her 2008-08-13.

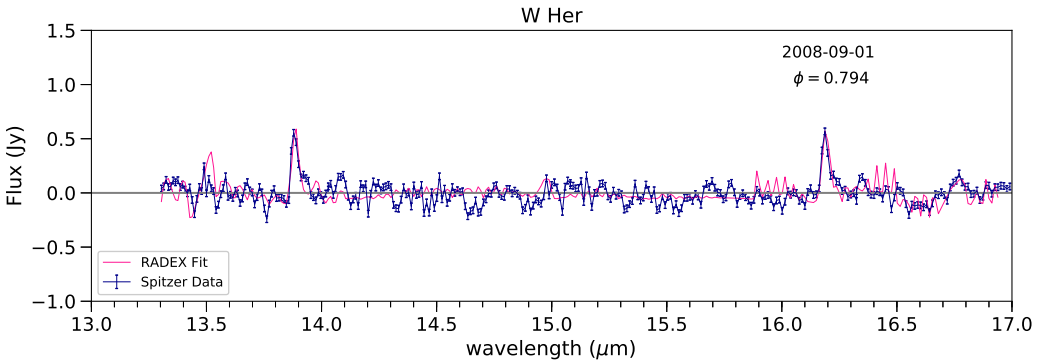

Figure A.13: Result from slab model calculations performed with RADEX for W Her 2008-09-01.

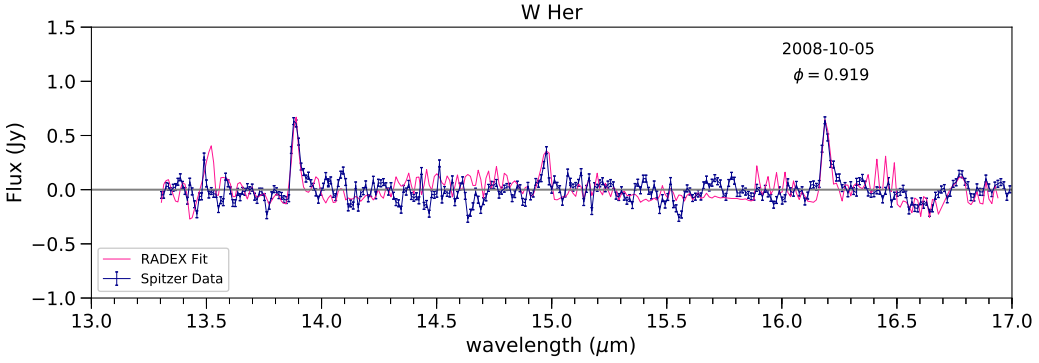

Figure A.14: Result from slab model calculations performed with RADEX for W Her 2008-10-05.

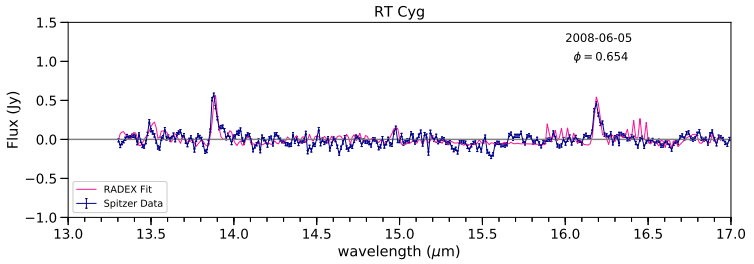

Figure A.15: Result from slab model calculations performed with RADEX for RT Cyg 2008-06-05.

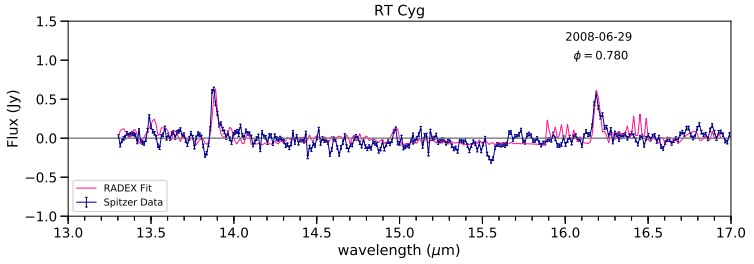

Figure A.16: Result from slab model calculations performed with RADEX for RT Cyg 2008-06-29.

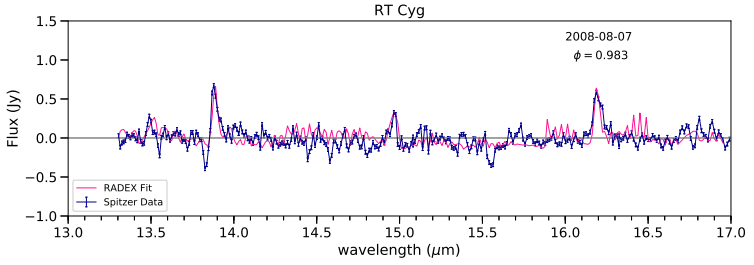

Figure A.17: Result from slab model calculations performed with RADEX for RT Cyg 2008-08-07.

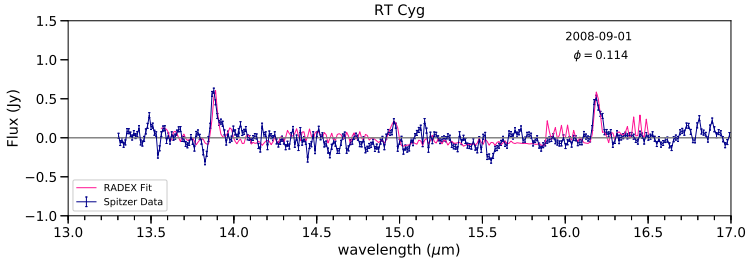

Figure A.18: Result from slab model calculations performed with RADEX for RT Cyg 2008-09-01.

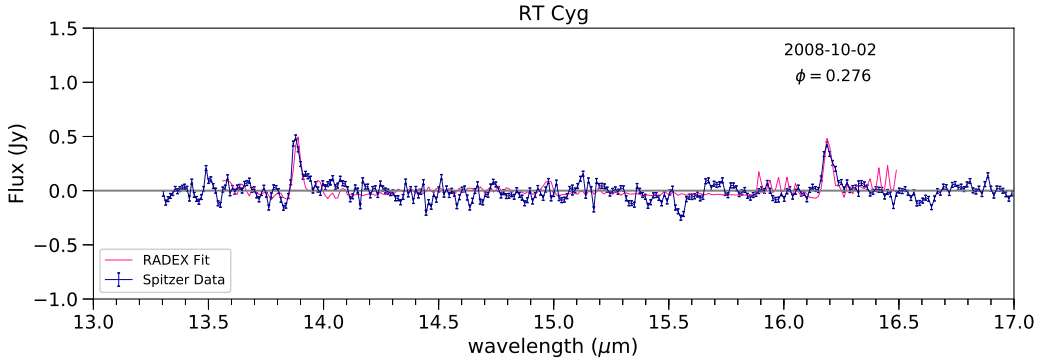

Figure A.19: Result from slab model calculations performed with RADEX for RT Cyg 2008-10-02.

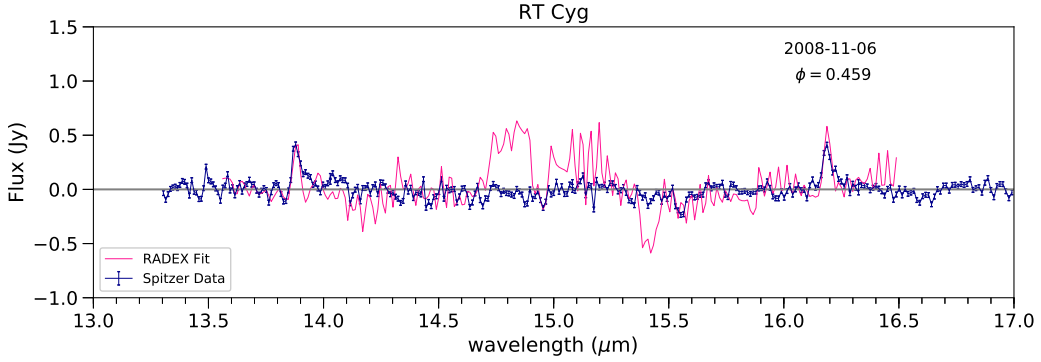

Figure A.20: Result from slab model calculations performed with RADEX for RT Cyg 2008-11-06.

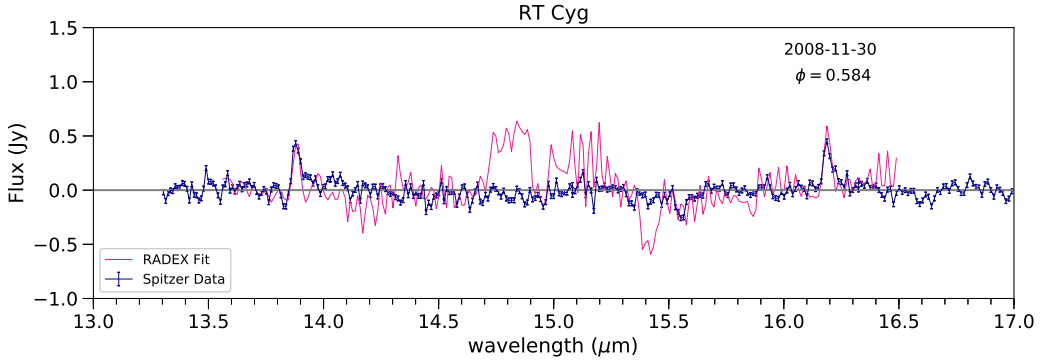

Figure A.21: Result from slab model calculations performed with RADEX for RT Cyg 2008-11-30.

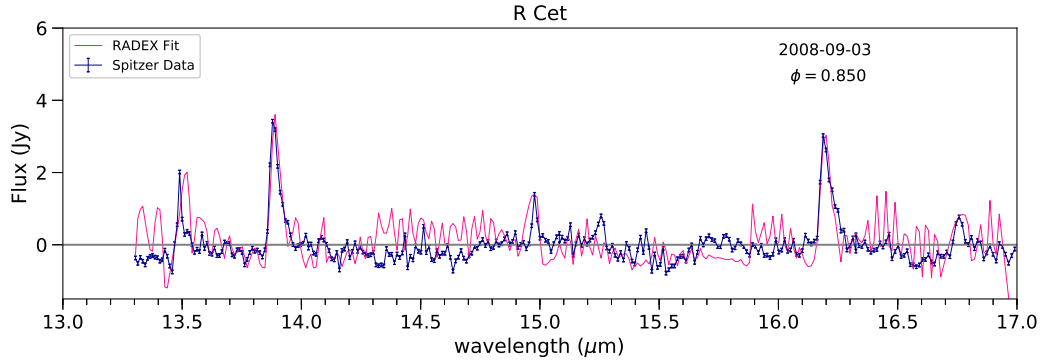

Figure A.22: Result from slab model calculations performed with RADEX for R Cet 2008-09-03.

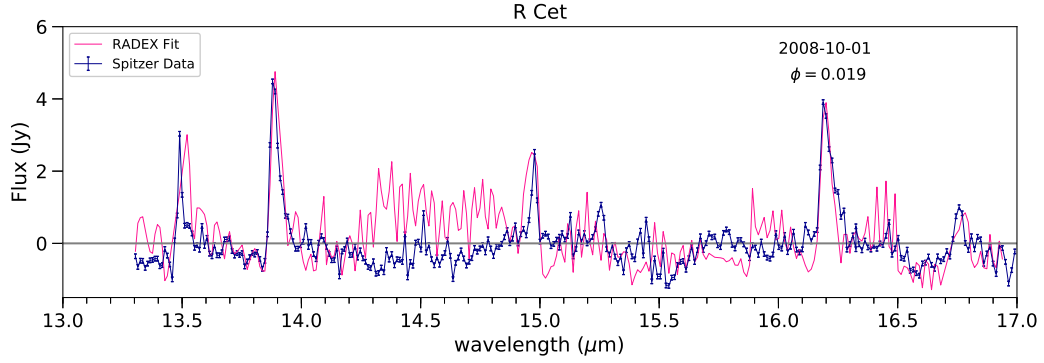

Figure A.23: Result from slab model calculations performed with RADEX for R Cet 2008-10-01.

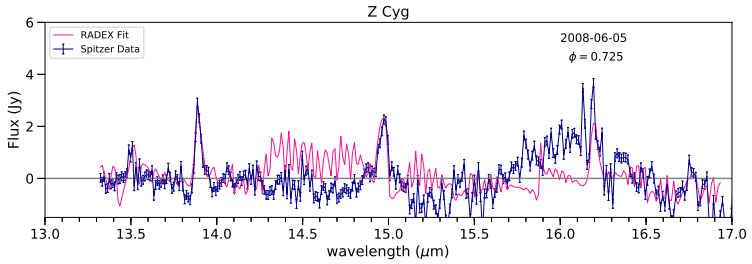

Figure A.24: Result from slab model calculations performed with RADEX for RT Cyg 2008-06-05.

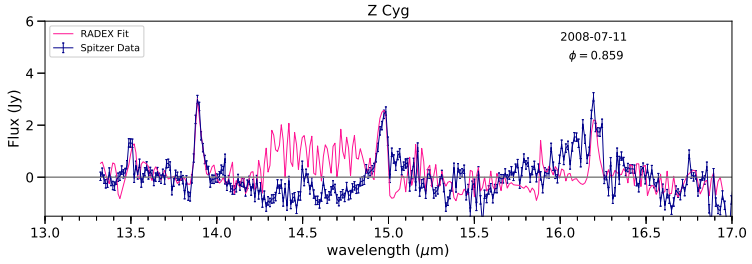

Figure A.25: Result from slab model calculations performed with RADEX for RT Cyg 2008-07-11.

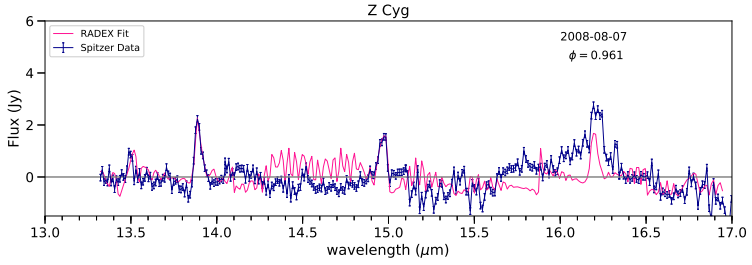

Figure A.26: Result from slab model calculations performed with RADEX for RT Cyg 2008-08-07.

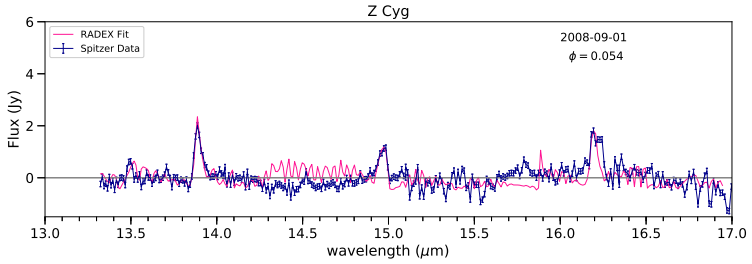

Figure A.27: Result from slab model calculations performed with RADEX for RT Cyg 2008-09-01.

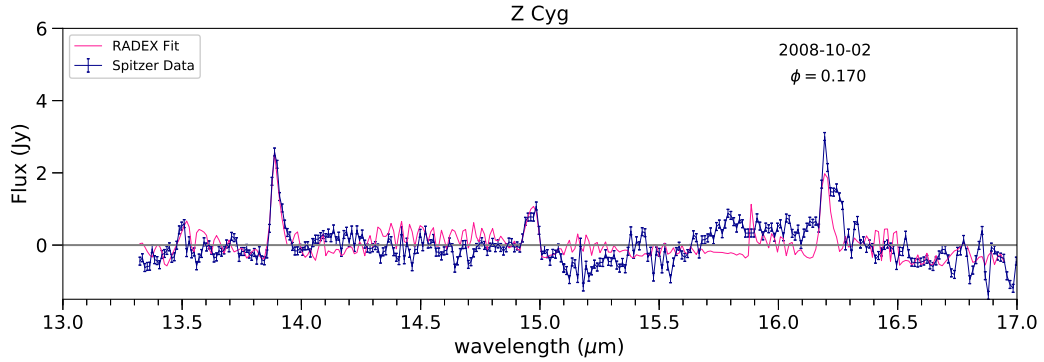

Figure A.28: Result from slab model calculations performed with RADEX for RT Cyg 2008-10-02.

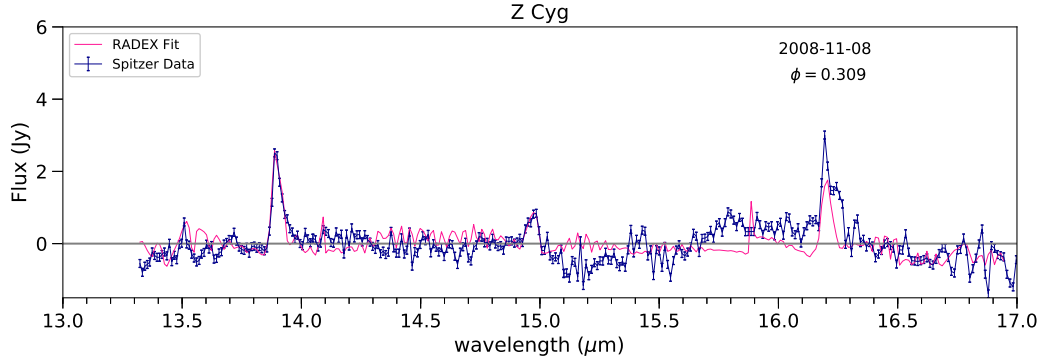

Figure A.29: Result from slab model calculations performed with RADEX for RT Cyg 2008-11-08.

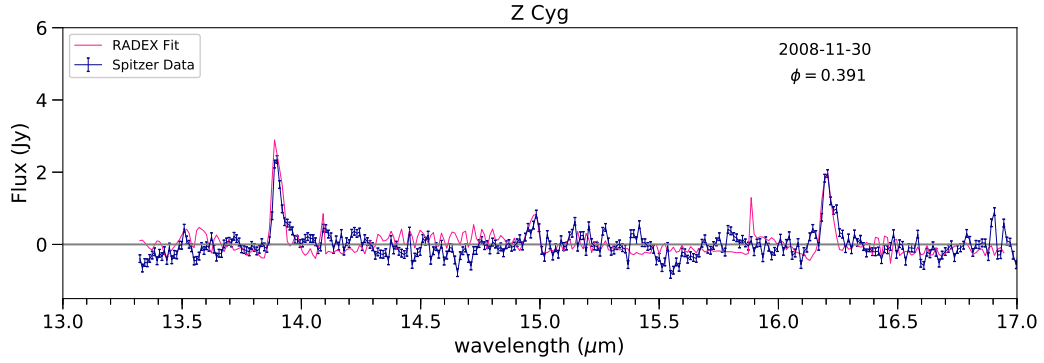

Figure A.30: Result from slab model calculations performed with RADEX for RT Cyg 2008-11-30.

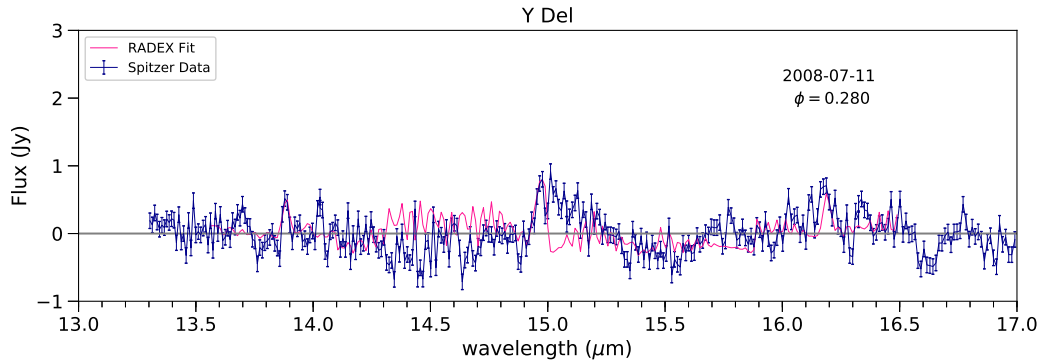

Figure A.31: Result from slab model calculations performed with RADEX for Y Del 2008-07-11.

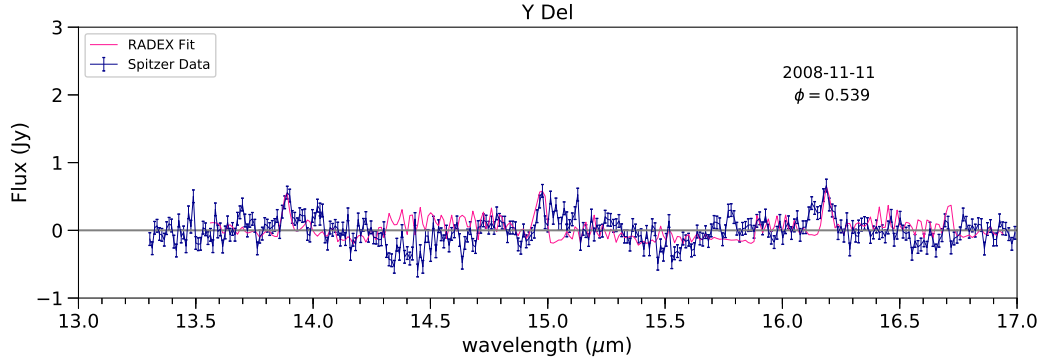

Figure A.32: Result from slab model calculations performed with RADEX for Y Del 2008-11-11.

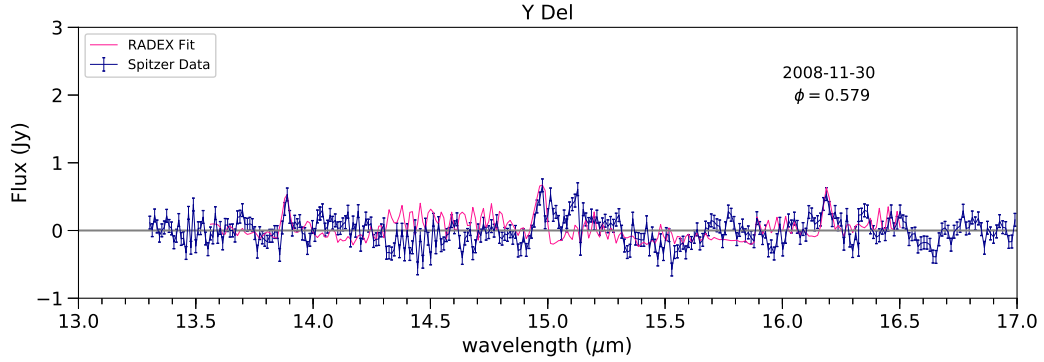

Figure A.33: Result from slab model calculations performed with RADEX for Y Del 2008-11-30.

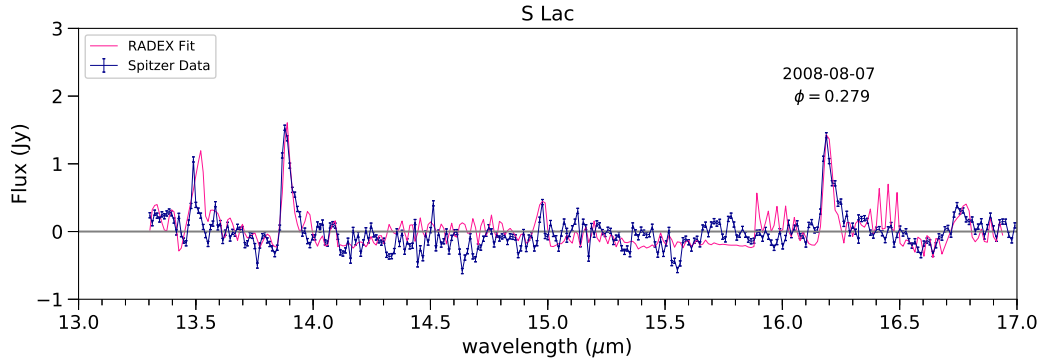

Figure A.34: Result from slab model calculations performed with RADEX for S Lac 2008-07-08.

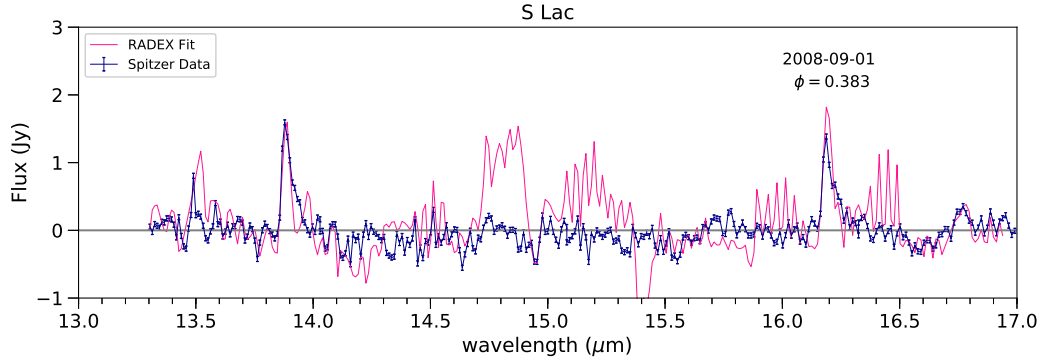

Figure A.35: Result from slab model calculations performed with RADEX for S Lac 2008-09-01.

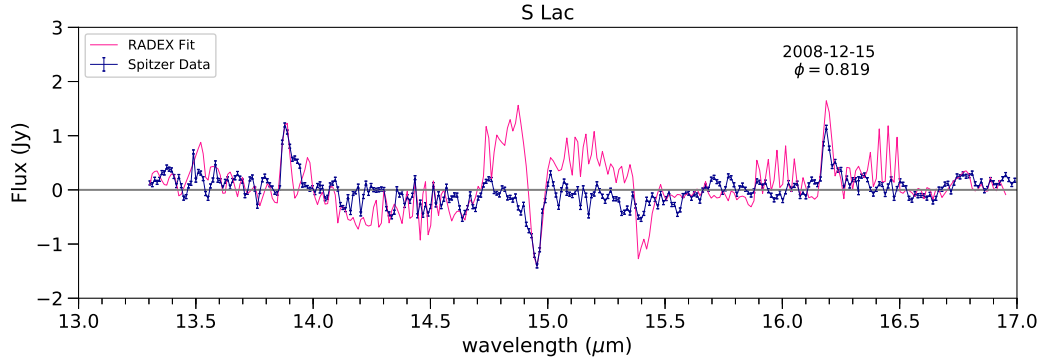

Figure A.36: Result from slab model calculations performed with RADEX for S Lac 2008-12-15.

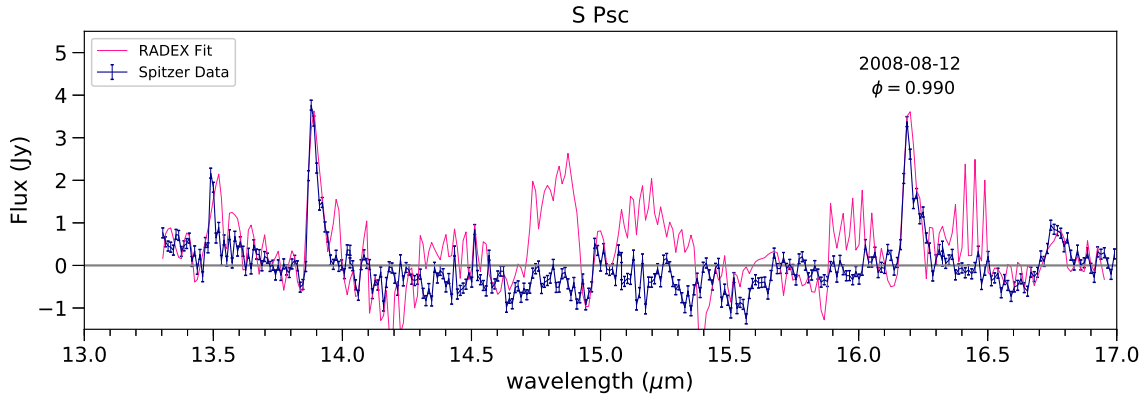

Figure A.37: Result from slab model calculations performed with RADEX for S Psc 2008-08-12.

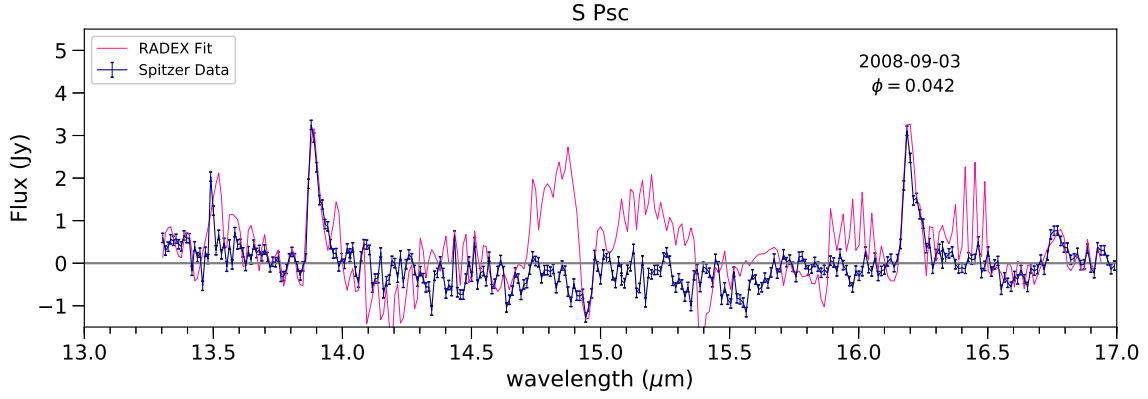

Figure A.38: Result from slab model calculations performed with RADEX for S Psc 2008-09-03.

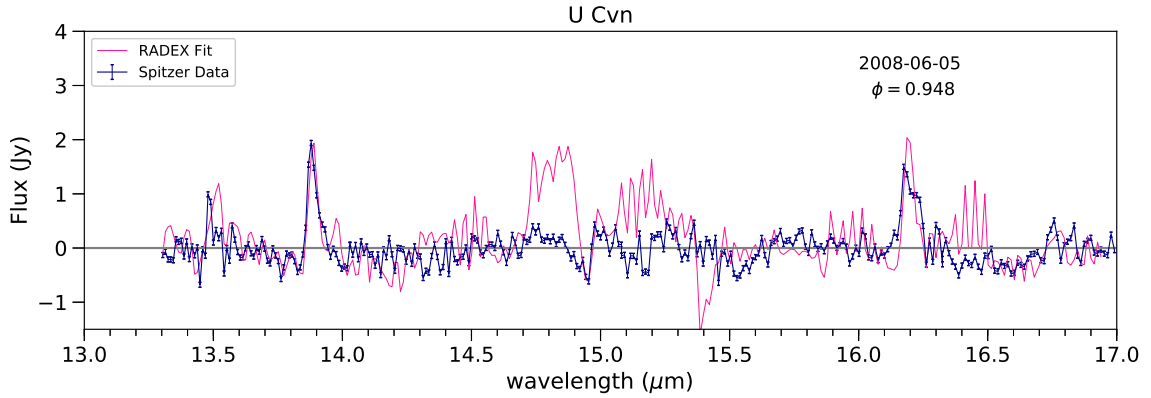

Figure A.39: Result from slab model calculations performed with RADEX for U Cvn 2008-06-05.

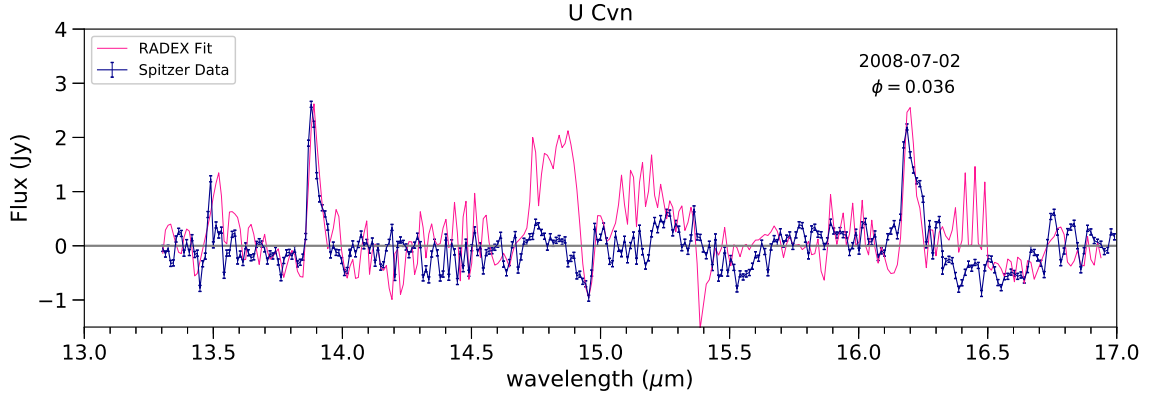

Figure A.40: Result from slab model calculations performed with RADEX for U Cvn 2008-07-03.

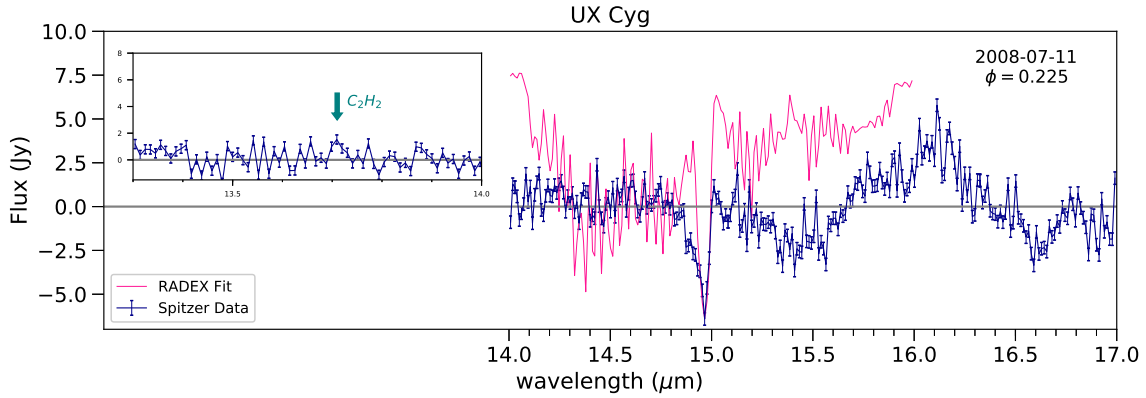

Figure A.41: Result from slab model calculations performed with RADEX for UX Cyg 2008-07-11.

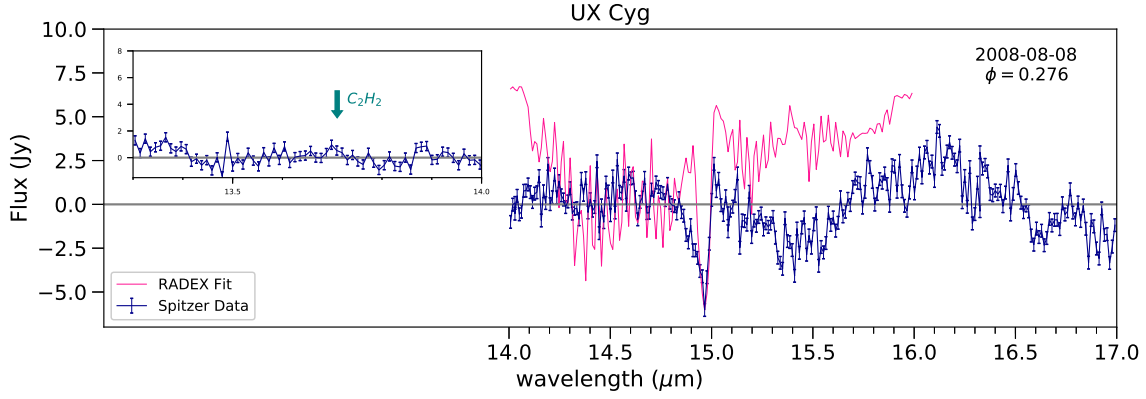

Figure A.42: Result from slab model calculations performed with RADEX for UX Cyg 2008-08-08.

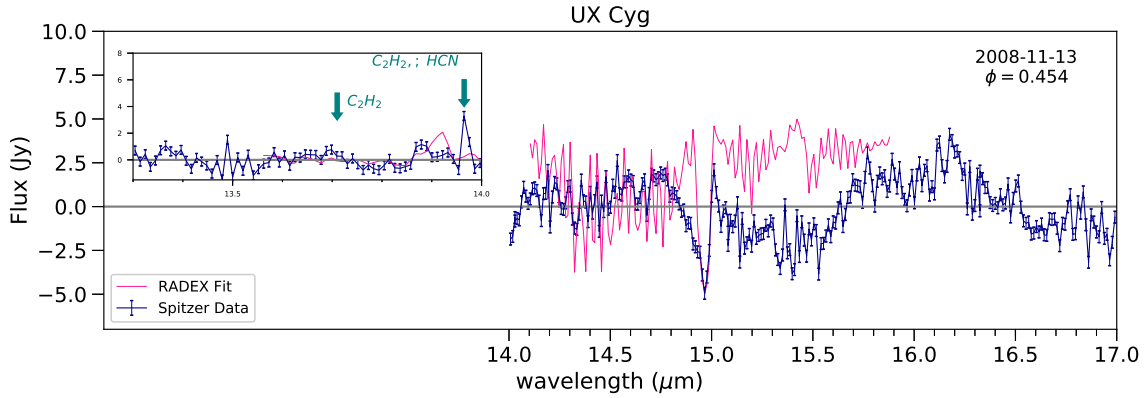

Figure A.43: Result from slab model calculations performed with RADEX for UX Cyg 2008-11-13.

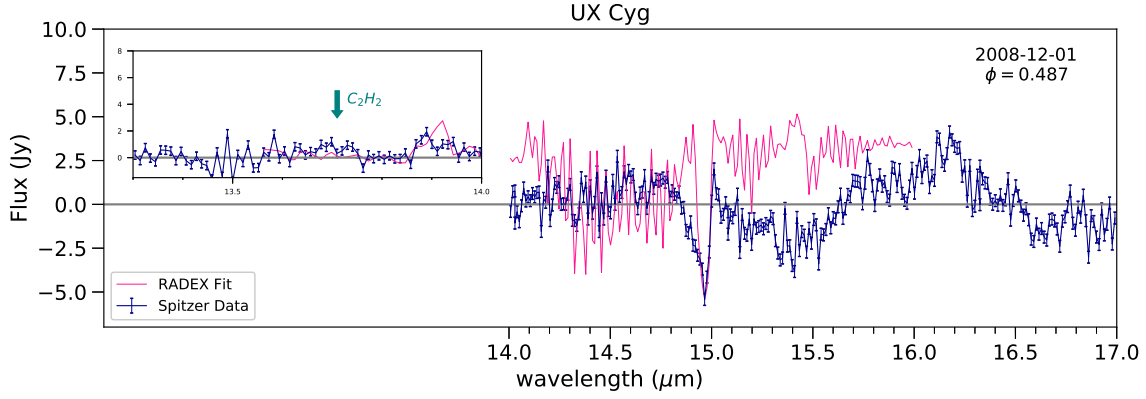

Figure A.44: Result from slab model calculations performed with RADEX for UX Cyg 2008-12-01.

APPENDIX B

B.1 17.62 μm Line Profiles

Model paramters for each fit are reported in Tables 6.4, 6.5 and 6.6 for M-type Miras, S-type Miras, and C-type Miras, respectively.

B.1.1 M-types

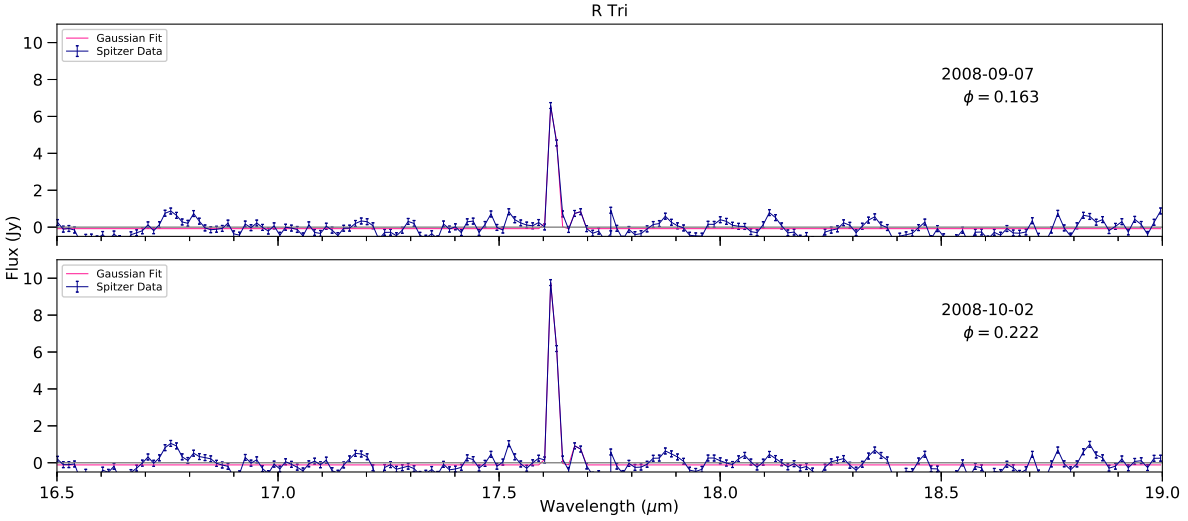

Figure B.1: Gaussian profile fits of the 17.62 μm feature in the M-type R Tri.

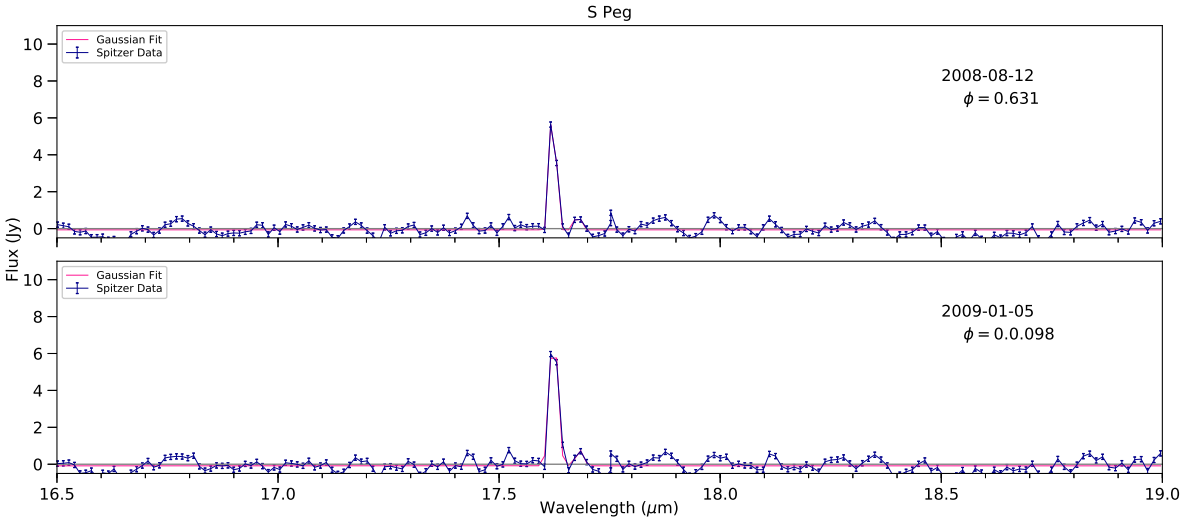

Figure B.2: Gaussian profile fits of the 17.62 μm feature in the M-type S Peg.

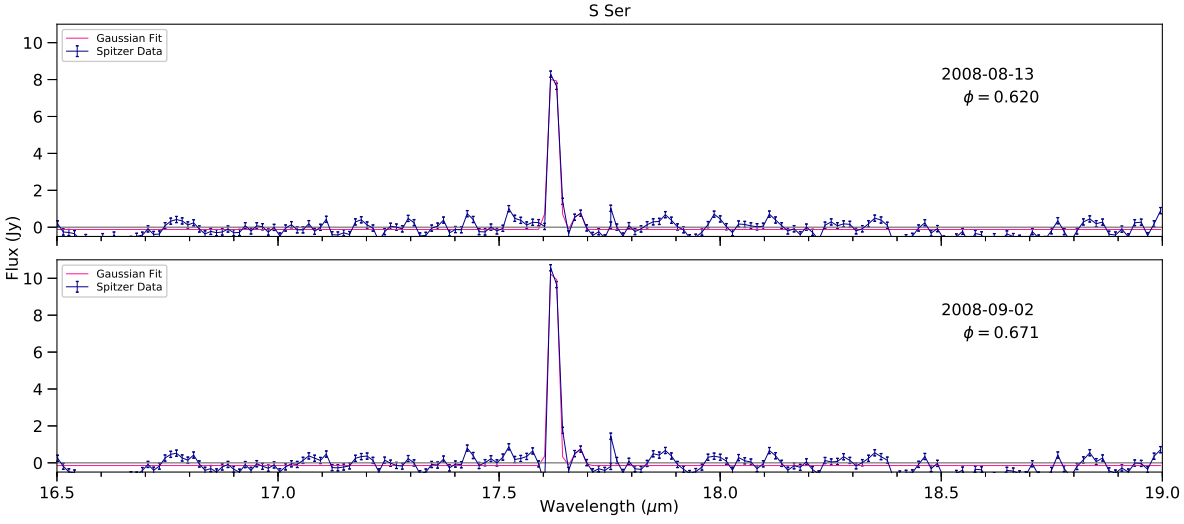

Figure B.3: Gaussian profile fits of the 17.62 μm feature in the M-type S Ser.

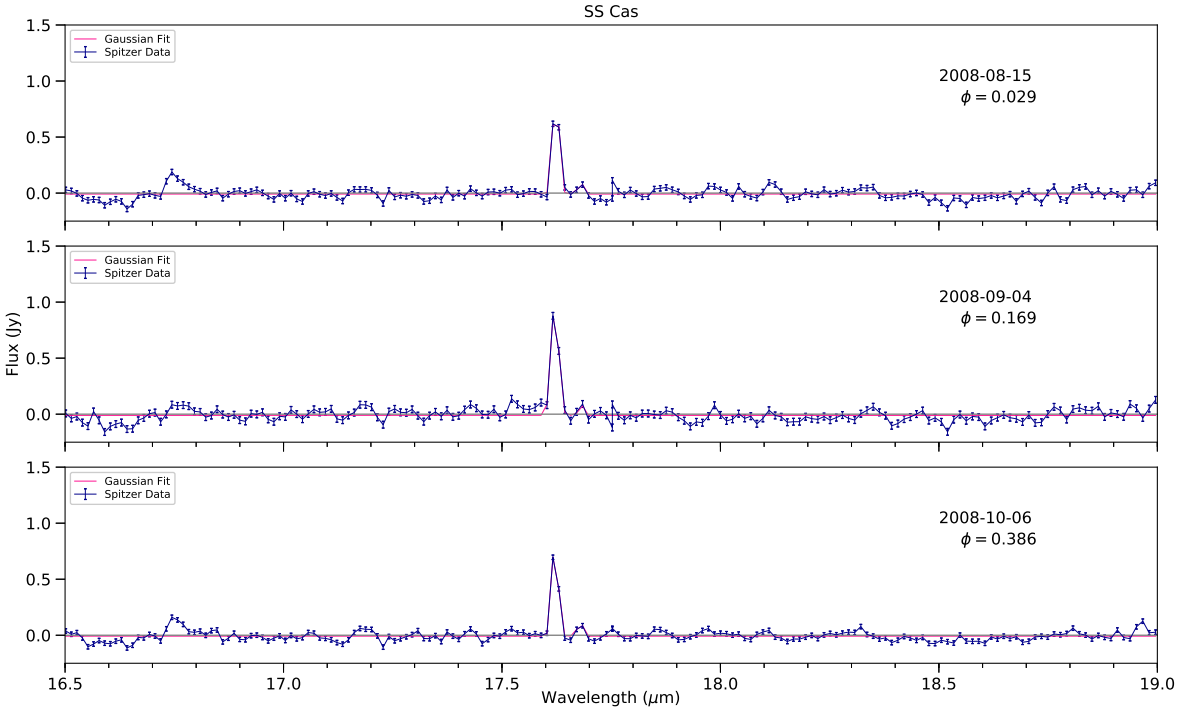

Figure B.4: Gaussian profile fits of the 17.62 μm feature in the M-type SS Cas.

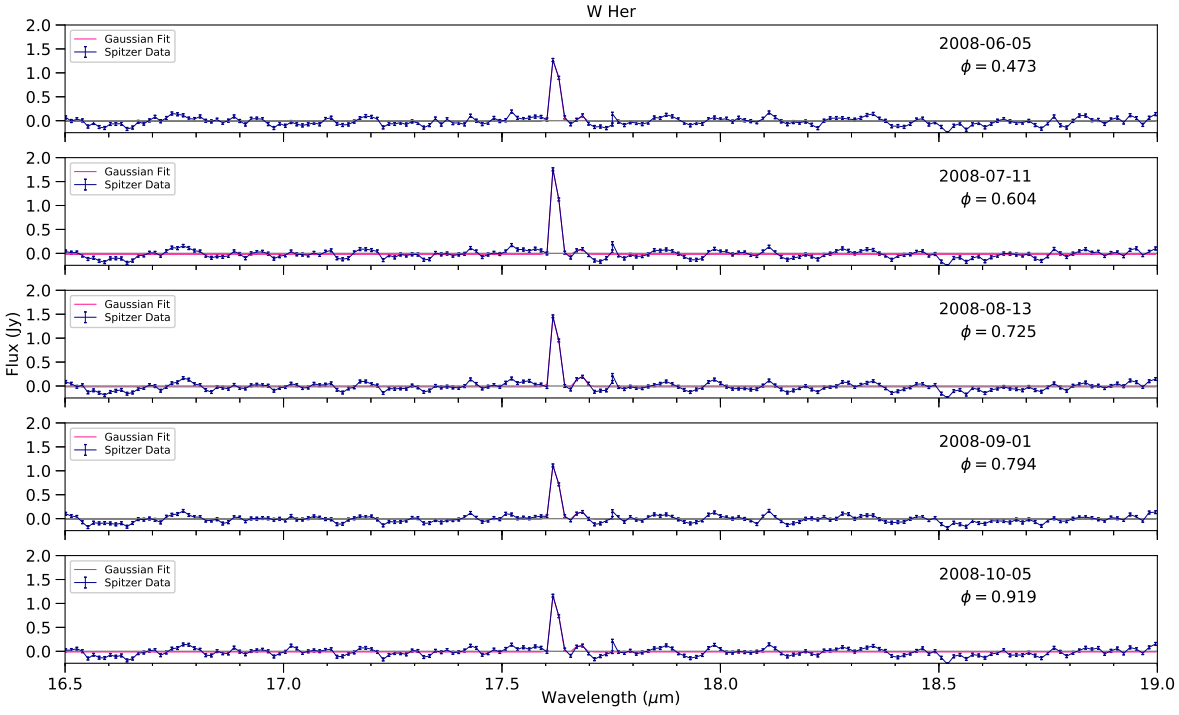

Figure B.5: Gaussian profile fits of the 17.62 μm feature in the M-type W Her.

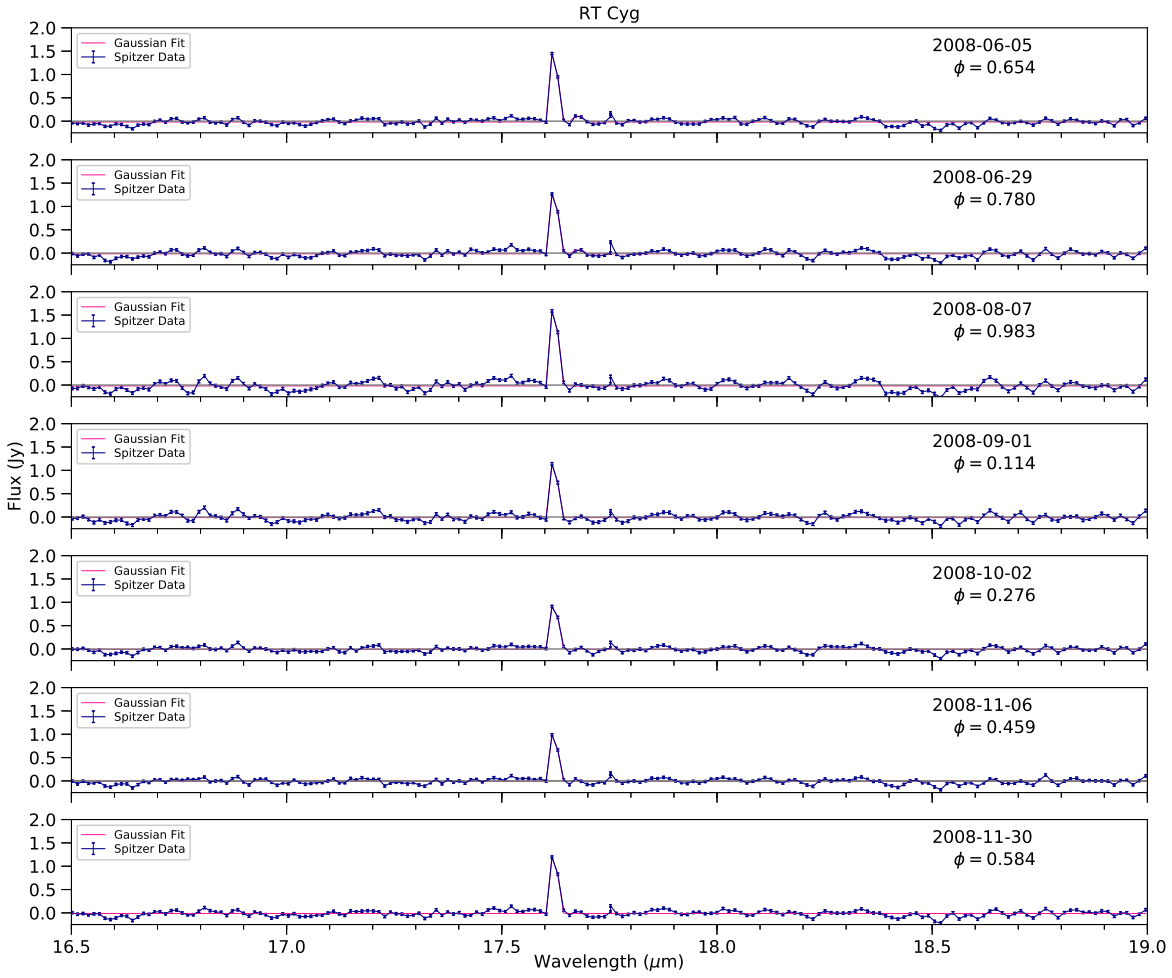

Figure B.6: Gaussian profile fits of the 17.62 μm feature in the M-type RT Cyg.

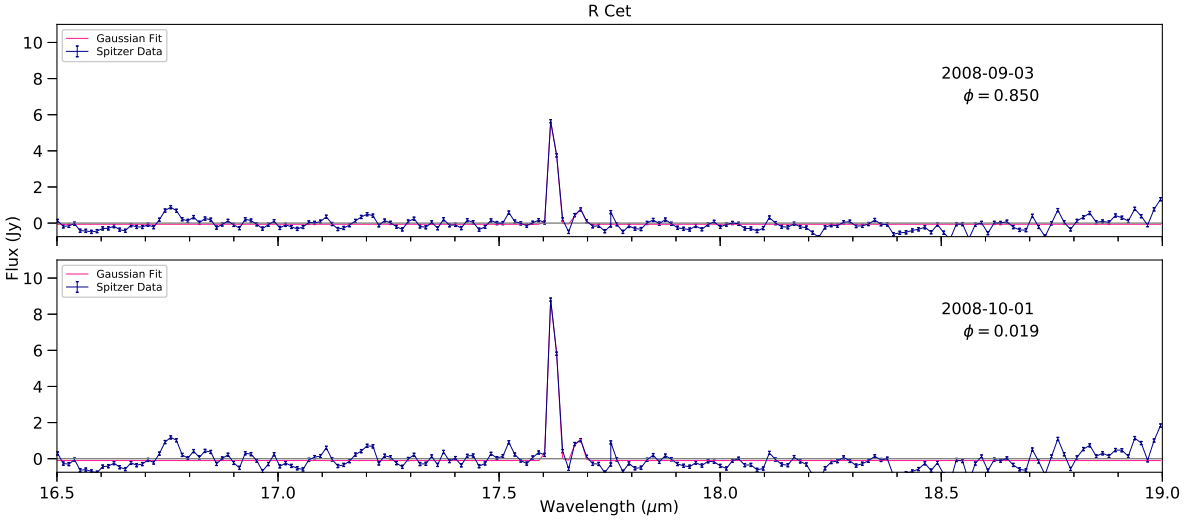

Figure B.7: Gaussian profile fits of the 17.62 μm feature in the M-type R Cet.

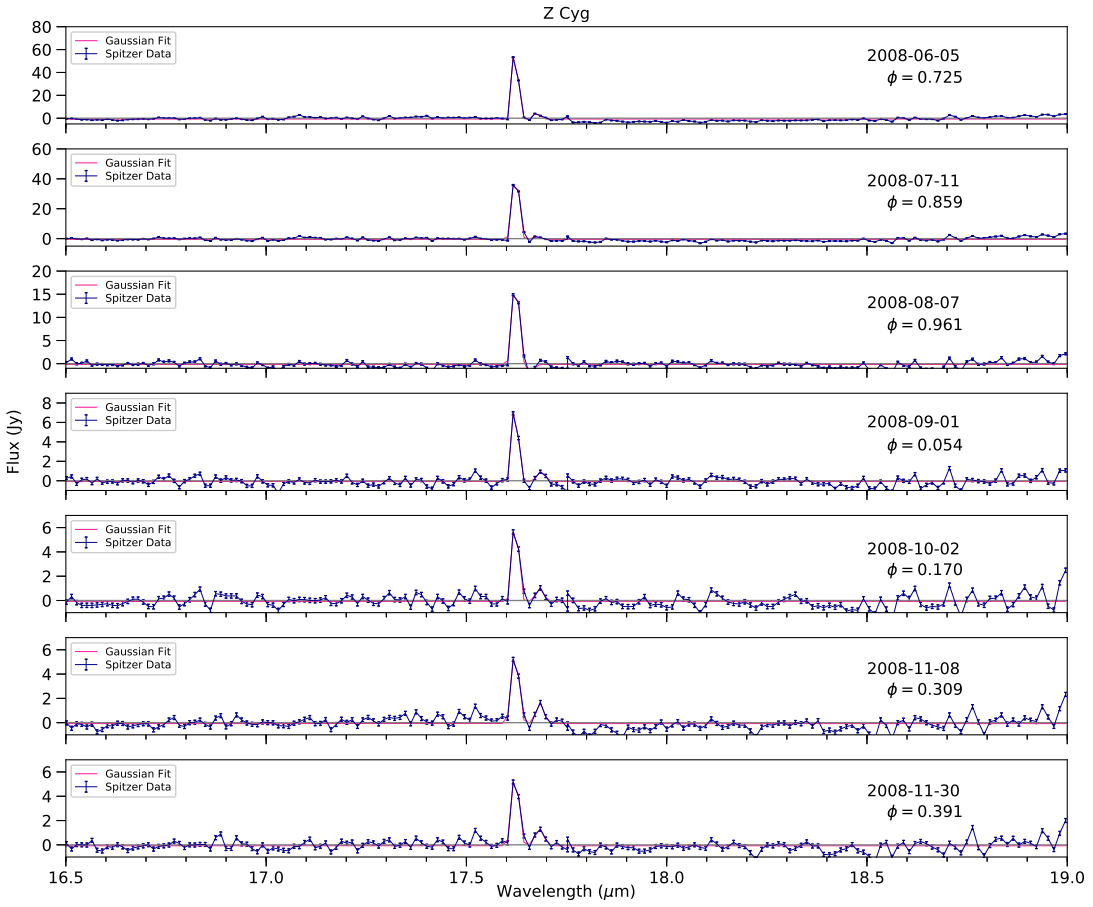

Figure B.8: Gaussian profile fits of the 17.62 μm feature in the M-type Z Cyg. Note the scale change in the flux-axis from $\phi = 0.725$ through $\phi = 0.170$.

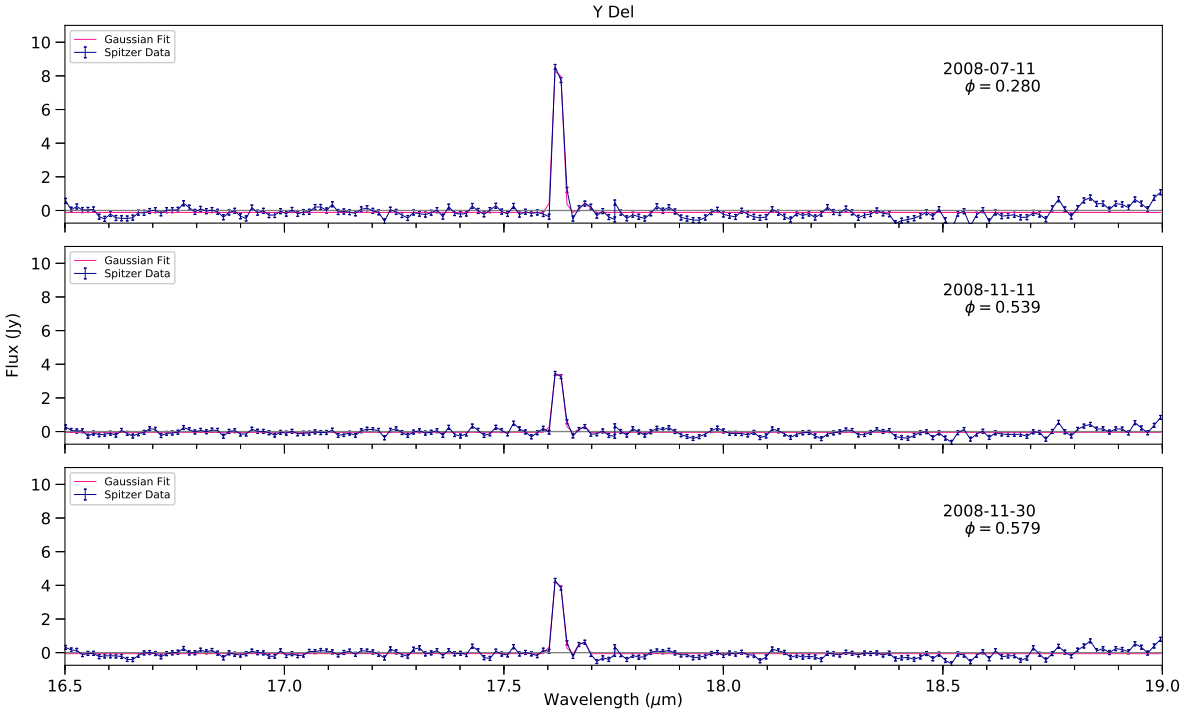

Figure B.9: Gaussian profile fits of the 17.62 μm feature in the M-type Y Del.

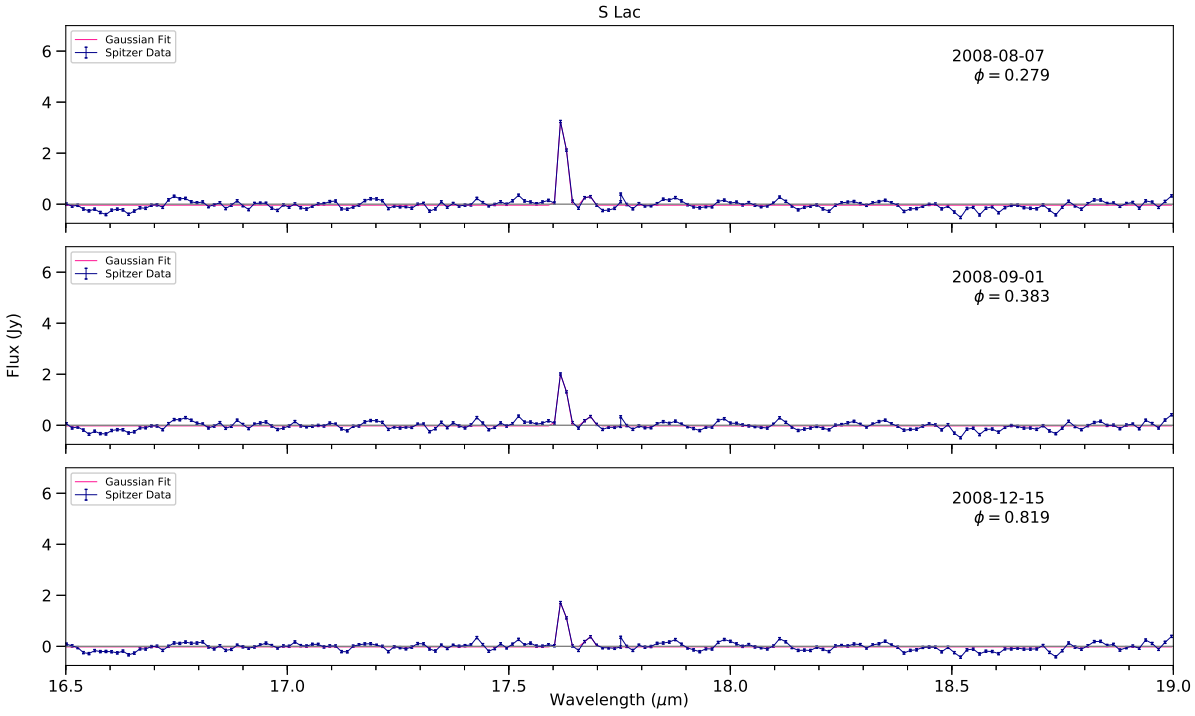

Figure B.10: Gaussian profile fits of the 17.62 μm feature in the M-type S Lac.

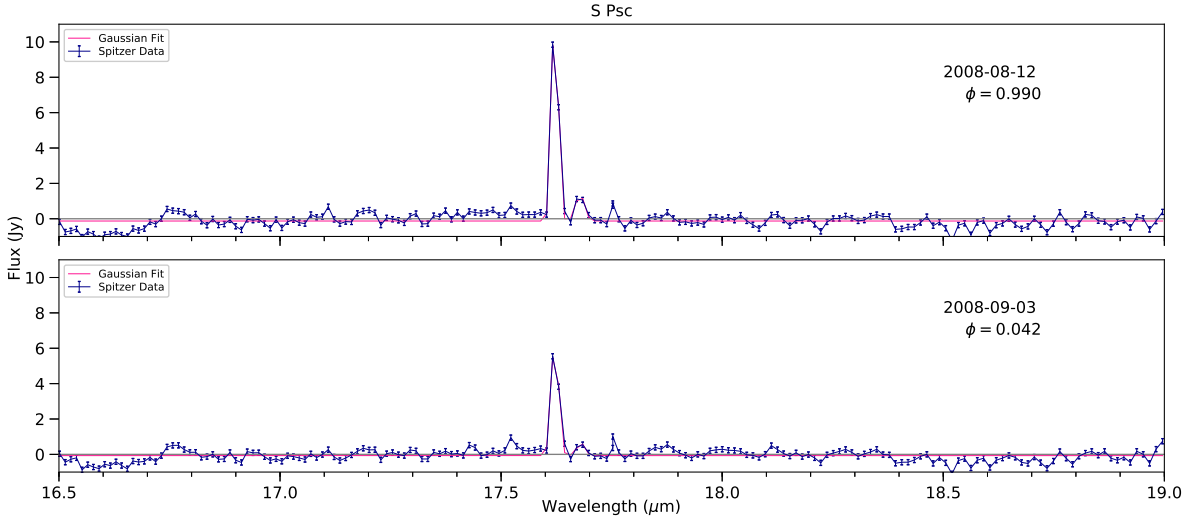

Figure B.11: Gaussian profile fits of the 17.62 μm feature in the M-type S Psc.

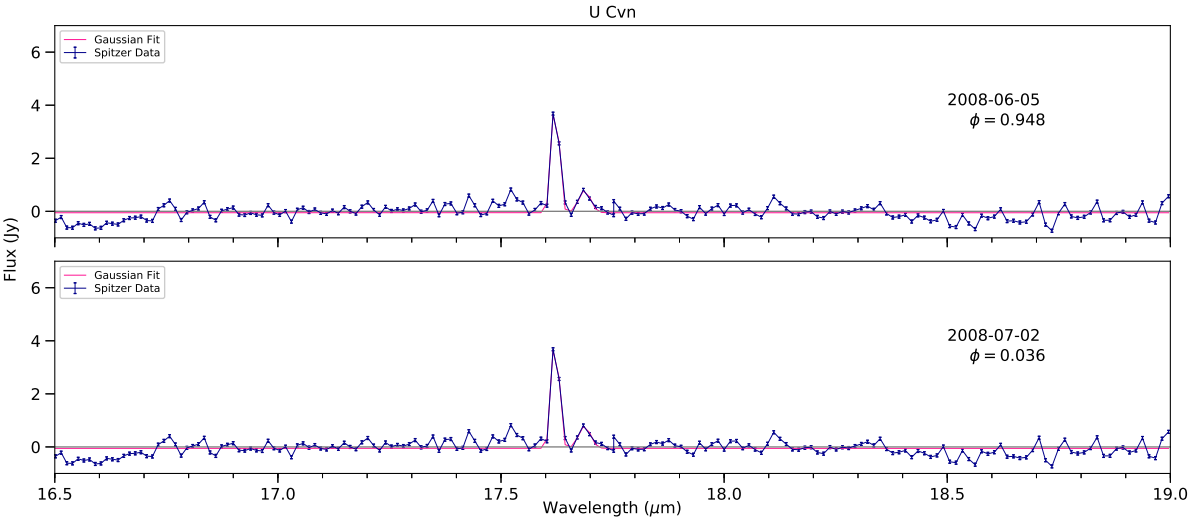

Figure B.12: Gaussian profile fits of the 17.62 μm feature in the M-type U Cvn.

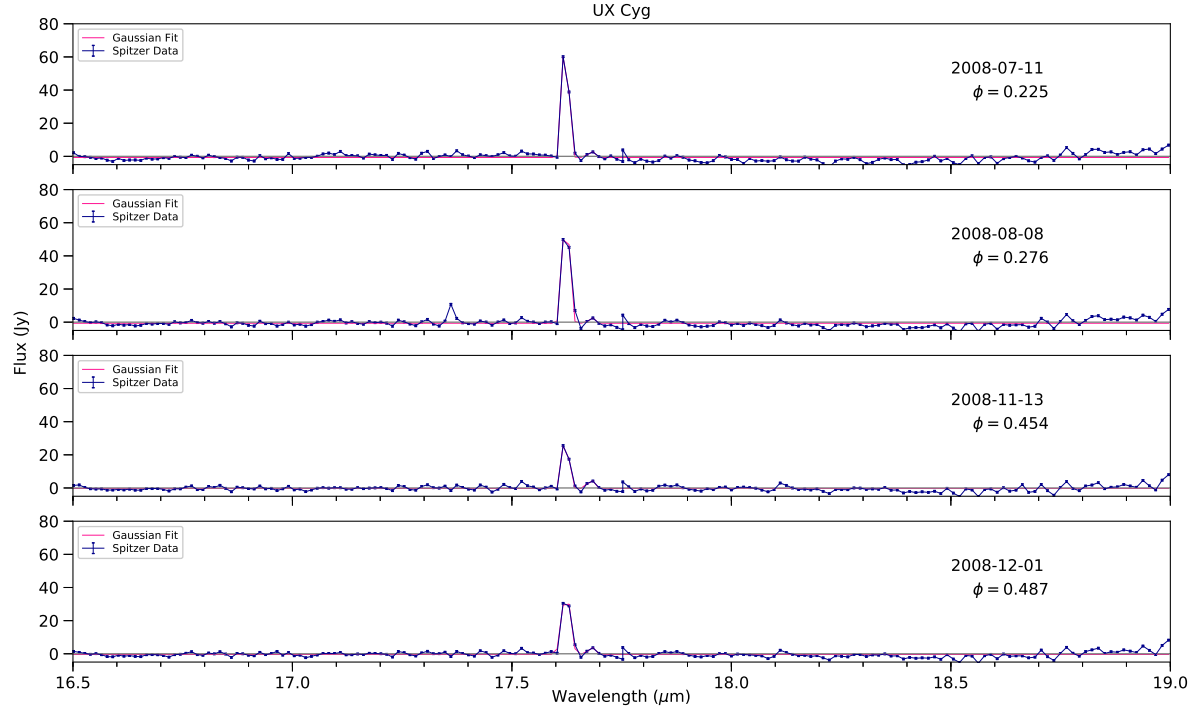

Figure B.13: Gaussian profile fits of the 17.62 μm feature in the M-type UX Cyg.

B.1.2 S-types

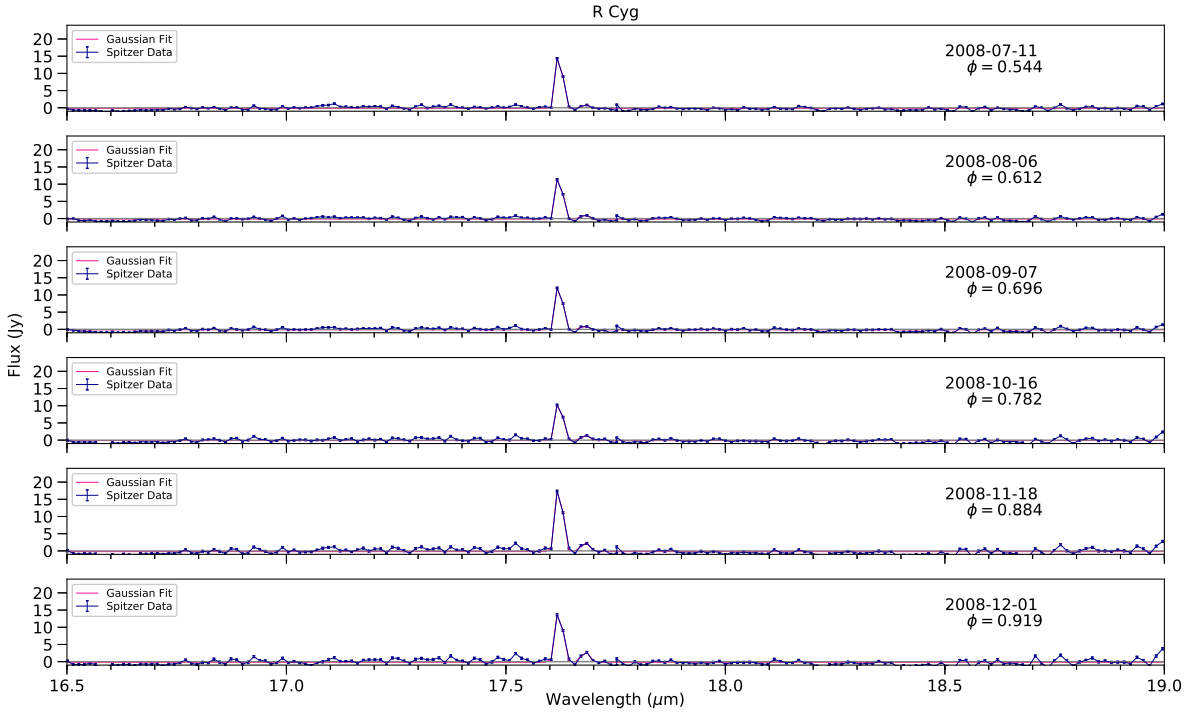

Figure B.14: Gaussian profile fits of the 17.62 μm feature in the S-type R Cyg.

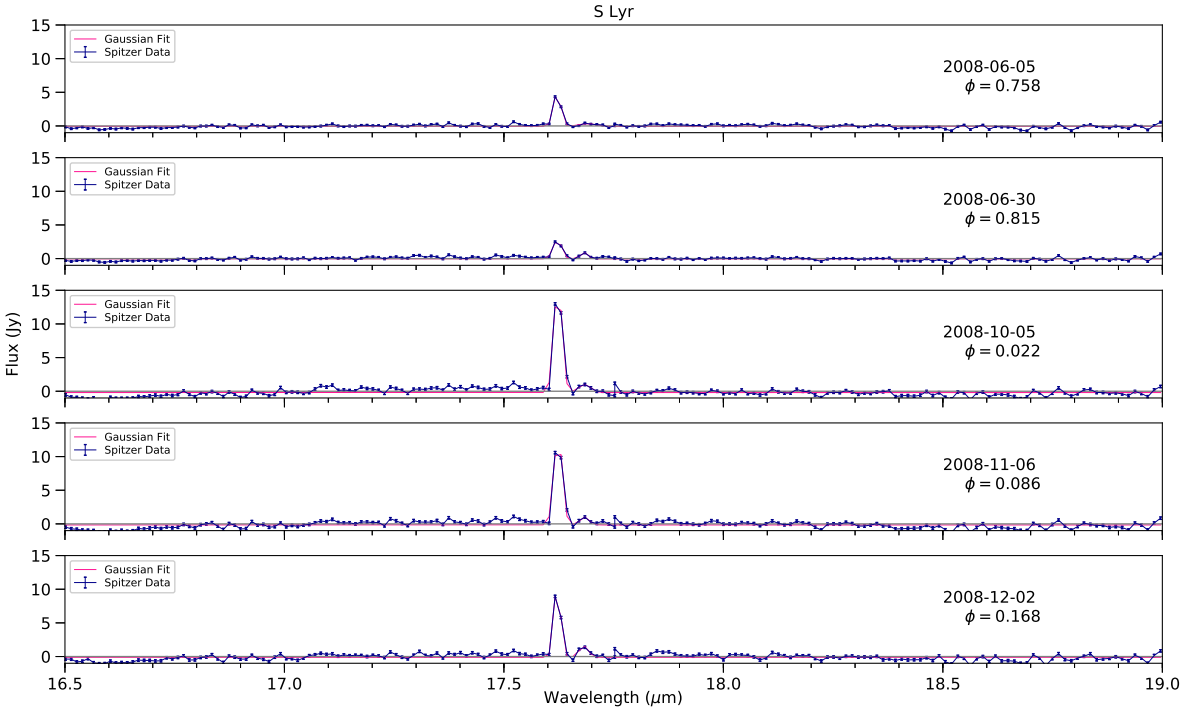

Figure B.15: Gaussian profile fits of the 17.62 μm feature in the S-type S Lyr.

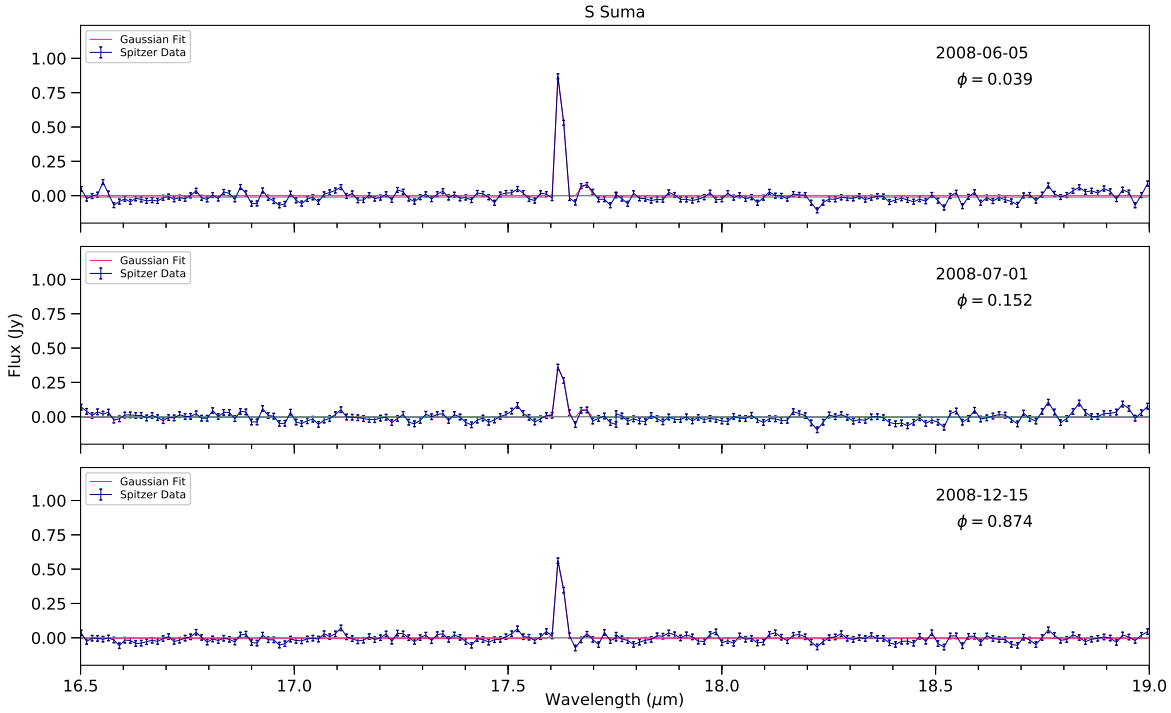

Figure B.16: Gaussian profile fits of the 17.62 μm feature in the S-type S Uma.

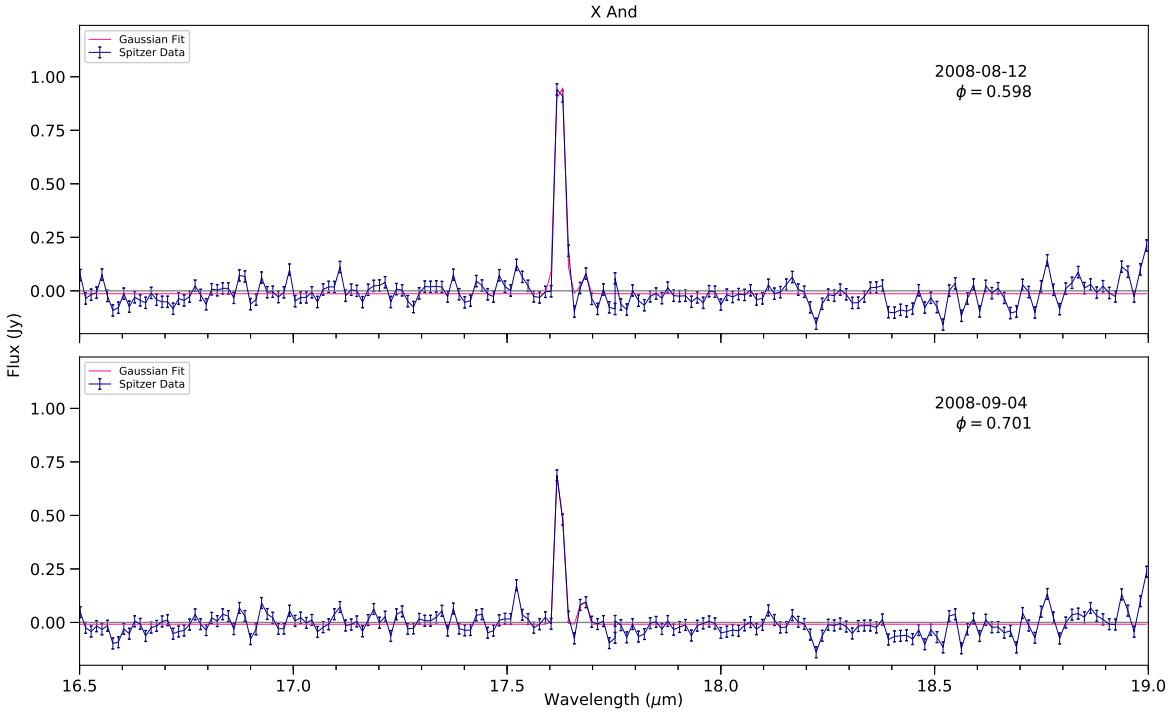

Figure B.17: Gaussian profile fits of the 17.62 μm feature in the S-type X And.

B.1.3 C-types

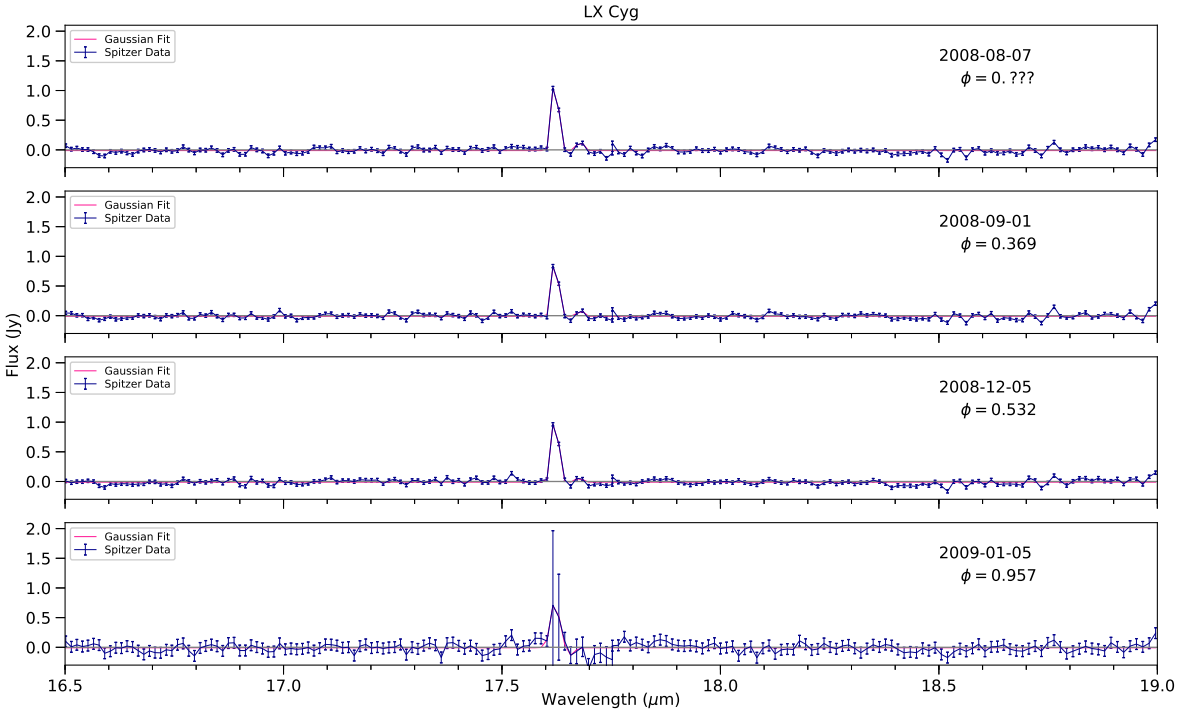

Figure B.18: Gaussian profile fits of the 17.62 μm feature in the C-type LX Cyg.

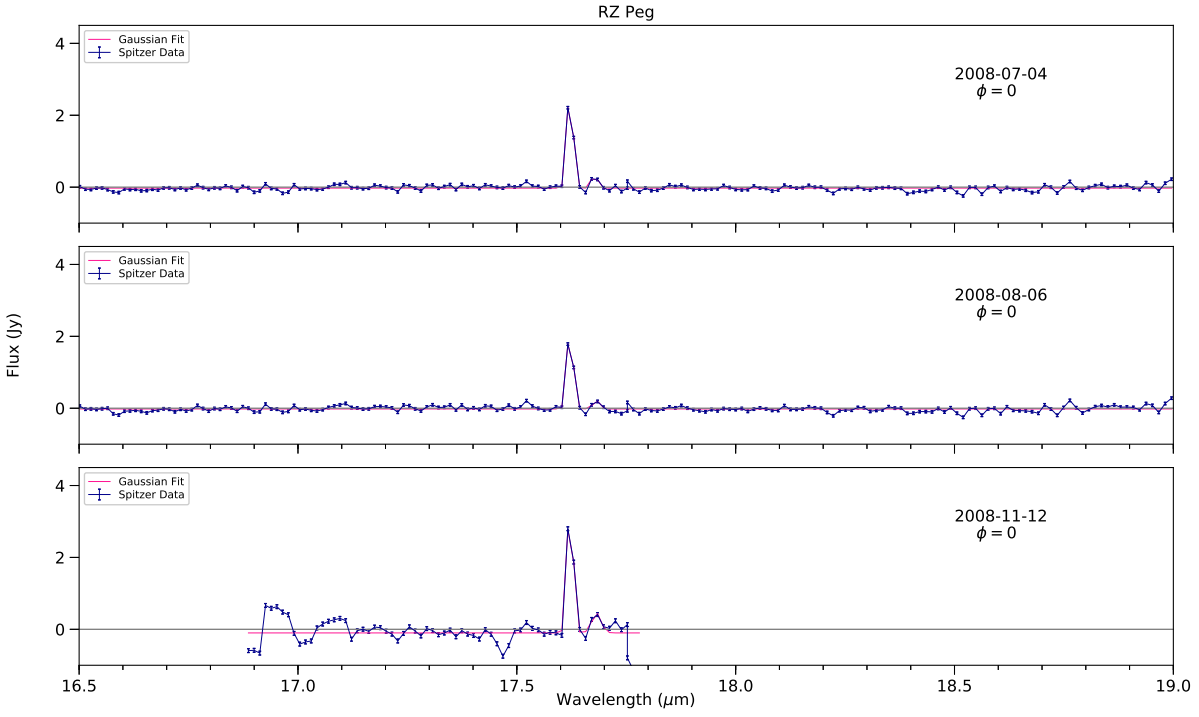

Figure B.19: Gaussian profile fits of the 17.62 μm feature in the C-type RZ Peg.

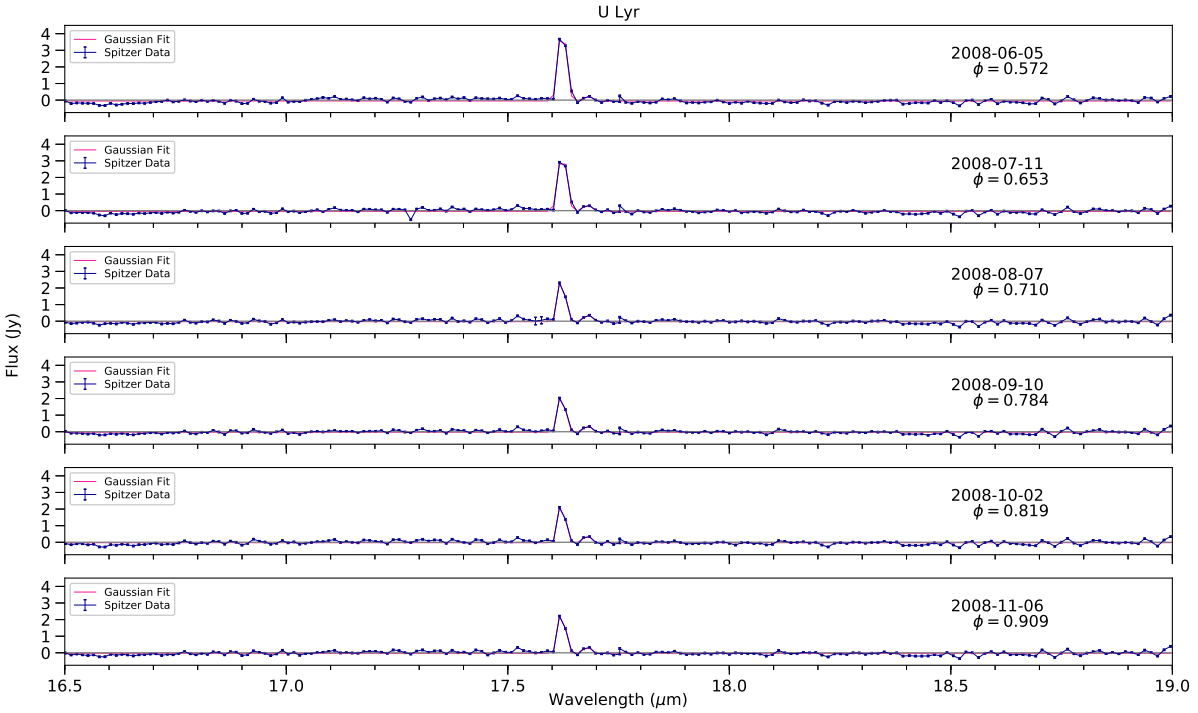

Figure B.20: Gaussian profile fits of the 17.62 μm feature in the C-type U Lyr.

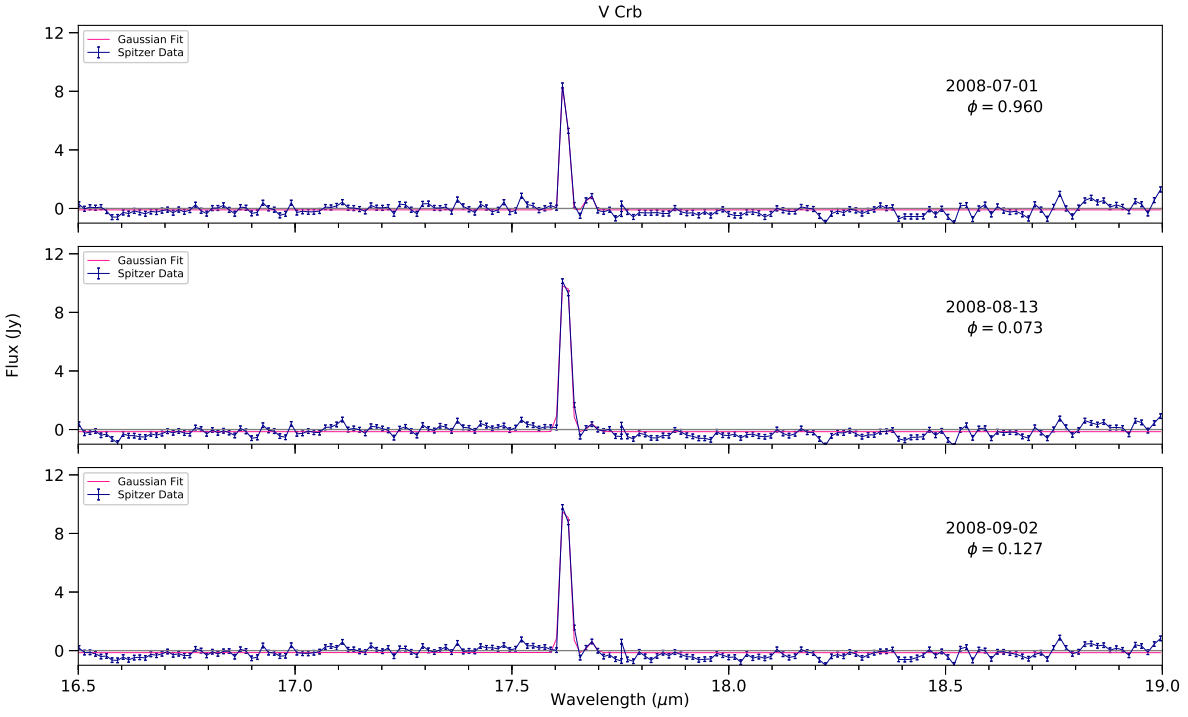

Figure B.21: Gaussian profile fits of the 17.62 μm feature in the C-type V Crb.

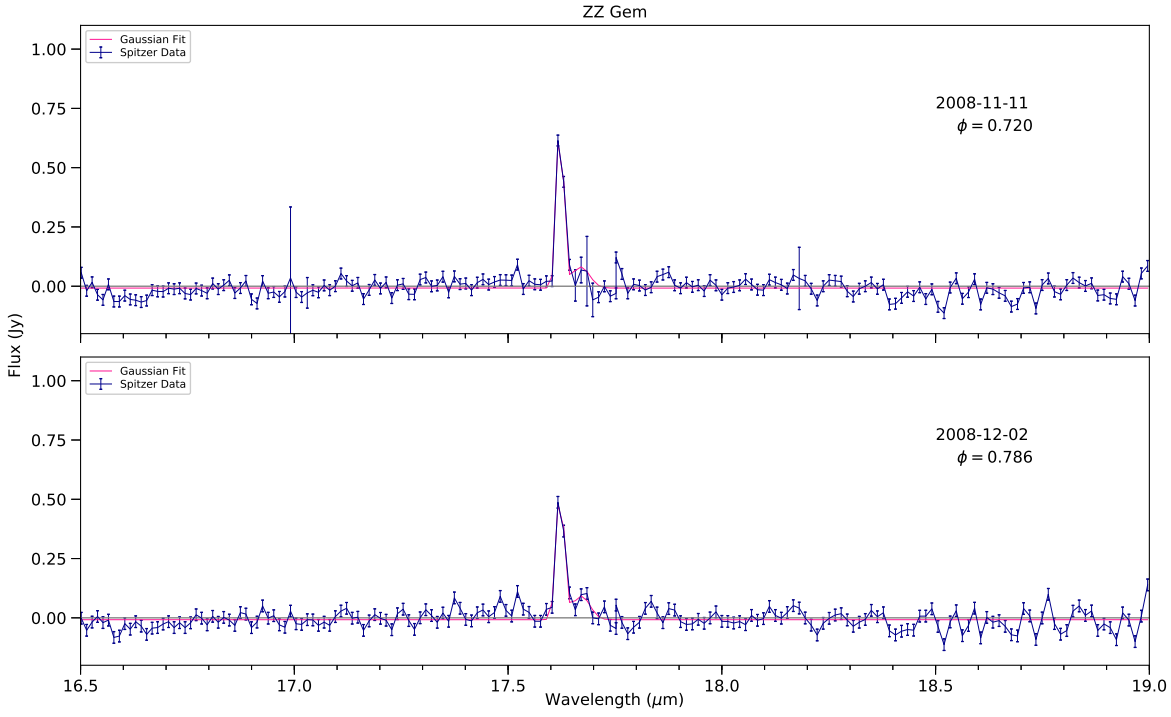

Figure B.22: Gaussian profile fits of the 17.62 μm feature in the C-type ZZ Gem.

APPENDIX C

PERMISSIONS

Permission to use the publication *Mid-IR spectra of the M-type Mira variable R Tri observed with the Spitzer IRS* published in the *Monthly Notices of the Royal Astronomical Society*, Volume 493, Issue 1, p.807-814

Rights retained by ALL Oxford Journal authors

- The right, after publication by Oxford Journals, to use all or part of the Article and abstract, for their own personal use, including their own classroom teaching purposes;
- The right, after publication by Oxford Journals, to use all or part of the Article and abstract, in the preparation of derivative works, extension of the article into book-length or in other works, provided that a full acknowledgement is made to the original publication in the journal;
- The right to include the article in full or in part in a thesis or dissertation, provided that this is not published commercially;

For the uses specified here, please note that there is no need for you to apply for written permission from Oxford University Press in advance. Please go ahead with the use ensuring that a full acknowledgment is made to the original source of the material including the journal name, volume, issue, page numbers, year of publication, title of article and to Oxford University Press and/or the learned society.

The only exception to this is for the re-use of material for commercial purposes, e.g. republication or distribution of an article by a for-profit publisher or medical communications company etc. Permission for this kind of re-use is required and can be obtained by using Rightslink.

With Copyright Clearance Center's Rightslink ® service it's faster and easier than ever before to secure permission from OUP titles to be republished in a coursepack, book, CD-ROM/DVD, brochure or pamphlet, journal or magazine, newsletter, newspaper, make a photocopy, or translate.

- Simply visit: Oxford Academic and locate your desired content.
- Click on (Order Permissions) within the table of contents and/ or at the bottom article's abstract to open the following page:
- Select the way you would like to reuse the content
- Create an account or login to your existing account
- Accept the terms and conditions and permission is granted

For questions about using the Rightslink service, please contact Customer Support via phone 877/622-5543 (toll free) or 978/777-9929, or email Rightslink customer care.

A MID-INFRARED STUDY OF MIRA VARIABLE ATMOSPHERES: PHASE DEPENDENT ANALYSIS OF SPECTRAL LINES OBSERVED WITH THE SPITZER IRS

by

Dana K. Baylis-Aguirre